EFFECTS OF POST-PRINTING HEAT TREATMENT AND ADDITION OF CERAMIC-BASED NANOPARTICLES ON THE MICROSTRUCTURE AND MECHANICAL PROPERTIES OF WIRE ARC ADDITIVE MANUFACTURED PH 13-8Mo MARTENSITIC STAINLESS STEEL

by

Mahya Ghaffari

Submitted in partial fulfilment of the requirements
for the degree of Doctor of Philosophy

at

Dalhousie University
Halifax, Nova Scotia
December 2022

I dedicate my thesis to my beloved husband, **Alireza**, for his endless love and support
and my adorable parents who encouraged and guided me throughout my life.
I also dedicate my thesis to all proud, intelligent, strong, and brave Iranian women.
"**Woman Life Freedom**"

TABLE OF CONTENTS

LIST OF TABLES

LIST OF FIGURES

ABSTRACT

Precipitation hardening martensitic stainless steels offer an outstanding combination of strength and corrosion resistance under harsh environmental conditions while maintaining their moderate toughness. The reasonable weldability of these alloys makes them suitable candidates for wire arc additive manufacturing (WAAM) with a significant deposition rate, high material usage efficiency, and lower capital and fabrication costs as compared to traditional subtractive manufacturing methods. Aiming to accelerate the widespread adoption of this state-of-the-art manufacturing technology, in the first phase of this research, the fabrication feasibility of the PH 13-8Mo martensitic stainless steel through the WAAM was investigated. The obtained results proved the successful fabrication of a sound and defect-free PH 13-8Mo part with a great combination of hardness, ductility, and tensile strength. However, the complex thermal history experienced by different locations of the component caused a gradual increase of microhardness and ultimate tensile strength values along the building direction owing to the non-uniform distribution of residual δ-ferrite and retained austenite. Moreover, the intrinsic directional heat sink towards the substrate resulted in the formation of a columnar structure of primary δ-ferrite grains, leading to a strong cubic texture and anisotropy in ductility. To address this issue, in the second phase of the performed research, different post-printing heat treatment cycles, including solution and aging treatments at different temperatures, were applied on the additively manufactured PH 13-8Mo samples to modify the microstructural features, promote the equiaxed grain structure, eliminate the anisotropic behaviour, and improve the mechanical properties. It was revealed that the solution treatment at 1050 °C for 1 h resulted in the dissolution of undesired δ-ferrite and removal of the columnar structure and anisotropic ductility, while the following aging at 500 °C for 4 h led to the maximum hardness and tensile strength due to the formation of optimum sized β-NiAl precipitates in a fully martensitic matrix. Despite the benefits of post-printing heat treatment, it increases the lead time and cost of the fabrication process, which is contrary to the value proposition of WAAM technology. Thus, in the third phase of this research, the potential grain refinement and strengthening through the introduction of TiC and TiB_2 reinforcing ceramic nanopowders into the molten pool during WAAM processing was investigated. Although both inoculant agents refined the columnar primary δ-ferrite grains and provoked the precipitation of in-situ hard TiC/M_3B_2 phases, TiB_2 nanopowders were found to be a more effective grain refiner as compared to TiC reinforcing particles. Overall, the fabrication feasibility of PH 13-8Mo alloy via WAAM was validated, while further microstructural and mechanical properties improvement was accomplished through the implementation of appropriate post-printing heat treatment cycle or by the addition of TiC and TiB_2 nanopowder inoculants during the deposition process.

LIST OF ABBREVIATIONS AND SYMBOLS USED

3D	Three-Dimensional
Ac_1	Austenite-Start Temperature
Ac_3	Austenite-Finish Temperature
Ac_4	Ferrite-Start Temperature
AF	Acicular Ferrite
AM	Additive Manufacturing
APS	Average Particle Size
B	Bainite
BCC	Body-Centred Cubic
BD	Building Direction
C_0	Solute Concentration
Cr_{eq}	Chromium Equivalent
CSLM	Confocal Scanning Laser Microscope
CX	Corrax®
d	Grain Size
DED	Directed Energy Deposition
DMLS	Direct Metal Laser Sintering
EBM	Electron Beam Melting
EBSD	Electron Backscattered Diffraction
EDS	Energy-Dispersive X-ray Spectroscopy
E_r	Reduced Elastic Modulus
ER	Elastic Recovery
F	Ferrite
FCC	Face-Centered Cubic
FESEM	Field Emission Scanning Electron Microscope
G	Gibbs Free Energy
GMA	Gas Metal Arc
GMAW	Gas Metal Arc Welding
GTA	Gas Tungsten Arc
HAZ	Heat Affected Zone
H_{ind}	Indentation Hardness
HIP	Hot Isostatic Pressing
HRTEM	High-Resolution Transmission Electron Microscope
ICDD	International Centre for Diffraction Data
IPF	Inverse Pole Figure
k	Equilibrium Solute Partition Coefficient
L_0	Original Length
LBM	Laser Beam Melting
L-PBF	Laser-Powder Bed Fusion
LPI	Liquid Penetrant Inspection
M	Martensite
MA	Martensite-Austenite
M_f	Martensite Finish

M_l	Liquidus Slope
MMC	Metal Matrix Composite
M_s	Martensite Start
MSS	Martensitic Stainless Steel
Ni_{eq}	Nickel Equivalent
OM	Optical Microscope
P	Perlite
PA	Plasma Arc
PAG	Primary Austenite Grain
PBF	Powder Bed Fusion
PF	Pole Figure
PF	Polygonal Ferrite
PH	Precipitation Hardening
PHMSS	Precipitation Hardening Martensitic Stainless Steel
PI	Plasticity Index
PMZ	Partially Melted Zone
PoSAP	Position-Sensitive Atom Probe
PTA	Plasma Transferred Arc
PVA	Polyvinyl Alcohol
Q	Growth Restriction Factor
RT	Radiographic Testing
SAED	Selected Area Electron Diffraction
SEM	Scanning Electron Microscope
SLM	Selective Laser Melting
SS/AP	Non-Inoculated/As-Printed
SS+TiB_2/AP	TiB_2-Inoculated/As-Printed
SS+TiC/AP	TiC-Inoculated/As-Printed
SS/HT	Non-Inoculated/Heat-Treated
SS+TiB_2/HT	TiB_2-Inoculated/Heat-Treated
SS+TiC/HT	TiC-Inoculated/Heat-Treated
STEM	Scanning Transmission Electron Microscope
STEM-BF	STEM in Bright-Field Mode
STT	Surface Tension Transfer
TEM	Transmission Electron Microscope
U_e	Elastic Energy
U_p	Plastic Energy
U_t	Total Indentation Work
UT	Ultrasonic Testing
UTS	Ultimate Tensile Strength
WAAM	Wire Arc Additive Manufacturing
X-FEG	Extreme-Field Emission Gun
XRD	X-Ray Diffraction
γ	Retained Austenite
ΔL	Change in Length
μ	Average Lath Size
σ	Standard Deviation

ACKNOWLEDGEMENTS

First and foremost, I would like to express my sincere gratitude to my supervisor, Dr. Ali Nasiri, for his continual support, guidance, motivation, and particularly his patience throughout my Ph.D. program.

I am also very grateful to the rest of my supervisory committee, Dr. Kevin Plucknett and Dr. Kyle Tousignant for their insightful comments and motivations.

My sincere thanks also go to Dr. Mohsen Mohammadi, who provided me with an opportunity to collaborate with his research team and gave me access to the research facilities.

My appreciation also goes to my colleagues in our research group who contributed to my research activities and without them this research would have been vastly more difficult.

Finally, I must express my special thanks to my adorable husband, Alireza, for his love, scientific support, and unwavering patience during this challenging journey.

CHAPTER 1 INTRODUCTION

1.1 INTRODUCTION TO PRECIPITATION HARDENING MARTENSITIC STAINLESS STEELS

Precipitation hardening (PH) stainless steels are principally classified into three main categories, *i.e.*, austenitic, semi-austenitic, and martensitic stainless steels based on the stable phase as the matrix at room temperature [1]. The outstanding combination of strength and corrosion resistance, in addition to the moderate toughness, distinguishes the precipitation hardening martensitic stainless steels (PHMSSs) from other types of PH stainless steels [2][3]. Owing to their excellent properties, PHMSSs have a wide range of applications in different industries, including petrochemical, offshore, oil and gas, aerospace, shipbuilding, and defense sectors to fabricate various components, such as valves, fasteners, shafts, gears, jet engine parts, molding dies, and turbine blades [1][4][5][6]. The dominant chemical composition of these types of alloys consists of 13-17 wt.% Cr and 4-8 wt.% Ni, while carbon content is essentially less than 0.07 wt.%. Additionally, PHMSSs comprise other substitutional alloying elements, such as Nb, Cu, Al, Ti, and Mo to attain the required properties after heat treatment [4][7][8].

The PHMSS alloys are typically characterized by an austenite to martensite transformation, completing at a temperature just above room temperature; however, the obtained martensite contains a low carbon content, making it a soft matrix with a low hardness level [9][10]. Therefore, the primary source of strength in these alloys stems from the precipitation of different fine intermetallic compounds, including β-NiAl, Ni_3Al, Ni_3Ti, or copper-rich phases, which act as barriers to dislocation mobility [8][10][11][12]. In order for these hard phases to precipitate in the predominantly tough martensitic matrix, solution treatment is applied on PHMSS alloys at a temperature in the austenite single-phase region (above 850 °C) to attain a supersaturated martensitic structure, followed by subsequent aging treatment for 1 to 5 h at temperatures between ~400 and 600 °C [4][7][8][10]. Based on the content of alloying elements and heating/cooling rate, the precipitation process begins at 400-550 °C and ends at a temperature range of 500-600 °C [5][10]. However, the peak strength can be reached at a particular temperature, depending on the type, size, shape, distribution, coherency, and volume percentage of the precipitates [11][12]. For example, Ping *et al.* [8] performed aging treatment on a 13Cr–8Ni–2.5Mo–2Al PHMSS alloy at different temperatures ranging from 450 to 620 °C, and claimed that the maximum strength was achieved at 510 °C (see Figure 1.1), owing to the precipitation of high content of spherical nano-scale β-NiAl phases with great coherency with the martensitic matrix [8].

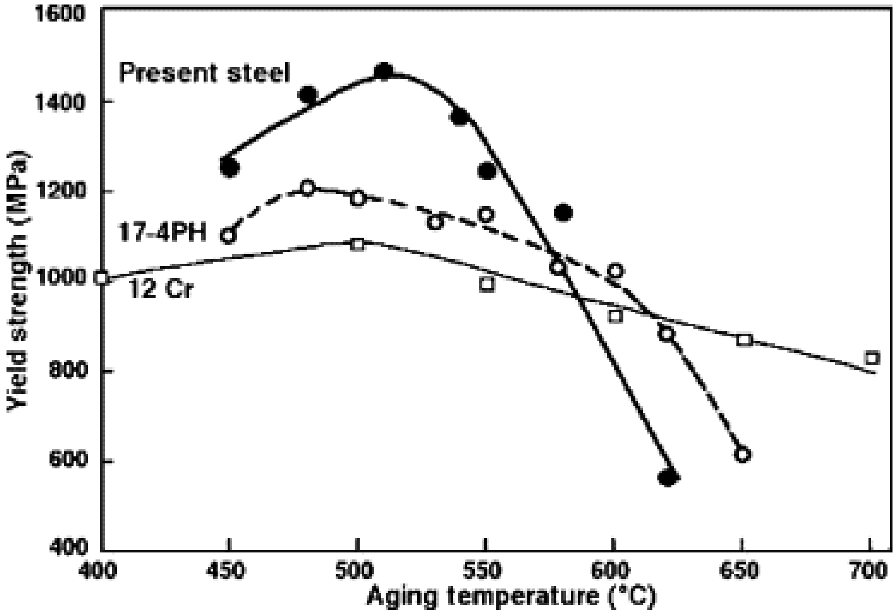

Figure 1.1 Effect of aging temperature on the yield strength of 12 Cr, 17-4PH, and 13Cr–8Ni–2.5Mo–2Al PH (denoted as present steel) alloys [8].

Different traditional manufacturing methods, such as casting, forging, and hot rolling, are usually employed to fabricate high-strength PHMSS components with poor formability and machinability, which induce a long design-to-market time and consequently higher cost to reach the finished product [13][14]. Recently, additive manufacturing (AM) technology has attracted lots of interests in developing PHMSS parts to benefit from the luxury of one-step fabrication of near-net-shape components, which considerably reduces production time and cost [13][15][16].

1.2 ADDITIVE MANUFACTURING TECHNOLOGY

Additive manufacturing, also known as three-dimensional (3D) printing or rapid prototyping, is a novel technique for manufacturing 3D-shaped components based on the layer-by-layer incremental deposition concept, which is a great alternative to traditional subtractive methods [17][18]. AM, as a flexible production technology, enables the development of metal matrix composites (MMCs) and customized functionally graded materials with unique applications, which are challenging to accomplish using conventional fabrication processes [17][18][19]. In recent decades, several AM methods have been developed for 3D-printing of a wide range of materials, including metals, ceramics, concretes, and polymers [20]. There are various approaches for classifying different AM systems according to different criteria. In a common approach, metallic AM methods can be categorized in terms of the adopted feeding technique of the feedstock material (either powder or wire) into two major types, *i.e.*, powder bed fusion (PBF) processes and directed energy deposition (DED) techniques [21]. Besides, a variety of power sources, including laser, electric arc, plasma, and electron beam, are employed in different processes [22]. Figure 1.2 shows the classification of different fusion-based AM methods for metallic components under two categories of PBF and DED systems. It should be pointed out that both PBF and DED techniques have been utilized for 3D-printing of PHMSS components in the published literature. These two categories will be briefly described in the following sections.

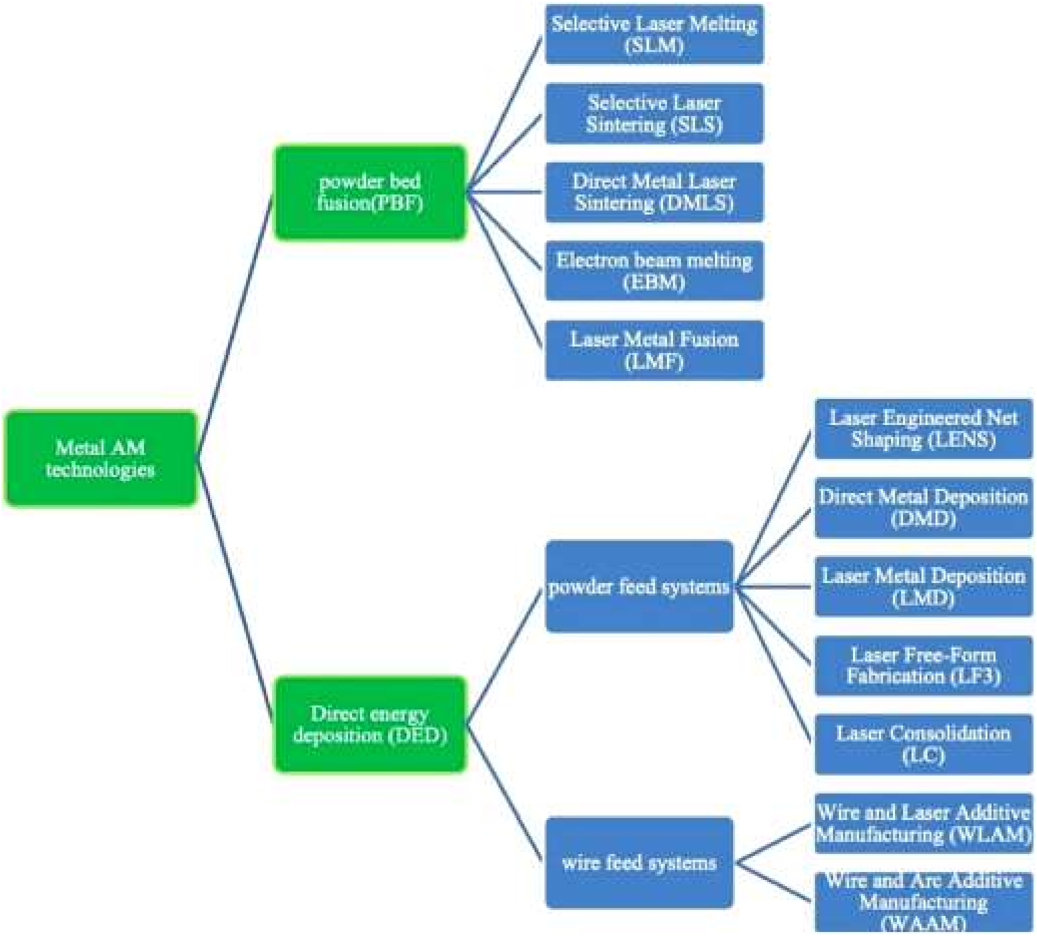

Figure 1.2 Classification tree of fusion-based AM methods based on the feeding technique of the feedstock material [23].

1.3 POWDER BED FUSION PROCESSES

In the PBF technique, a focused high-energy beam is programmed to selectively fuse (melt or sinter) a thin surface layer of a metallic powder bed in a layer-wise manner to build the designed 3D component [22][23]. The PBF processes are primarily suitable for fabricating small metallic parts with complex geometry, high resolution, great surface quality, and near-full density [22]. However, slow processing time, large number of process parameters, and high material waste are the main drawbacks of PBF processes [20][24]. Based on the energy source, laser-powder bed fusion (L-PBF) and electron beam melting (EBM) are two dominant divisions of PBF processes. In the L-PBF process, a focused laser beam melts the selected areas of a thin metal powder layer, according to 3D model data [23][25]. After completion of the laser scanning, the platform moves downward by one layer of thickness, allowing an additional layer of fresh powder to be added on the previously deposited surface, and the layer-by-layer fabrication is then repeated until the required bulk-form object is obtained [23][26]. The whole fabrication process is performed within a controlled atmosphere building chamber, which is filled with purified argon or nitrogen to prevent oxidation of the heated metallic component [25]. Figure 1.3 shows a schematic representation of the L-PBF process.

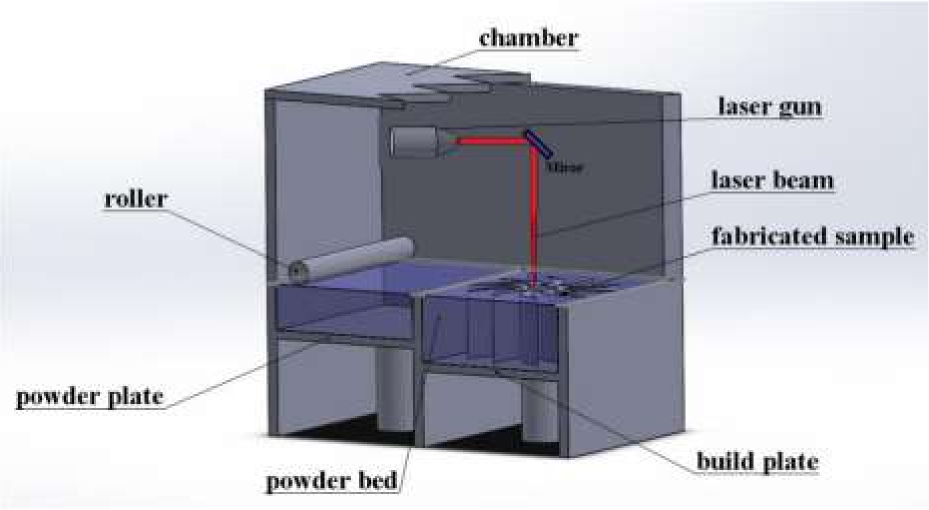

Figure 1.3 Schematic illustration of the L-PBF process [23].

In contrast to the L-PBF technology, the EBM system utilizes a high-energy density electron beam instead of the laser beam to fuse the metallic powders, which consequently requires a vacuum environment to allow the smooth transfer of electrons in the building chamber [27][28]. The electron beam is generated using a tungsten filament, accelerated with a high voltage, and then focused using electromagnetic lenses toward the building platform [27]. Figure 1.4 schematically demonstrates the EBM technique. Although the requirements for a vacuum chamber in the EBM technology lead to higher capital investments, EBM-fabricated parts are generally characterized by lower residual stress levels as compared to L-PBF, which eliminates post-process stress-relieving heat treatment [29]. However, the electron beam is slightly broader than the laser beam, resulting in less dimensional accuracy and lower quality of the surface finish [22].

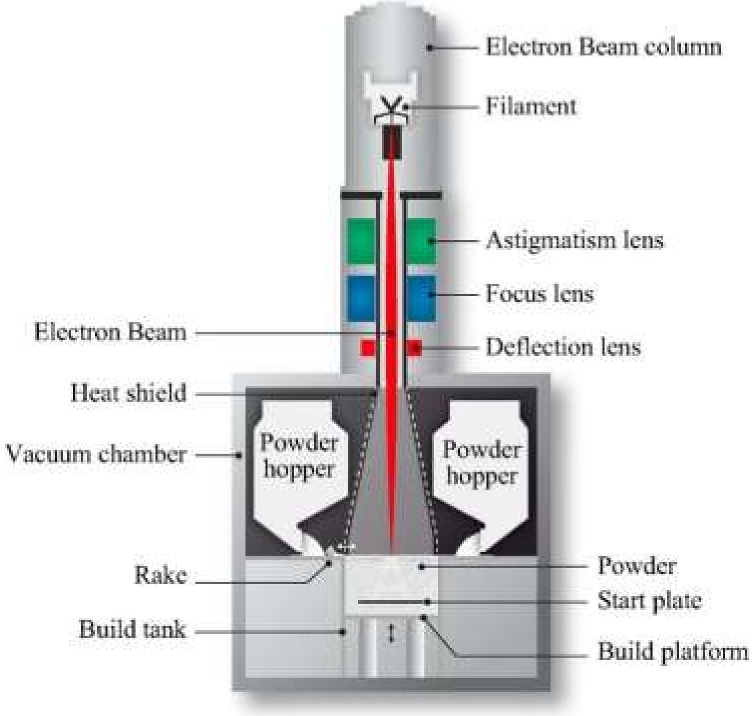

Figure 1.4 Schematic illustration of the EBM process [29].

1.4 DIRECTED ENERGY DEPOSITION

In the case of the DED processes, instead of a powder bed, the feedstock material (either powder or wire) is directly fed through a nozzle to selectively deposit the material layer by layer. The major benefit of DED processes, as opposed to PBF methods, is the capability of employing wire as the feedstock material, which offers high feedstock usage efficiency, avoiding the required powder recycling operations, and decreasing health and safety problems associated with fine powders [30]. Complementary to this, is the lower cost, greater availability, and broader options to select wire supplies as compared to powder products [31]. The most well-known DED process is wire arc additive manufacturing (WAAM), which implements an electric/plasma arc as the energy source, providing unconfined build volumes and significantly higher deposition rate (3–10 kg/h) as compared to PBF methods (0.1–0.6 kg/h) [22][30][32]. Therefore, the WAAM technique has great potential for fabricating medium to large-scale near-net shape components with more affordable capital investment as compared to PBF systems [22][30][31][32]. In this manufacturing method, the arc-based torch is typically mounted on a robotic arm connected to a computer controller, which is able to produce parts with low to medium complexity in design, and also repair large components [20][33]. Based on the arc source utilized to melt the feedstock wire, the WAAM technique is classified as gas tungsten arc (GTA), gas metal arc (GMA), and plasma arc (PA) processes [34]. Figure 1.5 shows a schematic illustration of the WAAM process using a GMA power source, which is the most commonly utilized process with higher heat input than other WAAM energy sources [34][35]. It was reported that the implementation of double electrode GMA technique could minimize the heat input and enhance the material usage efficiency to around 13% as compared to the normal GMA-based WAAM process [36].

The fabrication feasibility of engineering components using WAAM process has been investigated for a broad window of metallic materials ranging from Al-based [37][38], Ni-based [39][40], and Ti-based [41][42] to steels [43][44][45] and stainless steels, such as SS 316L [46][47], ER2594 [48], and 420 MSS [49][50]. Theoretically, weldability is the most crucial aspect affecting the WAAM fabrication feasibility since the process is developed from conventional multi-pass arc welding technology and relies on depositing consecutive weld beads on top of each other to build the whole component [31][51]. Consequently, PHMSS alloys with reasonable weldability are promising candidates for 3D-printing using the WAAM technique [31]. However, based on the existing literature, the majority of the published works on the AM-fabricated PHMSS parts have been predominantly focused on L-PBF methods, while limited studies were reported on employing the WAAM process [15][52]. Considering the distinct advantages of WAAM as compared to L-PBF methods, it offers great potential to fabricate large-scale engineering PHMSS components with elevated deposition rates and lower production and capital costs [6][53]. Regardless of the recent development of the WAAM process, the 3D-printing of ferrous materials using this technique comes with a number of metallurgical challenges, which will be discussed in the following section.

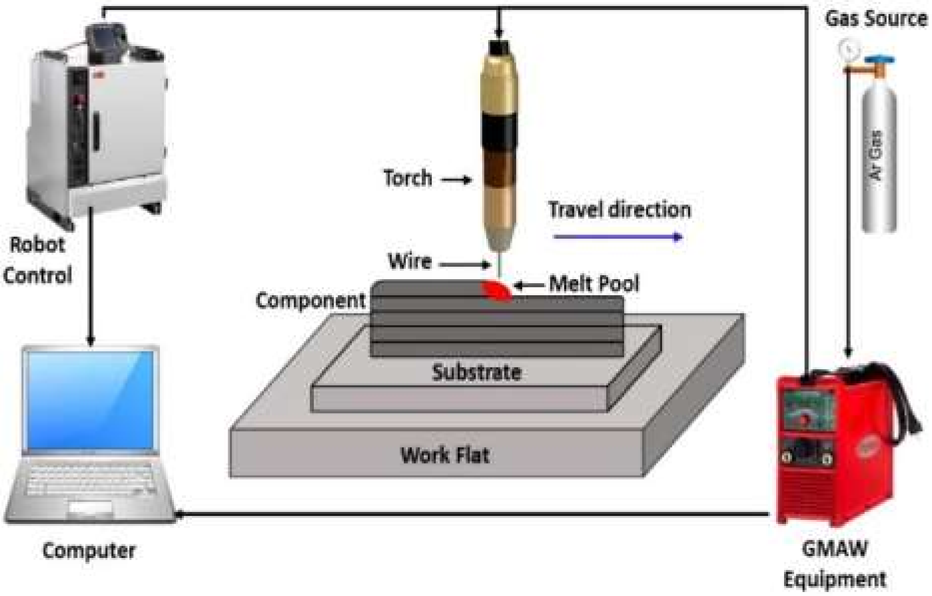

Figure 1.5 Schematic illustration of the WAAM process [54].

1.5 CHALLENGES WITH WAAM PROCESSING OF FERROUS ALLOYS

In recent years, several studies [36][55][56] have been conducted to investigate the technological challenges and metallurgical issues for WAAM processing of different ferrous alloys. One prominent metallurgical issue is associated with the dependence of the steel microstructure on the cooling rate during the manufacturing process, which leads to the segregation phenomena and the formation of non-equilibrium phases during rapid solidification [57][58]. It has been reported that different cooling rates along the building direction during the WAAM fabrication of 2Cr13 MSS resulted in various volume fractions of martensite and ferrite at different heights of the part [59]. Moreover, the retention of δ-ferrite as an undesirable non-equilibrium phase was observed in different studies on the WAAM fabrication of MSS parts as a result of rapid solidification [15][60][61][62]. It is well-established that the formation of residual δ-ferrite in the MSS microstructure is detrimental to the mechanical properties and corrosion resistance of the material [61][63][64]. Therefore, adopting the optimum process parameters is crucial to obtain a desired microstructure with an excellent combination of required properties according to the final service condition.

Another complexity during the WAAM processing of metallic materials is the steep directional temperature gradient, which could potentially cause preferred directionality in grain growth and textured columnar structure in the as-printed condition [18]. Moreover, the complex thermal cycles during successive melting and solidification of consecutive layers may result in potential side effects, such as non-uniform microstructure, solidification defects, and various mechanical properties at different locations or orientations of the WAAM-fabricated parts [65][66][67][68]. For example, Liberini *et al.* [69] observed microstructural heterogeneity along the building direction of a wall-shape WAAM-fabricated ER70S-6 component, characterized by a ferritic-pearlitic microstructure at the lower zone, equiaxed ferrite grains in the middle, and a bainitic lamellar structure at the top regions. The observed microstructural variation was attributed to the different thermal cycles experienced by different areas of the component during the deposition process [69]. In another study, Xu *et al.* [43] investigated the relationship between the microstructure and anisotropic tensile strength of an additively fabricated maraging steel, and concluded that both yield and ultimate tensile strengths (UTS) were higher in the horizontal direction than that of the vertical direction. The authors also observed hardness and tensile strength increment from the top to the bottom regions of the part, correlated to the presence of layer bands formed in the as-printed condition, as shown in Figure 1.6 [43]. To address the aforementioned problems associated with the WAAM process, several strategies have been suggested in the literature. Some of the solutions are applied during the deposition process, such as the implementation of in-situ processing methods, including laser shock peening [70], inter-pass cold rolling [71], and ultrasonic needle peening [72], or inoculation with alloying/ceramic additions [73]. On the other hand, some solutions are employed after the printing process, such as post-printing heat treatment and hot isostatic pressing (HIP) [21][58].

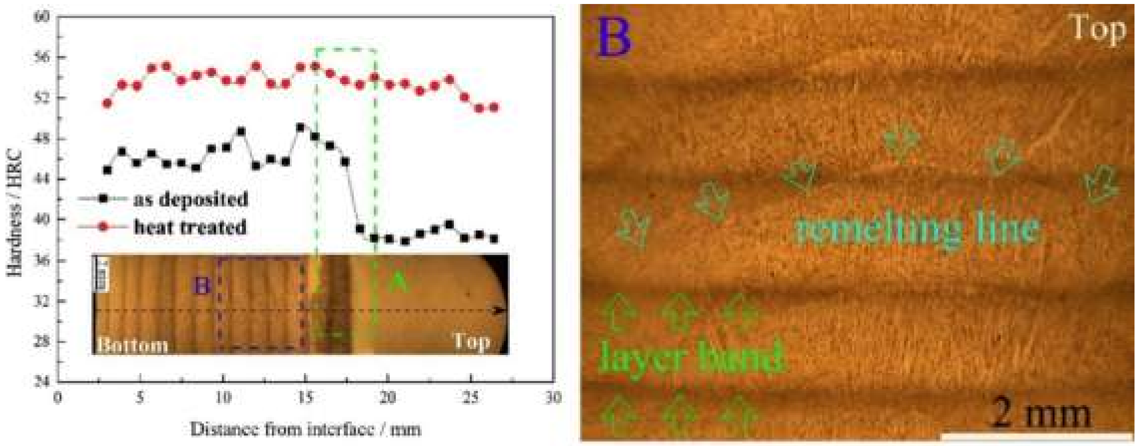

(a) microhardness measurements (b) enlarged Zone B

Figure 1.6 (a) Microhardness profile and (b) macrostructure of the WAAM-fabricated maraging steel [43].

1.6 POST-PRINTING HEAT TREATMENT OF ADDITIVELY MANUFACTURED PHMSS PARTS

Post-printing heat treatment of the printed materials is frequently conducted to control the microstructural features, relieve residual stresses, weaken the texture, minimize the orientation dependence of mechanical properties, and provide a range of mechanical properties for specific applications [21]. For example, Caballero *et al.* [45] successfully homogenized the microstructure and eliminated the columnar structure and anisotropic tensile behavior in a WAAM-fabricated 17-4 PH stainless steel by applying solution and aging treatments at 1040 and 480 °C, respectively.

PH 13-8Mo, 17-4 PH, and 15-5 PH are the most common commercial grades of PHMSS, which are identified by the amounts of Cr (first number) and Ni (second number) as their primary alloying elements [74][75]. According to the literature, PH 13-8Mo provides superior strength, fracture toughness, and ductility in addition to greater resistance to stress corrosion cracking, pitting, and hydrogen embrittlement in comparison to other widely used grades of PHMSS [4][5][7][76][77][78]. For the first time, Guo *et al.* [5] comprehensively investigated the formation of small precipitates during the aging of a wrought PH 13-8Mo alloy utilizing a position-sensitive atom probe (PoSAP) instrument, and reported that the NiAl-enriched zones begin to emerge after 15-40 min of aging at 510 °C and even after less than 6 min of aging at 593 °C [5]. Li *et al.* [4] suggested that the excellent strength of PH 13-8Mo alloys arises from the perfect coherency and low lattice mismatch of β-NiAl precipitates with the martensitic matrix, forming a strong precipitate/matrix interface.

It should be noted that the mechanical behaviour of the PH 13-8Mo alloy is also determined by the relative amount of other secondary phases, such as carbides and reverted austenite, which may form depending on the aging time and temperature [79]. For example, it has been reported that the reversion of austenite during overaging at 620 °C reduced the hardness value, while improving sulfide stress corrosion cracking resistance in a laser welded PH 13-8Mo MSS [80]. Therefore, a fundamental understanding of the size, shape, type, and volume fraction of the precipitates and secondary phases is required for heat treatment optimization of PHMSSs according to their intended applications and service conditions [8][12].

Numerous investigations have been carried out to optimize the heat treatment cycle of conventionally fabricated PH 13-8Mo alloys, while there have only been a limited number of studies on the post-printing heat treatment of AM-fabricated counterparts. Due to the distinct microstructural features associated with AM fabricated parts, traditionally recommended heat treatment cycles for conventionally fabricated materials are not necessarily applicable to AM-fabricated parts [81][82]. For example, Hadadzadeh *et al.* [83] investigated the effect of different post-printing heat treatments on the L-PBF-fabricated CX parts, and reported that direct aging treatment significantly increased the hardness of the samples as compared to the common standard solution-aging treatment, owing to the precipitation of β-NiAl phases in addition to the martensite lath size refinement. It should be pointed out that CX (Corrax®) is the commercial name for the PH 13-8Mo alloy powder, developed by EOS GmbH [84]. The recommended heat treatment cycle for CX parts includes solution treatment at 900 °C for 1 h, followed by aging treatment at 530 °C for 3 h, which has been performed on L-PBF-processed CX samples by different researchers [83][84][85][86]. Chang *et al.* [85] reported a significant improvement in hardness value as a result of the recommended solution-aging treatment on the L-PBF-fabricated CX samples as compared to solution-treated or aged samples (see Figure 1.7).

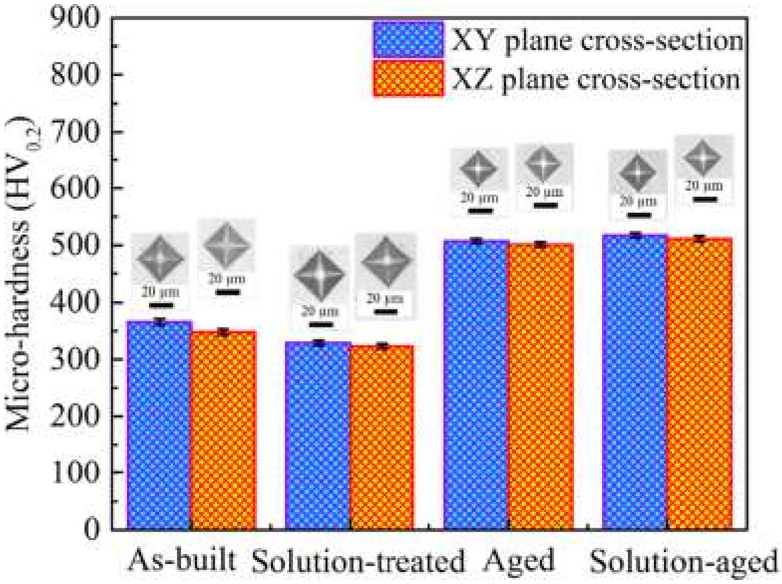

Figure 1.7 Microhardness of the L-PBF-fabricated CX parts after applying different post-printing heat treatment cycles [85].

Despite the aforementioned benefits, adding a post-printing heat treatment step to the production cycle of an engineering part is expected to increase both lead time and cost of the final product, which is contrary to the value proposition of WAAM technology. Moreover, employing a poorly designed post-printing heat treatment cycle can result in excessive oxidation, part distortion, high probability of crack formation/propagation, residual stress accumulation, or even reduced mechanical strength. In addition, the improvement in strength after post-printing heat treatment generally sacrifices the ductility of the material, which is a major concern for PHMSS structural applications [13]. In recent years, introducing alloying elements or ceramic particles as inoculant agents during the WAAM process has been shown to yield an outstanding balance between strength and ductility [13]. This can be obtained by increasing the nucleation sites within the melt pool, which leads to a substantially reduced grain size (or martensite lath size) and also interruption of the columnar grain growth in the PHMSS microstructure [30].

1.7 ADDITION OF CERAMIC-BASED INOCULANTS DURING AM OF PHMSS PARTS

The introduction of inoculant agents to the molten metal for facilitating the grain nucleation process is a widespread practice during traditional casting, while its potential for grain refinement during AM processing has not yet been thoroughly explored [66]. Recently, a limited number of studies investigated the effect of inoculation on the microstructural features, mechanical properties, and corrosion performance of AM-fabricated ferrous alloys using SiC [87], TiC [13][88], WC [89][90], TiB_2 [91], and TiN [92] ceramic particles.

TiC and TiB_2 reinforcing particles were found to be ideal candidates for the inoculation of ferrous alloys due to their great combination of high melting point temperature, excellent hardness, low density, as well as reasonable wear and corrosion resistance [93][94]. In addition, their high-temperature chemical stability and excellent wettability in molten iron make TiC and TiB_2 suitable reinforcing agents for fabricating Fe-based MMCs [95][96]. AlMangour *et al.* reported several attempts on the addition of TiC and TiB_2 reinforcements into the powder bed during the L-PBF processing of 316L stainless steel [17][26][93][97][98] and H13 steel [95][99], resulting in grain refinement and better physical and mechanical properties as compared to the non-inoculated counterparts [17][26]. It is notable that the nano-size inoculant agents can provide a more efficient contribution to the resultant mechanical properties due to further grain refinement, higher densification level, and better particle–matrix wettability [26][97].

A systematic literature review on the ceramic inoculation during AM processing of ferrous alloys revealed that most of the existing studies were focused on the L-PBF-fabricated components [13][17][26][93][95][97][99][98][100], while ceramic reinforcing of WAAM-processed steels was only investigated in a single study by Rodrigues *et al.* [67]. As shown in Figure 1.8, they customized the WAAM machine to be able to directly inject the SiC powders during the deposition of successive tracks of a high strength low alloy steel with the purpose of microstructural refinement, promoting equiaxed grains, and enhancing the mechanical properties of the as-printed part [67].

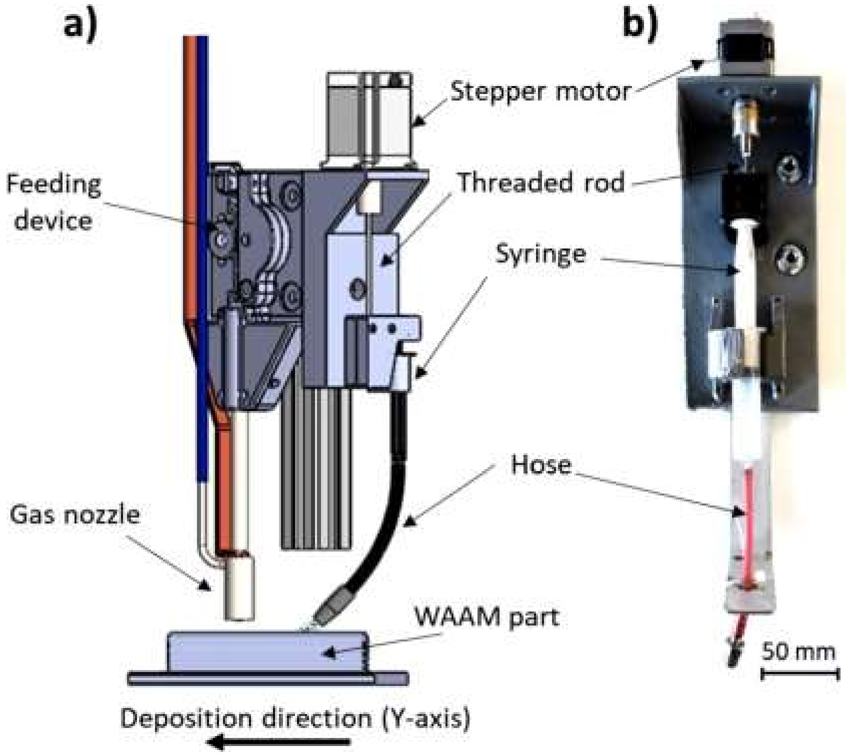

Figure 1.8 (a) Schematic and (b) actual illustration of the customized WAAM machine with the capability of direct injection of powders for in-situ inoculation [67].

1.8 MOTIVATION AND RESEARCH OBJECTIVES

Considering the high market demand for decreasing the fabrication steps, reducing lead time, down-sizing the on-hold inventory, and minimizing the number of components in a distinct structure, AM technology has the potential to revolutionize the fabrication methodology and supply chain systems by providing on-site fabrication alternatives for metallic components sourcing. However, this state-of-the-art technology has not yet been fully industrialized, primarily due to the lack of in-depth knowledge of the microstructural features and uncertainties in the in-service performance of the additively manufactured parts versus the conventionally fabricated counterparts. Therefore, this Ph.D. research aims to facilitate the adoption of AM technology by disclosing the associated metallurgical challenges and potential solutions to different industrial sectors, wishing to use metal 3D-printing technology as a fast on-site fabrication process to reduce surplus inventory and become self-reliant on their spare parts.

Accordingly, the first phase of this research was aimed to investigate the WAAM fabrication feasibility of PH 13-8Mo MSS with specific applications in the areas of plastic injection molding dies and steam turbine last stage blades [4][101]. In the second phase, different post-printing heat treatment cycles were designed to optimize the in-service performance of the WAAM-fabricated parts. Ultimately, in the third phase, potential grain refinement capacity and strengthening of the alloy were investigated through the addition of ceramic-based TiC and TiB_2 nanopowder inoculants during the deposition process.

1.9 ORGANIZATION OF THE THESIS

This thesis is prepared in a paper-based format, in which the stemmed journal papers on the WAAM processing of the PH 13-8Mo MSS are presented in chapters 2, 3, and 4, followed by overall conclusions and future works in chapter 5. In addition to the above chapters that cover the primary structure of this thesis, the author has been also involved in a few side projects during her Ph.D. program on the WAAM processing of low-carbon low-alloy steel (ER70S-6) and martensitic stainless steel (ER420) alloys, which are presented as appendices 1 and 2 at the end of this thesis. In total, as a result of the research activities during this Ph.D. program, 19 articles were published in or submitted to peer-reviewed journals (five articles as the first author and 14 articles as the co-author). Moreover, the thesis's outcomes were presented at different conferences (three papers as the first author and seven papers as the co-author).
The details of each publication are listed below:

Journal Papers:

1. **Mahya Ghaffari**, Alireza Vahedi Nemani, Sajad Shakerin, Mohsen Mohammadi, Ali Nasiri, "Grain Refinement and Strengthening of PH 13-8Mo Martensitic Stainless Steel through TiC/TiB_2 inoculation during Wire Arc Additive Manufacturing", *Submitted to Acta Materialia*, **(IF= 9.209)**.
2. **Mahya Ghaffari**, Alireza Vahedi Nemani, Ali Nasiri, "Microstructural Evolution and Mechanical Performance after Precipitation Hardening of PH 13-8Mo Martensitic Stainless Steel Fabricated by Wire Arc Additive Manufacturing", *Materialia*, Vol. 24, p. 101507 (2022).

3. **Mahya Ghaffari**, Alireza Vahedi Nemani, Ali Nasiri, "Microstructure and Mechanical Behaviour of PH 13-8Mo Martensitic Stainless Steel Fabricated by Wire Arc Additive Manufacturing", *Additive Manufacturing* **(IF= 11.632)**, Vol. 49, p. 102374 (2022).

4. **Mahya Ghaffari**, Alireza Vahedi Nemani, Ali Nasiri, "Interfacial Bonding between a Wire Arc Additive Manufactured 420 Martensitic Stainless Steel Part and Its Wrought Base Plate", *Materials Chemistry and Physics* **(IF= 4.778)**, Vol. 251, p. 123199 (2020).

5. **Mahya Ghaffari**, Alireza Vahedi Nemani, Mehran Rafieazad, Ali Nasiri, "Effect of Solidification Defects and HAZ Softening on the Anisotropic Mechanical Properties of a Wire Arc Additive-Manufactured Low-Carbon Low-Alloy Steel Part", *The Journal of the Minerals, Metals & Materials Society (JOM)* **(IF= 2.597)**, Vol. 71(11), pp. 4215-4224 (2019).

6. Alireza Vahedi Nemani, **Mahya Ghaffari**, Salar Salahi, Ali Nasiri, "On the Microstructural Characteristics and Corrosion Performance of As-Printed and Heat-Treated PH 13-8Mo Martensitic Stainless Steel Fabricated by Wire Arc Additive Manufacturing", *Submitted to Materials Today Communications* **(IF= 3.662)**.

7. Salar Salahi, Alireza Vahedi Nemani, **Mahya Ghaffari**, Ali Nasiri, "On the Interfacial Microstructure and Electrochemical Properties of a 420 Martensitic Stainless Steel Repaired via Wire Arc Additive Manufacturing", *Submitted to Materials Today Communications* **(IF= 3.662)**.

8. Salar Salahi, **Mahya Ghaffari**, Alireza Vahedi Nemani, Ali Nasiri, "Electrochemical Performance of the Interfacial Region between an AISI 420 and a Wire Arc Additive Manufactured PH 13–8Mo Martensitic Stainless Steel", *Submitted to Materials Chemistry and Physics* **(IF= 4.778).**

9. Jonas Lunde, Salar Salahi, Alireza Vahedi Nemani, **Mahya Ghaffari**, Ali Nasiri, "Effect of the Tempering Process on the Corrosion Performance of Wire Arc Additively Manufactured 420 Martensitic Stainless Steel", *Corrosion* **(IF= 1.770)**, Vol. 78(9), pp. 850-864 (2022).

10. Alireza Vahedi Nemani, **Mahya Ghaffari**, Ali Nasiri, "On the Nucleation Site and Formation Sequence of Secondary Phases during Isothermal High-Temperature Aging of Wire Arc Additively Manufactured PH13-8Mo Stainless Steel", *Vacuum* **(IF= 4.11)**, Vol. 201, p. 111076 (2022).

11. Salar Salahi, Alireza Vahedi Nemani, **Mahya Ghaffari**, Jonas Lunde, Ali Nasiri, "On Microstructure, Crystallographic Orientation, and Corrosion Properties of Wire Arc Additive Manufactured AISI 420 Martensitic Stainless Steel: Effect of the Inter-layer Temperature", *Additive Manufacturing* **(IF= 11.632)**, Vol. 46, p. 102157 (2021).
12. Salar Salahi, **Mahya Ghaffari**, Alireza Vahedi Nemani, Ali Nasiri, "Effects of Secondary-Phase Formation on the Electrochemical Performance of a Wire Arc Additive Manufactured 420 Martensitic Stainless Steel under Different Heat Treatment Conditions", *Journal of Materials Engineering and Performance*, **(IF= 2.036)**, Vol. 30(9), pp. 6618-6629 (2021).
13. Alireza Vahedi Nemani, **Mahya Ghaffari**, Salar Salahi, Jonas Lunde, Ali Nasiri, "Effect of Interpass Temperature on the Fraction of Retained Austenite in a Wire Arc Additive Manufactured ER420 martensitic stainless steel", *Materials Chemistry and Physics* **(IF= 4.778)**, Vol. 266, p. 124555 (2021).
14. Mehran Rafieazad, Alireza Vahedi Nemani, **Mahya Ghaffari**, Ali Nasiri, "On Microstructure and Mechanical Properties of a Low-Carbon Low-Alloy Steel Block Fabricated by Wire Arc Additive Manufacturing", *Journal of Materials Engineering and Performance* **(IF= 2.036)**, Vol. 30(7), pp. 4937-4945 (2021).
15. Ayda Shahriari, **Mahya Ghaffari**, Ladan Khaksar, Ali Nasiri, Amir Hadadzadeh, Babak Shalchi Amirkhiz, Mohsen Mohammadi, "Corrosion Resistance of 13wt.% Cr Martensitic Stainless Steels: Additively Manufactured CX versus Wrought Ni-Containing AISI 420", *Corrosion Science* **(IF= 7.72)**, Vol. 184, p. 109362 (2021).
16. Alireza Vahedi Nemani, **Mahya Ghaffari**, Salar Salahi, Ali Nasiri, "Effects of Post-Printing Heat Treatment on the Microstructure and Mechanical Properties of a Wire Arc Additive Manufactured 420 Martensitic Stainless Steel Part", *Materials Science and Engineering: A* **(IF= 6.044)**, Vol. 813, p. 141167 (2021).
17. Alireza Vahedi Nemani, **Mahya Ghaffari**, Ali Nasiri, "Comparison of Microstructural Characteristics and Mechanical Properties of Shipbuilding Steel Plates Fabricated by Conventional Rolling versus Wire Arc Additive Manufacturing", *Additive Manufacturing* **(IF= 11.632)**, Vol. 32, p. 101086 (2020).
18. Alireza Vahedi Nemani, **Mahya Ghaffari**, Ali Nasiri, "On the Post-printing Heat Treatment of a Wire Arc Additively Manufactured ER70S Part", *Materials* **(IF= 3.748)**, Vol., 13(12), p. 2795 (2020).

19. Mehran Rafieazad, **Mahya Ghaffari**, Alireza Vahedi Nemani, Ali Nasiri, “Microstructural Evolution and Mechanical Properties of a Low Carbon Low Alloy Steel Produced by Wire Arc Additive Manufacturing”, *The International Journal of Advanced Manufacturing Technology* **(IF= 3.563)**, Vol. 105(5), pp. 2121-2134 (2019).

Conference Papers:

1. **Mahya Ghaffari**, Ali Nasiri, “Effect of Post-Process Heat Treatment on the Microstructure and Tensile Behaviour of Wire Arc Additive Manufactured 13-8 PH Martensitic Stainless Steel”, *Canadian Society for Mechanical Engineering (CSME) International Congress*, Edmonton, Canada (2022).
2. **Mahya Ghaffari**, Ali Nasiri, “Effects of Columnar Grain Growth and Inhomogeneous Microstructure on the Anisotropic Mechanical Properties of a Wire Arc Additive Manufactured PH 13-8Mo Martensitic Stainless Steel”, *60th Annual Conference of Metallurgists*, Halifax, Canada (2021).
3. **Mahya Ghaffari**, Alireza Vahedi Nemani, Ali Nasiri, “Anisotropy in Mechanical Properties of a Wire Arc Additive Manufactured Low Carbon Low Alloy Steel”, *Canadian Society for Mechanical Engineering (CSME) Congress*, London, Canada (2019).
4. Ali Nasiri, **Mahya Ghaffari**, Alireza Vahedi Nemani, “Additive Manufacturing of CX Stainless Steel: a comparison between small-scale and large-scale fabrication methods”, *61st Annual Conference of Metallurgists (COM)*, Montreal, Canada (2022).
5. Elham Afshari, **Mahya Ghaffari**, Alireza Vahedi Nemani, Ali Nasiri, “Tribological performance of 13–8Mo maraging stainless steel fabricated via wire arc additive manufacturing in as-printed and heat-treated condition”, *61st Annual Conference of Metallurgists (COM)*, Montreal, Canada (2022).
6. Alireza Vahedi Nemani, **Mahya Ghaffari**, Salar Salahi, Ali Nasiri, “Effect of post-printing solution-aging heat treatment on the microstructure and corrosion properties of a wire arc additive manufactured PH 13-8Mo martensitic stainless steel”, *33rd Canadian Materials Science Conference*, Toronto, Canada (2022).
7. Salar Salahi, **Mahya Ghaffari**, Alireza Vahedi Nemani, Ali Nasiri, “Electrochemical Performance of a Wire Arc Additive Manufactured PH 13–8Mo-AISI 420 Martensitic Stainless Steels Dissimilar Metal Combination”, *Canadian Society for Mechanical Engineering (CSME) Congress*, Edmonton, Canada (2022).

8. Alireza Vahedi Nemani, **Mahya Ghaffari**, Salar Salahi, Ali Nasiri, “On the Hardening and Subsequent Tempering of a Wire Arc Additive Manufactured 420 Martensitic Stainless Steel”, *60th Annual Conference of Metallurgists*, Halifax, Canada (2021).

9. Salar Salahi, **Mahya Ghaffari**, Alireza Vahedi Nemani, Ali Nasiri, “Microstructural Evolution and Electrochemical Performance of the Interfacial Region between a Wrought and a Wire Arc Additive Manufactured 420 Martensitic Stainless Steel”, *60th Annual Conference of Metallurgists*, Halifax, Canada (2021).

10. Alireza Vahedi Nemani, **Mahya Ghaffari**, Ali Nasiri, “Post-Printing Heat Treatment of a Wire Arc Additively Manufactured Low Carbon Low Alloy Steel”, *Canadian Society for Mechanical Engineering (CSME) Congress*, London, Canada (2019).

CHAPTER 2 MICROSTRUCTURE AND MECHANICAL BEHAVIOUR OF PH 13-8MO MARTENSITIC STAINLESS STEEL FABRICATED BY WIRE ARC ADDITIVE MANUFACTURING

Mahya Ghaffari[1], Alireza Vahedi Nemani[2], Ali Nasiri[3]

1- Graduate Student, Dalhousie University, Halifax, Nova Scotia, Canada
2- Post-Doctoral Fellow, Dalhousie University, Halifax, Nova Scotia, Canada
3- Assistant Professor, Dalhousie University, Halifax, Nova Scotia, Canada

Status: Published Journal Paper, Journal of Additive Manufacturing (IF= 11.632), Volume 49, Page 102374

Authors' Contribution

Mahya Ghaffari: Conceptualization, Fabrication Process, Investigation, Writing - original draft.

Alireza Vahedi Nemani: Methodology, Validation, Investigation, Writing - review & editing.

Ali Nasiri: Supervision, Writing - review & editing, Funding acquisition.

2.1 ABSTRACT

Wire arc additive manufacturing (WAAM) was applied to fabricate precipitation hardened (PH) 13-8Mo martensitic stainless steel parts for applications in injection molding equipment, aerospace components, and marine. The microstructural features, microhardness evaluation, and room temperature tensile properties of the as-printed parts have been comprehensively investigated at different locations and orientations. The experimental results showed that the predominant microstructure of the WAAM fabricated PH 13-8Mo stainless steel part mainly consists of vermicular and lathy remnant δ-ferrite embedded in a low-carbon fine martensitic matrix in addition to a small fraction of retained austenite. The content of both retained austenite and remnant δ-ferrite reduced through the building direction of the WAAM fabricated wall, causing a gradual increase of microhardness and ultimate tensile strength values from the bottom to the top of the component. Moreover, the measured tensile strength and ductility in horizontal and vertical directions of the wall revealed anisotropic mechanical properties associated with the columnar growth of primary δ-ferrite grains structure formed during the solidification of the material, creating a strong cubic texture along the building

direction. The present study, for the first time, revealed successful implementation of WAAM technology to fabricate PH 13-8Mo stainless steel parts with comparable hardness and tensile strength with respect to other fabrication methods.

2.2 INTRODUCTION

The fabrication feasibility of complex parts through the layer-by-layer deposition of feedstock material with significant reduction in the fabrication time and cost is the principal advantage of additive manufacturing (AM) in comparison to subtractive manufacturing techniques [15][16]. Among all AM methods, wire arc additive manufacturing (WAAM) appears to be one of the most efficient metal fabrication techniques due to its high material deposition rate (~3–8 kg/h), ideal for building/repairing customized large-scale engineering components with reduced environmental impact [32][102][103][104][105]. In this technology, wire is used as the feedstock material and an electric arc or plasma as the heat source [15][103]. The WAAM technique can be classified into different categories based on the energy source employed to melt the metal wire, including gas metal arc (GMA), gas tungsten arc (GTA), and plasma arc (PA) [34]. It has been reported [34][35] that GMA-WAAM is the most commonly used process for building large-size parts by virtue of its significantly higher energy input as compared to other heat sources.

It should be noted that implementing the appropriate process parameters plays a crucial role in fabricating a structurally sound end-product with acceptable performance [34]. In addition, since the material experiences complex and frequent heating and cooling cycles during the consecutive deposition process, the presence of microstructural inhomogeneity and consequently, anisotropic mechanical properties would be expected in WAAM fabricated components [106][107]. For instance, Baufeld *et al.* [108] investigated the microstructure and mechanical properties of a deposited Ti-6Al-4V part through gas tungsten arc additive manufacturing (GTA-AM), and reported the formation of large and elongated columnar prior β grains, leading to anisotropy in strain and ultimate tensile strength (UTS) along the horizontal and vertical directions.

Due to the similarities of WAAM and multi-pass welding processes, a variety of commercially available welding consumables have been successfully used to additively fabricate a wide range of metallic alloys, such as Ti-6Al-4V, aluminum, steel, copper, brass, and nickel alloys [44][109]. Among stainless steels, the previous studies have shown the feasibility of fabricating austenitic stainless steels, such as SS 304 [110][111], SS 316L [46][47], and SS 308LSi [112], duplex stainless steels, such as 2209 [113][114], and ER2594 [48], as well as martensitic stainless steel 420 [49][50], through WAAM.

Precipitation hardened martensitic stainless steels (PHMSS) are also another suitable candidates for WAAM due to their reasonable weldability and excellent combination of strength and corrosion resistance without loss of toughness, considered to be desirable for demanding aerospace, marine, and petrochemical applications [2][9][74][115]. The significantly high strength of PHMSS makes them difficult to be manufactured via conventional fabrication processes. Thus, AM can be considered as a great alternative for fabrication of near-net-shape PHMSS parts in one-step [115].

PH martensitic stainless steels solidify as δ-ferrite and transform to austenite upon cooling to intermediate temperatures, which finally transforms to martensite at room temperature [9][10]. The obtained martensitic structure in PHMSS is relatively finer and softer as compared to other martensitic stainless steels due to its low carbon content (commonly less than 0.07 wt. %) [9]. Therefore, aging treatment is conducted to further increase the strength of the material by precipitation of homogeneously distributed fine intermetallic compounds embedded in a relatively tough martensitic matrix [8][9][10][116]. The commercial grades of PHMSS include 17-4 PH, 15-5 PH, and PH 13-8Mo, which are designated based on the content of Cr (first number) and Ni (second number) as their main alloying elements [74][75]. Although these three grades are all precipitation-hardened martensitic stainless steels, they have significant differences in terms of the microstructural characteristics, mechanical properties, corrosion resistance, application, and cost owing to their compositional variations. For example, 17-4 PH contains ~17 wt. % Cr, ~4 wt. % Ni, ~4 wt. % Cu, and no Al, while PH 13-8Mo is composed of ~13 wt. % Cr, ~8 wt. % Ni, ~1 wt. % Al, and no Cu. Therefore, the main precipitates formed as a result of aging treatment would be Cu-rich phases in 17-4 PH, and β-NiAl in PH 13-8Mo [8][9][10]. From the application perspective, PH 13-8Mo is commonly utilized when an excellent strength and toughness combined with good stress corrosion resistance is needed, while 17-4 PH is used for applications requiring high strength and a moderate level of corrosion resistance. Overall, PH 13-8Mo yields a superior strength and hydrogen embrittlement resistance as compared to 17-4 PH, primarily due to the coherency between β-NiAl precipitates and the matrix as opposed to incoherent Cu-rich precipitates in 17-4 PH steel [117]. In addition, the higher content of Molybdenum in PH 13-8Mo alloy improves its pitting resistance relative to 17-4 PH [76]. Moreover, it has been reported that PH 13-8Mo showed a better sulfide stress corrosion cracking resistance than that of 17-4 PH and 15-5 PH with a similar strength level [77].

The existing literature on additive manufacturing of 17-4 PH, 15-5 PH, and PH 13-8Mo stainless steels has been mainly focused on implementing laser-based AM methods, except for only two reported studies on wire-based AM of 17-4 PH stainless steel [15][52]. Most of these works have predominantly investigated the influence of process parameters [15][52][118][119][120], atmosphere condition [121][122], post-fabrication heat treatments [15][58][123][124][125][126][127], and shot peening [128][129] on the macrostructure, microstructure, and mechanical properties of the fabricated parts. Among all, only a limited number of studies reported the AM of PH 13-8Mo stainless steel. For instance, Asgari *et al.* [6] successfully built a nearly fully dense stainless steel CX alloy with a similar chemical composition to PH 13-8Mo using direct metal laser sintering (DMLS). They detected austenite and lath martensite phases in the microstructure of the DMLS-built CX sample with superior tensile strength (1113 MPa) [6] as compared to other stainless steels, such as 17-4 PH (~1000 MPa) [124] and SS 316L (691 MPa) [130] fabricated by AM method. In another similar attempt, Shahriari *et al.* [131] investigated the anisotropy in the microstructure and corrosion performance of the side and top planes of the CX sample fabricated by laser-powder bed fusion technique. In contrast to laser-based AM methods, WAAM has the advantages of much higher deposition rate, lower capital and fabrication costs, more readily available feedstock materials, and larger fabricated size [53]. Accordingly, WAAM of PH 13-8Mo alloy provides a great potential for fabrication of industrial parts with a wide range of engineering applications in different sectors requiring large metallic components with an excellent combination of strength and corrosion resistance, such as maritime, offshore oil and gas, shipbuilding, aerospace, nuclear, and defence [6].

To the best of the authors' knowledge, there is no published research in the literature on the feasibility of wire arc additive manufacturing of PH 13-8Mo stainless steel. Therefore, for the first time, the current work focuses on the fabrication of WAAM-PH 13-8Mo parts, aiming to investigate possibly formed microstructural heterogeneities in the structure and their impact on the mechanical properties of the as-printed component. Furthermore, comparisons have been made between the obtained mechanical properties of the WAAM parts herein and PH 13-8Mo stainless produced by laser-based AM techniques.

2.3 MATERIALS AND METHODS

2.3.1 Materials and Fabrication Process

In this study, the wire arc additive manufactured wall (Figure 2.1a) with a geometric size of ~180 × 80 × 12 mm^3 formed by deposition of 100 consecutive layers was fabricated using a commercial PH 13-8Mo welding wire with a diameter of 1.143 mm (0.045 in) and the nominal chemical composition given in Table 2.1, taken from the supplier's (United States Welding Corporation) data sheet [132]. An S-350 Power Wave Lincoln Electric GMAW machine equipped with an advanced surface tension transfer (STT) mode and a torch mounted on a 6-axis Fanuc robot was employed as the heat source of the process. The fabrication set-up and the equipment used for the WAAM process are shown in the authors' previous study [133]. Through depositing several trial layers over a 25 mm thick AISI420 martensitic stainless steel substrate, process parameters were optimized to fabricate a defect-free wall as follows: average arc current of 135 A, arc voltage of 28 V, wire feed speed of 67 mm/s (160 in/min), and travel speed of 4 mm/s (9 in/min). In order to protect the melt pools from oxidation and other environmental contaminations, a mixture of 90% He, 7.5% Ar, and 2.5% CO_2 (commercially known as Blueshield 9) with a flow rate of 20 L/min was employed as the shielding gas. Additionally, a back-and-forth scanning strategy aligned with the deposition direction was adopted herein to improve the uniformity of the deposited layers, leading to building a straight wall. During the WAAM process, 100±10 °C interpass temperature was implemented between the deposition of consecutive layers measured and controlled using a digital non-contact infrared thermometer with the measurement range of -60 to 1000 °C.

Table 2.1 The nominal chemical composition of the PH 13-8Mo feedstock wire (wt. %).

Cr	**Ni**	**Mo**	**Al**	**Mn**	**Si**	**C**	**S**	**N**	**Fe**
12.25-13.25	7.5-8.5	2-2.5	0.9-1.35	0.1	0.1	0.05	0.01	0.01	Bal.

2.3.2 Microstructural Characterization

To investigate possible microstructural heterogeneities throughout the WAAM fabricated wall, various samples from different locations were cut, mirror polished, and then etched for 20 s using Fry's reagent. The square enclosed areas in Figure 2.1a show the approximate locations of metallographic samples prepared from the bottom, middle, and top of the component. The microstructural features of all samples were characterized using an optical microscope (Nikon Eclipse 50i) and a scanning electron microscope (FEI MLA 650FEG) equipped with an energy-dispersive X-ray spectroscopy (EDS) detector. Phase constitution of the as-printed samples was identified by means of X-ray diffraction (XRD) technique using a Rigaku Ultima IV X-ray diffractometer with a Cu-K_α radiation and a scan step size of 0.02° covering a 2θ range of 3–100° at 40 kV and 44 mA. To analyze the XRD raw data and determine the volume fraction of various phases, MDI JADE 2010 software using International Centre for Diffraction Data (ICDD) databases was employed. In addition, to identify the solidification-induced crystallographic orientation and texture of the formed microstructure, electron backscattered diffraction (EBSD) analysis using an HKL Nordlys II detector and Channel 5 software was conducted over two areas of 600 × 600 μm^2 and 30 × 30 μm^2 with a step size of 0.75 μm and 0.2 μm, respectively.

2.3.3 Mechanical Properties Evaluation

A 574 Wilson Rockwell hardness testing machine with a C diamond indenter under 150 kgf load was utilized to measure the hardness of the as-printed wall towards the building direction with an interval spacing of 5 mm. In addition, a Buehler Micromet hardness tester with a load of 500 g was employed to investigate the microhardness variations through the melt pools' centers and heat affected zones (HAZs) of adjacent layers. To ensure repeatability and obtain meaningful average values, both Vickers and Rockwell hardness measurements were repeated five times. An Instron 5585H-250 kN load frame equipped with an extensometer for precise elongation measurements was employed to perform uniaxial tensile tests at the strain rate of 1 mm/min. Tensile test coupons were water jet cut from the machined as-printed wall with the gauge dimensions of 25 × 5 × 5 mm^3 as recommended by the ASTM E8m-04 standard [134]. As shown in Figure 2.1a, tensile testing was carried out at least five times on both vertical samples (along the building direction) and horizontal samples (along the deposition direction) of the WAAM manufactured part to examine the possible anisotropic response in tensile behaviour.

2.4 RESULTS AND DISCUSSION

2.4.1 Microstructural Characterization

Figure 2.1a depicts the fabricated WAAM PH 13-8Mo stainless steel wall, comprised of 100 consecutive deposited layers with minor spattering during the manufacturing process. It should be noted that no sign of macroscopic defects, such as cracks and lack of fusions, between the layers of the component were detected. Since controlling the interpass temperature is the most efficient way to reduce the amount of process-induced residual stress, and also prevent interpass cracks, defects, and possible distortion in the as-printed parts [116], 100±10 °C interpass temperature was implemented during deposition of the wall as suggested by Lauro and Mandina [135]. It is also notable that the maximum interpass temperature should not exceed 150 °C so that every single deposited layer can undergo the martensitic transformation during the deposition process. Otherwise, as the build grows, the temperature of initially deposited layers will inevitably drop below M_s of the alloy and a couple of previously deposited tracks will transform to martensite all together simultaneously upon cooling to room temperature resulting in a significant volume change, which could potentially lead to the formation of quench cracking [135].

The side view (XZ face) macrostructural morphology of the WAAM PH 13-8Mo wall captured by a stereo microscope is shown in Figure 2.1b. It can be seen that during the rapid solidification process, the large unidirectional columnar grains have grown antiparallel to the heat dissipation direction, which is aligned with the building direction. These primary grains nucleated on the substrate and have grown epitaxially across each subsequent layer nearly for the entire height of the component. The width of these columnar grains varied randomly from one column to another in the range of 50–200 µm, as shown in Figure 2.1b. It is important to note that the formation of such a coarse columnar grain structure could potentially lead to a preferential texture and anisotropic mechanical properties [108][136], which will be thoroughly elucidated in the following sections.

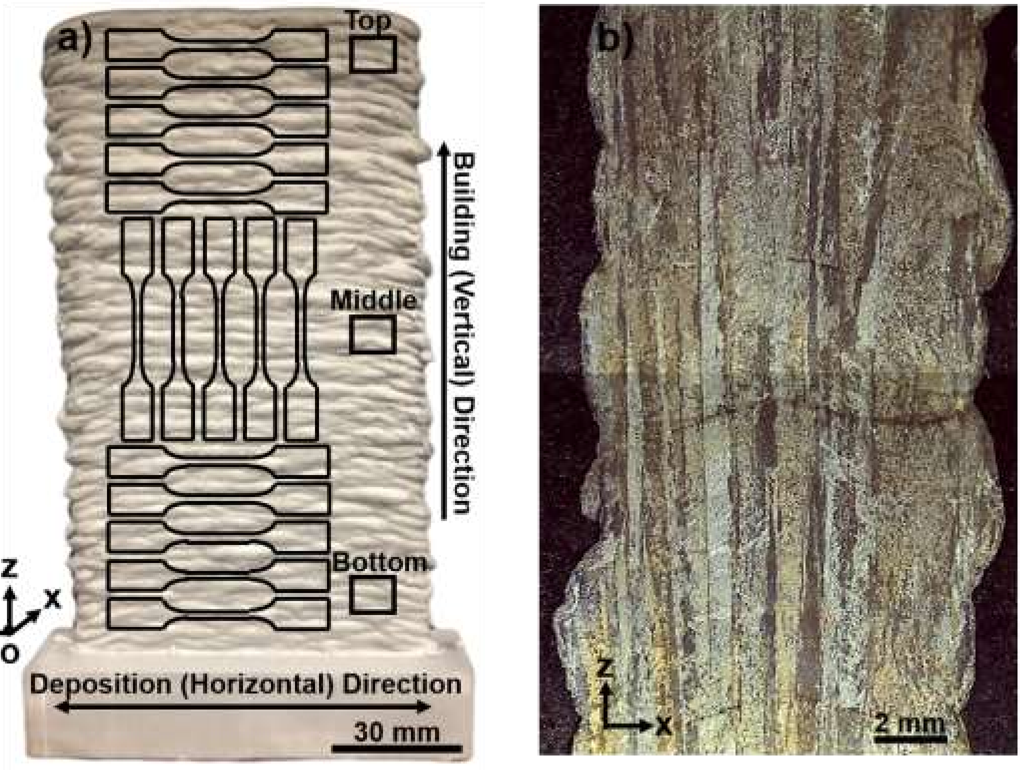

Figure 2.1 (a) As-printed WAAM PH 13-8Mo stainless steel wall showing the locations of extracted samples for metallographic and tensile testing, (b) stereo microscope image taken from the side view (XZ face) of the fabricated component.

The most common way to predict the solidification mode of stainless steels is based on the chromium to nickel equivalent ratio (Cr_{eq}/Ni_{eq}), which can be estimated according to the empirical equations (1) and (2) derived from the modified WRC-1992 diagram (Figure 2.2) [2][9]:

$$Cr_{eq} = \%\,Cr + \%\,Mo + 2.2\,\%\,Ti + 0.7\,\%\,Nb + 2.48\,\%\,Al \tag{2.1}$$

$$Ni_{eq} = \%\,Ni + 35\,\%\,C + 20\,\%\,N + 0.25\,\%\,Cu \tag{2.2}$$

Accordingly, the Cr_{eq}/Ni_{eq} ratio of the PH 13-8Mo alloy (with the chemical composition listed in Table 2.1) is approximately 1.79, which is greater than ~1.7, causing the formation of primary ferrite solidification mode (F-mode), meaning the solidification process starts with the formation of high-temperature δ-ferrite phase [2].

Based on the above discussion, the coarse columnar grains shown in Figure 2.1b can be identified as high-temperature primary δ-ferrite grains formed initially due to the F-mode solidification of the PH 13-8Mo alloy. In the very first deposited layer, these primary δ-ferrite grains experience a competitive growth at the initial stage of the solidification process. Therefore, the grains whose easy growth direction (<100> for cubic materials) coincides with the heat dissipation direction have higher chance to grow at the expense of crowding out the grains with less favourable crystallographic orientation [137][138]. This growth mechanism leads to reducing the number of grains while increasing the grain size, which justifies the formation of coarse primary columnar grains shown in Figure 2.1b. During depositing the subsequent layers, the solidification process started with the epitaxial growth of primary δ-ferrite on the columnar grains of the previous layer. This orientation-dependent directional growth pattern is maintained nearly through the whole height of the wall.

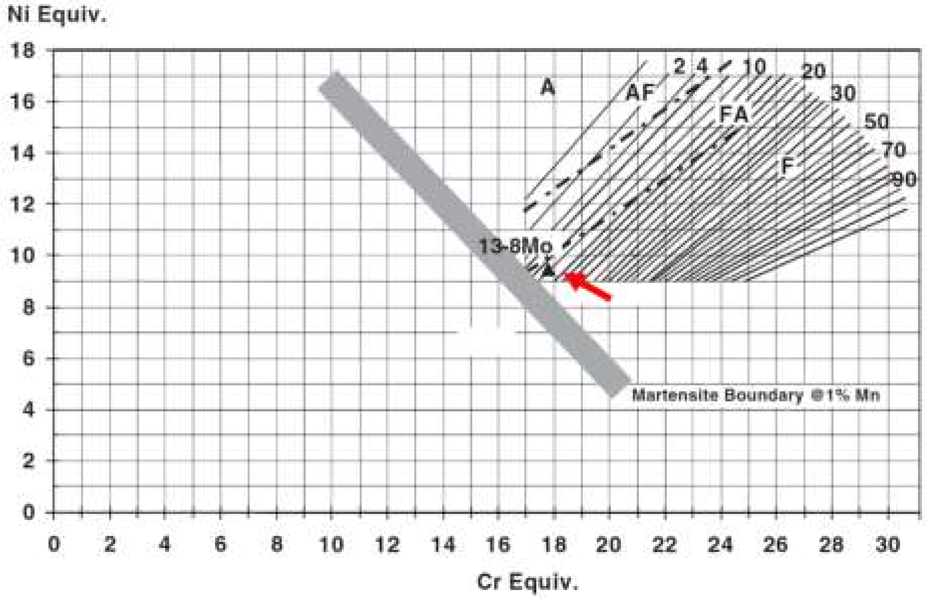

Figure 2.2 The modified WRC-1992 diagram showing the solidification mode of stainless steels (modified from [9]).

Figure 2.3 illustrates the scanning electron microscope (SEM) images showing the details of microstructural features inside two adjacent columnar grains. The dominant microstructure of the additively manufactured PH 13-8Mo component at room temperature is mainly characterized by residual δ-ferrite embedded in a matrix of fine low-carbon martensite. The formation of this microstructure can be elucidated based on the phase diagram of PHMSS presenting the sequence of phase transformations as follows [9]:

$$L \rightarrow L + \delta\text{-ferrite} \rightarrow \delta\text{-ferrite} \rightarrow \delta\text{-ferrite} + \gamma \rightarrow \delta\text{-ferrite} + \gamma + M \rightarrow \delta\text{-ferrite} + M \quad (2.3)$$

Accordingly, the cooling process of this alloy involves two main solid-state transformations including, (*i*) δ-ferrite to austenite, which is a diffusion-controlled transformation [2], and then (*ii*) austenite to martensite, which is a shear transformation [78]. However, the fast cooling rate and non-equilibrium nature of the AM process [46] limits the diffusional transformation of δ-ferrite to austenite. Consequently, a considerable fraction of δ-ferrite phase remains untransformed, while most of the resultant austenite will transform to martensite. Thus, the presence of a significant portion of residual δ-ferrite in a martensitic matrix should be expected at room temperature. The formation of a similar microstructure was also reported in the welded structure [139] and wire arc additive manufactured 17-4 PH stainless steel alloy [15][52].

The orientation and morphology of remnant δ-ferrite phases vary between columns of primary δ-ferrite grains, as shown in Figure 2.3a. The δ-ferrite phases appeared in two main morphologies, *i.e.,* vermicular and lathy, as demonstrated in Figure 2.3b and c, respectively. The room temperature morphology of residual δ-ferrite is controlled by three main factors including, (*i*) cooling rate, (*ii*) Cr_{eq}/Ni_{eq} ratio, and (*iii*) crystallographic orientation relationship between δ-ferrite and austenite [137][140][141][142]. It has been reported that a higher cooling rate and higher Cr_{eq}/Ni_{eq} ratio lead to the formation of a higher fraction of lathy rather than vermicular morphology [140][142]. It is important to note that since in AM of PH 13-8Mo alloy, the cooling rate and the Cr_{eq}/Ni_{eq} ratio are identical in adjacent columns, the morphology of δ-ferrite highly depends on the crystallographic orientation relationship between the primary high-temperature δ-ferrite and subsequently transformed austenite during the post-solidification solid-state transformation. If the closed-packed planes of the primary δ-ferrite are parallel to those of the austenite, the transformation will have a planar interface leading to the formation of vermicular residual δ-ferrite at room temperature [137]. Otherwise, the transformation of δ-ferrite to austenite proceeds along the habit plane of the austenite phase leading to retention of δ-ferrite phase with a lathy morphology [137]. As shown in Figure 2.3, these two morphologies of residual δ-ferrite are formed randomly in different primary columnar grains based on the formed random orientation relationship between δ-ferrite and austenite.

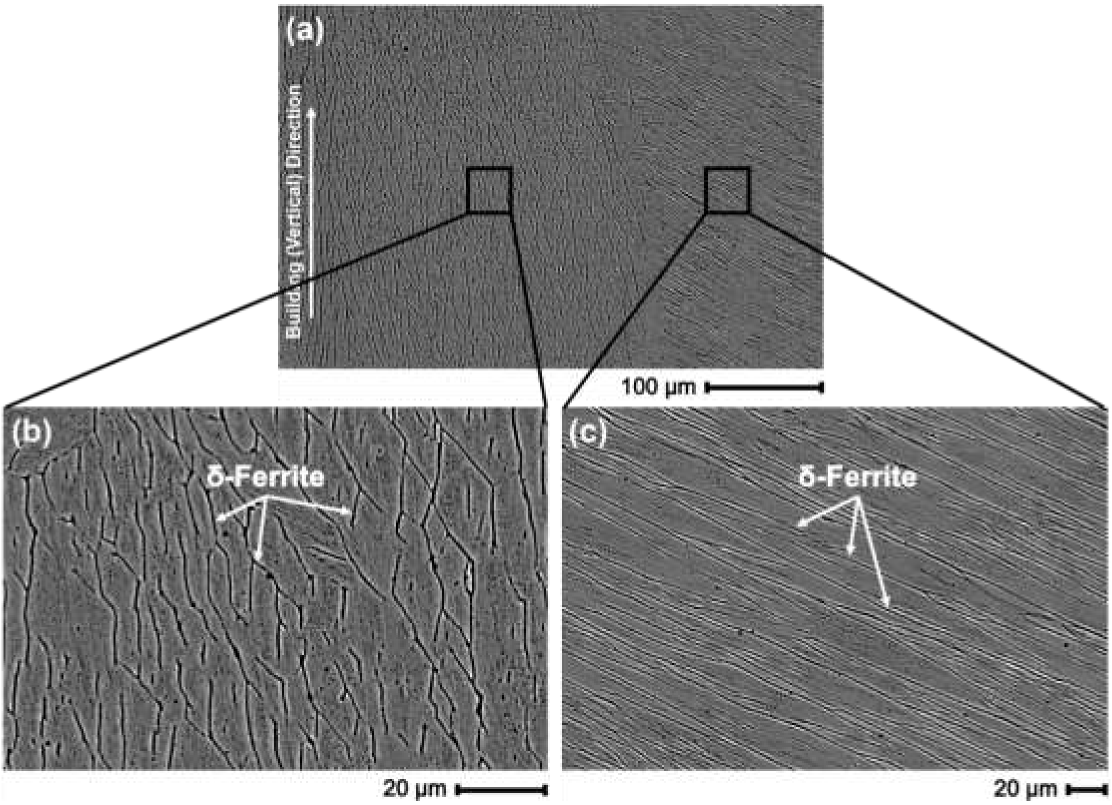

Figure 2.3 (a) Low magnification SEM micrograph of adjacent columnar grains, and high magnification SEM images taken from (b) vermicular δ-ferrite, and (c) lathy δ-ferrite.

The relative fraction of residual δ-ferrite highly depends on the cooling rate in the post-solidification process [78]. The diffusional transformation of δ-ferrite to austenite could significantly be restricted at higher cooling rates resulting in the retention of higher volume fraction of δ-ferrite at room temperature. On the other hand, at slower cooling rates, sufficient time would be provided for completion of the diffusional transformation, and consequently, a negligible amount of δ-ferrite is expected to present at room temperature [78]. The SEM images taken from various locations of the fabricated wall shown in Figure 2.4, *i.e.*, the top, middle and the bottom regions, revealed location-dependency of the volume fraction of δ-ferrite along the building direction. The cooling rate varies from the bottom to the top regions due to (*i*) the effect of substrate heat sink, (*ii*) the implementation of interpass temperature (100±10 °C), and (*iii*) heat accumulation in the part as the fabrication process progresses. The heat transfer mode in the bottom regions is mostly controlled by the severe heat sink effect from the substrate, providing a relatively high cooling rate. On the other hand, as the fabrication process proceeds, the heat transfer would be more dominated by conduction through the heat accumulated previously deposited layers, leading to a reduction in the cooling rate from the bottom to the top of the component. Consequently, the volume fraction of δ-ferrite in the top regions is significantly reduced as compared to the middle and the bottom of the wall, as shown in Figure 2.4.

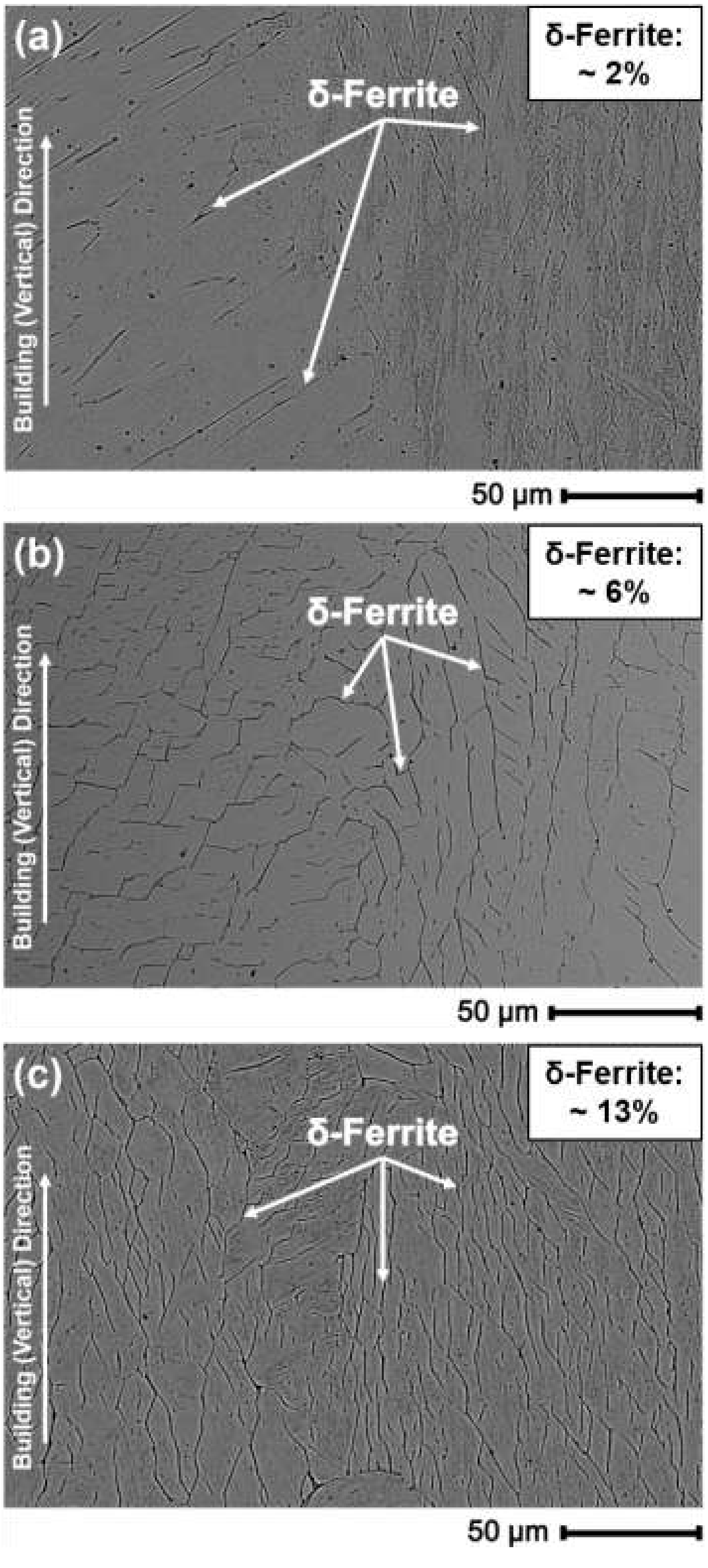

Figure 2.4 SEM images comparing the fraction of δ-ferrite formed in the (a) top, (b) middle, and (c) bottom regions of the fabricated wall.

According to EDS elemental maps (see Figure 2.5), δ-ferrite phases are highly enriched in chromium (as a ferrite promoter element) and depleted in nickel (known as an austenite promoter element) relative to the martensitic matrix. Moreover, the EDS line scan and Al concentration map analysis results (Figure 2.5d and e) also detected the presence of randomly distributed spherical inclusion particles with diameters mostly in the range of 0.5–5.0 μm, primarily composed of O and Al. The formation of Al-rich oxides can be attributed to the existence of oxygen in the shielding gas and potential moisture on the feedstock material [143].

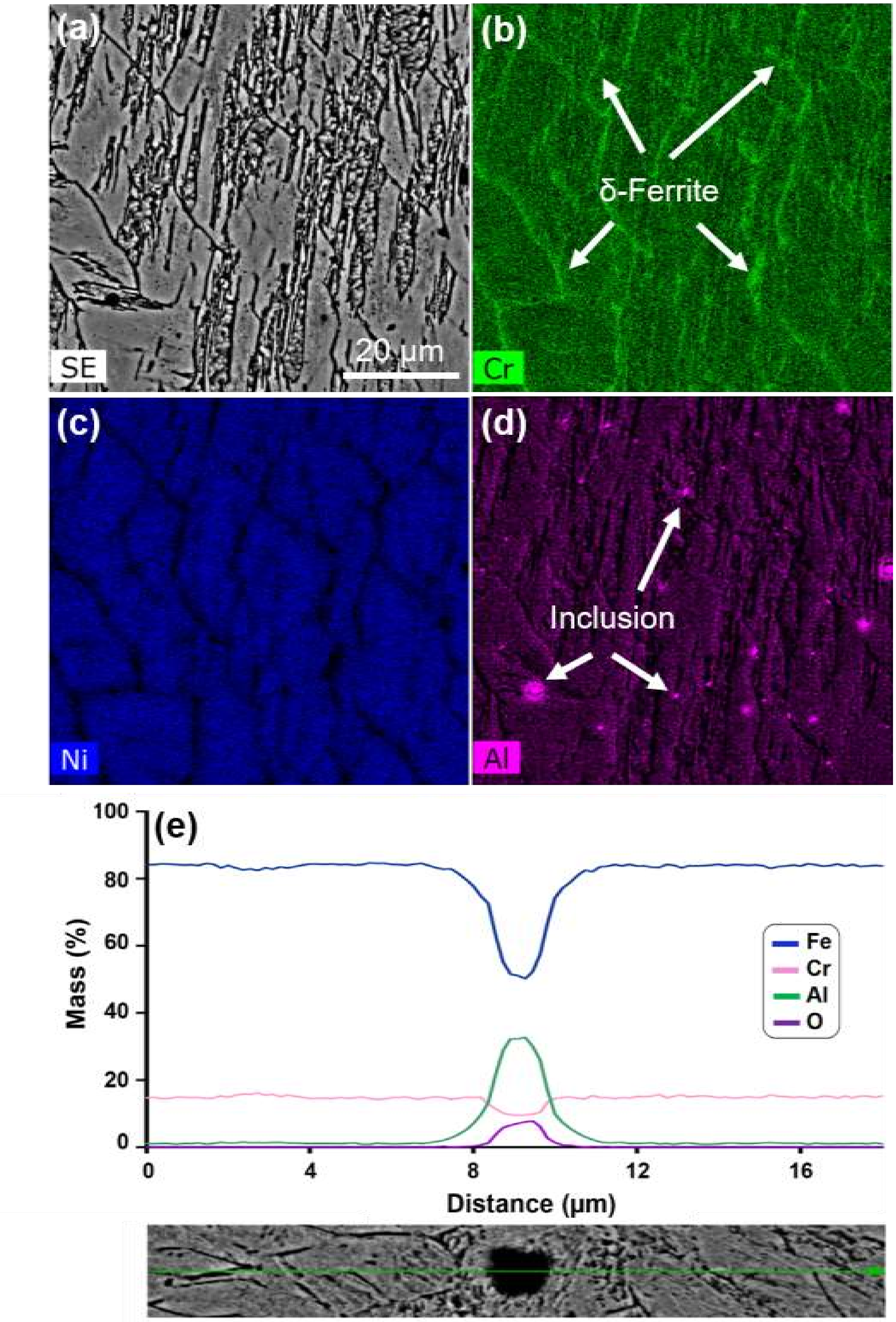

Figure 2.5 The EDS elemental concentration maps and line scans taken from the as-printed microstructure of WAAM PH 13-8Mo sample.

Figure 2.6 demonstrates an optical microscope (OM) and a magnified SEM image from the transition of one layer to the next deposited layer revealing the formation of HAZ. According to Figure 2.6b, the HAZ can be characterized by a fully martensitic microstructure in which much of the δ-ferrite phase has been disappeared. During the deposition of each consecutive layer, the temperature of the HAZ adjacent to each melt pool can be raised to the austenite stability region providing enough heat to initiate the diffusion-controlled transformation of δ-ferrite to austenite. In other words, the conditions for complete dissolution of δ-ferrite phases in HAZ are provided, leaving a fully austenitic microstructure at a high temperature, which is transformed into martensite during the subsequent cooling process [10].

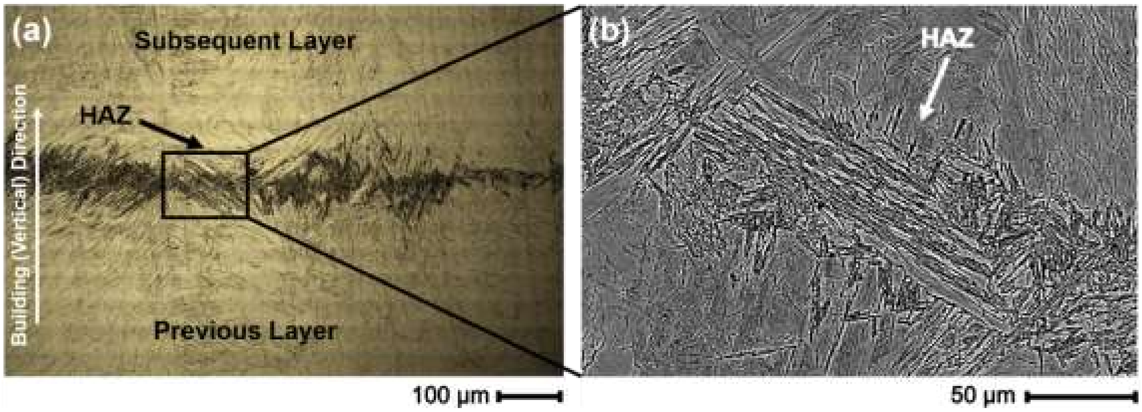

Figure 2.6 (a) OM and (b) SEM micrographs of the HAZ between two subsequent deposited layers.

In order to obtain a deep understanding of the crystallographic orientation and more accurate phase identification, EBSD measurements were carried out on the as-printed WAAM PH 13-8Mo part. Figure 2.7a exhibits the inverse pole figure (IPF) map of the sample along the building direction (z-axis). It is obvious that the coarse primary grains are generally aligned with the building direction, which is in agreement with the previous discussion on the competitive growth of primary δ-ferrite grains. The pole figures (PFs) of the body-centred cubic (bcc) phase (Figure 2.7f) further confirmed the competitive growth by revealing a strong texture aligned with the building direction (BD) for the {100} series of planes with a maximum intensity of 16.19. The high magnification IPF (Figure 2.7b) also clearly reveals fine martensite laths with nearly the same orientation for each primary columnar grain. According to the high magnification band contrast map with superimposed lath boundaries misorientations (Figure 2.7c), the laths misorientations are mostly characterized by having high density (58%) of low angle grain boundaries (2°-15°), indicating a high dislocation density in the as-printed sample. The formation of high density of dislocations can be related to the martensitic transformation during the deposition process.

The EBSD phase map presented in Figure 2.7d illustrates that the matrix has a bcc crystallographic structure (red region), representing both the residual δ-ferrite and lath martensitic structure. Although the formation of retained austenite was not detected in the SEM micrographs, the EBSD phase map (Figure 2.7d) showed the presence of small grains with face-centered cubic (fcc) structure (blue regions), confirming the formation of low volume fraction of retained austenite (2.2%) in the as-printed structure. The existence of retained austenite can be attributed to the presence of Ni (8 wt. %), as an austenite stabilizing element, in the feedstock material, and also the complex thermal history experienced by the material during sequential heating and cooling cycles associated with the nature of the AM process [144]. It is important to note that the implemented interpass temperature (100±10 °C) for the fabrication process lies between martensite start ($M_s \approx$ 120 °C [2][145]) and finish ($M_f \approx$ 30 °C [2]) temperatures of the PH 13-8Mo alloy, leading to an incomplete transformation of the austenite to martensite. Accordingly, the microstructure of each deposited track at the interpass temperature would be a mixture of δ-ferrite, martensite, and retained austenite. Further deposition of the subsequent layer increases the temperature of the previous layer to a temperature higher than M_s providing sufficient driving force for rejection of carbon atoms from martensite (with limited solubility for carbon ~0.02%) and diffusion to austenite (with an fcc crystal structure possessing much higher carbon solubility ~2.1%) [146]. The presence of a higher concentration of carbon as an austenite stabilizing element decreases both M_s and M_f, leading to the formation of a higher fraction of retained austenite at room temperature [147]. Such in-situ thermal treatment resembles the quenching and partitioning heat treatment, which is designed to improve the fraction of retained austenite in the martensitic steels [148]. The high magnification IPF of the fcc phase (Figure 2.7e) clearly shows that most of the retained austenite grains have the same crystal orientation, affirming their similar solidification-induced primary austenite grains originality, rather than being newly nucleated reversed austenite formed during the reheating process as a result of deposition of the subsequent layer. This can be also confirmed based on the pole figure map of the fcc phase (Figure 2.7g), showing a strong {100}<001> cubic texture component with the maximum intensity of 20.50 aligned with the building direction.

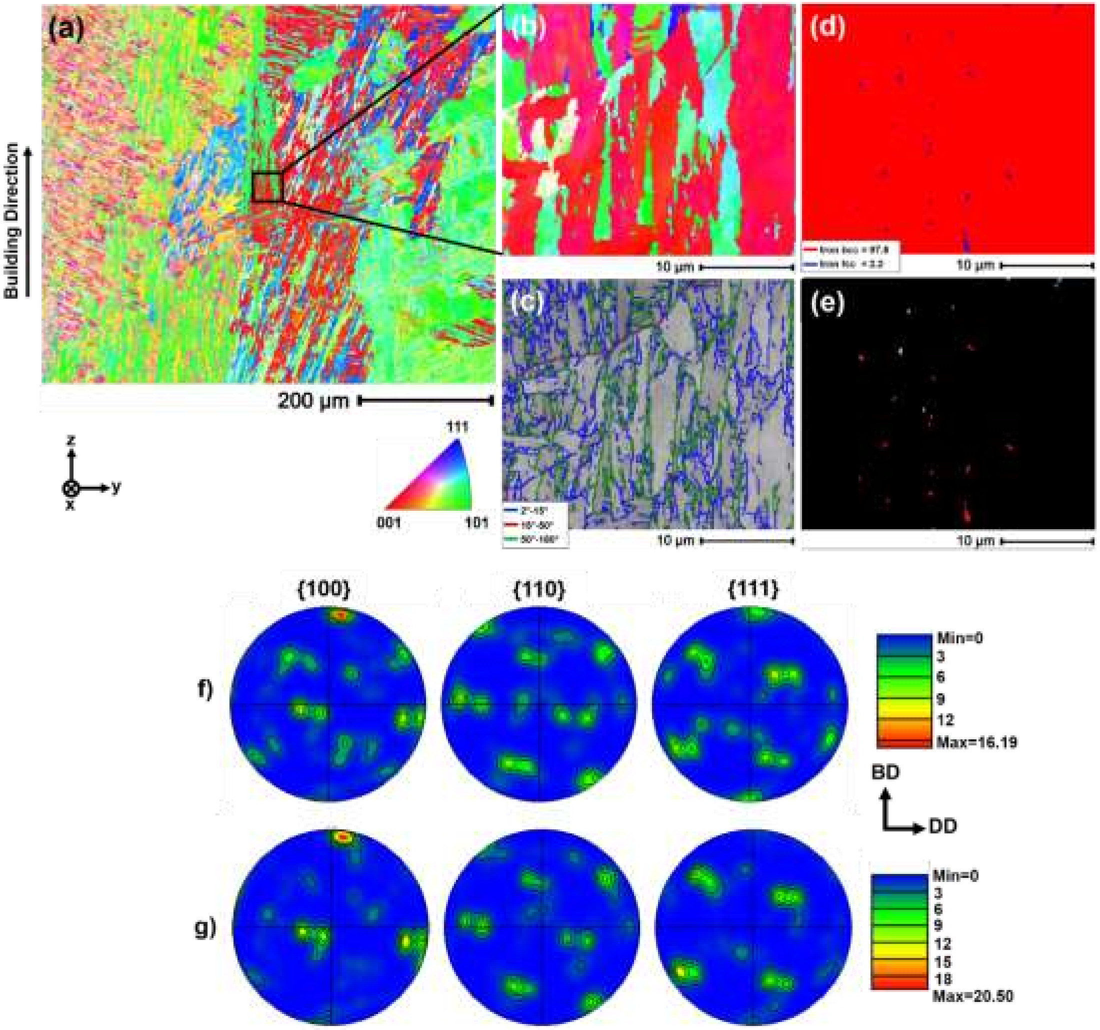

Figure 2.7 (a, b) Multi-scale EBSD-IPF maps, (c) band contrast map with superimposed lath boundaries, (d) phase map, (e) IPF-z of fcc phase, and pole figures of (f) bcc and (g) fcc phases.

To compare the volume fraction of retained austenite at different locations of the fabricated component, X-ray diffraction analysis was carried out on the samples prepared from three different regions, including the bottom, middle, and top of the wall, as shown in Figure 2.8. The characteristic peaks of iron bcc and iron fcc (retained austenite) were found in all regions through the height of the component. It can be observed that the retained austenite content showed a decreasing trend from the bottom (~24%) to middle (~14%) and top (~10%) regions of the wall. The variation of retained austenite volume fraction can be attributed to the number of sequential heating and cooling cycles (in-situ quenching and partitioning cycles) experienced by different locations of the wall [149]. The bottom regions of the component were exposed to the maximum number of sequential heating and cooling cycles leading to the formation of a higher fraction of retained austenite. On the other hand, the topmost layers have the lowest amount of retained austenite due to experiencing a less number of heating and cooling cycles during the fabrication process as compared to the middle and bottom regions.

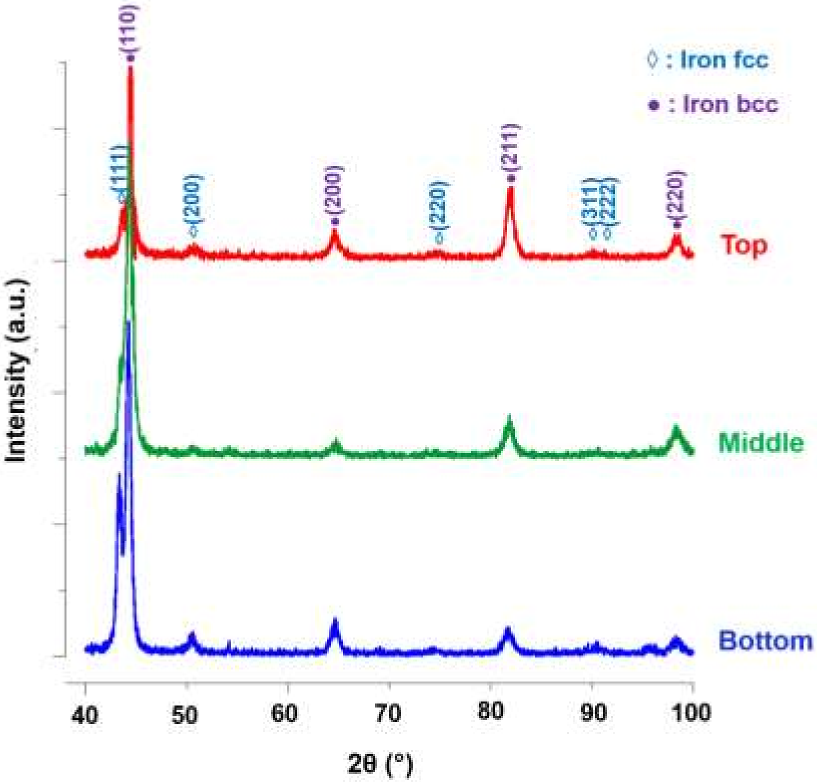

Figure 2.8 The X-ray diffraction patterns taken from the bottom, middle, and top regions of the as-printed PH 13-8Mo MSS wall.

In summary, from the microstructural characterization results, it can be concluded that the overall microstructure of the wire arc additively manufactured PH 13-8Mo stainless steel component primarily consists of vermicular and lathy remnant δ-ferrite and a low volume fraction of retained austenite embedded in a low-carbon fine martensitic matrix. Notably, the volume fraction of both δ-ferrite and retained austenite decreases from the bottom to the top of the fabricated wall due to variations of thermal histories experienced by different deposited layers across the building direction. It is important to note that the microstructure of the as-printed sample is free from precipitates, such as carbides, which can be ascribed to the extremely low carbon content of PH 13-8Mo alloy (< 0.05 wt. %) [10]. The absence of carbides was also reported in the as-printed laser-based additive manufactured CX parts [6][131].

2.4.2 Mechanical Properties Evaluation

Rockwell hardness profile along the building direction of the WAAM PH 13-8Mo wall, with an interval spacing of 5 mm, is presented in Figure 2.9. It is evident from the plot that the hardness value had a slight increasing trend approaching the top regions of the component with a significant boost in the topmost 3-5 layers. It can be observed that the minimum hardness value corresponded to the bottom regions is ~34.1 HRC as compared to the maximum value of ~37.5 HRC related to the topmost layer, which shows an approximately 10% increase in the hardness from the bottom to top regions. This increasing trend could potentially be attributed to three main features varying through the building direction, including (*i*) volume fraction of residual δ-ferrite, (*ii*) retained austenite content, and (*iii*) the number of reheating cycles. Since δ-ferrite and austenite phases are inherently much softer as compared to martensite, the lower volume fraction of these two phases relative to martensite in the top regions can be considered as a contributing factor to the increasing trend in the hardness value through the height of the component. Furthermore, the bottom layers of the component were subjected to reheating cycles more frequently, leading to a partial stress-relieving process. In contrast, the top layers experienced the least number of reheating cycles, resulting in their less stress-relieved martensitic matrix. It is notable that the average hardness value of the additively manufactured PH 13-8Mo part (35.4±0.8 HRC) is consistent with the measured hardness for the 3D-printed CX part (35±1 HRC) using the laser-powder bed fusion technique [83]. It is interesting to mention that the hardness of the PH 13-8Mo alloy can potentially be improved to more than 50 HRC by implementing a solutionizing and aging heat treatment via the formation of homogeneously distributed fine NiAl precipitates in a matrix of tempered martensite [6][83], which is the subject of the authors' next study.

The Vickers microhardness variations through the melt pools' centers and HAZs of five adjacent layers in the middle region of the WAAM PH 13-8Mo wall are also shown in the inset of Figure 2.9. The observed periodic trend in microhardness profile can be rationalized by microstructural variations across the adjacent layers. The microhardness value was found to be lower in the melt pool centers with a high volume fraction of soft δ-ferrite phases, as compared to the HAZs comprising of a negligible amount of δ-ferrite in a nearly fully martensitic matrix (see Figure 2.6). The range of fluctuation in the microhardness values was measured to be ~6.2±1.8 $HV_{0.5}$ from the melt pool centers to the HAZs.

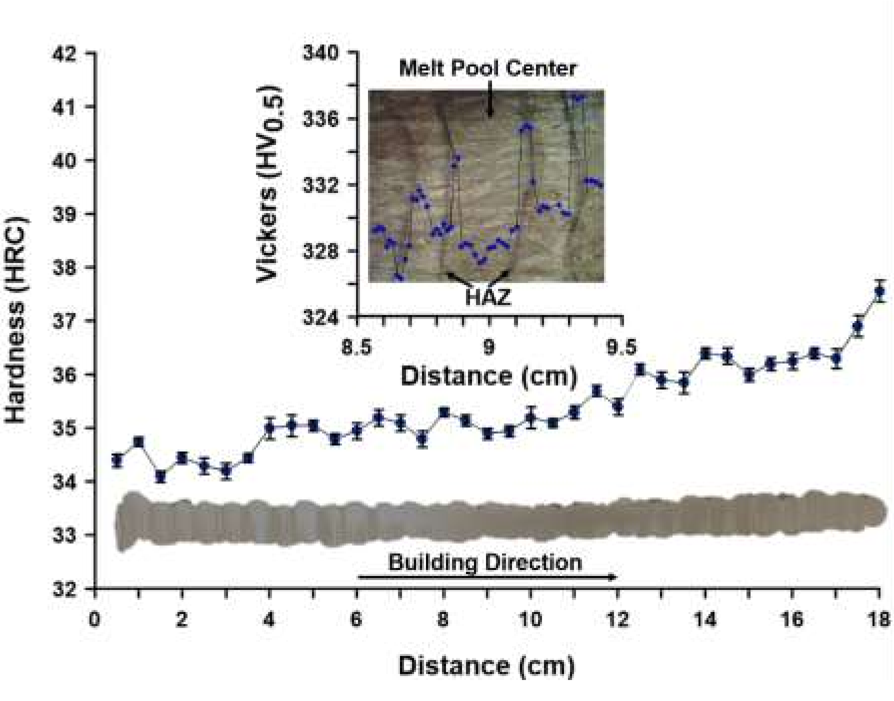

Figure 2.9 Rockwell hardness profile along the building direction of the WAAM PH 13-8Mo wall, and Vickers microhardness variations through the melt pools' centers and HAZs of five adjacent layers in the middle region shown in the inset.

Uniaxial tensile tests were also performed on samples prepared from different locations and directions of the fabricated component (as drawn in Figure 2.1a) in order to further investigate the influence of microstructural variations on the mechanical performance of the fabricated part. Figure 2.10 exhibits the results obtained from the tensile testing on the vertical (building direction) and horizontal (deposition direction) samples. Comparing the horizontal samples at different locations of the wall reveals that the top regions possess a relatively higher UTS (1167±12 MPa) as compared to the bottom regions with the UTS of 1063±14 MPa. Furthermore, the top regions with 12.1±0.8% elongation showed a slightly more ductile behaviour than the bottom regions with 10.8±0.9% elongation. The results of uniaxial tensile tests are consistent with the microstructural characterizations and microhardness evaluations showing a lower fraction of δ-ferrite and retained austenite in the top regions owning higher microhardness value as compared to the bottom regions. The higher toughness of the top region can be ascribed to its lower volume faction of δ-ferrite (see Figure 2.4), which is known as a deleterious phase to both hardness and toughness of stainless steels [63].

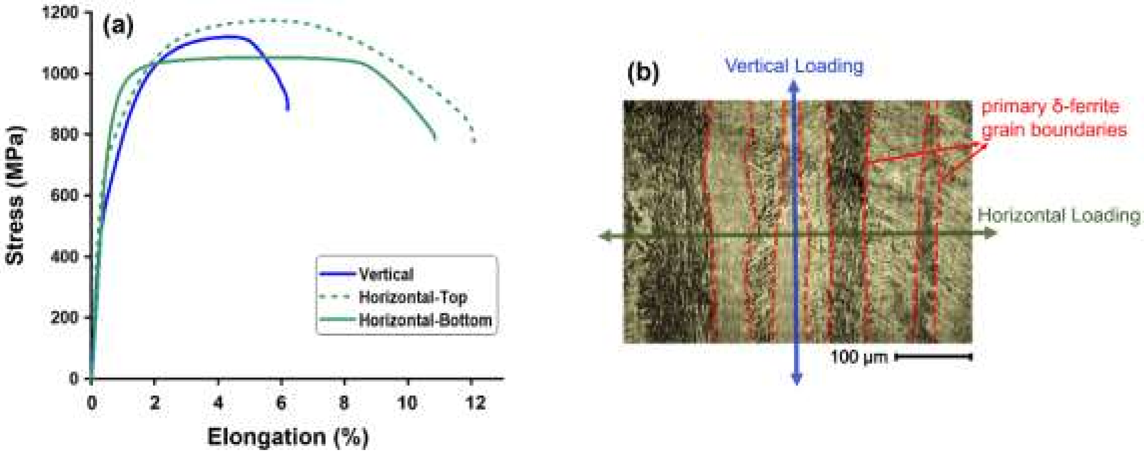

Figure 2.10 (a) Stress-strain curves of the as-printed wall in the vertical and horizontal directions and (b) relative orientation between tensile loading direction and primary columnar crystals.

In addition to the observed mechanical properties' heterogeneity from the bottom to the top of the wall in the horizontal direction (even though not significant), horizontal and vertical samples showed a more noticeable anisotropic mechanical response mainly in terms of ductility. The average UTS value of the vertical samples (1120±15 MPa) was comparable to that of the horizontal samples (1115±17 MPa), while the elongation percentage increased from 6.1±1.1% to 11.4±1.8% from the vertical to horizontal direction. It is important to note that the overall average UTS value for the WAAM PH 13-8Mo (1117±18 MPa) is comparable to the measured tensile strength of the DMLS-built CX stainless steel part (1113 MPa) [6], and higher than that of as-printed WAAM fabricated 17-4 PH parts (994 MPa) [15]. The observed anisotropic performance in the WAAM PH 13-8Mo part can be attributed to the columnar primary δ-ferrite grain structure formed during the solidification of the material producing a preferential texture along the building direction as confirmed by the EBSD analysis results (see Figure 2.7). The same mechanical anisotropic characteristics have been previously reported in wire arc additively manufactured 316L stainless steel [136], where the formation of vertically upward growth of the coarse columnar crystals led to anisotropic mechanical properties in horizontal and vertical directions. As shown in Figure 2.10b, the loading direction in the vertical samples is parallel to the long axis of the columnar structure, resulting in the presence of a limited number of primary δ-ferrite grain boundaries perpendicular to the tensile direction. On the other hand, the horizontal samples include a higher density of primary δ-ferrite grain boundaries perpendicular to the loading direction. Accordingly, the fabricated part behaves similar to a coarse-grained material in the vertical samples, while in the horizontal samples, a relatively finer grained-structure response is anticipated, justifying the observed anisotropic ductility [136]. To obtain more isotropic mechanical properties in AM fabricated components, various post-printing methods can be implemented to refine the as-printed grains structure and diminish the formation of the primary columnar crystals. These include applying appropriate heat treatment cycles [15] or introducing inter-pass inoculants [73][150], which both are subjects for the authors' future research.

To further investigate the failure mechanism of the horizontal and vertical samples, SEM analysis at different magnifications was performed on the fractured surfaces after uniaxial tensile testing. As depicted in Figure 2.11a and c, the horizontally prepared tensile sample, which showed a more ductile behaviour, revealed fractured surfaces mostly consist of deep and large conical depressions and uniformly distributed cup-like dimples, suggesting that the fracture mechanism was predominantly governed by the formation and coalescence of tiny micro-voids. The observed fractography features characterize a ductile fracture with a relatively large amount of plastic deformation during uniaxial tensile testing.

Although the fractographs taken from the vertical sample (Figure 2.11b and d) also consist of dimples, the size and depth of the dimples were found to be different from the ones detected on the horizontal samples, which could potentially be attributed to their different ductility. Higher magnification SEM images from the fractured surfaces (Figure 2.11c and d) revealed that the formed dimples on the vertical sample are shallower and smaller in diameter, implying the experienced lower degree of plastic strain by the vertical sample as compared to the horizontal sample. Furthermore, the cracks detected on the fractured surface of the vertical tensile sample are another compelling piece of evidence for the less ductile nature and premature fracture of the vertical samples than the horizontal ones with a fully ductile fracture response, consistent with the obtained uniaxial tensile testing results.

A more detailed analysis of the fractured surfaces (Figure 2.12a) revealed the presence of tiny spherical inclusions remained inside the dimples and micro-voids. The EDS elemental concentration maps (Figure 2.12b-e) confirmed that the inclusions were mostly rich in Al and O and depleted in Fe and Cr. It is notable that the presence of Al-rich oxide inclusions was detected in the as-printed structure of the fabricated part (Figure 2.5). These inclusions are considered as nucleation sites for the formation of micro-voids during tensile loading.

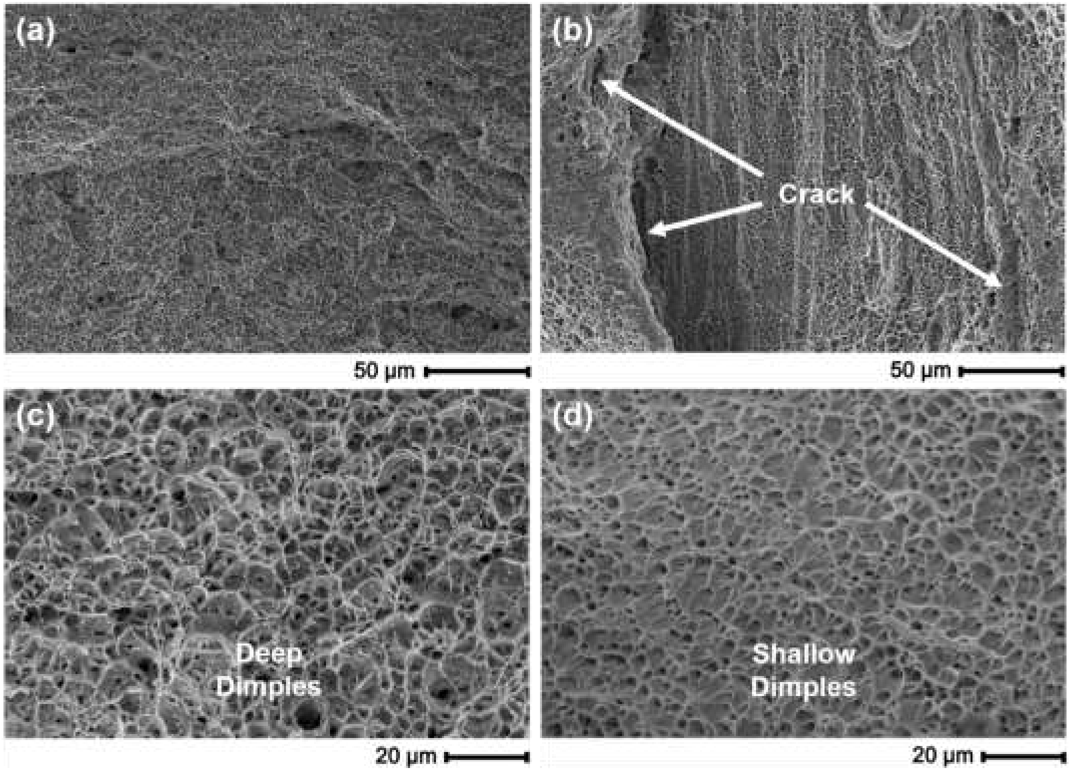

Figure 2.11 Multi-scale SEM micrographs taken from the fractured surfaces after tensile testing along the (a, c) horizontal and (b, d) vertical directions.

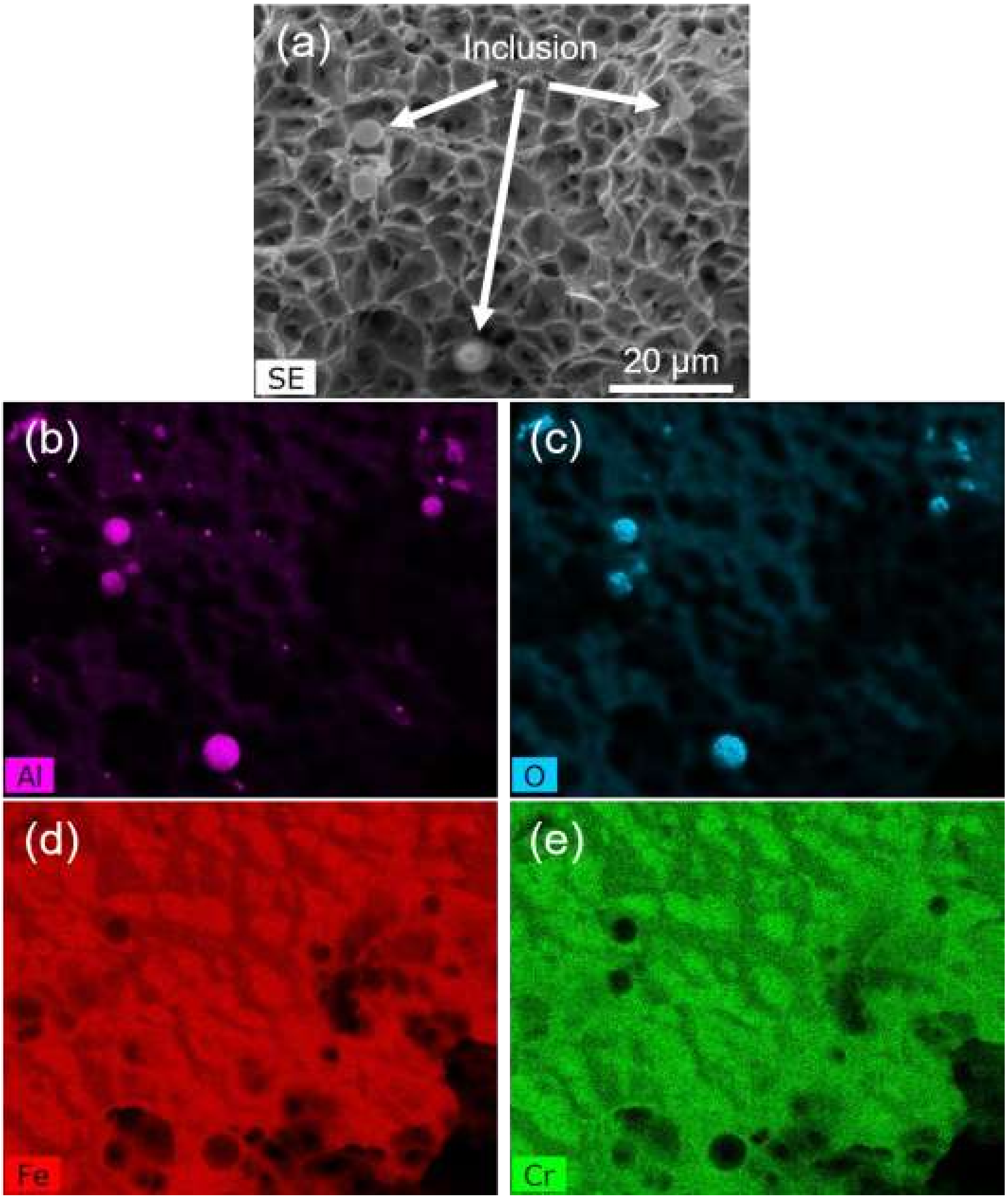

Figure 2.12 (a) High magnification SEM image, and (b-e) EDS elemental maps of the fractured surface showing the nature of the oxide inclusions.

2.5 CONCLUSIONS

This study reports the successful implementation of wire arc additive manufacturing for the first time to fabricate defect-free thin-wall PH 13-8Mo martensitic stainless steel parts, with wide range of applications in different industries, requiring high strength and high corrosion resistant large metallic components. The results of microstructural characterizations, microhardness measurements, uniaxial tensile tests, and fractography of the as-printed parts led to the following conclusions:

1. The as-printed macrostructure of the WAAM PH 13-8Mo wall was found to consist of large unidirectional columnar grains grown preferentially parallel to the building direction of the part, creating a strong {100}<001> cubic texture along the building direction.
2. The as-printed microstructure of the part was dominantly characterized by residual δ-ferrite phase with vermicular and lathy morphologies distributed in a martensitic matrix in addition to a slight volume fraction of retained austenite.
3. The complex thermal history of the fabrication process led to the formation of inhomogeneous microstructural features through the building direction. In particular, the content of both retained austenite and δ-ferrite phases were reduced from the bottom to the top of the fabricated wall.
4. The fabricated wall showed a slightly superior hardness and UTS in the top layers than those of the bottom layers ascribed to the lower volume fraction of retained austenite and δ-ferrite in the top regions of the component. Moreover, microhardness evaluations across subsequently deposited layers revealed a slightly higher microhardness value in the HAZs as compared to the melt pools' centers, associated with the dissolution of remnant δ-ferrite in the HAZs, creating a nearly fully martensitic microstructure in HAZs.
5. The results of uniaxial tensile tests showed that the average UTS of the WAAM PH 13-8Mo (~1117 MPa) was comparable to DMLS-built CX stainless steel part and superior to 17-4 PH parts fabricated by either WAAM or selective laser melting reported in the literature.
6. The ductility of the as-printed component was revealed to be noticeably anisotropic along the building and deposition directions due to the preferential orientation of primary columnar δ-ferrite crystals along the building direction, formed during the non-equilibrium solidification process.

Acknowledgments

The authors gratefully acknowledge the support of Natural Sciences and Engineering Research Council of Canada (NSERC) [grant number RGPIN-2017-04368], Canada Research Chair program, Ocean Frontier Institute, and Dalhousie University for sponsoring this work.

CHAPTER 3 MICROSTRUCTURAL EVOLUTION AND MECHANICAL PERFORMANCE AFTER PRECIPITATION HARDENING OF PH 13-8MO MARTENSITIC STAINLESS STEEL FABRICATED BY WIRE ARC ADDITIVE MANUFACTURING

Mahya Ghaffari[1], Alireza Vahedi Nemani[2], Ali Nasiri[3]

1- Graduate Student, Dalhousie University, Halifax, Nova Scotia, Canada
2- Post-Doctoral Fellow, Dalhousie University, Halifax, Nova Scotia, Canada
3- Assistant Professor, Dalhousie University, Halifax, Nova Scotia, Canada

Status: Published Journal Paper, Journal of Materialia, Volume 24, Page 101507

Authors' Contribution

Mahya Ghaffari: Conceptualization, Fabrication Process, Investigation, Writing - original draft.

Alireza Vahedi Nemani: Methodology, Validation, Investigation, Writing - review & editing.

Ali Nasiri: Supervision, Writing - review & editing, Funding acquisition.

3.1 ABSTRACT

In the present study, wire arc additive manufactured precipitation hardening (PH) 13-8Mo martensitic stainless steel was subjected to various solution and aging treatments to eliminate the columnar structure, non-equilibrium phases (e.g., δ-ferrite), inhomogeneous microstructure, and anisotropic ductility, detected in the as-printed part. The microstructural characterizations showed that 1050 °C was the optimum solutionizing temperature to remove the columnar grain structure and deleterious δ-ferrite phases, leading to a fully martensitic microstructure with a slightly higher hardness as compared to the as-printed part. The subsequent aging treatment at 450 and 500 °C led to the formation of nanometric and coherent β-NiAl precipitates inside the martensite laths, resulting in a substantial microhardness and tensile strength improvement. Higher temperature aging at 550 and 600 °C caused the formation of other secondary phases, *i.e.,* Cr-rich carbides and reverted austenite, respectively, contributing to enhanced ductility at the expense of reduced tensile strength of the material. The

implemented post-printing heat treatment was found to be efficient in suppressing the observed anisotropic ductility in the as-printed part, primarily dictated by the texture weakening that occurred during solution treatment.

3.2 INTRODUCTION

Precipitation hardening martensitic stainless steels (PHMSSs) provide superior strength compared with austenitic and ferritic stainless steels while maintaining their moderate ductility as well as outstanding corrosion resistance under harsh environmental conditions [2][3]. Owing to such properties, PHMSSs are ideal materials for the fabrication of valves, shafts, fittings, pins and lock washers, landing gear parts, or steam power plant turbine blades used in a wide range of industries, such as aerospace, defense, petrochemical industries, among others [3][4][5][9]. These types of alloys are typically low-carbon steels (<0.07 wt. %C) containing 13 to 17 wt. % Cr and 4 to 8 wt. % Ni, in addition to other substitutional alloying elements, such as Mo, Cu, Al, Co, and Ti, which are added to achieve the desired properties during post-process heat treatment [4][7][8]. PHMSSs commonly solidify as δ-ferrite with a body-centered cubic (bcc) structure, which subsequently transforms to austenite upon cooling to intermediate temperatures, and finally transforms to low-carbon martensite with a martensite finish (M_f) temperature just above room temperature [9][10]. Despite the low carbon content of martensite in these alloys, their primary strengthening arises from the obstruction of dislocations motion by the formation of various intermetallic nano-size compounds, such as β-NiAl, Ni_3Ti, Ni_3Al, or copper-rich precipitates within the predominantly soft martensitic matrix [8][10][11][12]. To form these fine precipitates, PHMSSs are primarily subjected to solution treatment at temperatures above 850 °C in the austenite single-phase region, followed by subsequent cooling to room temperature to obtain a fully supersaturated martensitic structure, and then undergo further aging treatment at moderate temperatures (400 to 620 °C) for 1 to 5 h [4][7][8][10]. According to the literature [5][10], depending on the heating rate and alloying elements content, the nucleation of precipitates starts at a temperature range of 400-550 °C and finishes between 500 and 600 °C. However, the maximum strength is achieved at a certain temperature, influenced by the type, shape, size, coherency, and volume fraction of the formed precipitates as well as the chemical composition of the matrix [11][12]. Ping *et al.* [8] investigated the microstructural characteristics of 13Cr–8Ni–2.5Mo–2Al PHMSS and reported the formation of a high volume fraction of ultra-fine (1–6 nm) β-NiAl precipitates during aging at 450-620 °C, while the peak strength was obtained at 510 °C. These precipitates were claimed to be spherical in shape and evenly dispersed through the martensitic matrix with perfect coherency [8]. Among the most common grades of PHMSSs (*i.e.,* PH 13-8Mo, 17-4 PH, 15-5 PH), the best combination of strength, ductility, and fracture toughness, as well as higher resistance to hydrogen embrittlement, pitting corrosion, and sulfide stress corrosion cracking is offered by PH 13-8Mo [4][5][7][78][151]. Therefore, the present work is focused on the PH 13-8Mo stainless steel, with a particular application in plastic injection molding dies [152]. There was a lack of information about the detailed characteristics of the fine precipitates produced during aging treatment of PH 13-8Mo alloy until 2003, when Guo *et al.* [5] were able to provide a comprehensive description of the precipitation evolution during aging in a wrought PH 13-8Mo using a position-sensitive atom probe (PoSAP) instrument. They suggested that the formation of NiAl-enriched zones start after 15-40 min during aging at 510 °C and even in less than 6 min of aging at 593 °C [5]. Although they reported that the morphology of NiAl particles transforms from spherical to plate-like or needle shape at longer aging times and temperatures [5], most of the later studies showed that the β-NiAl precipitates remain spherical even at the final stages of the aging process [8][153][154]. One of the desirable characteristics of β-NiAl precipitates that directly contributes to the high strength of the PH 13-8Mo alloy is their great coherency and low lattice misfit with the martensitic matrix [4]. Besides the precipitation of β-NiAl, the formation of other secondary phases, such as carbides, reversion of the martensite to austenite, and recovery of martensite at higher aging temperatures can also affect the mechanical properties of the alloy [7][12][155]. Tsay *et al.* [80] investigated the strength level and stress-corrosion susceptibility of PH 13-8Mo laser welds in a saturated H_2S solution and found that the presence of reverted austenite in the overaged condition (620 °C) causes a relatively lower hardness but superior sulfide stress corrosion cracking resistance in comparison with the samples aged at lower temperatures. Therefore, the desired aging temperature should be developed based on the in-service application to conform to the required mechanical and corrosion properties.

Despite the superior mechanical performance of PHMSS alloys as compared to other families of stainless steels, they suffer from poor machinability and formability leading to expensive and time-consuming post-processes to reach the intended design through conventional forming and machining methods [14]. As an ideal alternative, additive manufacturing (AM) techniques allow the fast production of high-strength PHMSS parts with complex geometry without dies or considerable post-machining [14]. A large number of studies have been conducted on assessing the microstructural characteristics and mechanical properties of heat-treated PHMSS alloys fabricated through conventional manufacturing methods, while the studies related to the AM parts with distinct as-printed microstructure are very limited. Recently, EOS GmbH [84] introduced and commercialized the powder form of PH 13-8Mo alloy under the name Corrax® (CX) with a very similar chemical composition to the conventional counterpart raw material. Accordingly, the existing studies on additively manufactured PH 13-8Mo components have been dominated by powder-based AM methods, aiming to investigate the effect of process variables [131][156] and post-printing treatments [83][85][86][101] on the microstructure, mechanical, and corrosion properties of the printed parts. For the first time, Asgari *et al.* [157] claimed the successful selective laser melting (SLM) of pre-alloyed CX powder in which the fabricated part was reported to exhibit a higher tensile strength as compared to SLM fabricated 17-4 PH and 316 L stainless steels. In a later study, Hadadzadeh *et al.* [83] performed different post-printing heat treatment cycles, including solution treatment, solution-aging, and direct aging on the SLM-CX samples, and proposed that the maximum hardness (502 $HV_{0.3}$) was achieved for the samples directly aged from the as-printed state (336 $HV_{0.2}$) due to the presence of β-NiAl precipitates in a refined martensitic matrix. In a similar study, Chang *et al.* [85] could improve the microhardness of the SLM CX samples from 357 $HV_{0.2}$ in the as-printed condition to 514 $HV_{0.2}$ by applying appropriate solution-aging treatment. Another relevant study was carried out by Shahriari *et al.* [86] to compare the corrosion resistance of the heat-treated SLM CX part with a quenched-tempered 420 MSS. They reported that the solutionized-aged SLM CX sample comprises of a homogenized microstructure with less retained/reverted austenite and Cr-rich carbides in comparison with the quenched-tempered 420 MSS sample, which resulted in a higher corrosion resistance [86].

It should be noted that the SLM technique is basically suitable for fabricating relatively small and complex components; however, the difficulty of controlling a large number of process variables, high cost of the vacuum set-up, and material wastage are the main challenges of this technology [24]. Conversely, the wire arc additive manufacturing (WAAM) method is extensively used for producing large-scale near-net-shape products due to its much superior deposition rate, lower capital cost, and efficient material utilization [53]. Considering the remarkable benefits of WAAM technology, the expanded use of this method to build PHMSS components for industrial domains that require high strength and excellent corrosion-resistant large-scale components is becoming an imminent trend. However, the high heat input associated with the nature of the arc-based heat sources leads to a significant directional temperature gradient and complex thermal history experienced by different locations of the WAAM parts, which result in microstructural variations and anisotropic properties that differ from conventionally fabricated materials [51][65]. Moreover, in real applications of PHMSS alloys, the components are typically subjected to extreme mechanical loads and harsh environmental conditions [11]. In view of the above facts, applying proper post-printing heat treatment cycle(s) is vital to homogenize the microstructure and obtain the required mechanical and corrosion properties of additively manufactured parts [106].

Since a small variation in aging temperature can significantly change the type, size, shape, and volume fraction of the secondary phases, a fundamental understanding of the precipitates formation sequences along with the resultant mechanical properties at different solution/aging temperatures are imperative to the successful development of proper post-printing heat treatment cycles [8][12]. According to the literature, the only heat treatment cycle performed on the SLM CX parts was aging treatment at 530 °C for 3 h with or without prior solution treatment at 900 °C for 1 h, which is recommended by EOS GmbH [84][83][85][86]. Therefore, not only there is no investigation on the effect of post-printing heat treatment on the WAAM PH 13-8Mo, but also the literature is bereft of information regarding the impact of different aging temperatures on the microstructure and mechanical properties of additively manufactured PH 13-8Mo stainless steels. In the authors' previous work [151], the fabrication feasibility of PH 13-8Mo stainless steel parts through wire arc additive manufacturing was studied, and it was found that there is a noticeable anisotropy of ductility along the building and deposition directions. In the current investigation, various post-printing heat treatment cycles were applied to WAAM 13-8Mo parts to reduce/eliminate the inhomogeneous microstructure and anisotropic mechanical properties, and further ameliorate the mechanical properties of the as-printed part.

3.3 MATERIALS AND METHODS

3.3.1 Materials Preparation and Fabrication Process

In this study, wire arc additive manufacturing was employed to fabricate a ~120 × 210 × 12 mm^3 wall-shaped part (Figure 3.1a and b) using a commercial PH 13-8Mo stainless steel feedstock wire with a diameter of 1.143 mm. The nominal chemical composition of the feedstock wire (in wt.%) was 12.25-13.25 Cr, 7.5-8.5 Ni, 2-2.5 Mo, 0.9-1.35 Al, 0.1 Mn, 0.1 Si, 0.05 C, 0.01> S, 0.01> N, and Fe balance [132]. The wall was built on an AISI 420 martensitic stainless steel plate employing an S-350 Power Wave Lincoln Electric gas metal arc (GMA) machine equipped with a torch mounted on a 6-axis Fanuc robot using optimized process parameters reported in the authors' previous work [151]. During the deposition process of the wall, the interpass temperature of 100±10 °C was maintained between each deposited layer using a digital non-contact infrared thermometer with a measurement range from -60 to 1000 °C.

3.3.2 Post-fabrication Heat Treatment Process

Different post-fabrication heat treatment cycles were carried out on the as-printed WAAM PH 13-8Mo samples using a Thermo-Scientific Lindberg furnace in an Argon atmosphere. The samples were first subjected to solution treatment at different temperatures, *i.e.,* 900, 950, 1050, and 1150 °C for 60 min, followed by still-air cooling to room temperature. Since the temperature of 1050 °C was selected as the optimum solutionizing temperature, at the next step of the heat treatment process, only the 1050 °C solutionized samples were aged for 4 h at different temperatures, *i.e.,* 400, 450, 500, 550, and 600 °C. Accordingly, the solution-treated samples were marked as S900, S950, S1050, S1150, and the aged samples were denoted by A400, A450, A500, A550, and A600.

3.3.3 Microstructural Characterizations

Metallographic observations were made on the as-printed and heat-treated specimens etched with Fry's reagent using an optical microscope (OM, Nikon Eclipse 50i) and a scanning electron microscope (SEM, FEI MLA 650F) equipped with energy-dispersive X-ray spectroscopy (EDS) and electron backscattered diffraction (EBSD) detectors. To further study the sub-micron microstructural features of the samples and identify the type, size, shape, and distribution of potential secondary phases, a scanning transmission electron microscope (STEM, Talos 200X) equipped with an extreme field emission gun (X-FEG) source operating at 200 kV was also employed. The TEM thin foils with a diameter of 3 mm were prepared using a twin-jet electro-polisher in an electrolyte containing 10 vol.% perchloric acid and 90 vol.% methanol at a voltage of 16 V and a constant temperature of -40 °C.

In addition, X-ray diffraction (XRD) technique using a Rigaku Ultima IV X-ray diffractometer with Cu-K_α radiation operated at 40 kV and 44 mA was used for phase identification and detection of the relative amount of retained/reverted austenite in the as-printed and heat-treated samples. A step size of 0.02° was used to cover a 2θ scanning range from 40 to 100° with a scanning rate of $5°\text{min}^{-1}$. Moreover, to identify the onset of various phase transformation temperatures, the dilatometry technique using a Netzsch DIL 402 dilatometer was performed in an Ar environment at heating and cooling rates of 20 °C/s with the peak temperature of 1200 °C.

3.3.4 Mechanical Properties Evaluations

Vickers microhardness measurements were performed on the as-printed and heat-treated samples using a Buehler Micromet hardness tester with a load of 500 g. Different micromechanical properties were also measured by a Nanovea PB1000 Hardness Tester under a peak load of 5 N and a loading rate of 2 mN/s. Each plotted microhardness and indentation graphs are the mean value of at least 10 readings from different positions of each sample to confirm the reproducibility of the results. Tensile test specimens were extracted by water jet cutting from the machined wall in accordance with ASTM E8M standard [134], with a gauge length, width, and thickness of 25 mm, 5 mm, and 5 mm, respectively. As shown in Figure 3.1b, tensile test coupons were prepared in two different sets of samples to investigate the possible anisotropic properties in the as-printed and heat-treated specimens: one set with a tensile axis along the building direction, denoted as vertical samples, and the second set with tensile axis along the deposition direction, denoted as horizontal samples. To perform the uniaxial tensile test, an Instron 5585H-250 kN load frame equipped with an extensometer was employed at a strain rate of 1 mm/min. The tensile tests were repeated at least three times to ensure the repeatability of the obtained values.

3.4 RESULTS AND DISCUSSION

3.4.1 Microstructural Characteristics

OM micrographs of the fabricated WAAM wall using PH 13-8Mo stainless steel feedstock wire are shown in Figure 3.1c and d, exhibiting a multilayered columnar structure elongated through the whole height of the wall divided by the fusion lines. During the deposition of the initial layer, the unidirectional columnar grains nucleated on the base metal, followed by an epitaxial growth antiparallel to the predominant heat flow path during the deposition of each subsequent layer, which eventually resulted in a columnar structure along the building direction (z-axis) of the wall (see Figure 3.1d).

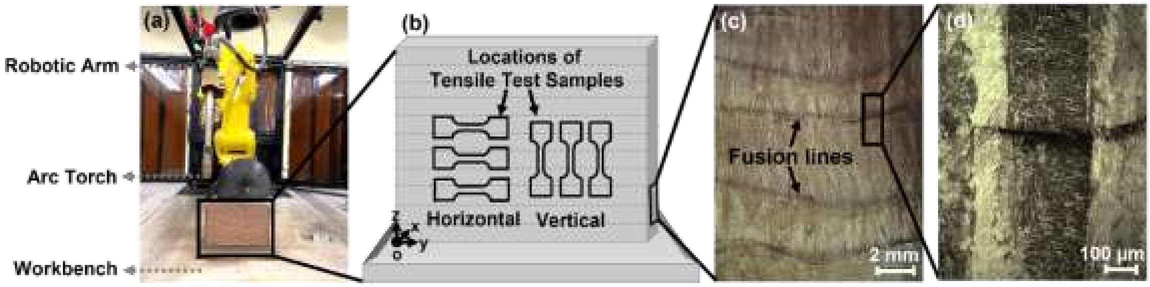

Figure 3.1 (a) The WAAM fabrication set-up, (b) schematic illustration of the WAAM fabricated PH 13-8Mo stainless steel wall, indicating the orientations of samples prepared for tensile testing, (c) low, and (d) high magnifications OM micrographs taken from the x-z plane.

The solidification mode and microstructural variations of stainless steels are particularly controlled by the chromium to nickel equivalent ratio (Cr_{eq}/Ni_{eq}), which determines the balance between ferrite and austenite phases [2][9][158]. Based on the modified WRC-1992 diagram [2][9], the predicted solidification mode of PH 13-8Mo alloy with $Cr_{eq}/Ni_{eq} > 1.7$ is F-mode, meaning solidification is expected to begin with the nucleation of δ-ferrite phase [2][151]. Therefore, the observed columnar grains in Figure 3.1c and d can be characterized as primary δ-ferrite grains formed at the initial stages of the solidification process. According to the literature [9], these primary δ-ferrite phases will transform to austenite and then martensite during cooling to room temperature. However, considering the rapid and non-equilibrium cooling associated with the WAAM process [46], a high volume fraction of δ-ferrite phases will remain untransformed at room temperature, which are visible in the SEM image confirmed by the EDS mapping shown in Figure 3.2a. Moreover, a certain amount of film-like retained austenite was also detected in the TEM micrograph of the as-printed sample (see Figure 3.2b), while no other secondary phases or precipitates, such as β-NiAl or carbides, were observed at higher magnification TEM image (Figure 3.2c). The formation of retained austenite resulted from the segregation of austenite stabilizing element (Ni), and also in-situ quenching and partitioning heat treatment arisen from implementing 100 °C interpass temperature, which is between the martensite start ($M_s \approx 120$ °C) and finish ($M_f \approx 30$ °C) temperatures of the alloy [83][151][159]. Another metallurgical feature captured by high magnification TEM image in the as-printed sample (Figure 3.2d) was the presence of low-density sets of integrated micro-twins in some random areas. The high magnification bright and dark field TEM images along with its corresponding selected area electron diffraction (SAED) pattern shown in Figure 3.2e and f confirm the formation of twins during the fabrication process. The existence of micro-twins in the PH 13-8Mo and 15-5 PH alloys are also reported by several authors in the literature [153][160][161]. The formation of micro-twins at the martensite lath boundaries in martensitic stainless steels could be attributed to the accommodation of the shape deformation during cooperative (back-to-back) growth of adjacent martensite laths at high cooling rates [161][162]. Overall, the microstructure of the as-printed part was predominantly identified as residual δ-ferrite along with a low content of retained austenite embedded in a low-carbon martensitic matrix. A similar microstructure was also observed by other researchers in the case of wire arc additive manufacturing and also welding of other grades of PHMSS, *i.e.,* 17-4 PH alloy [52][15][139]. A detailed description of the microstructure of the WAAM PH 13-8Mo has been reported in the authors' previous study [151], declaring that the volume fraction of residual δ-ferrite and retained austenite increased from the bottom to the top of the wall as a result of cooling rate reduction as the building process progresses along the height of the wall. Accordingly, it was concluded that this heterogeneous and columnar structure led to anisotropic mechanical properties in the as-printed PH 13-8Mo sample [151].

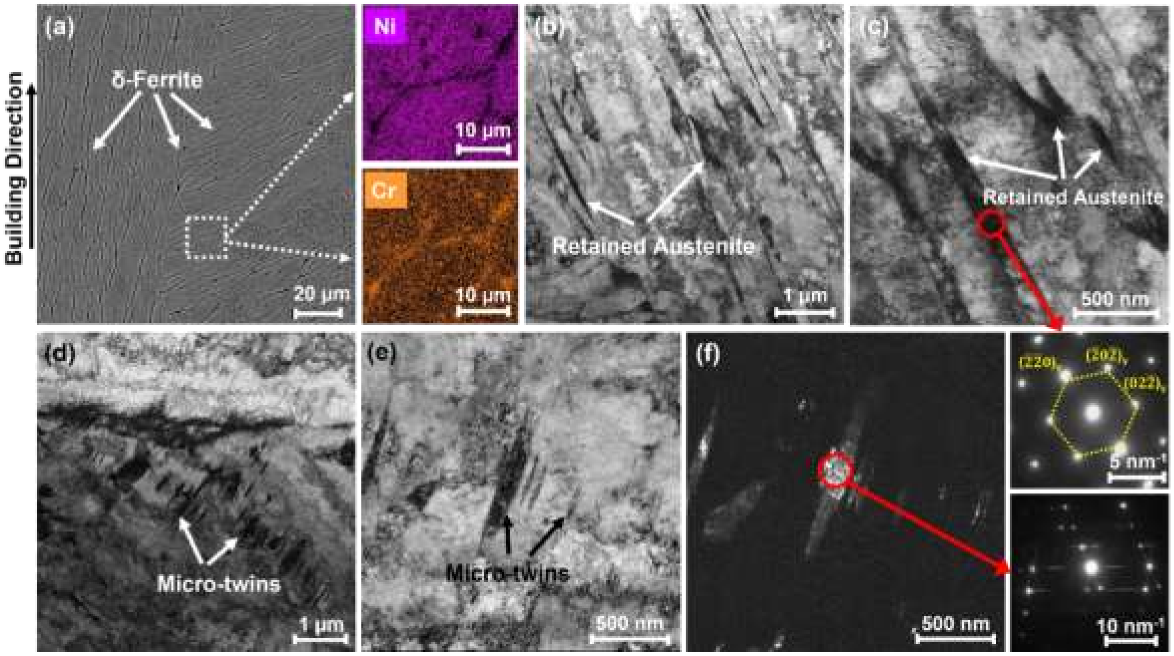

Figure 3.2 (a) SEM micrograph along with the associated EDS mapping taken from the as-printed sample, showing residual δ-ferrite, (b & c) multi-magnification TEM images along with the corresponding SAED pattern, indicating the formation of retained austenite, (d) low, and (e & f) high-magnification bright and dark field TEM images along with its corresponding SAED pattern, confirming the formation of micro-twins.

In order to eliminate the undesired residual δ-ferrite, heterogeneous microstructure, columnar grain structure, anisotropic ductility, and also improve the mechanical properties of the WAAM-PH 13-8Mo part, solution treatment followed by the aging process at different temperatures were applied to the as-printed samples. According to the dilation curve obtained from the dilatometry test of a small sample prepared from the as-printed part (see Figure 3.3), the single-phase austenite stability region was determined to be between ~720 °C (Ac_3) and ~1150 °C (Ac_4), suggesting that the solutionizing temperature must be selected in this range to achieve a fully martensitic microstructure in the solution-treated condition. Therefore, to obtain the optimum solutionizing temperature, as-printed samples were subjected to the solution treatment at different temperatures *i.e.,* 900, 950, 1050, and 1150 °C for 1 h followed by air-cooling.

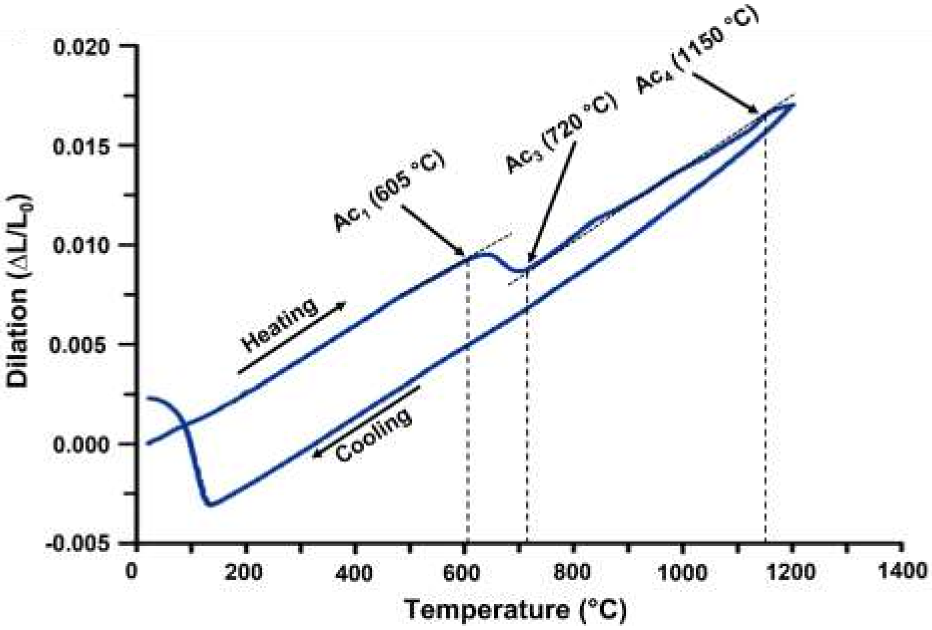

Figure 3.3 Dilation ($\Delta L/L_0$) *vs* temperature (ΔL is the change in length, L_0 is the original length) curve of the WAAM PH 13-8Mo sample, revealing austenite-start temperature (Ac_1), austenite-finish temperature (Ac_3), and ferrite-start temperature (Ac_4).

As suggested by ASM [163] and EOS GmbH [84], the standard heat treatment for PH 13-8Mo alloy includes air cooling from 900-930 °C followed by an aging process, which was frequently employed by different researchers [10][80][83][85][86][152]. However, as can be seen in Figure 3.4a and b, neither the columnar structure nor the residual δ-ferrite was eliminated in the solution-treated sample at 900 °C herein. Therefore, solution treatment should be implemented at above 900 °C to reach the fully austenite region and trigger sufficient recrystallization of primary δ-ferrite grains. This shows that the initial columnar structure of the wire arc additively manufactured parts results in different required post-fabrication heat treatment parameters as compared to the conventionally fabricated counterparts. According to Figure 3.4c and d, although the columnar structure was eliminated at the higher solutionizing temperature (950 °C), the presence of a small amount of δ-ferrite indicated that 950 °C was not high enough to entirely dissolve undesired δ-ferrite phases, confirmed by EDS elemental maps (enclosed in Figure 3.4d).

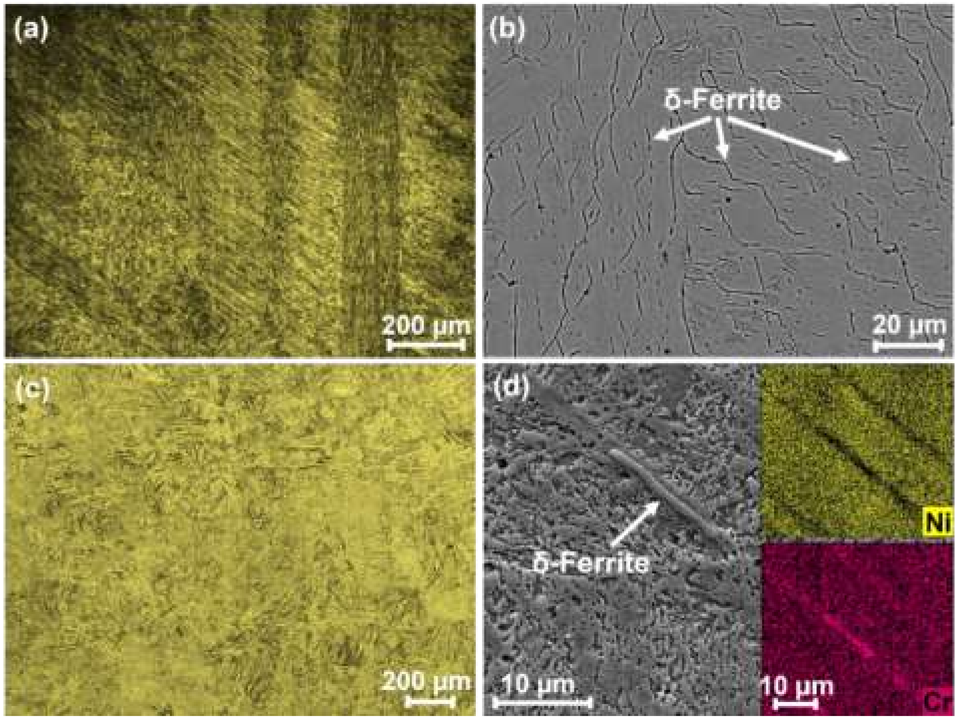

Figure 3.4 OM and SEM images taken from (a & b) S900, and (c & d) S950 samples.

Interestingly, no δ-ferrite was observed in the microstructure of the solution-treated sample at 1050 °C (Figure 3.5a), confirming the complete dissolution of undesired δ-ferrite at this temperature. In addition, the TEM bright field and the corresponding SAED pattern illustrated in Figure 3.5b revealed the removal of retained austenite, resulting in a fully martensitic microstructure with a high density of dislocations. The elimination of retained austenite during the solution treatment process can be correlated to the redistribution of segregated Ni atoms and also experiencing single heating and cooling cycle to below martensite finish temperature ($M_f \approx 30$ °C [151]) of the alloy, resulting in a fully martensitic transformation during cooling to ambient temperature [83][153]. Moreover, the EBSD inverse pole figures (IPF-z) and phase maps taken from both as-printed and S1050 samples depicted in Figure 3.6, confirm the elimination of columnar structure and removal of retained austenite in the sample solution-treated at 1050 °C. The obtained pole figures (PFs) of the bcc phase related to the as-printed sample showed a strong cubic texture aligned with the building direction, suggested by the high maximum intensity of 15.91, observed for {100} planes (see Figure 3.7a), while no strong texture component was detected in {110} and {111} series of planes. The stronger texture at {100} planes for the as-printed sample is ascribed to the directional solidification along the maximum thermal gradient parallel to the building direction. On the other hand, the pole figures of S1050 (Figure 3.7b) exhibit a weaker cubic texture with a lower maximum intensity of 3.23 in {100} planes in addition to several pole components at {110} and {111} planes. The removal of the preferential texture along the building direction in the S1050 sample can be correlated to the recrystallization and growth of new polygonal austenite grains formed during the solution treatment process.

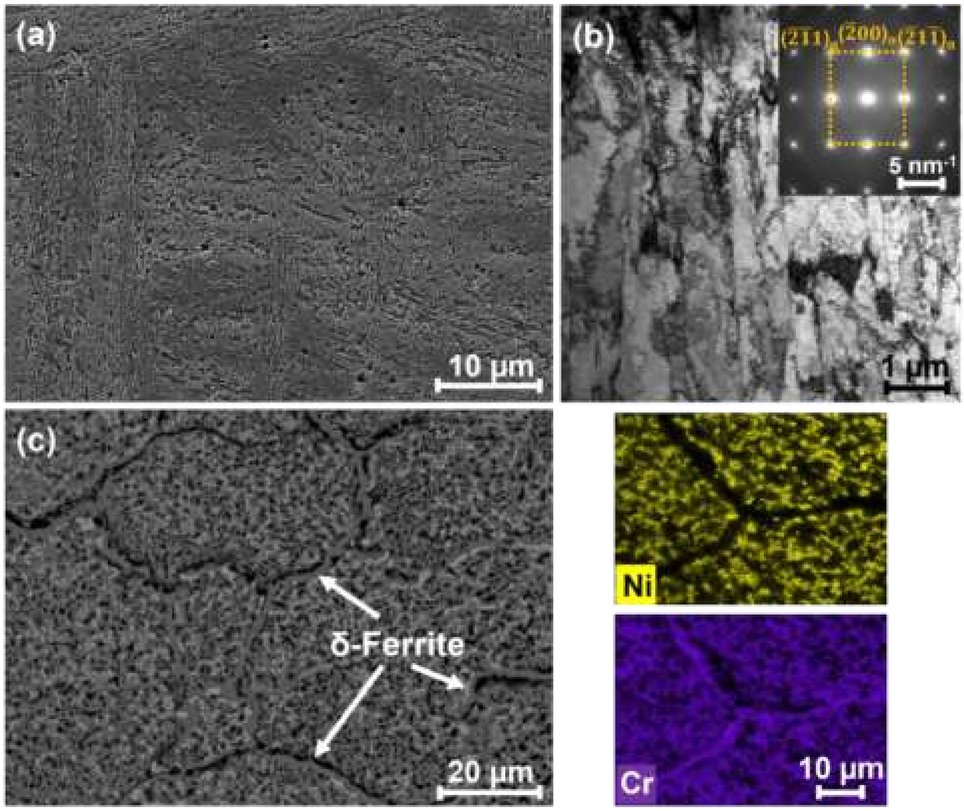

Figure 3.5 (a) SEM and (b) TEM micrographs of S1050 sample, and (c) SEM image along with the corresponding EDS maps of Cr and Ni taken from S1150 sample.

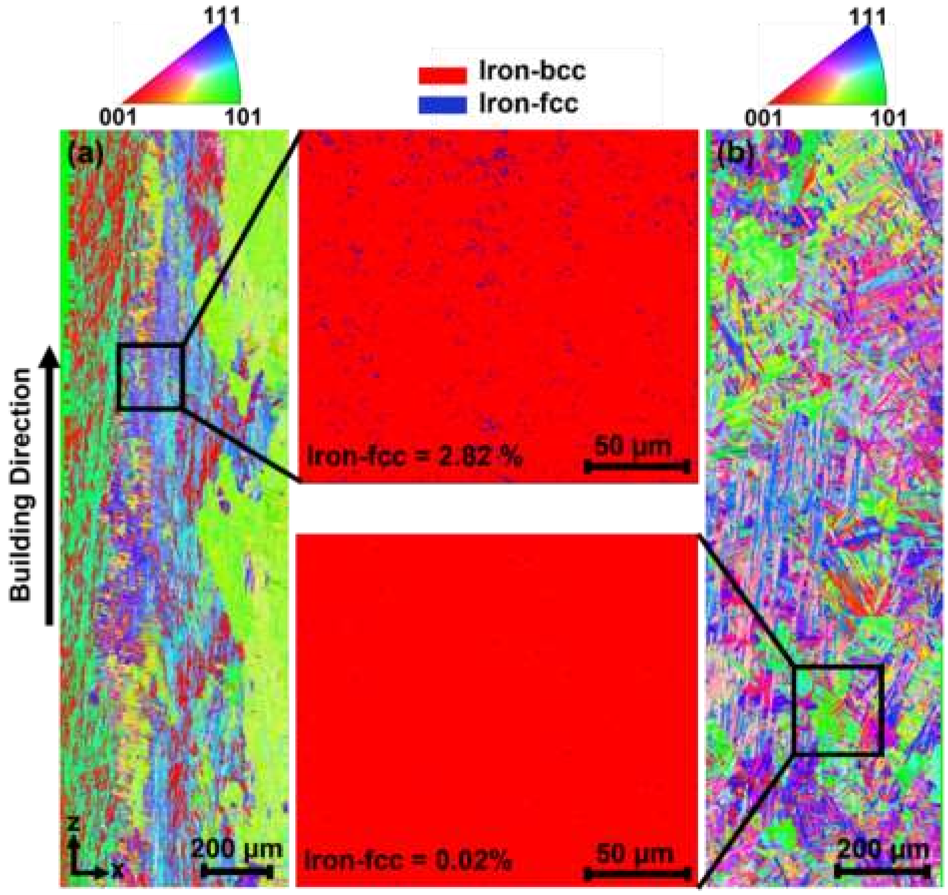

Figure 3.6 IPF-z and phase maps of (a) as-printed and (b) S1050 samples, showing the removal of columnar structure and retained austenite as a result of solution treatment (the step size was 0.75 µm).

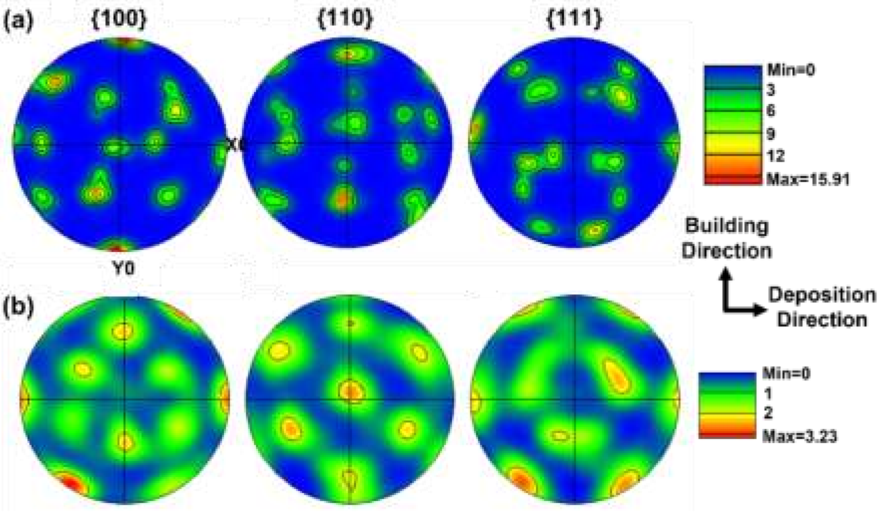

Figure 3.7 EBSD pole figures of bcc phase taken from the (a) as-printed and (b) S1050 samples.

Figure 3.5c illustrates the SEM micrograph and corresponding EDS elemental maps taken from the sample solution-treated at 1150 °C, indicating the presence of δ-ferrite with a higher concentration of Cr as a ferrite stabilizer and lower content of Ni as an austenite stabilizer. According to the dilation curve presented in Figure 3.3, the single austenite phase is stable below 1150 °C, hence the δ-ferrite phase has expectedly started to re-form along the primary austenite grain boundaries at 1150 °C.

In view of the microstructural characteristics detected in different solution-treated samples, 1050 °C was determined as the appropriate solutionizing temperature due to the annihilation of columnar grain structure and complete dissolution of residual δ-ferrite phase resulting in a fully martensitic microstructure, which was the principal purpose of the solution treatment. It is important to note that no precipitates or other microstructural inhomogeneities were evident in the solution-treated samples, which was consistent with the microstructural observations of the solution-treated samples in the literature [153].

As the second step of the post-printing heat treatment, the aging process at five different temperatures, *i.e.,* 400, 450, 500, 550, and 600 °C for 4 h was applied to the 1050 °C solutionized sample. Figure 3.8a depicts the SEM image associated with the sample aged at 400 °C, exhibiting a fully martensitic microstructure. Higher magnification TEM image along with the corresponding SAED pattern further confirmed a martensite lath structure with no observable intermetallic precipitates (see Figure 3.8b). This observation revealed that aging at 400 °C was not adequate for precipitate formation during the aging process. However, as shown by bright field and dark field TEM images in Figure 3.8c and d, increasing the aging temperature up to 450 °C promoted the formation of nanometer-scale spherical precipitates (indicated by white arrows) within the lath boundaries. According to the associated SAED pattern, the randomly distributed precipitates were indexed as β-NiAl intermetallic compounds with a B2 (CsCl) structure [8][11][153]. It is notable that B2 super-lattice structure includes two overlapping cubic cells, in which Al atoms locate at the corners of the primary sub-cell and Ni atoms reside in the corners of the secondary sub-cell [8][11][153]. It has been reported that the formation of β-NiAl precipitates within the lath boundaries could be attributed to the mechanism of pipe diffusion of solute-rich clusters (Ni and Al) along or near the dislocation lines within the lath boundaries [11][164][165]. Considering the difficulties in the exact size-measurement of ultra-fine precipitates, the diameter of precipitates could be estimated as 2-10 nm with less than 20 nm inter-particle spacing. It is known that the lattice parameter of β-NiAl precipitates (0.2887 nm) is quite close to the lattice constant of ferrite (0.2866 nm), which results in a perfect coherent interface between the precipitates and the matrix, significantly contributing to the strengthening of the alloy [4][8][11][165]. The corresponding high-resolution TEM (HRTEM) image taken from a β-NiAl particle in the A450 sample (Figure 3.8e) exhibits a low lattice mismatch interface, confirming the coherency of the precipitate with the martensitic matrix.

As can be seen in Figure 3.8f, the TEM image taken from the sample aged at 500 °C also shows the formation of fine spherical-shaped β-NiAl precipitates uniformly distributed in the martensitic matrix. The corresponding EDS elemental maps also confirm that the precipitates were enriched in Al and Ni, and depleted in Fe and Cr. No noticeable microstructural differences were observed between the samples aged at 450 and 500 °C, except for an insignificant growth in the diameter of precipitates from 2-10 to 10-15 nm. Similar resistance to coarsening for β-NiAl precipitates has been previously observed by other researchers in PH 13-8Mo alloy aged at temperatures between 450 to 620 °C [8][80][153]. Three justifications were suggested for the coarsening resistance of β-NiAl precipitates in the literature, *i.e.*, (i) the negligible lattice parameter mismatch between the martensitic matrix and β-NiAl particles [5], (ii) the low diffusion coefficient of Al in the α-iron matrix (3.1×10^{-25} m^2s^{-1}) [4], and (iii) micro-segregation of solute atoms, such as Mo and Cr at the interfaces of particles and matrix [8]. No other secondary phases were detected in the samples aged at 450 and 500 °C.

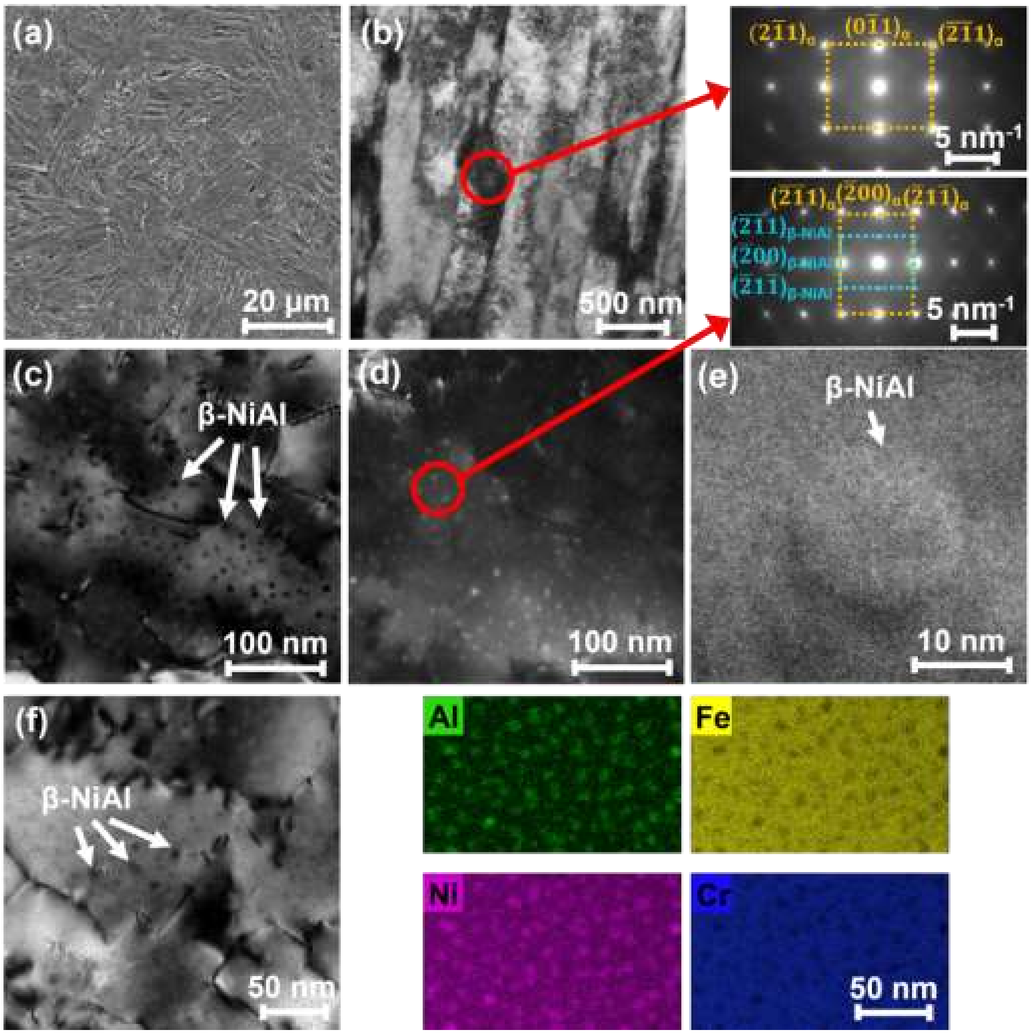

Figure 3.8 (a & b) SEM and TEM images along with the corresponding SAED pattern taken from A400 sample, (c-e) bright field and dark field TEM images along with the associated SAED pattern and HRTEM image taken from A450 sample, and (f) TEM image along with corresponding EDS elemental maps taken from A500 sample.

As illustrated in Figure 3.9, TEM analysis on the sample aged at 550 °C revealed the formation of another secondary phase with an ellipsoidal morphology and an average aspect ratio (length/width) of about 3, in addition to the spherical β-NiAl precipitates. According to the corresponding SEAD pattern shown in Figure 3.9c, the fine ellipsoidal phases were indexed as Cr-rich $M_{23}C_6$ carbides with an fcc crystal structure (a = 1.0730 nm [12]). This observation is in agreement with a study conducted by Ping *et al.* [8] on the aging treatment of a similar alloy (13Cr-8Ni-2.5Mo-2Al) at different temperatures, where $M_{23}C_6$ carbides were only observed at aging temperatures above 550 °C. The nucleation site of the carbide particles was investigated by higher magnification TEM images shown in Figure 3.9b and d. According to Figure 3.9b, the carbides were mostly nucleated homogeneously in the matrix (within martensite laths), while Figure 3.9c revealed the local accumulation of the carbides on the boundaries of pre-existing micro-twins, which were initially detected in the as-printed sample (see Figure 3.2d-f). The formation of $M_{23}C_6$ carbides on incoherent twin boundaries as a preferential nucleation site was also reported during the aging treatment of a 304 austenitic stainless steel [166].

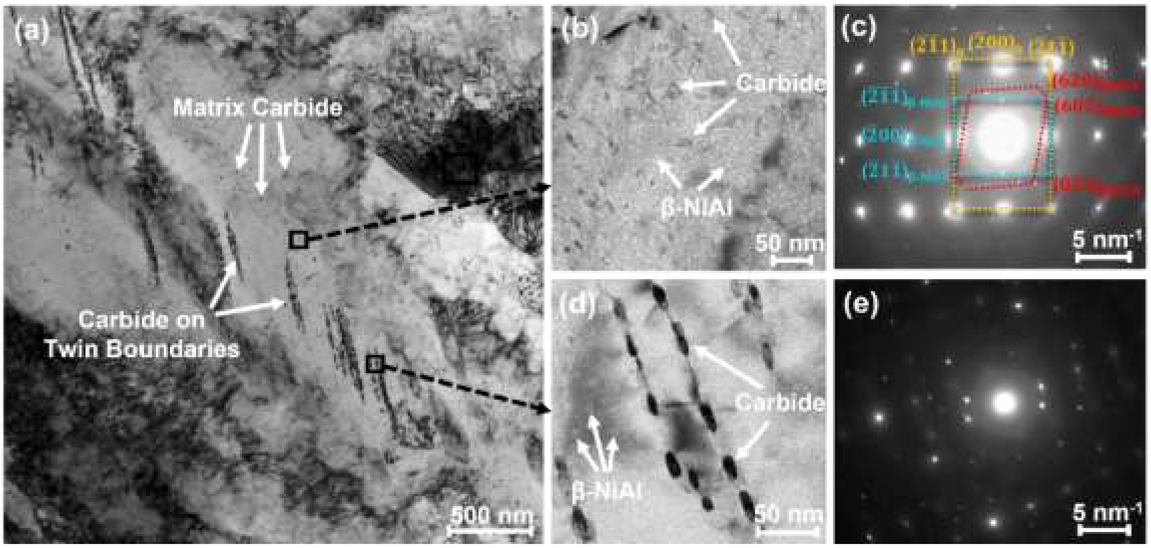

Figure 3.9 (a) Low magnification bright-field TEM micrograph of A550 sample. Higher magnification TEM images along with the corresponding SAED patterns: (b & c) showing the homogenous distribution of carbides within martensite laths (matrix carbide) and (d & e) local accumulation of carbides on twin boundaries.

Figure 3.10 shows multi-scale TEM micrographs of the sample aged at the highest temperature (600 °C). The high magnification TEM image presented in Figure 3.10b revealed that the density of β-NiAl precipitates decreased as a result of their slight growth to an average size of 15-25 nm, while they still remained spherical and coherent with the matrix, which is confirmed by HRTEM image shown in Figure 3.10c. Tsay *et al.* [80] also reported that β-NiAl precipitates are resistant to substantial coarsening and are able to maintain their shape and coherent interface with the matrix even after 4 h of aging at 593 °C. As can be seen in Figure 3.10a, in addition to the presence of β-NiAl intermetallic compounds, considerable amounts of relatively large and dark constituents also appeared in the TEM image of the A600 sample. The associated electron diffraction pattern taken from a selected area of these constituents revealed that the dark phases can be indexed as austenite (Fe-fcc, a = 0.3666 nm [8]).

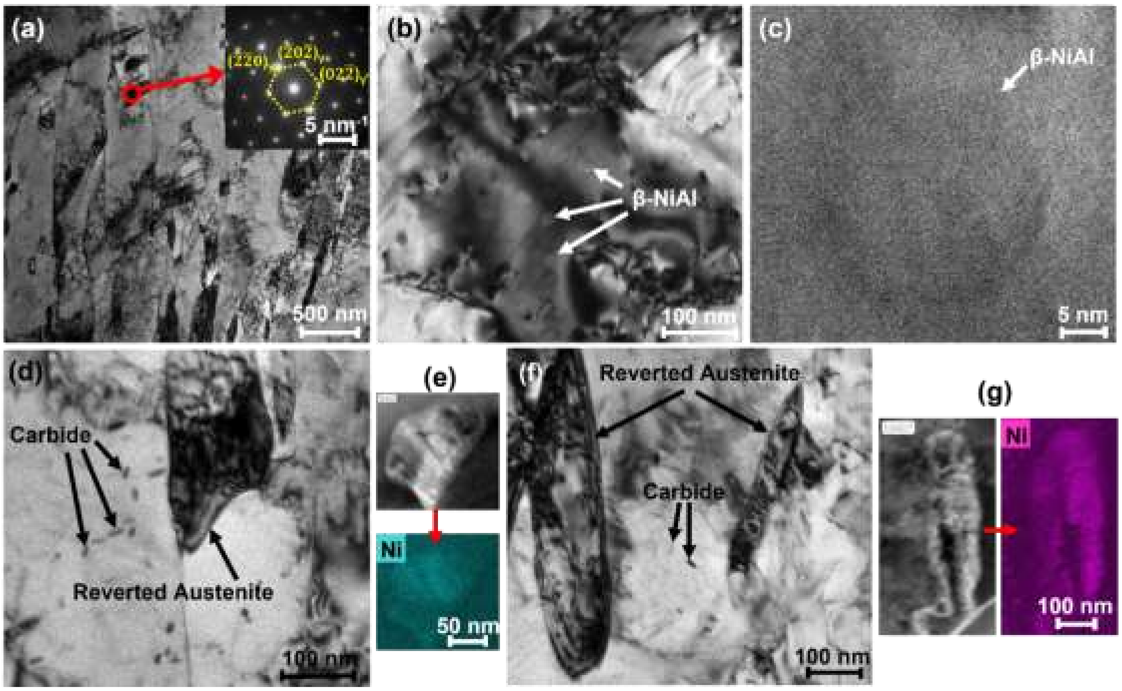

Figure 3.10 (a) Low magnification TEM micrograph along with the electron diffraction pattern taken from the selected area of the A600 sample, (b) high magnification TEM and (c) HRTEM images of β-NiAl precipitates. High magnification TEM images along with corresponding EDS elemental maps of the (d & e) elongated and (f & g) blocky reverted austenite.

In order to better distinguish the nature of the austenite phase formed in the as-printed and A600 samples, XRD and EBSD analyses were carried out. Figure 3.11a and d illustrate the IPF maps taken from a small area of the as-printed and A600 samples along with their lath boundary maps (Figure 3.11b and e), revealing primary austenite grains (PAGs). In order to recognize the orientation of the observed austenite phases, the fcc-IPF maps were also obtained from the EBSD data (see Figure 3.11c and f). According to Figure 3.11c, all the fcc phases in each PAG of the as-printed sample had the same orientation, affirming their retained-nature from the same grain. Based on this observation, one can claim that the fcc phase detected in the as-printed sample could be characterized as retained austenite. On the other hand, the fcc-IPF map taken from the A600 sample (Figure 3.11f) revealed that the fcc phases identified in each PAG possess random orientations, suggesting the recrystallization/nucleation of newly formed austenite phases during the aging process. Therefore, the fcc phases observed in the sample aged at 600 °C can be considered as reverted austenite. The XRD analysis was also performed on the as-printed (AP) and aged samples at the lowest (400 °C), moderate (500 °C), and the highest (600 °C) temperatures, and the results are plotted in Figure 3.12. Accordingly, the peaks of iron fcc were not detected in the samples aged at 400 and 500 °C, as the amount of austenite was less than the measurable limit of the used XRD apparatus. On the other hand, the as-printed and 600 °C aged samples were characterized by high-intensity peaks of fcc at (111), (200), (220), and (311) planes, indicating the presence of a high-volume fraction of austenite (~15% and ~24%) in AP and A600 samples, respectively. The absence of austenite in A400 and A500 samples supports the formation of reverted austenite in the A600 sample developed during the high-temperature aging process as opposed to retained austenite formed during the solidification process in the as-printed sample [7][8][164]. The results of EBSD and XRD analyses agree with the dilatometry measurement, which predicts the austenite start temperature (Ac_1) to be around 600 °C (see Figure 3.3).

According to the low magnification TEM image of the A600 sample (Figure 3.10a), the reverted austenite phases appeared either in a blocky shape with a size of about 170×170 nm^2 (see Figure 3.10d) or with an elongated morphology (~400-700 nm long and ~50-160 nm wide) (see Figure 3.10f). The formation of reverted austenite during the high-temperature aging process can be attributed to the locally high concentration of austenite stabilizing alloying elements in pre-existing high-energy sites, *e.g.* high dislocation density zones, leading to a reduction in M_f of the alloy to below room temperature, which suppresses the transformation of reverted austenite to martensite upon the subsequent cooling process [7][11][152]. The EDS elemental maps exhibited in Figure 3.10e and g manifest a higher concentration of Ni in the reverted austenite phase herein. Accordingly, it can be claimed that the elongated reverted austenite phases are formed due to the micro-segregation of Ni on the lath boundaries, while blocky morphology phases are nucleated from Ni-enriched crystal defects, such as dislocations inside the martensite laths [4][7][11][152]. It has been reported that the nucleation of reverted austenite at higher aging temperatures can be assisted by the presence of Cr-rich carbides with very restricted solubility for Ni, which increases the relative concentration of this element in their vicinity [167]. Interestingly, higher magnification TEM images of the blocky and elongated reverted austenite phases (Figure 3.10d and f) confirmed the formation of carbides in the vicinity of the reverted austenite, which is supported by the XRD analysis, showing the co-existence of austenite and carbides in the A600 sample (see Figure 3.12). Several studies [8][80][152][164][168] also reported the existence of blocky or elongated morphologies of reverted austenite in addition to carbides or β-NiAl precipitates in PH 13-8Mo alloy at the aging condition above 575 °C.

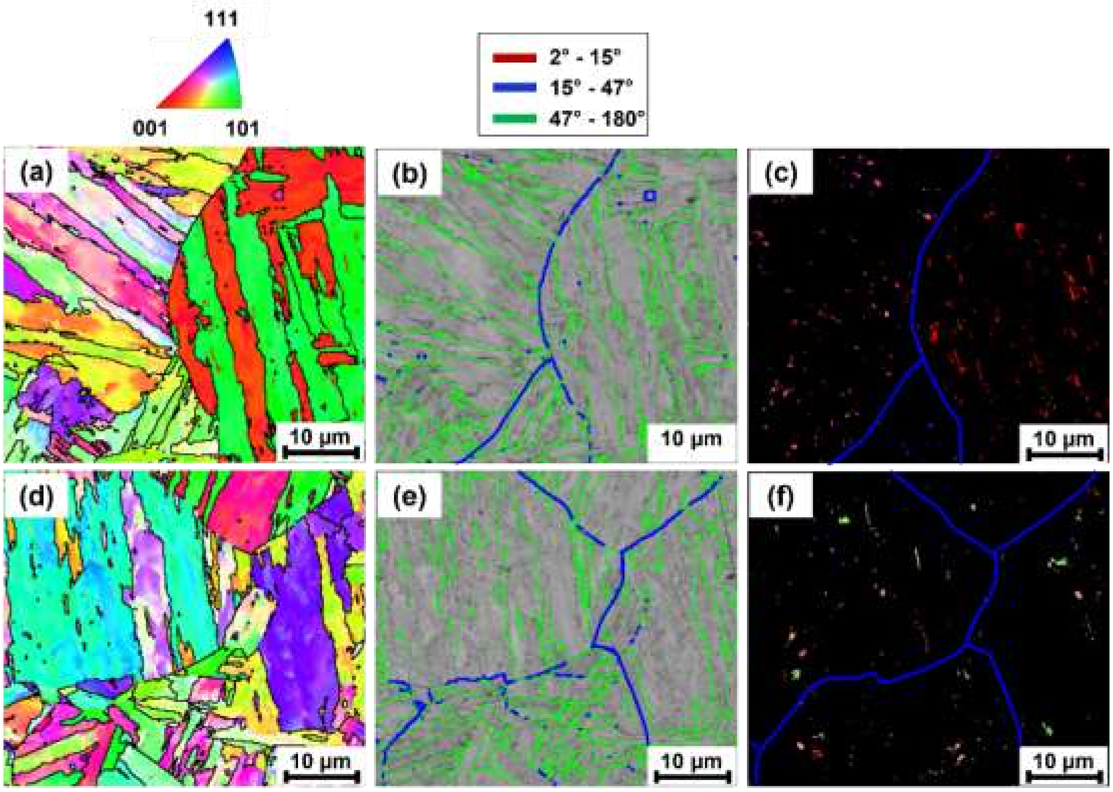

Figure 3.11 IPF-z, grain boundary map, and IPF-z of fcc phase taken from the (a-c) as-printed and (d-f) A600 samples (step size was 0.18 µm).

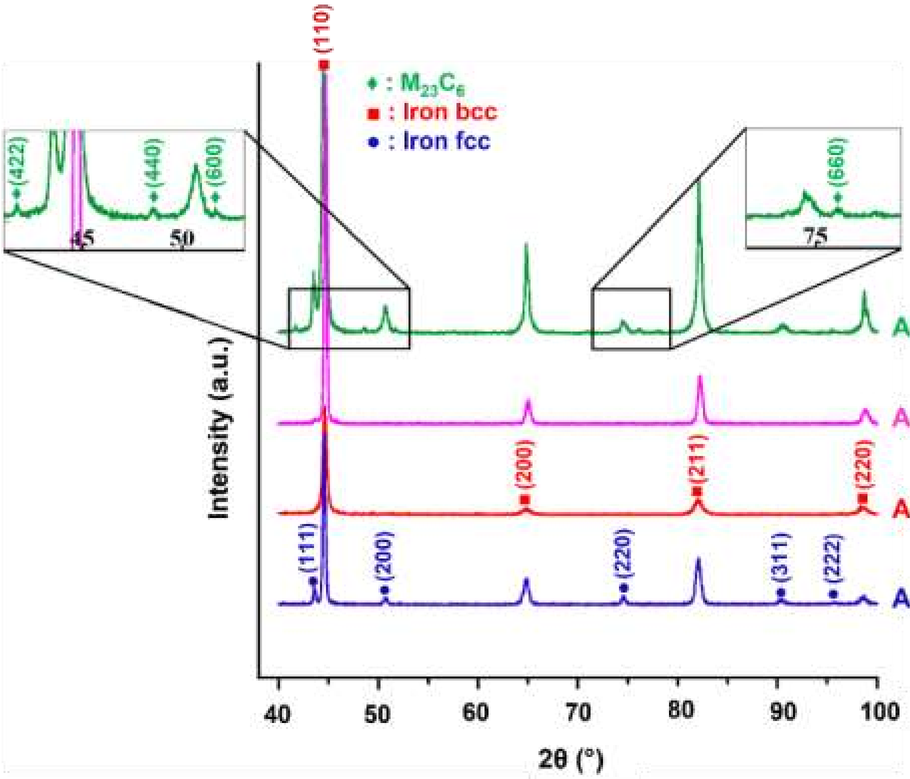

Figure 3.12 The X-ray diffraction patterns taken from the as-printed and aged samples at 400, 500, and 600 °C.

Figure 3.13 shows a schematic summary of different microstructural features formed in WAAM PH 13-8Mo that resulted from different heat treatment cycles performed on this alloy. The WAAM PH 13-8Mo stainless steel in the as-printed condition was dominantly characterized by a columnar structure, including remnant δ-ferrite along with a low amount of retained austenite embedded in a low-carbon martensitic matrix. After solution treatment at 1050 °C, the columnar structure was eliminated, δ-ferrite phases were completely dissolved, and the volume fraction of retained austenite significantly decreased. The microstructure of the sample aged at 400 °C remained the same as the solution-treated sample since this temperature was not adequate for the formation of any secondary phases. However, aging at 450 °C resulted in the nucleation of fine spherical β-NiAl precipitates uniformly distributed within the martensite laths. Increasing the aging temperature up to 500 °C did not significantly alter the microstructure except for a small growth in the size of precipitates. In the case of aging at 550 °C, another secondary phase, *i.e.,* Cr-rich $M_{23}C_6$ carbide, was found to form in addition to β-NiAl precipitates. Finally, besides the β-NiAl intermetallic phases and carbide particles, a relatively high-volume fraction of blocky and elongated reverted austenite phases were also identified in the sample aged at 600 °C.

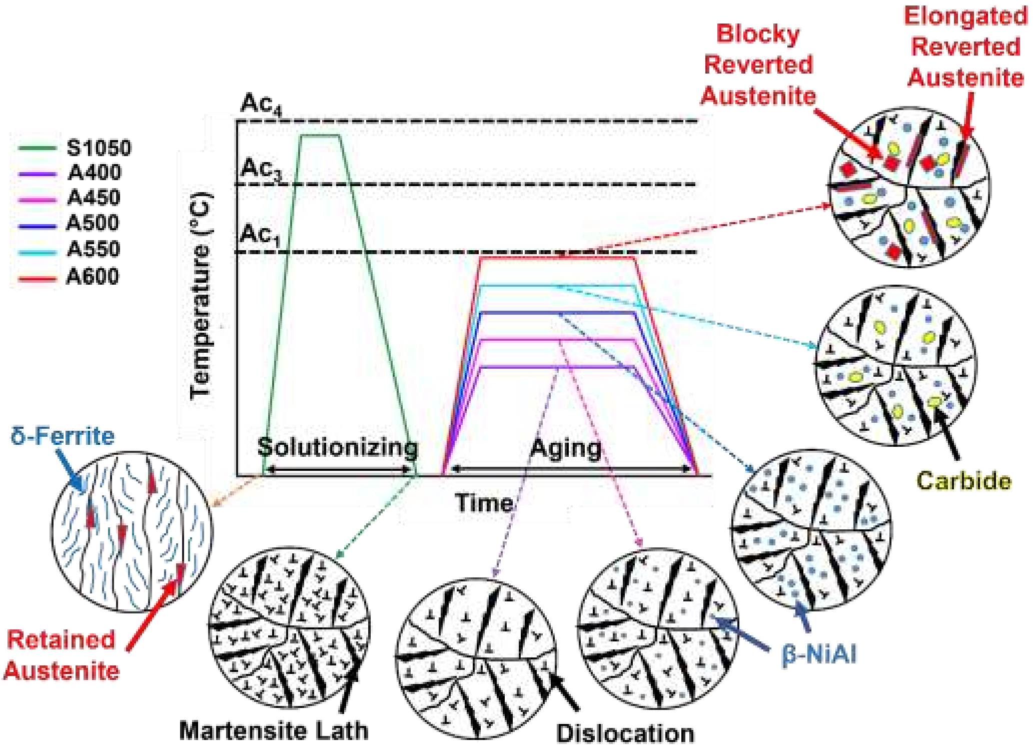

Figure 3.13 Schematic illustration summarizing different microstructural features for the as-printed and heat-treated WAAM PH 13-8Mo samples.

3.4.2 Mechanical Properties Evaluation

The results of Vickers microhardness measurements of the as-printed and heat-treated samples are plotted as bar charts shown in Figure 3.14. According to Figure 3.14a, the minimum microhardness value (326 ± 11 $HV_{0.5}$) was recorded for the as-printed sample consisting of a high-volume fraction of soft δ-ferrite embedded in a martensitic matrix along with a low content of retained austenite. A slight increase in the hardness value to 339 ± 8 and 351 ± 5 $HV_{0.5}$ was observed in S900 and S950 samples, respectively, which can be attributed to the partial dissolution of the δ-ferrite phase during the solution treatment. Moreover, a comparison between the samples solution-treated at different temperatures reveals that the maximum microhardness value was attained for S1050 (396 ± 2 $HV_{0.5}$) with a fully martensitic microstructure. The complete removal of δ-ferrite and retained austenite phases, which are inherently softer than martensite, validates the higher microhardness value of the S1050 sample as compared to the as-printed and other solution-treated samples. On the other hand, re-formation of a relatively high-volume fraction of δ-ferrite on the primary austenite grain boundaries during solution treatment at 1150 °C (see Figure 3.5c) reduced the microhardness to around 311 ± 7 $HV_{0.5}$ in the S1150 sample.

According to Figure 3.14b, an increasing trend was observed in the microhardness values of the aged samples from 373 ± 2 to 507 ± 4 $HV_{0.5}$ for A400 and A450 samples, followed by a further increase to the maximum value of 538 ± 3 $HV_{0.5}$ for the aging condition of 500 °C. On the other hand, raising the aging temperature to 550 and 600 °C led to a fair reduction of microhardness to 474 ± 4 $HV_{0.5}$ for A550 and a drastic drop to 294 ± 6 $HV_{0.5}$ for the A600 sample.

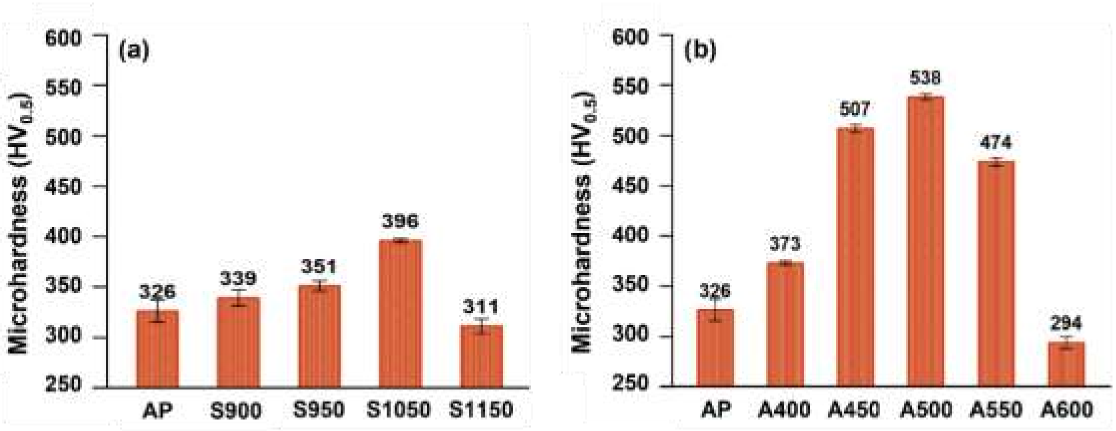

Figure 3.14 Vickers microhardness values of the as-printed in comparison with (a) solution-treated and (b) aged samples.

To better characterize micromechanical properties of the as-printed and aged samples, indentation experiments were performed and the resultant load versus depth diagrams, representing the mean values for each sample, are presented in Figure 3.15a. Under the same maximum load of 5 N, the as-printed sample revealed a larger indentation depth (8.43 µm) as compared to any sample aged at lower than 600 °C, confirming the effectiveness of the applied post-process aging treatment up to a certain temperature in improving the hardness of the material. Other micromechanical characteristics can also be obtained using the indentation hardness (H_{ind} in GPa) and reduced elastic modulus so-called indentation modulus (E_r), which are supportive in evaluating the performance of the part in the service conditions [169][170][171][172]. For example, the ratio of indentation hardness to the reduced elastic modulus ($\frac{H_{ind}}{E_r}$) is a tribological representative of the material (wear resistance) and ($\frac{H_{ind}^3}{E_r^2}$) indicates the resistance of the material to plastic deformation under contact loading, also known as yield pressure [172][173]. The indentation curves (Figure 3.15a) were also used to calculate the elastic energy (U_e), plastic energy (U_p), and the total indentation work (U_t) done by the indenter during loading, which can be obtained by adding the elastic and plastic energies ($U_t = U_e + U_p$). It is notable that U_e can be calculated by the integral of the unloading segment, while U_t is the area between the loading curve and the depth axis [169][171][173]. Other micromechanical properties, such as elastic recovery (ER) and plasticity index (PI) can also be calculated based on values of indentation hardness (H_{ind}) and reduced elastic modulus (E_r) using equations 1 and 2. The elastic recovery is associated with the released energy during unloading, and the plasticity index reflects the intrinsic plasticity of the material indicative of higher formability and ductility under loading at room temperature [169][171].

$$ER = \left(\frac{U_e}{U_t}\right) \approx 5\left(\frac{H_{ind}}{E_r}\right) \tag{3.1}$$

$$PI = \left(\frac{U_p}{U_t}\right) \approx 1 - 5\left(\frac{H_{ind}}{E_r}\right) \tag{3.2}$$

The measured depth, H_{ind}, and E_r values obtained through the indentation testing of each sample along with the calculated properties are summarized in Table 3.1. To better observe the trend in measured/calculated data, the obtained values are also plotted in different bar charts depicted in Figure 3.15. According to Figure 3.15b and c, the values of H_{ind}, H_r, ($\frac{H}{E_r}$) and ($\frac{H^3}{{E_r}^2}$) display a similar enhancing trend as a result of increasing the aging temperature from 400 to 450 and 500 °C, which is consistent with the microhardness measurement results. According to the traditional tribological theories, there is a reciprocal relationship between wear resistance and hardness of the materials, meaning a harder material yields a higher wear resistance [173]. However, the mentioned values are just quantitative representative of the mechanical behavior and not exact wear resistance and plastic formability of the material. The improving pattern in the hardness, wear, and plastic deformation resistance up to the aging temperature of 500 °C coincides with the nucleation and growth of the intermetallic precipitates (β-NiAl) from the solid solution, which act as reinforcement agents in the soft martensitic matrix. Ping *et al.* [8] suggested that the strengthening effect in this range of aging temperatures is mainly governed by the cutting mechanism, which is correlated to the stress required for dislocations to cut through or separate fine and coherent precipitates from the matrix. On the other hand, the slightly lower micromechanical properties of the A550 sample can be related to the precipitation of relatively large Cr-rich carbides in the martensitic matrix [8]. However, the adverse effect of $M_{23}C_6$ carbides on the hardening response was found to be negligible, which can be attributed to the formation of a small fraction of $M_{23}C_6$ carbides due to the low carbon content of the alloy.

On the other hand, the A600 sample can be characterized by a significant over-aging behavior according to the substantial drop in the micromechanical indexes ($\frac{H_{ind}}{E_r}$ and $\frac{{H_{ind}}^3}{{E_r}^2}$), which is mainly ascribed to the presence of a relatively high volume fraction of reverted austenite as a soft phase formed at the highest aging temperature. Hochandel *et al.* [7] also studied the aging process of the investment cast PH 13-8Mo alloy and reported a reduction in the hardness values as a result of increasing the aging temperature from 510 to 621 °C due to the formation of reverted austenite. Another complementary factor, which plausibly contributed to the over-aging behavior that occurred at 600 °C, is the slight precipitates coarsening from ~10-15 nm in A500 sample to ~15-25 nm in A600, coinciding with an increase in the inter-particle spacing of precipitates from ~10 nm to ~40 nm in A500 and A600 samples, respectively. It has been reported that the coarsening of the precipitates to more than a critical size combined with the expansion of particle inter-spacing lead to a transition in the precipitate-dislocation interaction mechanism from cutting to Orowan [8]. Consequently, it would be much easier for dislocations to by-pass the precipitates, resulting in a higher tendency of the material to plastic deformation at the expense of reduced hardness [8]. Additional micromechanical characteristics, *i.e.,* plasticity index and elastic recovery, of the as-printed and aged samples are also presented in Figure 3.15d. The greater PI of the A600 sample as compared to other aging conditions is also another quantitative indication of the higher formability of this sample resulted from over-aging. Complementary to this, the lower ER of the A600 sample also reveals its lower resistance to impact loading [172]. Besides all the metallurgical justifications mentioned above, the recovery of martensite phase as a result of dislocation annihilation during the aging process can further contribute to the over-aging effect and consequently significant softening of the material at higher aging temperatures [7][8][12], supported by TEM analysis herein shown in Figure 3.16. Accordingly, a qualitative comparison between the dislocation densities of AP, A400, A500, and A600 samples manifests a considerable reduction in the dislocation density by increasing the aging temperature. As compared with the AP sample, the dislocation density slightly reduced in the A400 sample, while a sharp reduction can be observed in A500 and A600 samples showing the occurrence of a considerable martensite recovery at aging temperatures above 500 °C.

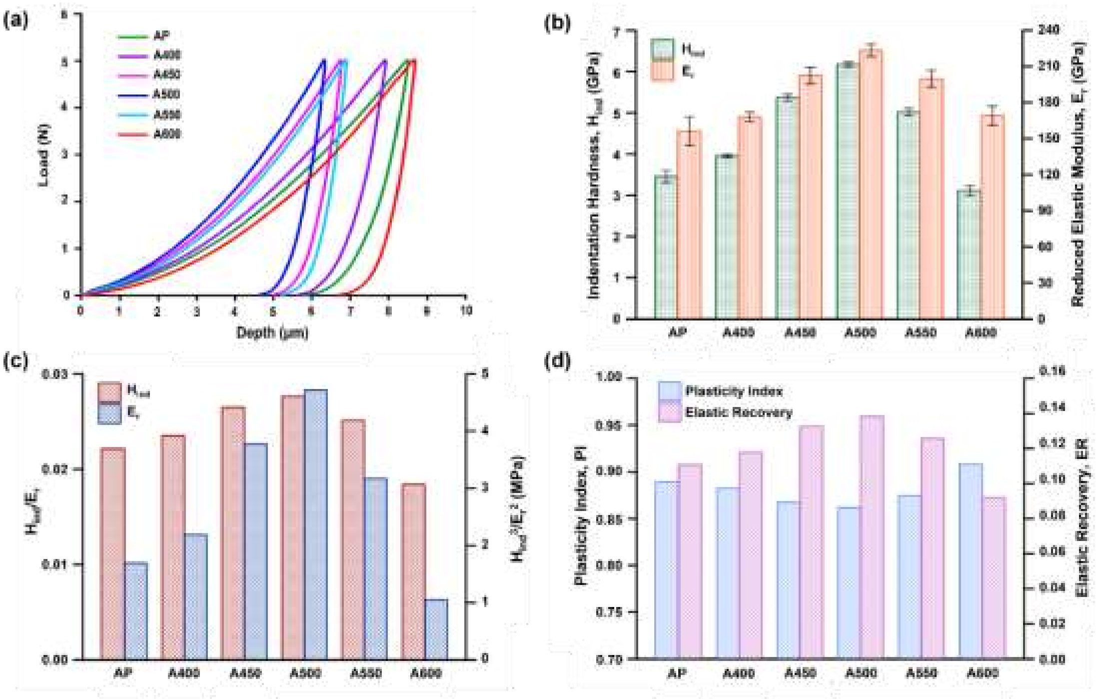

Figure 3.15 (a) Load *vs* depth curves and (b-d) indentation-derived micromechanical properties of the as-printed and aged samples, including indentation hardness (H_{ind}), reduced elastic modulus (E_r), wear resistance ($\frac{H_{ind}}{E_r}$), yield pressure ($\frac{H_{ind}^3}{E_r^2}$), plasticity index (PI), and elastic recovery (ER).

Table 3.1 Summary of the values of maximum depth, indentation hardness (H_{ind}), reduced elastic modulus (E_r), wear resistance ($\frac{H_{ind}}{E_r}$), yield pressure ($\frac{H_{ind}^3}{E_r^2}$), plasticity index (PI), and elastic recovery (ER) for the as-printed and aged samples.

Sample	**Max depth (µm)**	**H_{ind} (GPa)**	**E_r (GPa)**	**H_{ind}/E_r**	**H_{ind}^3/E_r^2 (MPa)**	**PI**	**ER**
AP	8.435 ± 0.315	3.45 ± 0.15	156.08 ± 12	0.022	1.69	0.110	0.889
A400	7.870 ± 0.087	3.95 ± 0.04	168.08 ± 4	0.023	2.19	0.117	0.882
A450	6.722 ± 0.062	5.37 ± 0.08	202.51 ± 7	0.026	3,77	0.132	0.867
A500	6.304 ± 0.055	6.17 ± 0.06	223.34 ± 5	0.028	4.71	0.138	0.861
A550	6.866 ± 0.062	5.02 ± 0.09	199.73 ± 7	0.025	3.17	0.125	0.874
A600	8.615 ± 0.083	3.11 ± 0.12	169.11 ± 8	0.018	1.05	0.091	0.908

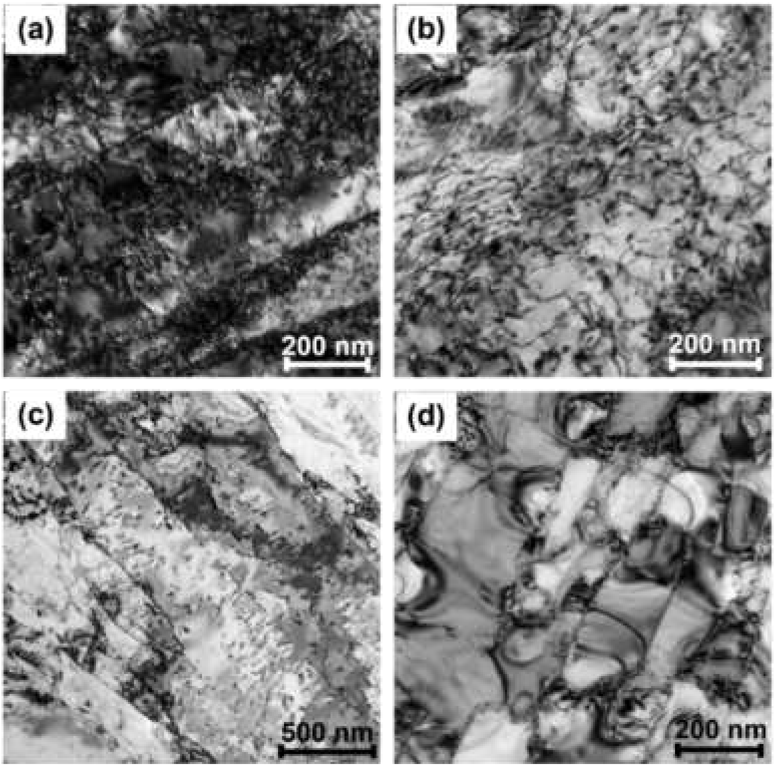

Figure 3.16 Qualitative comparison between the dislocation densities in (a) AP, (b) A400, (c) A500, and (d) A600 samples.

The uniaxial tensile test was also performed on the as-printed and aged samples prepared from both vertical and horizontal directions of the fabricated part as indicated in Figure 3.1a. The corresponding stress-strain curves of the as-printed sample, as well as the representative of the aged specimens at the lowest (400 °C), moderate (500 °C), and highest (600 °C) temperatures are illustrated in Figure 3.17a. The stress-strain curves of the as-printed samples revealed a comparable ultimate tensile strength (UTS) in horizontal (~1114 MPa) and vertical (~1121 MPa) directions, while a relatively significant anisotropy in ductility was observed between the horizontal sample with ~11.4% elongation and the vertical sample with ~6.3% elongation. The observed anisotropic ductility can be ascribed to the formation of coarse columnar primary δ-ferrite grains during the solidification process, resulting in a strong texture along the building (vertical) direction. Consequently, the horizontal sample acts similar to a fine-grained material in contrast to the vertical sample that owns a much lower density of grain boundaries perpendicular to the loading direction, leading to a direction-oriented mechanical performance in the as-fabricated part. In other words, when an additively manufactured sample with a columnar grain structure aligned with the building direction undergoes plastic deformation in the same orientation, dislocations face fewer grain boundaries to cross, which can result in premature failure at lower ductility. Such an anisotropic behavior as a result of a textured structure along the building direction was also observed in an additively manufactured 316 L austenitic stainless steel [174].

Interestingly, the aging-treated samples were characterized by a negligible difference in elongation percentage between the horizontal and vertical directions (see Figure 3.17a), confirming the successful elimination of process-induced anisotropic ductility through post-printing heat treatment. The isotropic performance in the heat-treated samples can be attributed to the removal of primary δ-ferrite grain boundaries during the solution treatment as a result of recrystallization and growth of new primary austenite grains leading to the formation of a fully martensitic microstructure during the subsequent cooling process. Therefore, the thermal treatment-induced disruption of the columnar structure along the building direction of the as-printed part resulted in a uniform and homogeneous microstructure with more isotropic properties.

To better understand the impact of different aging temperatures on the tensile performance of the material, the average values of UTS and elongation percentage corresponding to each condition are plotted in Figure 3.17b. As compared to the horizontal direction of the as-printed sample, aging treatment at 400 °C increased the tensile strength to ~1203 MPa accompanied by a slightly lower ductility (~9.9% elongation), which can be correlated to its fully martensitic microstructure different from the as-printed sample, containing soft δ-ferrite and retained austenite in its martensitic matrix. Moreover, as a result of the precipitation hardening effect of fine β-NiAl particles in the A450 and A500 samples, the UTS was improved to ~1420 MPa and ~1510 MPa, while total elongation further decreased to around 9.3% and 9%, respectively. Although both A450 and A500 samples had similar microstructural characteristics (*i.e.,* β-NiAl precipitates embedded in a martensitic matrix shown in Figure 3.8c and f), they were found to have considerably different UTS values. It has been reported that Al and Ni contents do not reach their stoichiometric concentration in β-NiAl precipitates at the initial stages of the aging process, adversely impacting their effectiveness in providing a strong pinning effect to hinder the dislocation movement and consequently can be easily sheared by dislocations [5][8]. This phenomenon can be considered as a justification for the measured variations in tensile strengths of A450 and A500 samples. On the other hand, after reaching the maximum strength in the A500 sample, the UTS reduced to 1350 MPa by raising the aging temperature to 550 °C, potentially ascribed to exceeding the critical size of β-NiAl precipitates. The formation of an insignificant amount of relatively large Cr-rich carbides can also contribute to the reduction of the strength in the A550 sample [8]. At the highest aging temperature (600 °C), the UTS value steeply dropped to about 910 MPa accompanied by restoration of ductility to around 12.1%, which is mainly attributed to the formation of reverted austenite [8][155], coupled with some other supplementary factors, *i.e.,* (i) presence of large $M_{23}C_6$ carbides [8], (ii) slight coarsening of β-NiAl precipitates [155], and (iii) martensite recovery caused by decreased dislocation density [7][12].

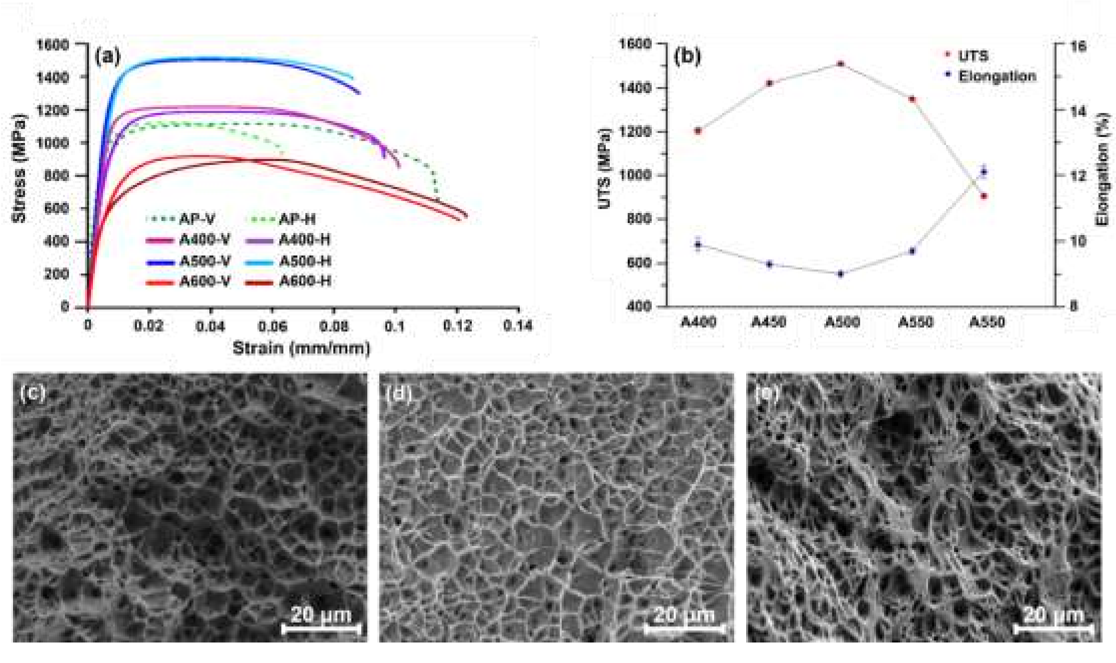

Figure 3.17 (a) Stress-strain curves of the AP, A400, A500, and A600 samples in both vertical and horizontal directions, (b) variation of tensile properties as a function of aging temperature, and (c-e) SEM micrographs taken from the fractured surfaces of A400, A500, and A600 samples, respectively.

Fractography investigations were carried out using SEM analysis on the specimens aged at 400, 500, and 600 °C, which are shown in Figure 3.17c-d. The fractography results of all aged samples revealed a typical ductile fracture characterized by a dominant dimple-like structure with large and deep cup-like depressions, confirming an extensive plastic deformation prior to fracture. This observation implies that the fracture was initiated by the formation of micro-voids at the regions of localized strain discontinuities, which could be lath boundaries or precipitate-matrix interfaces in the aged WAAM PH 13-8Mo material. The fractographs of the samples aged at different temperatures were almost identical with a minor difference between the size and depth of the dimples, which can be attributed to the degree of plastic deformation during the tensile testing. To be more precise, the larger dimples were formed in the A600 sample indicating its higher ductility, while the A500 sample with the highest strength revealed smaller and shallower dimples, consistent with its lower ductility as compared to other aged samples.

To sum up, the results of uniaxial tensile tests indicated that as the aging temperature increases to a certain level (500 °C herein), the strength of the WAAM PH 13-8Mo increases to a peak value (~1510 MPa) at the expense of a reduced ductility, which is consistent with the microhardness and micro-indentation measurements (see Figures 3.14 and 3.15). After reaching the peak of the secondary hardening, further increase in the aging temperature sharply decreases the tensile strength of the material to ~910 MPa, measured for the 600 °C aged sample in this study. It is worth mentioning that the mechanical properties of the 500 °C aged WAAM PH 13-8Mo sample satisfy the requirements of the ASTM A 564/A 564M-02a standard for a conventionally fabricated age-hardened PH 13-8Mo part, *i.e.,* UTS of 1515 MPa and elongation of 10% [175].

Overall, the appropriate aging temperature highly depends on the required properties based on the intended industrial domain and actual in-service conditions. For instance, in mild and non-corrosive environments where brittle fracture or impact loadings in-service conditions are not anticipated, it is advisable to perform the aging process at intermediate temperatures (~500 °C) to produce a high density of β-NiAl precipitates with optimum size, resulting in maximum achievable strength and hardness. On the other hand, if the end-product is exposed to a hydrogen-containing environment and potentially prone to hydrogen-induced cracking, toughness becomes more critical. For such applications, it is recommended to slightly compromise the strength and consider adopting the over-aging treatment to form a considerable volume fraction of reverted austenite to ensure higher ductility and toughness.

3.5 CONCLUSIONS

In this study, the effects of various post-printing heat treatments on the microstructural features and mechanical properties of a WAAM-PH 13-8Mo part were comprehensively studied, and the main conclusions were drawn as follows:

1. The as-printed part was characterized by a columnar structure of primary δ-ferrite grains preferentially aligned with the building direction, transformed to residual δ-ferrite and retained austenite phases embedded in a martensitic matrix.
2. The solution treatment at 1050 °C could successfully eliminate the columnar grain structure and completely dissolve undesired residual δ-ferrite phases, resulting in a fully martensitic microstructure, while either lower or higher solution temperatures were not effective in abating the strong texture formed in the as-printed sample and remove the undesired δ-ferrite patches from the microstructure.
3. Aging treatment at the lowest temperature (400 °C) was not sufficient to provoke the precipitation of secondary phases, while higher aging temperatures (450 and 500 °C) resulted in the nucleation and slight growth of β-NiAl precipitates. On the other hand, further increase in the aging temperature triggered the formation of $M_{23}C_6$ carbides at 550 °C and nucleation of reverted austenite at 600 °C.
4. The formation of coherent β-NiAl precipitates in the samples aged at 450 and 500 °C drastically improved the hardness of the material. However, a considerable hardness drop was recorded in samples aged at 550 and 600 °C due to further martensite recovery and formation of other secondary phases, *i.e.,* Cr-rich carbides and reverted austenite. The micromechanical analysis also confirmed the maximum reduced elastic modulus, wear resistance, and yield pressure in the sample aged at 500 °C,

while the highest value of plasticity index was related to the aging treatment at 600 °C.

5. The uniaxial tensile testing revealed a remarkably anisotropic ductility in the as-printed sample arisen from the strong cubic texture along the building direction, which was eliminated during post-fabrication heat treatment. Consistent with the microhardness measurements, the ultimate tensile strength showed an increasing trend by increasing aging temperature from 400 to 450 and 500 °C, followed by a decreasing pattern in the samples aged at 550 and 600 °C.
6. Overall, it can be concluded that various combinations of hardness, strength, and ductility obtained in the heat-treated WAAM PH 13-8Mo alloy during aging at different temperatures, provide the opportunity for the end-users to selectively implement the optimum aging temperature to achieve the desired mechanical properties based-on the intended service condition of the final product.

Acknowledgments

The authors gratefully acknowledge the support of Natural Sciences and Engineering Research Council of Canada (NSERC) [grant number RGPIN-2017-04368], Canada Research Chair program, Ocean Frontier Institute, and Dalhousie University for sponsoring this work. The authors also acknowledge that the electron microscopy was performed at the Canadian Centre for Electron Microscopy, a Canada Foundation for Innovation Major Science Initiatives funded facility.

CHAPTER 4 GRAIN REFINEMENT AND STRENGTHENING OF PH 13-8MO MARTENSITIC STAINLESS STEEL THROUGH TIC/TIB$_2$ INOCULATION DURING WIRE ARC ADDITIVE MANUFACTURING

Mahya Ghaffari[1], Alireza Vahedi Nemani[2], Sajad Shakerin[3], Mohsen Mohammadi[4], Ali Nasiri[5]

1- Graduate Student, Dalhousie University, Halifax, Nova Scotia, Canada
2- Post-Doctoral Fellow, Dalhousie University, Halifax, Nova Scotia, Canada
3- Post-Doctoral Fellow, University of New Brunswick, Fredericton, New Brunswick, Canada
4- Assistant Professor, University of New Brunswick, Fredericton, New Brunswick, Canada
5- Assistant Professor, Dalhousie University, Halifax, Nova Scotia, Canada

Status: Submitted Journal Paper, Journal of Acta Materialia, (IF= 9.209).

Authors' Contribution

Mahya Ghaffari: Conceptualization, Fabrication Process, Investigation, Writing - original draft.
Alireza Vahedi Nemani: Methodology, Validation, Investigation, Writing - review & editing.
Sajad Shakerin: Resources, Writing - review & editing.
Mohsen Mohammadi: Resources, Writing - review & editing.
Ali Nasiri: Supervision, Writing - review & editing, Funding acquisition.

4.1 ABSTRACT

This research investigates the role of TiC/TiB$_2$ nano-inoculants' addition to the PH 13-8Mo martensitic stainless steel structure during wire arc additive manufacturing (WAAM). The microstructural analysis revealed that the introduction of the ceramic-based inoculants promoted the transition of columnar-to-equiaxed grain structure, refined the primary δ-ferrite grains, increased the retained austenite content, and provoked the precipitation of in-situ TiC/M$_3$B$_2$ phases. Additionally, mechanical properties investigations showed that the TiC/TiB$_2$ inoculation abated the anisotropic ductility as compared to the non-inoculated sample, and also improved the microhardness and tensile strength, mainly because of the synergetic effects of grain refinement, dislocation strengthening, Orowan strengthening, and load transfer effect. Moreover, post-printing

solutionizing and aging treatments were found to further enhance the hardness and strength of both TiC- and TiB_2-reinforced components owing to the precipitation of nano-sized β-NiAl phases, while the accumulation of M_3B_2 phases in the intergranular regions led to the embrittlement of the TiB_2-inoculated sample. This work, for the first time, illustrates the great potential for the adoption of ceramic-based nanoparticles as reinforcing/grain refining agents during the WAAM process for the fabrication of reinforced-PH 13-8Mo stainless steel components with a homogenous microstructure, isotropic behaviour, and superior mechanical performance.

4.2 INTRODUCTION

Wire arc additive manufacturing (WAAM), as one of the well-established additive manufacturing (AM) processes, is a promising alternative to subtractive methods for one-step fabrication of near-net-shape large metallic parts with simple to medium complexity in design [72]. Excellent deposition rate (several kg/h) through high feedstock usage efficiency is the distinct characteristic of WAAM among other AM techniques [107][176]. However, the steep unidirectional temperature gradient as well as the intricate thermal cycles during consecutive melting and solidification of each deposited track through WAAM could potentially cause the formation of a complex solidified microstructure, textured columnar grain structure, solidification defects, and non-uniform mechanical behaviour at different heights/directions in the as-printed components [65][66][67]. One wise strategy to tackle such problems is implementing post-printing heat treatment, which can promote a more equiaxed and homogenous microstructure, if carefully designed, resulting in texture weakening and uniform/improved mechanical properties in printed components [107][106]. For example, Xu *et al.* [43] successfully eliminated the microstructural heterogeneity in a WAAM-processed maraging steel by employing appropriate post-process heat treatment, which minimized structural anisotropy and improved the tensile strength of the material. In a recent work conducted by the authors of the present study [177], various post-printing solution and aging treatment cycles were applied on a WAAM-fabricated precipitation hardening martensitic stainless steel (PH 13-8Mo) with excellent combination of strength, toughness, corrosion, and weldability, which is specifically attractive for plastic injection molding dies [86][152]. It was concluded that adopting the proper post-printing heat treatment not only eliminated the anisotropic mechanical properties but also provoked the precipitation of desired secondary phases in the martensitic matrix, which resulted in the improvement of hardness and strength of the material [177].

As the plastic injection molding process involves high temperature/pressure working conditions, strengthening the PH 13-8Mo alloy can prolong the lifespan of the injection mold dies [86][105][178]. On the contrary, post-printing heat treatment can be associated with increased cost and time in the manufacturing cycle of the component, which is unfavorable to the deployment of the WAAM process as an economically viable alternative to conventional manufacturing processes. Moreover, a poorly designed heat treatment process can potentially cause surface oxidation, distortion, residual stress accumulation, or even reduced strength in the part. Therefore, the implementation of other in-situ processing methods, such as laser shock peening [70], inter-pass cold rolling [71], and ultrasonic needle peening [72], as well as inoculation with alloying/ceramic additions [73], were also explored as effective strategies to stimulate columnar-to-equiaxed transition, grain refinement, and random crystallographic texture. The introduction of inoculants to alter the grain nucleation mechanism during solidification is also a common approach in the conventional casting industry, while its application/feasibility during the AM processes is yet to be further investigated [66]. In recent years, various ceramic inoculants, such as TiC [13][88], TiB_2 [91], TiN [92], SiC [87], and WC [89][90], have been employed during AM of ferrous alloys to tailor the microstructure of the as-printed parts with the purpose of improving the strength, ductility, wear, and corrosion resistance.

Amongst different ceramic reinforcing particulates, TiC and TiB_2 are attractive potential candidates for the inoculation of steels and stainless steels owing to their excellent corrosion and wear resistance as well as other outstanding characteristics, like great hardness, high melting point temperature, and low density, as listed in Table 4.1 [93][94]. Moreover, the adequate chemical and mechanical stability at elevated temperatures, along with their high wettability with Fe matrices [95][96], make TiC and TiB_2 ideal reinforcements for producing metal matrix composites (MMCs). In several studies conducted by AlMangour and their coworkers, TiC and TiB_2 particles were employed during selective laser melting (SLM) of H13 steel [95][99] and 316L stainless steel [17][26][93][97][98] to produce in-/ex-situ MMCs with superior physical and mechanical properties. According to their observations, the attained grain refinement through TiC and TiB_2 nano-inoculation doubled and even tripled the hardness value relative to the non-inoculated SLM-processed 316L part [17][26]. They also studied the impact of initial inoculant particle size, and reported that the strengthening effect of nano-sized TiC particles was more pronounced than microscale reinforcements due to the resultant finer grains, better particle–matrix wettability as well as higher densification level of the composite [26][97].

Table 4.1 Some mechanical and physical properties of TiC and TiB_2 ceramics.

	Hardness (GPa)	**Melting Point (°C)**	**Density (g/cm^3)**	**Elastic Modulus (GPa)**
TiC	~32 [179]	~3140 [13]	~4.93 [93]	~440 [93]
TiB_2	~25 [180]	~3225 [180]	~4.50 [180]	~565 [180]

A comprehensive literature review revealed that the majority of the attempts on ceramic inoculation of Fe-based materials are focused on the SLM-processed parts [13][17][26][93][95][97][98][99][100], while there is only one study available on the reinforced steels using the WAAM process, which was reported by Rodrigues *et al.* [67]. In their work, a customized WAAM machine was developed to directly apply reinforcing SiC particles in between the consecutive layers of a high strength low alloy steel to effectively refine the microstructure, produce more equiaxed grains, and improve the tensile properties of the as-printed material [67].

To the authors' best knowledge, the implementation of inoculant particles during AM of PH 13-8Mo stainless steel (neither through SLM nor WAAM) has never been investigated. Therefore, the present research was established to understand the impact of

TiC and TiB_2 nanopowder inoculants on the microstructural features, crystallographic texture, anisotropic behaviour, and mechanical performance of the WAAM-PH 13-8Mo stainless steel component. Furthermore, the influences of post-printing heat treatment on the microstructure and mechanical properties of the inoculated samples were compared with the as-printed parts.

4.3 EXPERIMENTAL PROCEDURE

4.3.1 Materials, WAAM Process, and Fabrication Procedure

In this study, the selected feedstock material for the WAAM process was a commercial grade PH 13-8Mo MSS solid wire with the nominal chemical composition of 12.25-13.25 Cr, 7.5-8.5 Ni, 2-2.5 Mo, 0.9-1.35 Al, 0.1 Mn, 0.1 Si, 0.05 C, and Fe balance (in wt.%), procured from U.S. Welding Corporation [132]. A robotic WAAM platform comprised of a Lincoln Electric S-350 Power Wave with a gas metal arc (GMA) power source and a 6-axis Fanuc robotic arm was adopted to build simple wall-shaped components on an AISI 420 MSS substrate, schematically shown in Figure 4.1a.

The interlayer inoculation was implemented using two different reinforcing ceramic particles, (*i*) TiC nanopowders (99+% purity) with a nominal average particle size (APS) of 40 nm (see Figure 4.1b and c) and (*ii*) TiB_2 nanopowders (97+% purity) having a nominal APS of 70 nm (see Figure 4.1d and e) (powder supplier: Nanochemazone Inc. Canada). The selected nanopowders were separately mixed with a small quantity of an organic binder comprised of 3 wt.% polyvinyl alcohol (PVA) to prepare a pasty mixture. Prior to the deposition of each track, the mixture was preplaced on the surface of the previous track as a precursor (see Figure 4.1a). It is notable that the PVA solution evaporates easily in contact with the warm previously deposited track, resulting in the adhesion of the inoculants to the previous layer. The as-printed TiC- and TiB_2-inoculated samples were marked as SS+TiC/AP and SS+TiB_2/AP, respectively (see Table 4.2). The optimal process variables used in the authors' previous study on the WAAM processing of non-inoculated PH 13-8Mo alloy [68] were also employed herein for fabricating

TiC/TiB_2-inoculated components in order to maintain the consistency of the experimental conditions.

4.3.2 Post-printing Heat Treatment Process

According to the authors' recent work [177], the optimum post-printing heat treatment cycle to achieve an ideal combination of mechanical properties in a WAAM-fabricated PH 13-8Mo stainless steel includes solutionizing at 1050 °C for 1 h, followed by further aging treatment at 500 °C for 4 h. Both heat treatment cycles were subjected to still-air cooling to room temperature. Therefore, this optimal heat treatment process was selected to apply on the inoculated samples using a Thermo-Scientific Lindberg furnace in an Ar atmosphere. Accordingly, the heat-treated TiC- and TiB_2-inoculated samples were denoted by SS+TiC/HT and SS+TiB_2/HT, respectively (see Table 4.2).

Table 4.2 The nomenclatures used for non-inoculated and inoculated samples studied herein.

Non-inoculated/ as-printed	**Non-inoculated/ heat-treated**	**TiC-inoculated/ as-printed**	**TiC-inoculated/ heat-treated**	**TiB_2-inoculated/ as-printed**	**TiB_2-inoculated/ heat-treated**
SS/AP	SS/HT	SS+TiC/AP	SS+TiC/HT	SS+TiB_2/AP	SS+TiB_2/HT

4.3.3 Microstructural Characterizations

For the microstructural analysis, the metallographic samples were prepared from the middle sections of the fabricated walls, following the standard metallographic procedures, and subsequently etched utilizing Fry's reagent for 5 s. Multi-scale microstructural characterizations were carried out employing a confocal scanning laser microscope (CSLM, VK-X1000) and a field emission scanning electron microscope (FESEM, FEI MLA 650F) in conjunction with an electron backscattered diffraction (EBSD) and energy-dispersive X-ray spectroscopy (EDS) detectors. Detailed characterization of sub-micron and nano-scale features was also performed using a scanning transmission electron microscope (STEM, Talos 200X) equipped with an extreme-field emission gun (X-FEG) source operating at 200 kV.

4.3.4 Mechanical Properties Measurements

Hardness evaluations were conducted on different samples utilizing a Buehler Micromet Vickers microhardness tester under a load of 5 N for a minimum of 10 indentations on each sample. The uniaxial tensile testing was performed using an Instron 5585H-250 kN load frame on the tensile test coupons extracted along the building (vertical) and deposition (horizontal) orientations (see Figure 4.1a). At least five coupons were tested under uniaxial tensile loading from each condition and orientation.

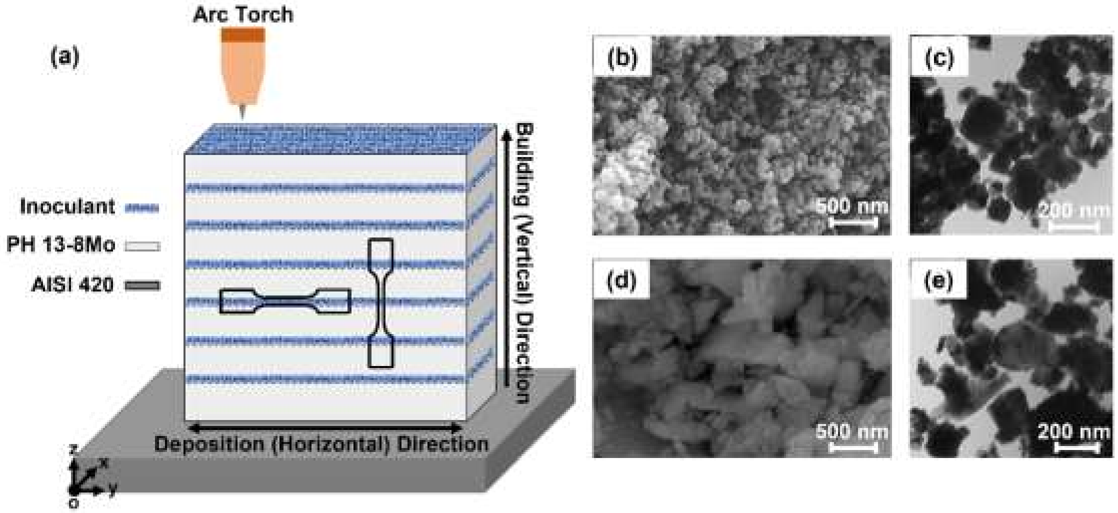

Figure 4.1 (a) The schematic illustration of a WAAM-processed inoculated part. SEM and TEM micrographs taken from (b and c) TiC and (d and e) TiB_2 nanopowders.

4.4 RESULTS AND DISCUSSION

4.4.1 Macrostructural Analysis of the As-printed Samples

Figure 4.2 illustrates the confocal macrographs taken from three orthogonal planes of the non-inoculated and TiC/TiB_2-inoculated samples in the as-printed condition. The formation of coarse columnar grains with a width in the range of 50-200 μm in the non-inoculated sample (SS/AP) is clearly detectable on the YZ and XZ planes (see Figure

4.2a). The equiaxed morphology in the XY plane also indicates the top view of the elongated columnar grains observed in SS/AP sample. From the authors' previous works [68][177], the formed columnar structure is ascribed to primary δ-ferrite grains nucleated from the substrate at the earliest stage of the solidification process of the very first deposited layer. Subsequently, the initially formed primary δ-ferrite grains have grown epitaxially across several layers since there were no available inoculants for the nucleation of new grains ahead of the progressing solidification front during the deposition of the consecutive layers. It is known that the columnar structure characteristic in additively manufactured parts may appear because of the extreme unidirectional thermal gradient along the primary heat flow orientation parallel to the building direction [13][68][177]. It is worthwhile to mention that the presence of columnar structure could potentially impose inherent anisotropic mechanical properties; therefore, it is essential to eliminate such textured structures to minimize the resultant detrimental side effects.

According to Figure 4.2b, although the addition of TiC inoculants, acting as nucleation sites, diminished the tendency to the formation of columnar grains, it was not effective in entire elimination of the unidirectional columnar structure. Hence, narrower columnar grains were occasionally observed in the SS+TiC/AP sample as compared to the SS/AP sample, which was characterized by tremendously coarse columnar grains. Similar results were reported during AM of TiC-inoculated 316L stainless steel parts, in which the partial disruption of columnar grains was associated with the synergetic effect of variations in chemical concentration and temperature gradient in the molten metal after the introduction of TiC nanoparticles, resulting in a surface tension gradient and Marangoni convection in the melt pool [97]. This mechanism is contrary to the characteristic directional crystal growth mechanism, which typically occurs during AM processes using non-inoculated feedstock materials.

With the same mechanism, the presence of TiB_2 nanopowders in the SS+TiB_2/AP sample led to the entire disruption of epitaxial growth, resulting in the formation of a fully equiaxed grain structure with no discernible columnar grains, as shown in Figure

4.2c. AlMangour *et al.* [98] also claimed that the addition of TiB_2 inoculant to the SLM-316L sample inhibited the extension of grains into subsequently deposited layers, resulting in a non-columnar structure. Therefore, according to the initial macrostructural characterizations using confocal scanning microscopy, it can be speculated that the addition of TiB_2 nanopowders was more efficient than TiC when it comes to the elimination of columnar structure during the WAAM of PH 13-8Mo alloy. This observation will be further elaborated using EBSD, SEM, and TEM techniques in the following sections.

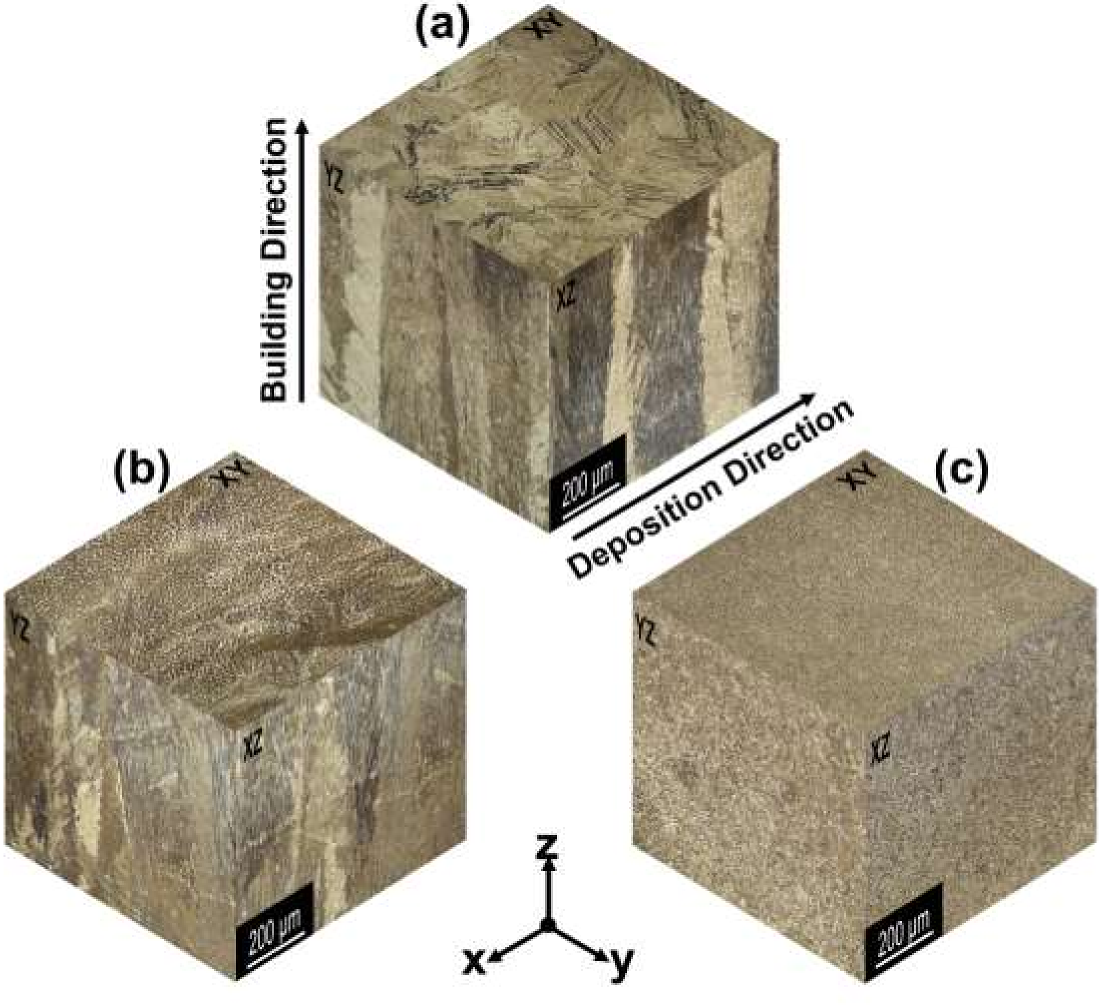

Figure 4.2 Confocal macrographs taken from three orthogonal planes of the (a) SS/AP, (b) SS+TiC/AP, and (c) $SS+TiB_2/AP$ samples.

4.4.2 Microstructural Characterizations and Texture Analysis of the As-printed Samples

Figure 4.3 depicts the EBSD inverse pole figure (IPF) maps along with their associated pole figures (PFs) from the side view (XZ plane) of the non-inoculated and inoculated samples. According to the IPF map from the non-inoculated sample (Figure 4.3a), the epitaxial columnar grains grew preferentially along the building direction (z), which agrees with the laser confocal microscopy analysis. The corresponding PF map of the SS/AP sample reveals a strong cubic texture component with the maximum intensity of 11.33 along the <100> crystal direction, which is the energetically favorable growth orientation for the cubic crystal structures [181] (see Figure 4.3b).

Contrarily, the TiC-inoculated sample (Figure 4.3c) contained a mixture of columnar and equiaxed primary δ-ferrite grains with a lower maximum texture intensity of 5.36 (Figure 4.3d), indicating a less anisotropic structure as compared to the SS/AP sample. AlMangour *et al.* [181] also observed a bimodal grain structure, including columnar and equiaxed grains in the SLM-fabricated 316L stainless steel reinforced with TiC particles. According to Figure 4.3e, the introduction of TiB_2 nanopowder had a more profound impact on the cessation of the epitaxial growth, producing many randomly oriented fine equiaxed grains with no strong preferential crystallographic orientation. Figure 4.3f also demonstrates a clear reduction in the maximum texture intensity to 1.60, affirming that the implementation of TiB_2 nanopowder efficiently inhibited the preferential texture tendency in WAAM-fabricated PH 13-8Mo alloy. Overall, it can be claimed that the equiaxed grains in the inoculated samples are small freshly nucleated grains, formed in the existence of TiC and TiB_2 nanopowders, that were able to grow in different directions.

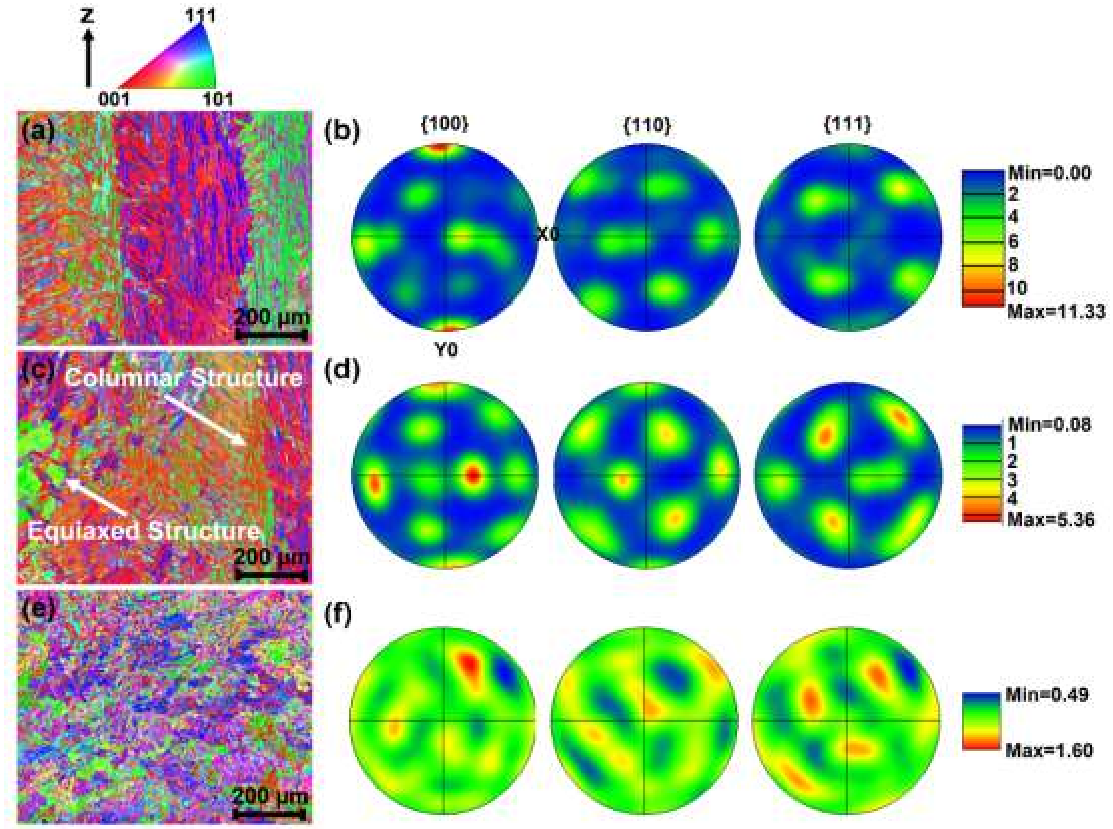

Figure 4.3 EBSD-IPF-z maps along with their associated PFs taken from the XZ plane of the (a,b) SS/AP, (c,d) SS+TiC/AP, and (e,f) SS+TiB_2/AP samples.

Figure 4.4a displays the SEM micrograph along with the associated EDS maps taken from the non-inoculated sample, showing the presence of Cr-rich residual δ-ferrite in two distinct morphologies *i.e.,* lathy and vermicular. The retention of δ-ferrite at room temperature was expected to occur due to the contributory effect of the high solidification rate involved in the WAAM process in addition to the high Cr content (~13 wt.%) as a ferrite stabilizer element [68]. Moreover, the TEM image, along with the associated selected area electron diffraction (SAED) pattern illustrated in Figure 4.4b, show the formation of a lath martensitic matrix containing film-like retained austenite (γ), mainly due to the existence of ~8 wt.% Ni as an austenite stabilizer element, which hinders the complete transformation of austenite to martensite during the cooling cycle.

In addition to residual δ-ferrite and retained austinite, the EDS elemental map of Al shown in Figure 4.4a confirms the formation of Al-rich oxides in the matrix. The oxygen (O) could possibly be originated from the shielding gas, ambient air, and/or residual moisture in the powder/PVA mixture. More details about the microstructural characteristics of the deposited layers and heat affected zones at different locations of the WAAM-fabricated PH 13-8Mo part were comprehensively discussed in the authors' recently published works [68][177].

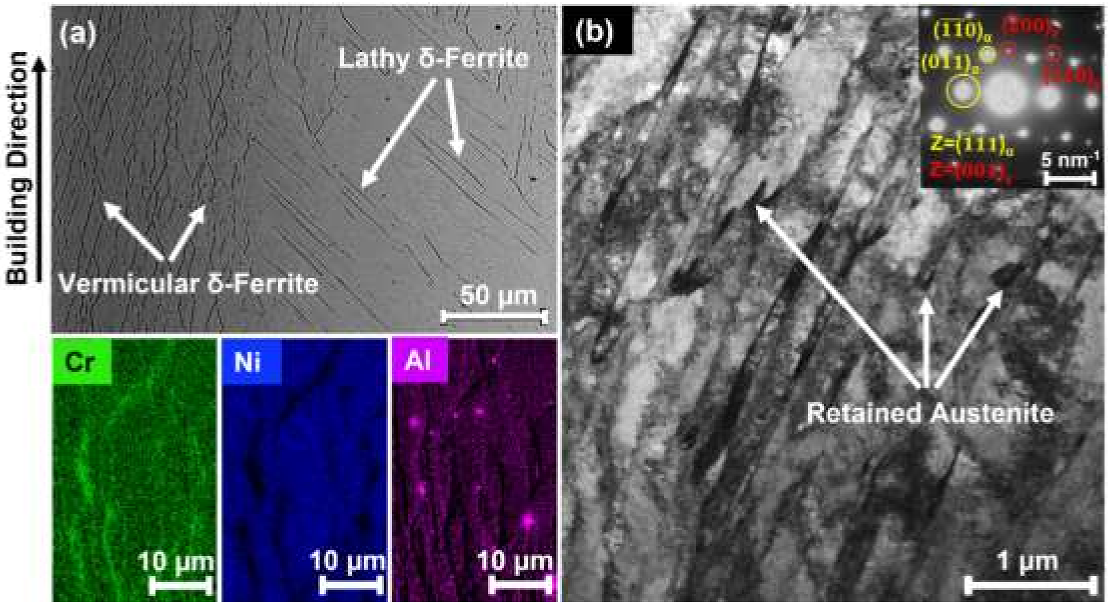

Figure 4.4 (a) SEM micrograph along with the associated EDS elemental mapping and (b) TEM bright-field image along with the corresponding SAED pattern taken from the non-inoculated sample (SS/AP).

Figures 4.5a and 4.6a illustrate low magnification SEM micrographs along with the associated EDS maps taken from the TiC- and TiB_2-reinforced samples, respectively. As confirmed by the concentration distribution of Cr and Ni, residual δ-ferrite was also detected in both inoculated samples; however, the morphology of δ-ferrite appeared to be different from that of the non-inoculated sample. During the solidification of the SS/AP sample, each columnar primary δ-ferrite grain owns a distinct crystallographic orientation with the subsequently transformed austenite, leading to a particular morphology of residual δ-ferrite (lathy or vermicular) along the whole of each specific columnar primary δ-ferrite grain [68][140]. On the other hand, the formation of equiaxed primary δ-ferrite grains in the reinforced samples caused a random orientation relationship between δ-ferrite and the subsequently transformed austenite, resulting in the formation of evenly distributed δ-ferrite islands, which are mostly retained in the intergranular regions of the primary austenite grains (see Fig 5a and 6a).

In addition to residual δ-ferrite, the presence of small Ti-rich particles in the EDS elemental map of Ti displayed in Figure 4.5a showed the existence of TiC particles, almost homogeneously distributed throughout the martensitic matrix of the SS+TiC/AP sample. Notably, due to the difficulties in detecting carbon by the EDS system in low magnification scans, it can be reasonably assumed that the evenly distributed Ti-enriched particles represent TiC phases. The TiC particles appeared in various sizes, ranging from tens to hundreds of nanometers; even a few are up to 900 nm, which are extremely courser than the original TiC nanopowder additives (~40 nm), indicating the formation of new in-situ TiC phases during the WAAM process.

A higher magnification SEM image of the larger TiC phases is presented in Figure 4.5b, which shows the cubic-shaped morphology of these newly formed in-situ particles encompassing another black phase at their interior. For further elucidation, a TEM close-up of one of these particles along with its corresponding EDS maps are displayed in Figure 4.5c. The high concentration of Ti and C reaffirms the TiC-nature of this phase, while the central region was enriched in Al and O. Thus, it can be suggested that the larger TiC particles can plausibly nucleate and grow on the existing Al_2O_3 inclusions in the structure. The heterogeneous nucleation of TiC on Al_2O_3 particles was also observed by Sharifitabar *et al.* [94] during gas tungsten arc cladding of 1045 steel utilizing a blend of TiO_2, Al, C, and Fe powders. Bahramizadeh *et al.* [182] also claimed that the lower free energy of Al_2O_3 particles is in favor of their formation during the early stages of solidification, which could subsequently serve as preferred primers for the non-homogeneous nucleation of cubic-shaped TiC particles.

According to the numerical modeling developed by Huang *et al.* [183], the maximum temperature of the molten metal during the WAAM process can increase up to around 2100 °C, which is well below the melting point of TiC (~3140 °C [13]) and fairly above the melting point of PH 13-8Mo stainless steel (~1450 °C [184]). Therefore, it is reasonable to assume that the initial melting of PH 13-8Mo feedstock wire produces a high-temperature fluid, encapsulating the nano-sized TiC powders. In addition, the lower density of TiC (~4.93 g/cm^3 [93]) as compared to PH 13-8Mo alloy (7.7 g/cm^3 [184]) results in upward floating of TiC particles in the liquid under the Marangoni convection effect, which leads to partial dissolution of original TiC nanopowders in the matrix. This partial dissolution enriches the melt pool from Ti and C alloying elements, facilitating the subsequent in-situ formation of TiC particles. Thereafter, during the solidification process, new TiC particles with a cubic morphology were formed from the molten metal either homogenously or by heterogeneous nucleation on the pre-existing Al_2O_3 particles.

The in-situ formation of TiC nanoparticles as a result of the partial dissolution of the original powders during the SLM process was also reported in the literature [185]. Wu *et al.* [96] studied the possible thermodynamic reactions between Fe-Ti and Fe-C based on the Fe-Ti-C ternary phase diagram during the laser melting deposition of TiC-inoculated 316L stainless steel. According to their calculations, the formation of TiC had the lowest Gibbs free energy (G) among other potential phases (Fe_3C, Fe_2Ti, and FeTi), which confirms the strong reaction tendency of Ti and C, producing in-situ TiC particles as the most thermodynamically favored phase as compared to other potential phases [96][186]. It is important to note that the theory of the partial melting of original TiC nanopowders is particularly valid in the melt pool centers, where the liquid is exposed to the maximum arc temperature, while the original TiC powders mostly remain intact in the melt pool boundaries being exposed to lower arc energy density [67]. Figure 4.7a and b, taken from a melt pool boundary region of SS+TiC/AP sample, shows the presence of original TiC nanopowders in the size range of around 20 to 50 nm, which remained intact in the matrix.

Overall, it can be perceived that two different types of TiC phases exist in the microstructure of the SS+TiC/AP sample, including (*i*) the intact TiC nanopowders, which appeared in the original size of the preplaced nanopowders, and (*ii*) the in-situ TiC particles, which either formed homogeneously within the matrix or heterogeneously on the pre-existing Al_2O_3 inclusions.

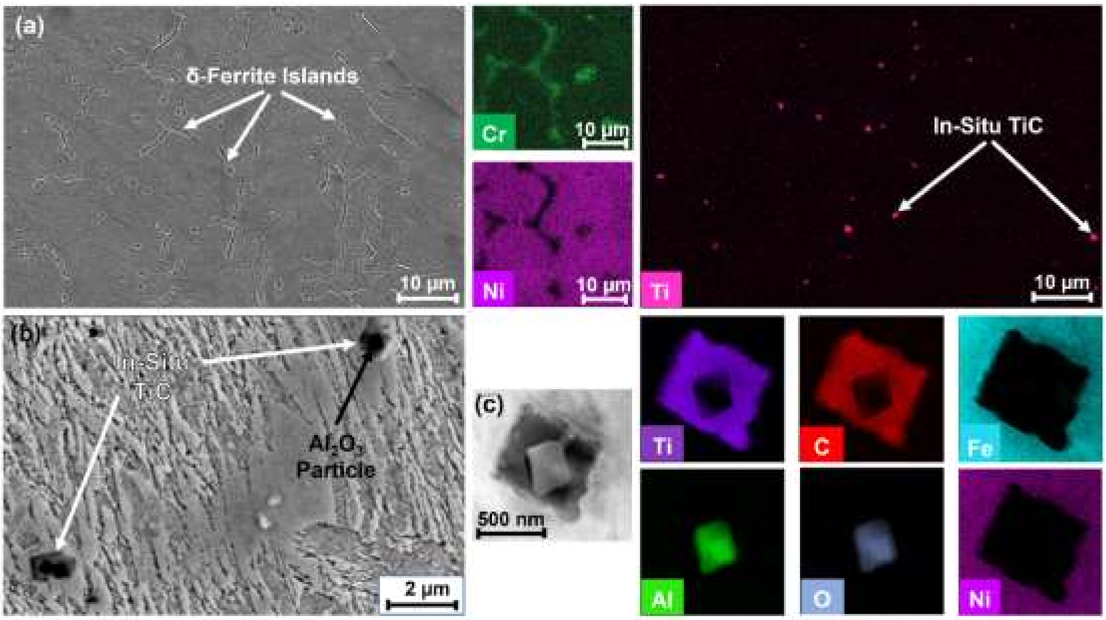

Figure 4.5 (a) Low-magnification SEM micrograph along with the associated EDS elemental maps of Cr, Ni, and Ti taken from the TiC-inoculated sample, (b) high-magnification SEM image, displaying large in-situ TiC particles, (c) TEM image along with the corresponding EDS elemental mapping taken from an in-situ TiC particle nucleated on an Al_2O_3 inclusion.

In the case of the TiB_2-inoculated sample, intergranular residual δ-ferrite and Ti-rich particles were also detected in the EDS elemental mapping associated with the low-magnification SEM image of the SS+TiB_2/AP sample, shown in Figure 4.6a. Higher magnification SEM image, inset in Figure 4.6a, revealed that two other phases, including cubic-shaped particles and skeleton-like phases, were formed in the SS+TiB_2/AP sample. According to the EDS elemental scans taken from the cubic particles (Figure 4.6b), the Ti-enriched phases could be characterized as in-situ TiC particles nucleated on the Al_2O_3 inclusions, which also formed during the deposition of the TiB_2-reinforced sample.

Similar to the case of the TiC-inoculated sample (SS+TiC/AP), the original TiB_2 nanopowders also partially dissolved during the melting process and enriched the melt pool in B and Ti alloying elements. Due to the slower diffusion of boron than carbon, Ti rapidly reacted with C, which resulted in the in-situ formation of TiC phases rather than TiB_2 [182][187]. Thereafter, during the final stages of the solidification process, the dissolved B, with an extremely low solubility in iron (<0.00012 wt.% [188]), segregated into the remaining liquid and formed hard skeleton-like M_3B_2-type borides, in which M mainly represents Cr, Fe and Mo atoms [182][189][190][191]. The EDS elemental maps taken from the skeleton-like phase in Figure 4.6c, along with the EDS point measurements shown in Table 4.3, confirm the formation of Mo-rich boride phases in the microstructure of the SS+TiB_2/AP sample. The formation of Mo-rich M_3B_2-type borides with a skeleton-like morphology has been previously observed in the coatings fabricated by the Plasma Transferred Arc (PTA) process using super-duplex and supermartensitic stainless steel powders with the addition of 1 and 3 wt.% boron [189]. According to Figure 4.7c and d, the intact TiB_2 nanopowders were also observed mainly in the melt pool boundaries, which experienced the minimum arc temperature.

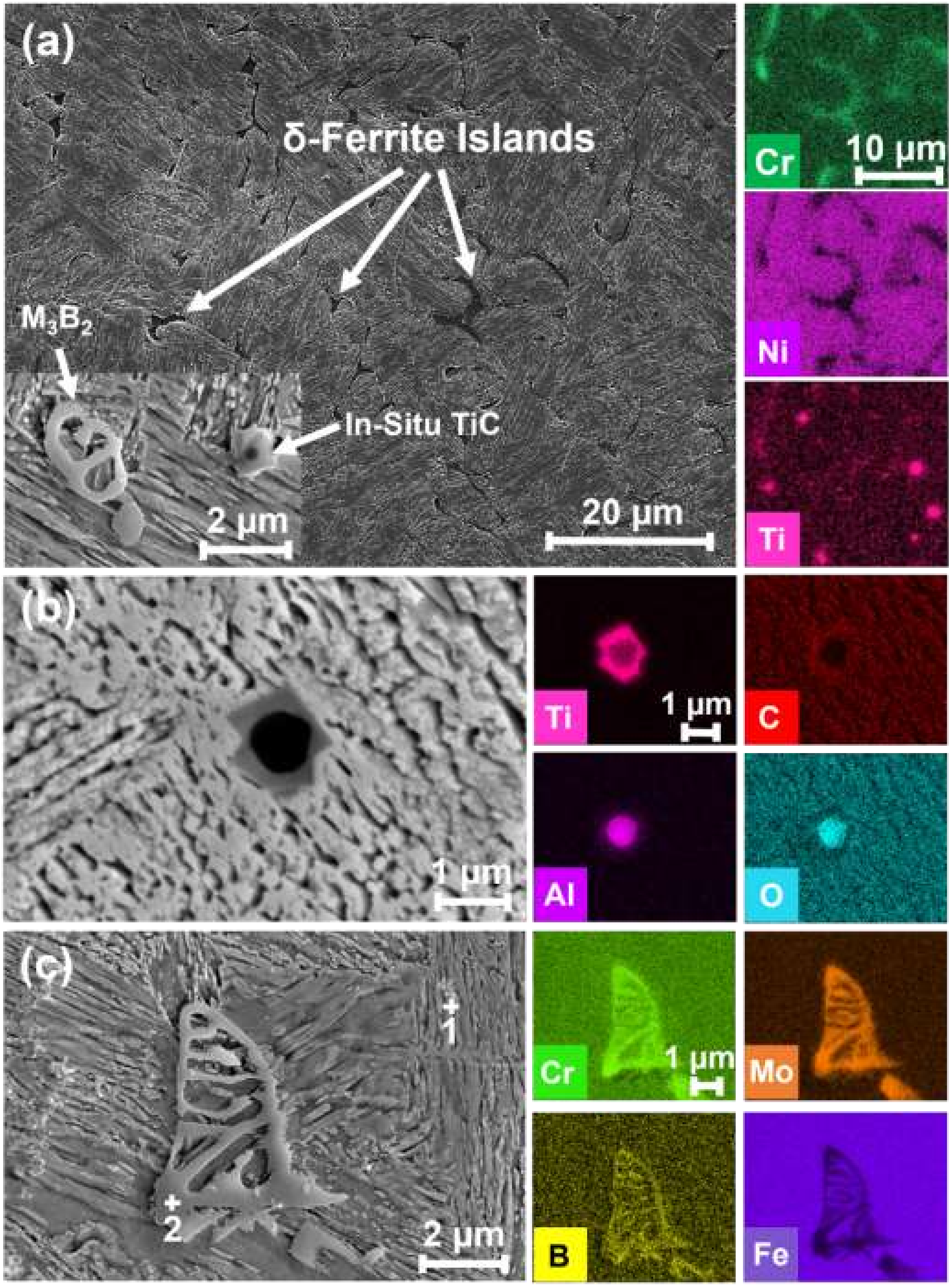

Figure 4.6 (a) SEM micrograph along with the associated EDS elemental maps of Ni, Cr, and Ti taken from the TiB_2-inoculated sample. High-magnification SEM images and EDS elemental mapping taken from (b) in-situ TiC particle and (c) M_3B_2-type boride.

Table 4.3 EDS-measured chemical composition (in wt.%) of the points shown in Figure 4.6c.

Point	Fe	Cr	Ni	Mo	B
1 (Matrix)	74.32	12.74	7.69	1.94	0.47
2 (M_3B_2)	31.88	21.30	1.51	19.59	22.37

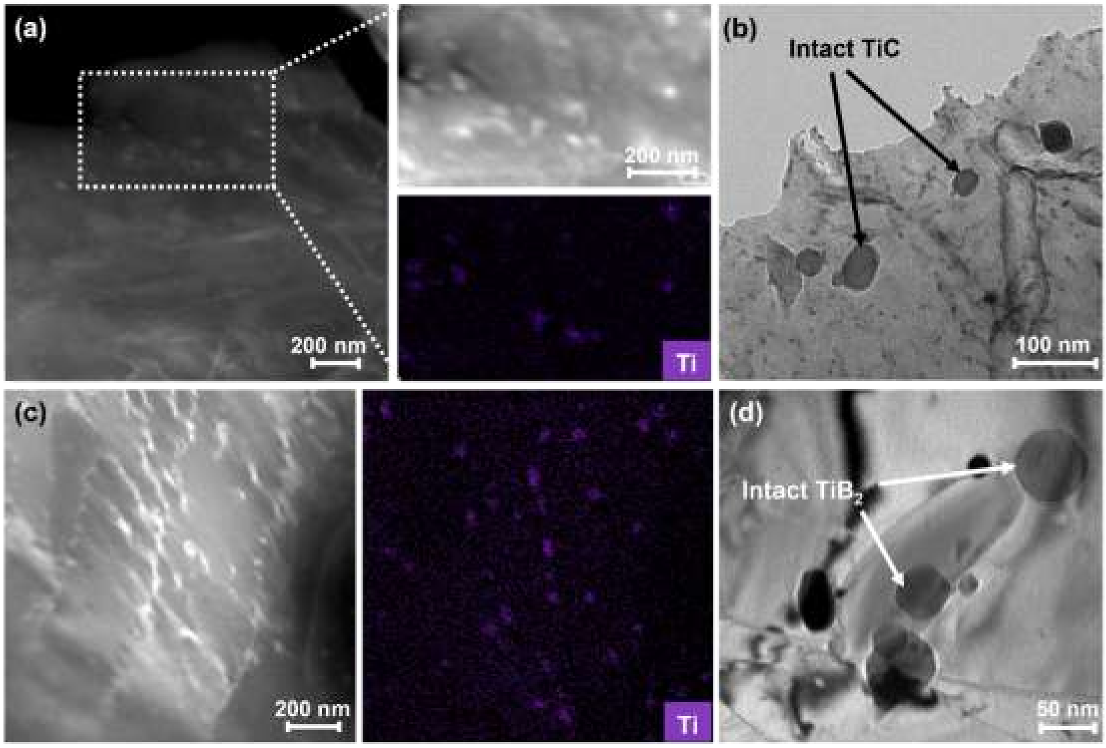

Figure 4.7 Multi-scale TEM micrographs along with the associated EDS elemental map of Ti taken from the melt pool boundaries of (a and b) SS+TiC/AP and (c and d) SS+TiB_2/AP samples, showing the presence of intact original nano-sized particles.

In addition to the mentioned phases above, the EBSD phase maps depicted in Figure 4.8 revealed the formation of retained austenite (iron-fcc) in the martensitic matrix (iron-bcc). It can be seen that the volume fraction of retained austenite raised from 2.59% for the non-inoculated sample to 9.33% and 5.29% in the TiC- and TiB_2-inoculated samples, respectively, which can be associated with the addition of Ti, C, and B to the chemical composition of the fabricated materials. In the case of the TiC-inoculated sample, carbon atoms act as a strong austenite stabilizer, which can dramatically reduce the martensite start (M_s) temperature with a coefficient of -330 to -474 in the M_s equation, while Ti as a ferrite stabilizer owns a coefficient of 0 to +3, which is negligible as compared to the influence of carbon content on the M_s temperature [192]. Lower M_s can depress the martensitic transformation and induce a higher volume fraction of retained austenite. This increase is insignificant since the nanopowders did not completely dissolve in the molten metal. A higher content of retained austenite was also detected in an AM-processed 15-5PH/TiC composite as compared to the TiC-free specimen [13].

In the case of the TiB_2-inoculated sample, it has been reported that the addition of boron to steels leads to the segregation of B at the primary austenite intergranular regions, which decreases the primary austenite grain size, and consequently improves the stability of austenite during the martensitic transformation [193].

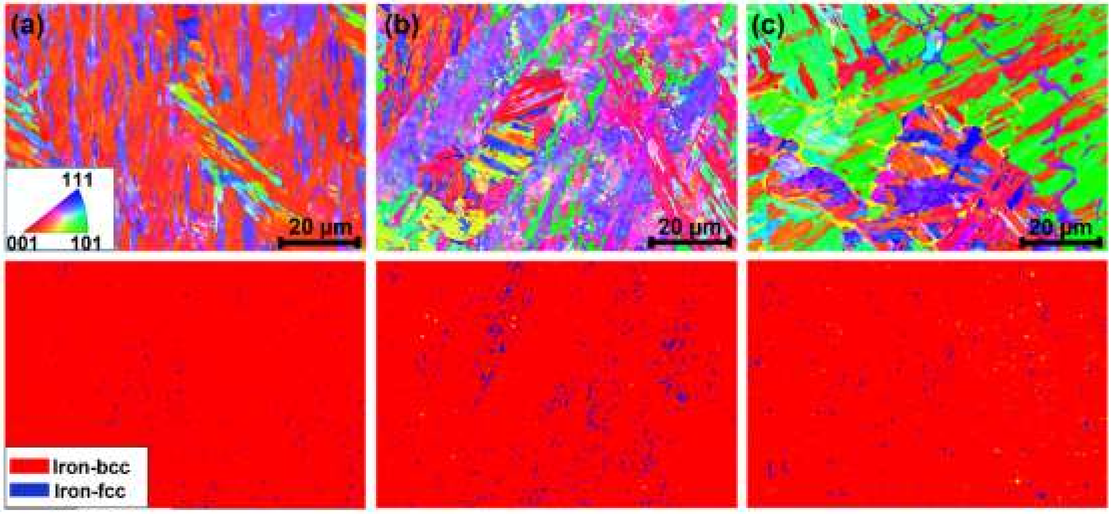

Figure 4.8 High magnification EBSD-IPF-z images along with the associated phase maps taken from (a) SS/AP, (b) SS+TiC/AP, and (c) SS+TiB_2/AP samples.

4.4.3 Grain Refinement Assessment in the TiC/TiB_2-inoculated Samples

Assuming that the size of the primary δ-ferrite grains affects the size of the subsequently formed primary austenite grains, and ultimately the size of formed martensite laths, a statistical examination of the lath size distribution of the inoculated and non-inoculated as-printed samples could provide a quantitative assessment of the effectiveness of TiC/TiB_2 inoculations on the grain refinement. Figure 4.9 shows the martensite lath size distribution along with the average lath size (μ) of different samples, which were derived from the EBSD raw data, shown in Figure 4.3. It can be clearly observed that the TiC inoculation fairly refined the average martensite lath size from ~2.62 μm for the SS/AP sample to ~1.56 μm for the SS+TiC/AP sample. A remarkable reduction in the martensite lath size was also reported in a TiC-inoculated 410 MSS coating produced through a laser surface cladding process [194]. Zhai *et al.* [195] also observed significant grain refinement by 16% and 68% during SLM of 316L stainless steel with the addition of 1 wt.% and 3 wt.% TiC, respectively.

Ultimately, the most efficient grain refinement was obtained as a result of TiB_2 inoculation, which reduced the average martensite lath size to ~0.67 μm in the SS+TiB_2/AP sample. According to the literature, the attained grain refinement by the introduction of inoculant particles can be ascribed to (*i*) a larger number of pre-existing nucleation sites [17][67][185][195], (*ii*) increased cooling rate [97][194], and/or (*iii*) development of constitutional undercooling, which leads to grain growth retardation [67][195][196][197][198][199]. All these factors are thoroughly discussed in the following sections.

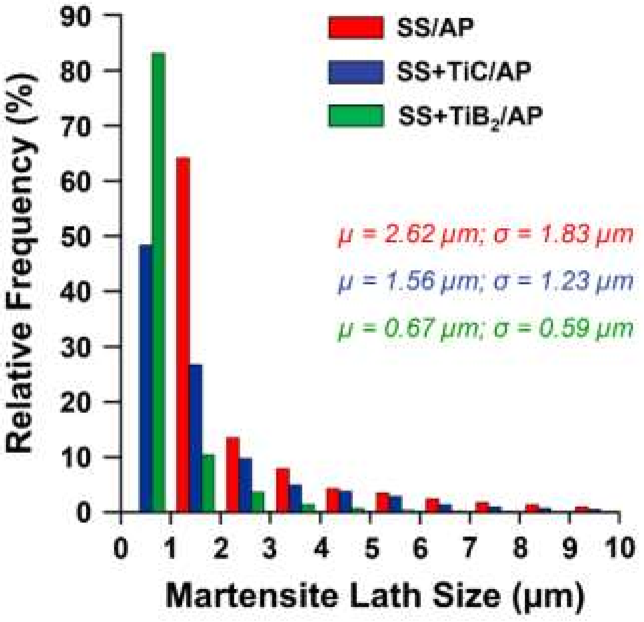

Figure 4.9 Quantitative measurement of the lath size distribution of the non-inoculated and inoculated samples (μ: average lath size, σ: standard deviation)

4.4.3.1 Effect of Nucleation Site

During the fabrication of the non-inoculated sample, the primary δ-ferrite grains of each layer epitaxially grow on the grains of the previous layer due to the lack of enough nucleation sites, resulting in a coarse columnar structure. However, the existence of TiC/TiB_2 nanoparticles in the molten metal of the inoculated samples catalyzes the heterogeneous nucleation of primary δ-ferrite grains by increasing the number of active nuclei agents, leading to a refined martensitic lath structure. The nano-inoculants could serve as potent nucleation sites owing to their small contact angle and great wettability with molten metal, which reduces the critical nucleus size and the activation energy required for the heterogeneous nucleation of δ-ferrite grains [17][67][185][195].

The superior grain refinement effectiveness of TiB_2 over TiC inoculants could be attributed to the present phases in the material. The microstructure of the TiC- and TiB_2-reinforced samples implies the co-existence of two nucleation agents (TiB_2 and TiC) in the SS+TiB_2/AP sample, while the TiC-inoculated sample only contains the TiC phase as the nucleation site. Consequently, a more refined martensite lath structure with almost no preferential texture along the building direction could be obtained in the TiB_2-reinforced sample.

4.4.3.2 Effect of Cooling Rate

Another contributing factor to grain refinement via the introduction of inoculants is the faster cooling during the solidification process of TiC/TiB_2 reinforced samples in comparison with the non-inoculated sample. The existence of TiC/TiB_2 nanopowders accelerates the heat dissipation from the molten metal due to the partial melting of original TiC/TiB_2 particles, which significantly lowers the thermal energy of the molten metal [88][97][194]. Therefore, the higher cooling rate achieved in the TiC/TiB_2-inoculated samples could constrain the crystal growth during the cooling cycle.

4.4.3.3 Effect of Constitutional Undercooling

The introduction of external components to a melt pool could potentially lead to grain refinement through a combination of nucleant agents and solute atoms [196]. The nucleant agents, such as TiC and TiB_2, contribute to grain refinement by providing more nucleation sites and increasing the cooling rate, as explained in the previous sections. On the other hand, the addition of solute atoms could effectively trigger grain refinement through constitutional undercooling, which is essential to activate adjacent nuclei [196][197][198]. Herein, the encapsulation of TiC and TiB_2 nanopowders by a large volume of the high-temperature molten metal results in their partial melting and dissolution of Ti, C, and B as solute atoms into the melt pool. Therefore, all three mentioned mechanisms synergistically contribute to grain refinement as a result of the addition of TiC and TiB_2 inoculants during WAAM processing of PH 13-8Mo alloy.

The solute atoms' contribution to the advancement of constitutional undercooling can be quantified by a term known as growth restriction factor (Q) [196][197][198]. A higher Q value indicates that the constitutionally undercooled zone develops faster, which accelerates the further nucleation ahead of the progressing solid-liquid plane, leading to more efficient grain refinement [196]. The growth restriction factor can be calculated using the following equation [195][196][197][198]:

$$Q = m_l C_0 (k - 1) \tag{4.1}$$

where m_l is the slope of the liquidus line in the phase diagram, C_0 is the solute concentration (wt.%), and k is the equilibrium solute partition coefficient [195][196][197][199]. Accordingly, the growth restriction factor is a common parameter to approximately predict a particular solute's effectiveness in grain refinement. Therefore, a solute with a greater Q value can be considered as a more effective grain refiner [195][200]. Since all other alloying elements are identical in both TiC- and TiB_2-inoculated alloys, only the effect of C and B on the Q value is considered herein. Table 4.4 shows the calculated growth restriction factor (Q value) for C and B solutes as $1434.39C_0$ and $1859.91C_0$, respectively. As it was not practically feasible to accurately measure the content of dissolved C and B solute elements in the matrix (in solid solution form), it has been assumed that the C_0 value is almost equal for both cases. This assumption is fairly reasonable as the heat input, molten metal characteristics, and melting point of TiC and TiB_2 particles are approximately the same (see Table 4.1). Therefore, the higher Q value associated with B implies its more effective grain refinement ability for the Fe system as compared to C. Accordingly, the detected finer martensite lath size distribution in the TiB_2-inoculated sample could be ascribed to the boron's greater growth restriction factor.

From a qualitative perspective, the superior grain refinement ability of boron as compared to carbon can also be elaborated based on their different solubility limits in iron as the matrix. Boron with extremely limited solubility in iron (~0.00012 wt.% [188]) is easily rejected to the liquid ahead of the solidification front, leading to considerable constitutional undercooling. Consequently, the boron enrichment at the solid-liquid interface will decrease the freezing range, further restricting the growth rate of columnar grain structure [67]. On the other hand, carbon with a relatively higher solubility limit in iron (~0.006 wt.% [188]) is less effective in promoting the constitutional undercooled region ahead of the solidification front. This mechanism justifies the influence of TiC and TiB_2 inoculation on the grain structure, in which the addition of TiB_2 entirely eliminated the columnar grain structure, while TiC could partially disrupt the columnar structure, leading to a combination of equiaxed and columnar grains (see Figures 4.2 and 4.3). Notably, the observed grain refinement can significantly contribute to the strengthening of the material, which will be discussed in section 3.5.

Table 4.4 The values of m_l (liquidus slope), k (equilibrium solute partition coefficient), C_0 (solute concentration), and Q (growth restriction factor) [from equation (1)] for the C and B solute elements.

Element	**m_l (K/mole^{-1})**	**k**	**$M_l(k-1)$**	**Q(K)**
C	-1802 [201]	0.204 [201]	1434.39	$1434.39C_0$
B	-1964 [201]	0.053 [201]	1859.91	$1859.91C_0$

4.4.4 Microstructural Analysis of the Heat-treated Samples

In the authors' previous work [177], the effect of post-printing heat treatment on the microstructural characteristics and mechanical performance of the non-inoculated WAAM-fabricated PH 13-8Mo sample was thoroughly investigated at various temperatures. It was concluded that the columnar grain structure of the as-printed material can be eliminated during the solutionizing at 1050 °C for 1 h, while the maximum tensile strength was achieved during aging treatment at 500 °C due to the formation of optimum-sized reinforcing β-NiAl precipitates and also the absence of detrimental carbides and soft reverted austenite from the structure. In view of this, the same heat treatment cycles were applied to the TiC/TiB_2-inoculated samples for possibly further grain refinement and mechanical properties improvement.

Figure 4.10a displays a low magnification SEM image associated with the heat-treated TiC-inoculated sample (SS+TiC/HT), showing the entire dissolution of the undesired residual δ-ferrite yielding a fully martensitic matrix. The formation of cubic TiC particles in the matrix was also observed in the higher magnification SEM image (see Figure 4.10b), revealing the stability of these particles during high-temperature heat treatment (*i.e.,* solutionizing at 1050 °C). It is notable that the presence of tiny pores that appeared as dark spots in the SEM images can arise from local pitting due to the longer etching time required to reveal the TiC particles.

A closer look at the microstructure under TEM (Figure 4.10c) revealed the co-existence of TiC particles and nano-sized spherical β-NiAl precipitates in the SS+TiC/HT sample. Although it was difficult to reveal an ideal contrast between the present phases by the TEM micrograph, the formation of β-NiAl precipitates was approved by the EDS elemental maps, disclosing nano-scale spherical phases, which are depleted in Fe and enriched in Al and Ni. Also, the EDS elemental map of Ti demonstrates the co-existence of TiC particles with relatively uniform distribution within the matrix. It is well-established that the comparatively identical lattice parameter of ferrite (bcc) and β-NiAl intermetallic compounds leads to a perfect coherency between the precipitates and the martensitic matrix, promoting the precipitation hardening of the material [177][202].

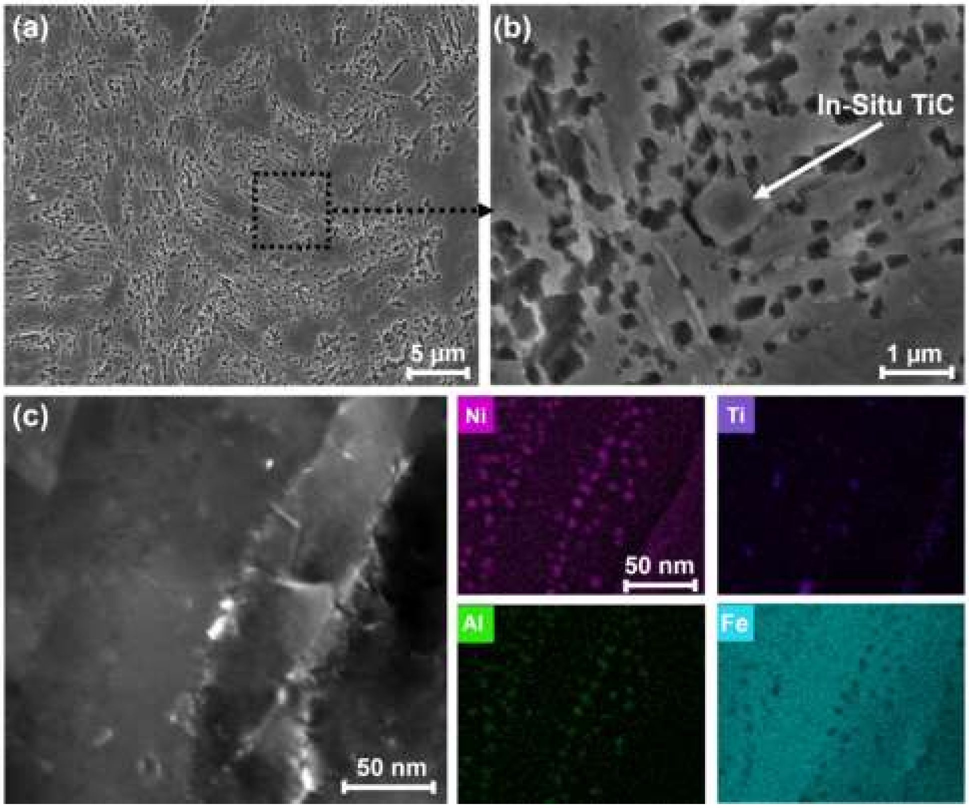

Figure 4.10 (a and b) Multi-magnification SEM images and (c) TEM image along with the associated EDS elemental maps taken from the heat-treated TiC-inoculated sample (SS+TiC/HT).

In the case of the heat-treated TiB_2-inoculated sample (SS+TiB_2/HT), a more complex microstructure was detected. Figure 4.11a displays the low magnification SEM image of the SS+TiB_2/HT sample, confirming that the solutionizing at 1050 °C successfully dissolved residual δ-ferrite in the martensitic matrix. In addition, some bright elliptical-shaped phases were detected mostly along the intergranular regions. The higher magnification SEM micrograph shown in Figure 4.11b also revealed the co-existence of the cubic TiC particles besides the bright intergranular phases, while there was no evidence of the existence of skeleton-like borides after the heat treatment. The EDS elemental maps from the newly revealed elliptical-shaped features (Figure 4.11c) showed their enrichment in Mo, Cr, and B, implying that the morphology of the M_3B_2-type borides has been changed from skeleton to ellipsoidal. It could be implicitly assumed that the M_3B_2-type borides dissolved during solutionizing, and subsequently re-precipitated in the preferential intergranular regions during the aging process. It has also been previously reported that during the air cooling cycle after solution heat treatment of martensitic steels, boron prefers to segregate at pre-existing crystal defects, such as primary austenite grain boundaries [203][204].

Further TEM analysis shown in Figure 4.11d, along with the associated EDS maps, confirm the formation of the nano-scale spherical β-NiAl precipitates alongside the Ti-rich particles. It should be noted that no $M_{23}C_6$-type carbide was evident in the SEM and TEM images of the heat-treated inoculated samples, which could be ascribed to the entire engagement of carbon atoms with Ti, which is known to be a stronger carbide former as compared to Cr and Mn [205].

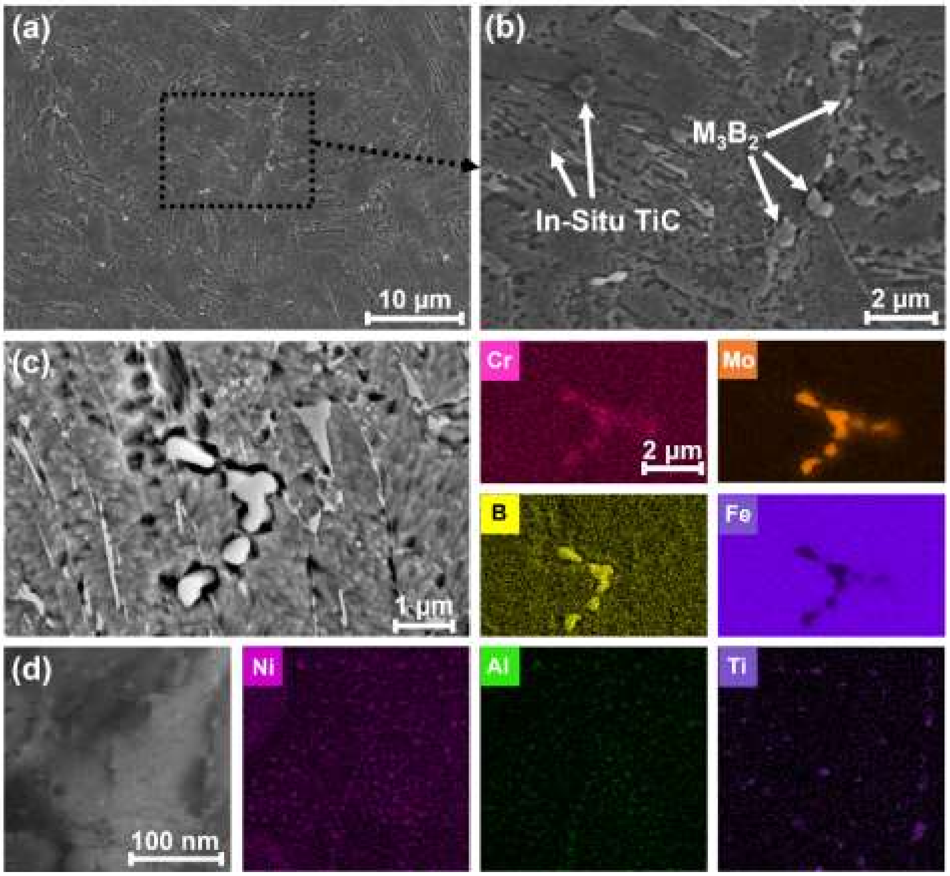

Figure 4.11 (a and b) Multi-magnification SEM micrographs taken from the heat-treated TiB_2-inoculated sample (SS+TiB_2/HT), (c) SEM micrograph along with the associated elemental mapping of the M_3B_2-type boride phases, and (d) TEM image along with the associated EDS elemental maps, showing the co-existence of β-NiAl precipitates alongside the Ti-rich particles.

Figure 4.12 schematically presents a summary of microstructural characteristics formed in the non-inoculated and inoculated WAAM-PH 13-8Mo samples in the as-printed and heat-treated conditions. The as-printed non-inoculated sample with a columnar structure consists of lathy and vermicular residual δ-ferrite, retained austenite, and Al_2O_3 inclusions in a martensitic matrix. The introduction of TiC nanopowders resulted in the formation of residual δ-ferrite islands, intact TiC, and cubic in-situ TiC phases nucleated on the Al_2O_3 inclusions. On the other hand, the introduction of TiB_2 nanopowders promoted the precipitation of skeleton-like M_3B_2-type borides besides the residual δ-ferrite islands, intact TiB_2, and in-situ TiC particles embedded in a martensitic matrix. Furthermore, solution and aging treatments led to the removal of the columnar structure, dissolution of residual δ-ferrite and retained austenite, as well as precipitation of spherical β-NiAl phases in both non-inoculated and inoculated samples. However, M_3B_2-type borides re-precipitated in the intergranular regions whilst their morphology changed to ellipsoidal in the heat-treated TiB_2-inoculated sample.

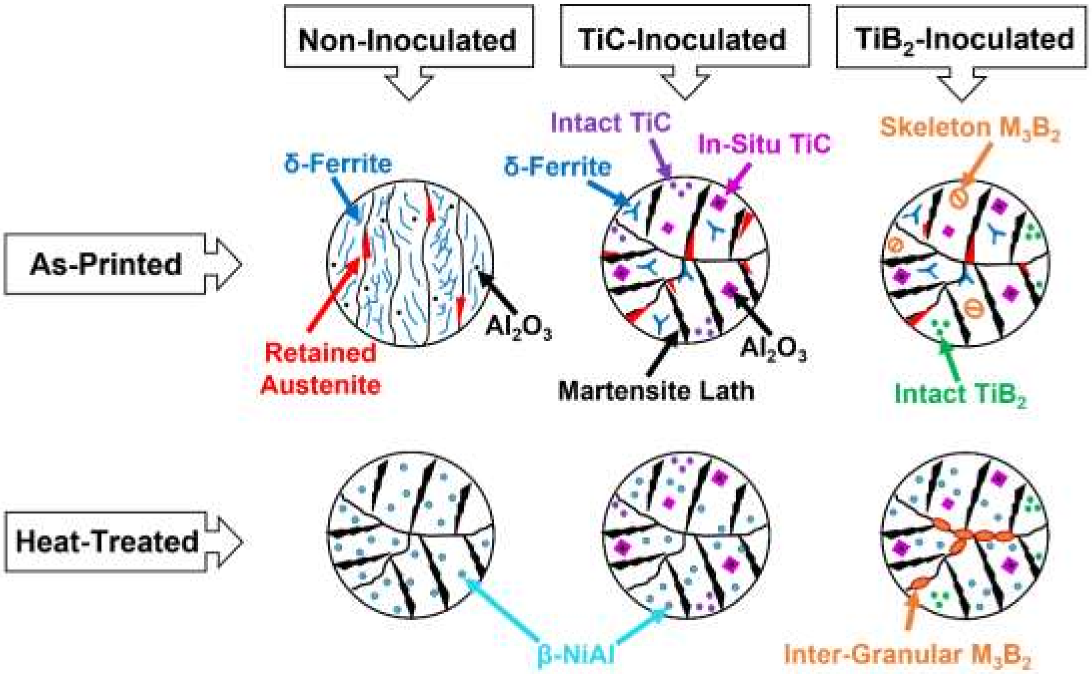

Figure 4.12 Schematic illustration summarizing microstructural characteristics formed in the non-inoculated and inoculated WAAM-PH 13-8Mo samples in the as-printed and heat-treated conditions.

4.4.5 Mechanical Properties

4.4.5.1 Microhardness and Tensile Strength of the As-printed and Heat-treated Samples

The results of the microhardness measurements of the as-printed and heat-treated samples are demonstrated in a box plot shown in Figure 4.13. Accordingly, a considerable microhardness improvement was observed from ~327 $HV_{0.5}$ for the non-inoculated sample to ~477 $HV_{0.5}$ and ~504 $HV_{0.5}$ for the SS+TiC/AP and SS+TiB_2/AP samples, respectively. Therefore, the addition of both TiC and TiB_2 nanopowders during the WAAM process of PH 13-8Mo alloy was found to be substantially effective in hardening of the alloy. Additionally, the post-printing heat treatment positively contributed to further increase of the microhardness in both inoculated and non-inoculated samples to ~538 $HV_{0.5}$, ~549 $HV_{0.5}$, and ~570 $HV_{0.5}$ for SS/HT, SS+TiC/HT, and SS+TiB_2/HT specimens, respectively.

It is obvious that the TiB_2-reinforced sample demonstrates superior microhardness in both as-printed and heat-treated conditions as compared to the TiC-reinforced sample. The significant hardness improvement by the introduction of TiC and TiB_2 reinforcements was also reported in inoculated 316L and AISI 420 stainless steel parts fabricated through the SLM process [17][178][195]. In another study, AlMangour *et al.* [26], compared the microhardness improvement as a result of TiC/TiB_2 inoculation during SLM processing of 316L stainless steel, and reported better mechanical performance in the TiB_2-reinforced samples in comparison with the TiC inoculation. Also, Bahramizade *et al.* [182] obtained a higher hardness in the in-situ fabricated TiC-Al_2O_3-TiB_2 composite relative to TiC-Al_2O_3 reinforced composite coating on 304 stainless steel substrate produced utilizing gas tungsten arc welding.

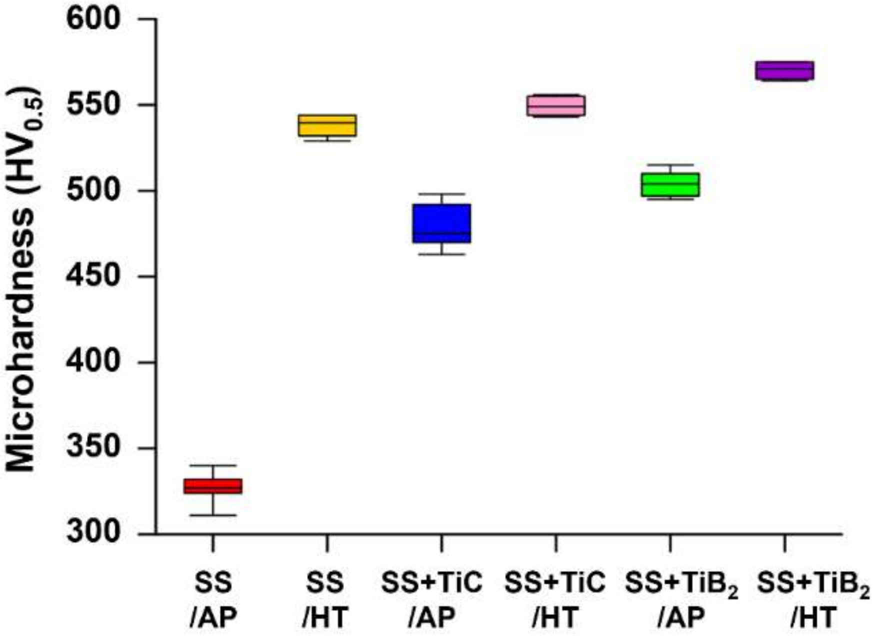

Figure 4.13 Vickers microhardness values of the non-inoculated and inoculated samples in the as-printed and heat-treated conditions.

Figure 4.14 demonstrates the stress-strain curves of the as-printed and heat-treated samples in both horizontal and vertical directions, and the summary of the tensile test results is listed in Table 4.5. Accordingly, the average ultimate tensile strength (UTS) value was raised from ~1117 MPa for the SS/AP sample to ~1434 MPa and ~1482 MPa for the SS+TiC/AP and SS+TiB_2/AP samples, respectively, which are reasonably comparable to the average UTS of the SS/HT sample (~1510 MPa). Moreover, solutionizing and aging treatments could further increase the tensile strength of the reinforced samples to the average UTS values of ~1527 MPa and ~1559 MPa for the SS+TiC/HT and SS+TiB_2/HT samples, respectively. Expectedly, the obtained tensile strength values were in agreement with the observed trend of microhardness data displayed in Figure 4.13.

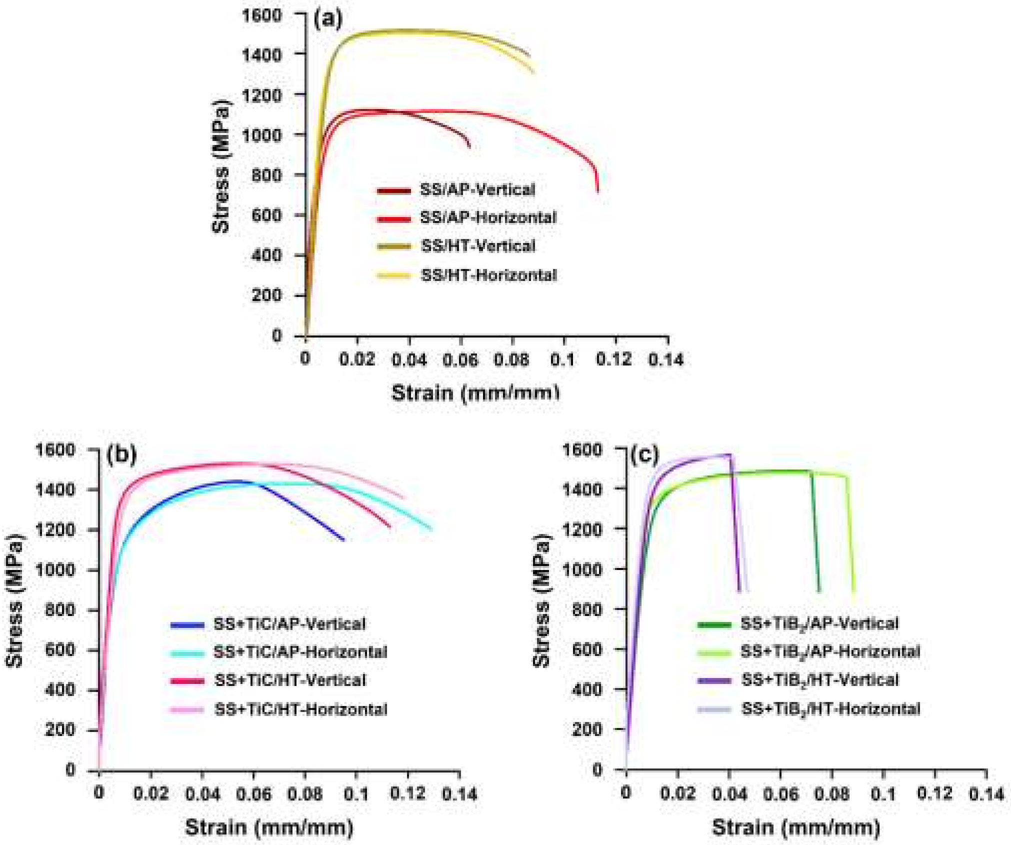

Figure 4.14 Stress-strain curves of the non-inoculated and inoculated samples in the as-printed and heat-treated conditions along both vertical and horizontal directions.

Table 4.5 Summary of the measured UTS and elongation values of all samples in different directions.

Sample	**UTS (MPa)**			**Elongation (%)**		
	Vertical	**Horizontal**	**Average**	**Vertical**	**Horizontal**	**Average**
SS/AP	1120 ± 15	1115 ± 17	1117± 18	6.3 ± 1.1	11.4 ± 1.8	8.8 ± 1.5
SS/HT	1517 ± 5	1503 ± 4	1510 ± 4	8.9 ± 0.1	9.1 ± 0.1	9.0 ± 0.1
SS+TiC/AP	1440 ± 12	1429 ± 10	1434 ± 10	9.5 ± 0.6	13.0 ± 0.9	11.2 ± 0.8
SS+TiC/HT	1529 ± 2	1525 ± 2	1527 ± 2	11.3 ± .1	11.8 ± 0.2	11.5 ± 0.1
SS+TiB_2/AP	1487 ± 8	1477 ± 9	1482 ± 9	7.3 ± 0.3	8.5 ± 0.2	7.9 ± 0.2
SS+TiB_2/HT	1564 ± 4	1555 ± 6	1559 ± 5	4.0 ± 0.1	4.0 ± 0.1	4.0 ± 0.1

4.4.5.2 Strengthening Mechanisms

The remarkable improvement in the microhardness and UTS values of the TiC/TiB_2-inoculated samples can be ascribed to the combined effects of four key contributors as follows:

(*i*) Grain refinement strengthening: Grain refinement is considered as one of the major contributing factors to mechanical properties improvement, which is described based on the well-known Hall-Petch relation ($\sigma = \sigma_0 + kd^{-1/2}$), where σ and d are the strength and grain size, respectively [13][17][185][194]. In the case of the inoculated samples, primary δ-ferrite grain refinement results in a higher fraction of resultant martensite lath boundaries, playing a pinning role against the dislocations motion under loading conditions [67]. Therefore, higher stress levels are required to mobilize dislocations across higher density of lath boundaries in the refined microstructure, leading to the strengthening of the material. In addition, the TiC/TiB_2 nanoparticles can restrict the movement of grain boundaries by the Zener pinning effect, which constrains the δ-ferrite grain growth during cooling to room temperature, leading to further grain refinement and strengthening [13][98].

(*ii*) Dislocation strengthening: The introduction of inoculant particles, like TiC and TiB_2, triggers the formation of a greater dislocation density owing to the faster cooling coupled with the dissimilarities in the thermal expansion coefficient and lattice parameters mismatch between the matrix and the reinforcing particle [13][26][67][88]. The higher density of tangled dislocations results in forest hardening, which is related to the complex dislocation interactions leading to anchoring mobile dislocations.

(*iii*) Nano-precipitation strengthening (Orowan strengthening): The presence of intact/in-situ nano-scale TiC and TiB_2 particles in the microstructure of the inoculated samples also plays a crucial role in the enhancement of the strength and hardness of the material. The hard reinforcing particles effectively generate obstacles to the dislocation propagation at their interface with the matrix, resulting in the accumulation and proliferation of the dislocations around the particles, which is known as Orowan strengthening mechanism [13][17][97][185][194].

(*iv*) Load-bearing strengthening/Load transfer effect: Improvement in the strength can also be caused by the effective load transfer from the soft low-carbon martensitic matrix to the hard ceramic-based TiC and TiB_2 nanoparticles owing to the strong interfacial bonding between particles and the matrix [13][17].

Considering the mentioned strengthening mechanisms, the superior mechanical strength of the TiB_2-inoculated sample, as compared to the TiC-inoculated one, could be correlated to the greater grain refinement ability of TiB_2 than TiC inoculants. In addition, load-bearing strengthening is more dominant in the TiB_2-inoculated sample due to the co-existence of multiple hard ceramic phases of TiB_2 and in-situ TiC/M_3B_2 phases, while the TiC-inoculated sample only contains intact/in-situ TiC particles. In the case of the heat-treated condition, the precipitation of coherent β-NiAl phases is the major contributing factor, leading to the better hardness and strength of the heat-treated samples as compared to the as-printed samples [177].

4.4.5.3 Ductility and Anisotropic Behaviour of the As-printed and Heat-treated Samples

According to the stress-strain curves shown in Figure 4.14a, a significant difference in the elongation values was obtained in the vertical (~6.3%) and horizontal (~11.4%) directions of the SS/AP sample. As comprehensively discussed in the authors' previous studies [68][177], the observed anisotropy in ductility can be ascribed to the strong texture along the vertical (building) orientation, arising from the formation of the coarse columnar structure in the non-inoculated sample (see Figures 4.2 and 4.3). In contrast to the non-inoculated sample, the elongation of the TiC-containing sample increased to ~9.5% and ~13% in the vertical and horizontal directions, respectively, which reveals a lower degree of anisotropy in ductility in the SS+TiC/AP sample (see Figure 4.14b).

The improvement in the ductility and slighter anisotropic behavior in the TiC-inoculated sample can be mostly correlated to its grain refinement, the formation of partially equiaxed primary δ-ferrite grains, as well as the presence of a higher content of retained austenite in comparison with the non-inoculated sample. The corresponding fractured surface of the as-printed TiC-inoculated sample, depicted in Figure 4.15a, also confirmed a ductile-type failure mode due to the numerous fine dimples formed as a result of micro-voids coalescence. As indicated in the high-magnification fractograph (Figure 4.15b), cubic-shaped TiC particles were found in several neighboring dimples, implying that the TiC particles served as preferential dimple initiation sites. During the uniaxial tensile testing, when the strain hardening capacity of the matrix comes to the saturation point, stresses are relaxed by debonding the reinforcing particles and forming a dimple, followed by transferring the stresses to the neighbour reinforcements. This recurring mechanism results in further particle debonding as a chain reaction, leading to the ductile fracture of the material by frequent nucleation and growth of micro-dimples around the reinforcements, which eventually finishes by the coalescence of the larger dimples initiated from the debonded particles.

On the other hand, the stress-strain curves of the as-printed TiB_2-reinforced sample (see Figure 4.14c) showed a slight improvement in elongation of the vertical sample to ~7.3%, while a significant decrease to 8.5% was observed in the horizontal direction. Although the anisotropic behaviour was drastically minimized in the SS+TiB_2/AP sample, a relatively lower ductility was observed as compared to the TiC-inoculated sample. Therefore, despite the fine equiaxed grain structure obtained in the SS+TiB_2/AP sample, the improvement in strength compromised the ductility of the material.

The corresponding fractured surface of the as-printed TiB_2-inoculated sample, depicted in Figure 4.15c and d, displayed a dimple-like fracture mode, while a high density of internal cracks was almost evenly distributed on the fractured surface. Considering the extremely limited solubility of boron in iron (~0.00012 wt.% [188]), the formation of internal cracks and brittleness of the TiB_2-inoculated sample can be associated with the segregation of boron atoms during the final stages of the solidification process of each layer, which can reduce the toughness of the material. Additionally, the inherent brittleness of the TiB_2 particles (K_{IC} of ~6.2 MPa $m^{1/2}$ [180]) can be a supplementary factor to the ductility deterioration in the SS+TiB_2/AP sample [206].

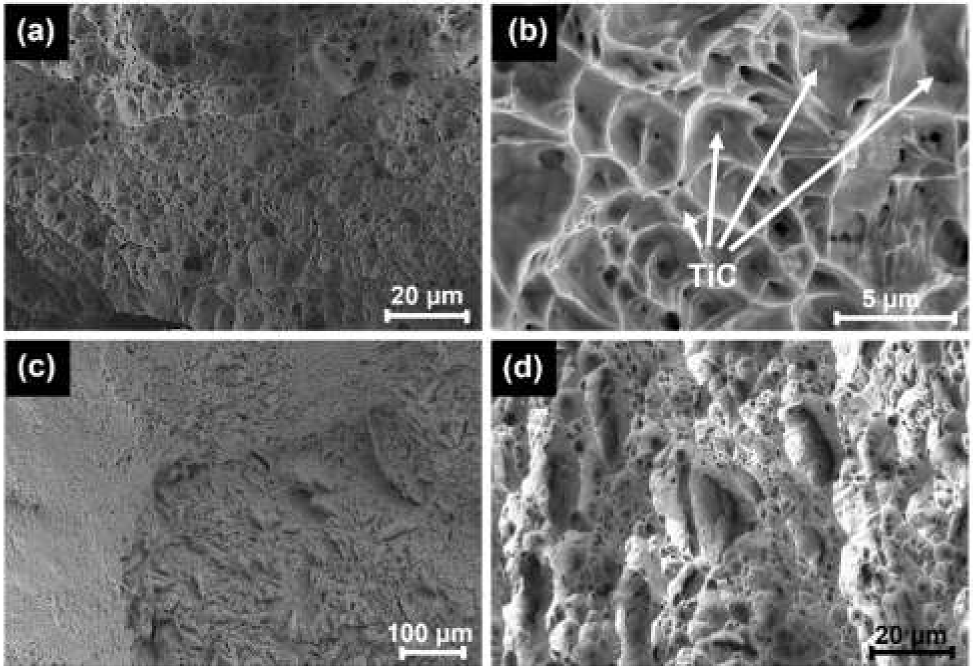

Figure 4.15 Multi-scale SEM images taken from the fractured surfaces of the (a and b) SS+TiC/AP and (c and d) SS+TiB_2/AP samples.

In the case of the heat-treated TiC-inoculated sample, the stress-strain curve illustrated in Figure 4.14b revealed that the anisotropic ductility was almost entirely diminished, which can be correlated to further grain refinement and elimination of columnar structure during the solution treatment. It should be noted that in addition to the high strength achieved in the SS+TiC/HT sample, the average elongation percentage reached the acceptable value of ~11.5%, which is even more than the obtained average elongation percentage for the SS/HT sample (~9%). The corresponding fractured surface of the SS+TiC/HT sample in Figure 4.16a and b also indicated a dimple-like fracture, consistent with the ductile nature of these samples.

On the other hand, the brittleness was noticeably intensified in the case of the heat-treated TiB_2 reinforced sample to an insignificant elongation percentage of ~4% in both horizontal and vertical directions (see Figure 4.14c). According to the low-magnification SEM micrograph of the SS+TiB_2/HT sample (Figure 4.16c), a very thin band at the edges of the fractured surface experienced a dimple-like ductile fracture, which rapidly transferred to a cleavage brittle fracture in the central regions. The high-magnification

SEM image taken from the central regions of the fractured surface shows the cleavage facets and river-like patterns, which are characteristics of brittle fracture (see Figure 4.16d). The brittleness of the SS+TiB_2/HT sample could be mainly associated with the accumulation of hard M_3B_2-type phases on the grain boundaries during the heat treatment process (see Figure 4.11), which leads to a brittle intergranular fracture. Fundamentally, the clustering of elastic ceramic phases confines the plastic deformation of the surrounding metal matrix, which induces greater stress levels at the particle-matrix interface, resulting in rapid debonding of the reinforcements [207]. It should be mentioned that the particle-matrix interface of intergranular reinforcements is usually considered as the Achilles heel of ceramic-metal composites due to the difference in the thermal expansion coefficient of the metallic matrix and the ceramic-based reinforcements [93]. Therefore, even a small amount of M_3B_2 accumulation in the intergranular regions can adversely impact the ductility of the material, leading to interfacial tearing and premature failure at deficient strains.

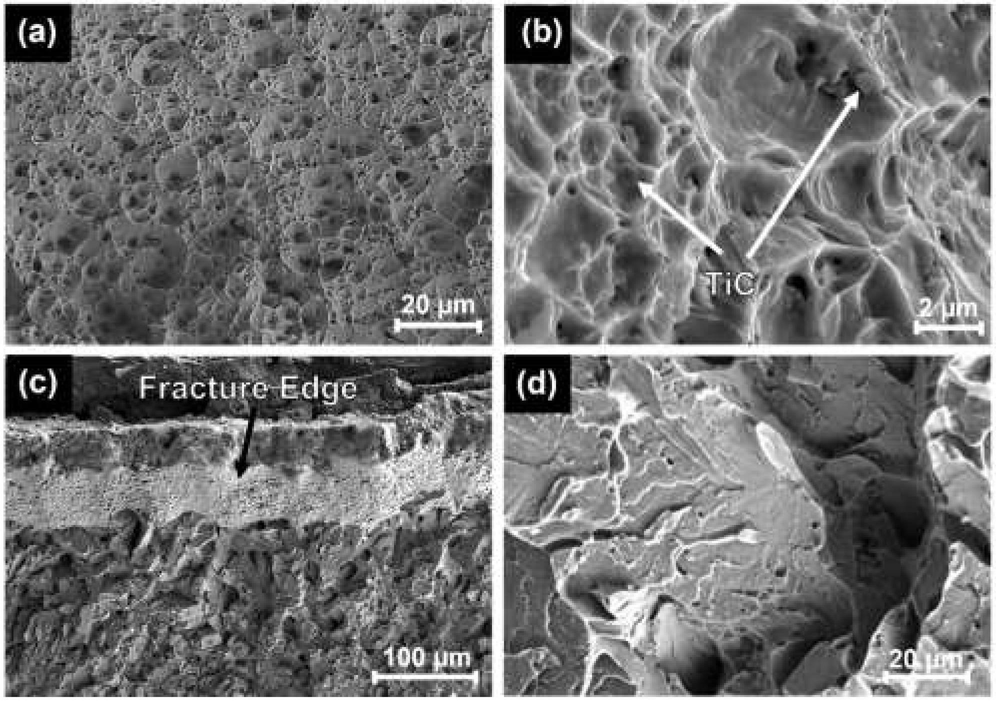

Figure 4.16 Multi-scale SEM fractographs taken from the fractured surfaces of the (a and b) SS+TiC/HT and (c and d) SS+TiB_2/HT samples.

Overall, the best combination of strength and ductility with minimum anisotropy was obtained for the heat-treated TiC-reinforced sample, which even exceeded the ASTM standard requirements for the PH 13-8Mo stainless steel alloy (*i.e.,* UTS of 1515 MPa and elongation of 10% [175]). With regards to the heat-treated TiB_2-inoculated sample, despite its superior strength and hardness, the accumulation of brittle phases at grain boundaries of this sample significantly diminished the ductility of the material. As such, conservative measures should be taken into account in practical applications of this reinforced material, particularly when used in heat treated condition.

4.5 CONCLUSIONS

For the first time, the present study investigated the potential grain refinement through the introduction of TiC and TiB_2 nano-inoculants between the consecutively deposited layers during WAAM of a PH 13-8Mo MSS. Comprehensive microstructural and mechanical properties characterizations were performed before and after post-printing heat treatment, and the main conclusions are summarized as follows:

1. Macrostructural observations revealed a columnar structure in the non-inoculated part, while grain refinement and columnar-to-equiaxed transition were achieved by introducing TiC/TiB_2 nanopowders between the deposited layers. However, TiB_2 inoculation was found to be more effective than TiC in refining the grains, resulting in an entirely equiaxed primary δ-ferrite grain structure at the initial stage of solidification.
2. The microstructure of the TiC-inoculated sample was composed of in-situ cubic-shaped TiC particles, resulting from partial melting of the nanopowders in the melt pool. On the other hand, in the TiB_2-inoculated sample, the dissolution of boron in the molten metal led to the formation of skeleton-like M_3B_2-type borides in addition to in-situ TiC particles.
3. Further post-printing solution and aging treatments triggered the precipitation of nano-sized β-NiAl phases in the non-inoculated and inoculated samples, while the morphology of M_3B_2-type borides changed to ellipsoidal phases accumulated on the grain boundaries of the TiB_2-inoculated sample.

4. The microhardness and UTS values of the as-printed alloy were considerably increased by approximately 46% and 28% in the TiC-inoculated sample, respectively, and 54% and 33% in the TiB_2-inoculated samples, which was primarily ascribed to the complementary effects of grain size strengthening, dislocation strengthening, Orowan strengthening, and load transfer effect. Also, the post-printing heat treatment further improved the hardness and UTS of the material owing to the precipitation of nano-scale coherent β-NiAl phases through the aging process.
5. The transition of columnar-to-equiaxed grain structure in the inoculated samples decreased the anisotropic ductility in comparison with the non-inoculated sample, while the segregation of boron during the final stages of the solidification process led to the embrittlement of the TiB_2-inoculated sample.
6. Although concurrent improvement in strength and ductility properties was achieved in the heat-treated TiC-inoculated sample, primarily driven by the refined grain structure of the alloy, the formation of intergranular M_3B_2-type borides intensified the brittleness in the heat-treated TiB_2-inoculated sample.

Acknowledgments

The authors gratefully acknowledge the support of Natural Sciences and Engineering Research Council of Canada (NSERC) [grant number RGPIN-2017-04368], Canada Research Chair program, Ocean Frontier Institute, and Dalhousie University for sponsoring this work. The authors also acknowledge that the electron microscopy was performed at the Canadian Centre for Electron Microscopy, a Canada Foundation for Innovation Major Science Initiatives funded facility.

CHAPTER 5 CONCLUSIONS

5.1 SUMMARY AND CONCLUSIONS

This Ph.D. research project aimed to develop thermo-mechanical processing routes for cost effective production and repair of PH 13-8Mo stainless steel components with enhanced mechanical properties through the WAAM process. The outcomes of the presented thesis facilitate the adoption of WAAM technology in different expanding industrial sectors, including aerospace, marine, petrochemical, and defense industries, for the fabrication of large-scale PH 13-8Mo stainless steel parts tailored for extreme service conditions, such as cyclic temperatures, extreme dynamic/impact loading, and corrosive atmospheres. In particular, tool and die industries are keen to additively re-manufacture PH 13-8Mo stainless steel dies for applications in plastic injection molding. Additionally, the excellent combination of tensile strength, fracture toughness, ductility, resistance to stress corrosion cracking and hydrogen embrittlement of PH 13-8Mo, make it a suitable candidate for substituting other types of stainless steels, such as 316L and 17-4PH in a variety of applications. Despite all these benefits, the production of 13-8Mo stainless steel parts has not yet been industrially developed using state-of-the-art WAAM technology, primarily due to the lack of solid knowledge of the microstructural characteristics and in-service performance of WAAM-fabricated components. Therefore, for the first time, the performed Ph.D. research was missioned to validate the WAAM fabrication feasibility of PH 13-8Mo stainless steel components and disclose the associated metallurgical challenges and to develop strategies for producing sound and defect-free engineering components with comparable mechanical properties to the conventionally manufactured counterparts. The obtained results demonstrated that the as-printed microstructure was predominantly characterized by residual δ-ferrite phase with vermicular and lathy morphologies distributed in a martensitic matrix in addition to a small volume fraction of retained austenite. However, the complex thermal cycles experienced by different locations of the fabricated wall resulted in microstructural inhomogeneity, in particular, reduced amounts of residual δ-ferrite and retained austenite through the building direction. Consequently, the microhardness and ultimate tensile

strength values were found to increase gradually from the bottom to the top of the component. Additionally, the steep directional heat sink towards the substrate led to the formation of large columnar primary δ-ferrite grains resulting in a strong cubic texture and noticeable anisotropy in ductility. Moreover, microhardness evaluations across subsequently deposited layers revealed a slightly higher microhardness value in the HAZs as compared to the melt pools' centers, associated with the dissolution of residual δ-ferrite in the HAZs, creating a nearly fully martensitic microstructure in HAZs.
The observed metallurgical heterogeneities and mechanical properties uncertainties could restrict the application of the as-printed PH 13-8Mo parts in service conditions. Therefore, two modification strategies, including (i) the application of appropriate post-printing thermal treatments and (ii) the addition of ceramic-based TiC and TiB_2 nanopowders, were developed by which the desired microstructure and mechanical properties in the WAAM-fabricated parts could be attained. Different post-printing heat treatment cycles were applied with the aim of modifying the microstructural features, promoting an equiaxed grain structure, eliminating anisotropic behaviour, and improving the mechanical properties. Accordingly, the as-printed samples were first subjected to solution treatment at 900, 950, 1050, and 1150 °C for 1 h, and it was concluded that the optimum solution treatment at 1050 °C resulted in the complete dissolution of undesired δ-ferrite and removal of the columnar structure and anisotropic ductility. Subsequently, the 1050 °C solutionized samples were aged at 400, 450, 500, 550, and 600 °C for 4 h. Although aging at 400 °C was not high enough to form any precipitates or secondary phases, the higher aging temperatures of 450 and 500 °C resulted in the precipitation of spherical and coherent β-NiAl intermetallics evenly distributed within the martensite laths. Increasing the aging temperature to 550 and 600 °C triggered the formation of Cr-rich $M_{23}C_6$ carbides and reverted austenite in addition to β-NiAl precipitates. According to the micro-mechanical testing results, the maximum hardness, yield pressure, reduced elastic modulus, and tensile strength were achieved in the 500 °C aged sample due to the formation of optimum-sized β-NiAl precipitates in a fully martensitic matrix. However, a significant hardness reduction was observed in the samples aged at 550 and 600 °C as a result of further martensite recovery and the formation of other secondary phases, *i.e.*, Cr-rich carbides, and reverted austenite. The tensile testing analysis in horizontal and

vertical directions also confirmed the abatement of anisotropic ductility after post-printing heat treatment, mainly due to the elimination of columnar structure.

Although the microstructural modification and mechanical properties improvement through post-printing heat treatment were validated herein, the implementation of an additional post-fabrication process into the production cycle of components can increase both production cost and time. As such, adopting in-situ modification techniques during the printing process by which improved microstructure and mechanical properties can be attained, are economically more viable. As an example, the addition of ceramic-based inoculants during the deposition of consecutive layers could play the same role as applying post-printing heat treatment in microstructural modification by providing a large number of grain nucleation sites, potential grain refinement, and preventing the formation of large columnar grains. In addition, the introduction of fairly hard nanoparticles embedded in the matrix could result in further mechanical performance enhancement. The addition of TiC and TiB_2 nano-particle inoculants into the structure of PH 13-8Mo parts through WAAM processing studied herein revealed that both inoculants refined the primary δ-ferrite grains and promoted the transition of columnar-to-equiaxed grain structure. However, TiB_2 nanopowders were found to be a more effective grain refiner as compared to TiC reinforcing particles, resulting in an entirely equiaxed primary δ-ferrite grain structure. The partial melting of the TiC nanopowders in the melt pool of the TiC-inoculated sample provoked the formation of in-situ cubic-shaped TiC particles during the solidification process. On the other hand, in the TiB_2-inoculated sample, the dissolution of boron in the molten metal led to the formation of skeleton-like M_3B_2-type borides in addition to in-situ TiC particles. The microhardness and UTS values were noticeably increased by almost 46% and 28% in the TiC-reinforced, respectively, and 54% and 33% in the TiB_2-reinforced samples. The observed superior mechanical properties were mainly ascribed to the synergetic effects of grain size strengthening, dislocation strengthening, Orowan strengthening, and the load transfer effect. The transition of a columnar-to-equiaxed grain structure in the inoculated samples decreased the anisotropic ductility as compared to the non-inoculated sample, while the segregation of boron led to the embrittlement of the TiB_2-inoculated sample. Although the mechanical properties obtained in the ceramic particles inoculated samples are comparable with their conventionally fabricated counterparts, subsequent post-printing solutionizing (1050 °C) and aging (500 °C) heat treatments were found to be effective in further improving the mechanical properties of the as-printed inoculated samples.

Overall, the discovered characteristic technological and metallurgical challenges associated with the WAAM production of PH 13-8Mo stainless steel components were addressed in this study. The outcomes of this Ph.D. research can be employed as a roadmap that facilitates the accelerated adoption of state-of-the-art WAAM technology for production and repair of PH 13-8Mo stainless steel components for wide range of applications in many industries.

5.2 FUTURE WORKS

This thesis investigated the effect of different heat treatment cycles after 3D-printing and the addition of ceramic-based nanopowders during the deposition process of wire arc additively manufactured PH 13-8Mo stainless steel. However, due to time constraints, it was not possible to investigate all different process variants, and also to take advantage of other existing materials characterization methods. Therefore, the author provides some recommendations and suggestions as possible future works for the current thesis.

1. As the WAAM process parameters were optimized adopting trial and error attempts to obtain the lowest level of splashing and defect-free parts, it is highly recommended to investigate the influence of some other variables, such as interpass temperature and shielding gas on the microstructural features of the component. Since the anisotropic mechanical properties were primarily driven by the microstructural nonuniformities and columnar structure, further process optimization could abate the anisotropic ductility and exclude the post-printing heat treatment requirements. Moreover, since the interpass temperature can affect the retained austenite content, it is beneficial to analyze the mechanical performance and also corrosion resistance of the WAAM-fabricated components deposited at various interpass temperatures.

2. Although PHMSS alloys are favourable materials for applications requiring excellent mechanical behaviour and corrosion performance, they might not exhibit satisfactory wear resistance depending on the in-service conditions. For example, in the plastic injection molding process, which was introduced as an application for PH 13-8Mo stainless steel, the dies are commonly exposed to extreme mechanical loads and harsh tribological conditions. Therefore, both post-printing heat treatment and ceramic-based particle additions can positively affect the wear resistance of the as-printed components. As such, it is highly recommended to conduct complementary wear and tribological response assessment of the as-printed, heat-treated, and inoculated samples, followed by a thorough comparison between the results obtained from different samples to investigate the wear resistance of the WAAM-fabricated parts. This topic is the subject of an upcoming study by the author's research group. In addition, since the presence of carbide and boride phases drastically affect the corrosion performance of the additively manufactured parts, it is essential to study the effect of adding ceramic reinforcements and also the subsequent heat treatment on the electrochemical response of the material.
3. Since the powder form (CX) of PH 13-8Mo alloy is commercially available in the market, further investigations on the effect of the introduction of TiC and TiB_2 nanopowders during PBF of CX counterparts is highly recommended. Moreover, as the grain refinement ability significantly depends on the size of the original powders, it is important to study the influence of employing larger powders (submicron-sized) instead of nanopowders during both WAAM and PBF methods.

APPENDIX AI EFFECT OF SOLIDIFICATION DEFECTS AND HAZ SOFTENING ON THE ANISOTROPIC MECHANICAL PROPERTIES OF A WIRE ARC ADDITIVE MANUFACTURED LOW CARBON LOW ALLOY STEEL PART

Mahya Ghaffari[1], Alireza Vahedi Nemani[2], Mehran Rafieazad[3], Ali Nasiri[4]

1- Graduate Student, Dalhousie University, Halifax, Nova Scotia, Canada
2- Post-Doctoral Fellow, Dalhousie University, Halifax, Nova Scotia, Canada
3- Consumable R&D and Welding Engineering Supervisor, Lincoln Electric, Toronto, Ontario, Canada
4- Assistant Professor, Dalhousie University, Halifax, Nova Scotia, Canada

Status: Published Journal Paper, Journal of the Minerals, Metals & Materials Society (JOM) (IF= 2.597), Volume 71(11), Pages 4215-4224.

Authors' Contribution

Mahya Ghaffari: Conceptualization, Investigation, Writing - original draft.

Alireza Vahedi Nemani: Methodology, Validation, Investigation, Writing - review & editing.

Mehran Rafieazad: Fabrication Process, Writing - review & editing

Ali Nasiri: Supervision, Writing - review & editing, Funding acquisition.

AI.1 ABSTRACT

Wire arc additive manufacturing (WAAM) is a pioneer additive-based technology for fabrication of large-scale engineering components. Despite many advancements in the field of additive manufacturing, formation of solidification defects, including discontinuities and microstructural imperfections, in the fabricated components are still inevitable, regardless of the used feedstock material or the selected fabrication process. In this study, the effects of solidification defects on the anisotropic mechanical properties in a low-carbon low-alloy steel (ER70S-6) wall produced by WAAM have been investigated. The microstructure and mechanical properties analysis of the fabricated part confirmed the formation of various solidification defects, *i.e.*, interpass lack of fusions, localized brittle zones, and grain coarsening in the heat affected zones, leading to an anisotropic behavior in ductility along the deposition versus the building directions of the

component. The contribution of discontinuities on the anisotropic mechanical properties was minimized through microstructural modifications of the fabricated part using post-printing normalizing heat-treatment.

AI.2 INTRODUCTION

Additive manufacturing (AM) also known as 3D-printing is an evolving technology that allows the fabrication of a component by depositing the feedstock material layer-by-layer to produce a three-dimensional, near-net shaped component, as opposed to the conventional manufacturing techniques, which are mostly based on subtractive methodologies [208]. Although during the last three decades, AM has been employed by only a limited number of industries for prototyping purposes, the technology has recently drawn substantial attention of the manufacturing sectors due to its time and cost efficiency [209].

Among various types of AM technologies, wire arc additive manufacturing (WAAM) is the only AM technique capable of producing meter-scale engineering components for applications in different industries, including marine, aviation, oil and gas, among many others [209][210]. Using wires as the feedstock material and an electric arc or plasma as the heat source leads to an extremely high deposition rate with the WAAM process [211]. Analogous to other direct energy deposition (DED) AM processes, the WAAM process is accompanied by sequential melting and solidification of the deposited material, making the process prone to form solidification defects [212], including discontinuities, such as hot cracks, pores and lack of fusions, as well as microstructural inhomogeneity and imperfections [213], such as grain coarsening or formation of adverse phases with a brittle nature in the heat affected zone (HAZ) [214]. Such a high susceptibility of the fabricated parts to manufacturing defects highlights the importance of establishing the quality assurance procedures to be able to guarantee the reliability of the additively manufactured components [212].

Different qualification procedures have been suggested so far to control the quality of both the AM fabrication process and the printed components, including (*i*) accurate logging and investigation of AM process parameters using fast Fourier transform data analyses techniques, and/or (*ii*) in-situ monitoring of individual deposited layers through thermal and optical imaging [213][215]. Additionally, simulation and modeling of various aspects of metal AM, *i.e.*, in-situ process control and ex-situ process simulations, have been developed that could potentially be adopted by manufacturers to envisage any possibility of discontinuity formation as well as microstructural heterogeneities [216].

The presence of defects in a component can lead to premature failure or drastic reduction in ductility/toughness of the part [103]. Furthermore, solidification-induced defects could potentially contribute to anisotropic mechanical properties along the deposition and building directions of an AM part, ascribed to the higher density of the interpass regions in the vertical direction, containing heat affected zones and possibly a higher density of discontinuities in the melt pool boundaries [217]. The anisotropy in microstructure and mechanical properties can be diminished or even be eliminated either by optimizing the process parameters or adopting appropriate post-fabrication heat treatment processes [218][219]. In a recent study, Xu *et al.* [220] reported that the microstructural heterogeneity and anisotropic mechanical properties in a WAAM fabricated maraging steel component were minimized through applying a solutionizing heat treatment followed by aging, which eliminated the microstructural inhomogeneity from the bottom to the top of the component. Therefore, conducting a comprehensive investigation on the formation of discontinuities and microstructural defects in the WAAM fabricated components and also implementing post-fabrication processes, such as heat treatment or hot-isostatic pressing (HIP) cycles, to alleviate these defects by transforming the microstructures to those fit for service conditions are extremely crucial.

This study aimed to investigate the influence of solidification defects on the anisotropic mechanical properties of a low carbon low alloy steel (ER70S-6) fabricated by wire arc additive manufacturing. Furthermore, the effects of a post-process normalizing heat treatment on the microstructure and mechanical properties of the WAAM-ER70S-6 part were studied. The microstructures of the as-printed and heat-treated samples were characterized using optical and scanning electron microscopy (OM and SEM) and electron backscatter diffraction (EBSD) analysis. In addition, Vickers microhardness measurements and uniaxial tensile testing along both deposition and building directions were carried out to evaluate the mechanical properties of the component.

AI.3 MATERIALS AND METHODS

AI.3.1 Material, Fabrication Process, and Post-fabrication Heat Treatment

In this study, a low carbon low alloy steel ER70S-6 wire with a diameter of 0.9 mm was used to build up a wall-shape component on the ASTM A36 mild steel as the base plate using wire arc additive manufacturing method. Figure I.1 represents the set-up of the WAAM process, the fabricated ER70S-6 wall, and the orientation of tensile testing samples along the deposition (horizontal) and building (vertical) directions. The nominal chemical composition of the feedstock wire (in wt.%) is 0.06-0.15% C, 1.40-1.85% Mn, 0.80-1.15% Si, ≤ 0.04% S, ≤ 0.03% P, ≤ 0.15% Cr, ≤ 0.15% Mo, ≤ 0.03% V, ≤ 0.5% Cu and Fe balance.

The surface of the base plate with the size of 250 mm × 150 mm × 12 mm was wire brushed, and then cleaned in acetone ultrasonically to remove oxide layers and degrease the surface prior to the deposition of the first layer of the part. A thin wall of ER70S-6 was fabricated in 50 consecutive layers, and each layer contained six passes, deposited parallel to each other with alternating directions, resulting in a wall with a height of 150 mm, length of 135 mm, and width of 22 mm. A Lincoln Electric gas metal arc welding (GMAW) machine utilizing an advanced surface tension transfer (STT) mode was used as the power source to precisely adjust the heat of the process independent from the wire feeding rate, while keeping the heat input as low as possible during fabrication [221]. Moreover, pure argon with the flow rate of 45 L/min was used as the shielding gas to protect the melt pool from any atmospheric contamination during the melting and solidification processes. The used GMAW torch was mounted on a 6-axis Fanuc robot, providing the degrees of freedom to accurately follow the deposition pattern. The travel speed (5 mm/s), wire feed angle (90°), and the deposition path were governed by the robot and other fabrication parameters including arc current (320 A), arc voltage (28 V), wire feeding rate (104 mm/s), and arc length (3 mm) were adjusted through the GMAW power supply. Moreover, a 10-min dwell time between the consecutive layers was implemented to ensure that the wall was cooled to the room temperature before depositing the next layer, contributing to the consistency of the cooling rate during solidification of each layer.

Post-fabrication normalizing heat treatment was also applied to the as-printed component with the cycle of austenitizing at 900 °C for 1 h, followed by still-air cooling to the room temperature. It should be noted that pure Ar gas was purged into the furnace during the heating cycle to minimize surface oxidation of the part.

AI.3.2 Microstructural Characterization

For microstructural analysis, metallographic specimens were cut from different locations of the fabricated wall to study microstructural variations along the building direction , followed by grinding, polishing, and then etching by 5% Nital for 20 s [222]. The microstructural analysis of the melt pool centers, melt pool boundaries, and the HAZs were carried out to evaluate the effect of complex thermal cycles associated with the WAAM process on the microstructural variations at different regions of the sample. Optical (Nikon Eclipse 50i) and field emission scanning electron microscopes (FEI MLA 650F) were employed to perform the microstructural characterization at different magnifications. To obtain a detailed and quantitative analysis of the grains' size distribution and orientation variation from the melt pool center to the HAZ, electron backscatter diffraction (EBSD) analysis with a step size of 1.4 µm and a tilt angle of 70° was performed over an area of 600 × 600 μm^2 covering the transition from a melt pool center to its adjacent HAZ, using Nordlys II HKL EBSD detector, Oxford Instruments.

AI.3.3 Mechanical Properties Evaluation

A Buehler Micromet hardness test machine with the applied load of 300 g and a holding time of 45 s was used to measure the microhardness distribution on different zones, including the melt pool centers, fusion boundaries, and HAZs. The microhardness measurements were also carried out in a vertical line along the building direction to evaluate the microhardness variations from the bottom to the top of the wall. It should also be noted that the samples were polished and etched before applying the indentations to evaluate the effect of different microstructures on the microhardness of the sample. To investigate the effect of solidification defects on the anisotropic mechanical behavior of the 3D-printed component, an Instron load frame was used to perform uniaxial tensile testing at the crosshead speed of 8 mm/min on samples prepared from the deposition (horizontal) and building (vertical) directions based on ASTM E8m-04 standard sub-size specimen with dimensions of 100 mm × 25 mm × 5 mm [223]. As shown in Figure I.1, tensile samples were prepared from different locations along both the deposition and the building directions. The open to the surface solidification defects on the horizontal and vertical tensile samples before and after tensile testing were detected by Leica A60 F stereo microscope.

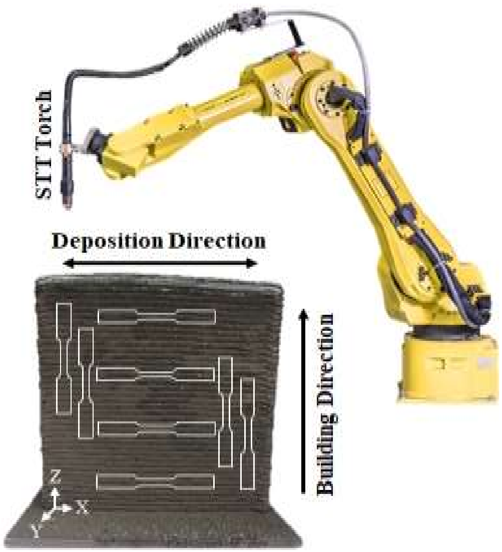

Figure I.1 The WAAM process set-up and the fabricated ER70S-6 wall.

AI.4 RESULTS AND DISCUSSION

Figure I.2a schematically illustrates two successive beads in the as-printed WAAM-ER70S-6 sample, indicating four distinguishable zones with distinct microstructures, *i.e.*, melt pool center, melt pool boundary, and the HAZ which covers two different regions in the previously solidified bead. The OM and SEM micrographs from different zones of the deposited beads are also depicted in Figure I.2b-e. The microstructure of the melt pool center (Figure I.2b), which is the dominant microstructure of the as-printed sample, contains polygonal ferrite (PF) grains along with small volume fraction of lamellar pearlite (P) formed in the grain boundaries, which is in agreement with the results reported in the recent studies on the WAAM of ER70S-6 [224][225][226][227]. However, a closer look at the microstructure of the melt pool boundary (Figure I.2c) revealed that adjacent to each melt pool boundary, a narrow region containing some non-equilibrium phases, such as acicular ferrite (AF) and bainite (B) were formed, ascribed to the faster cooling rate of each melt pool in the regions adjacent to the boundaries as compared to its center. Formation of AF and B constituents near the fusion line is also reported in previous studies during both welding [228] and wire arc additive manufacturing [229] of low carbon low alloy steels.

As clearly demonstrated in the schematic shown in Figure I.2a, the HAZ in the previously deposited bead is expanded through both the melt pool center and the fusion boundary, denoted as HAZ_1 and HAZ_2 in the schematic illustration, respectively. The microstructure in the HAZ_1 (Figure I.2d) consists of coarser ferrite grains compared to the melt pool center as the thermal effect of each solidifying bead facilitates the grain boundaries migration and stimulates the grain growth in the previously deposited track [230][231]. Differently, reheating the structure in the fusion boundaries (HAZ_2) as a consequence of the next layer deposition has resulted in the formation of some tiny bright constituents, known as martensite-austenite phase in the HAZ_2 (Figure I.2e), which will be characterized with more details in the following sections. It should be noted that the microstructural features of a single deposited layer shown in Figure I.2 were consistently repeated from the bottom to the top of the wall along the building direction. The uniform microstructure along the building direction can be ascribed to the 10-min interlayer dwell time, preventing the heat accumulation and complex thermal history during fabrication of the as-printed component.

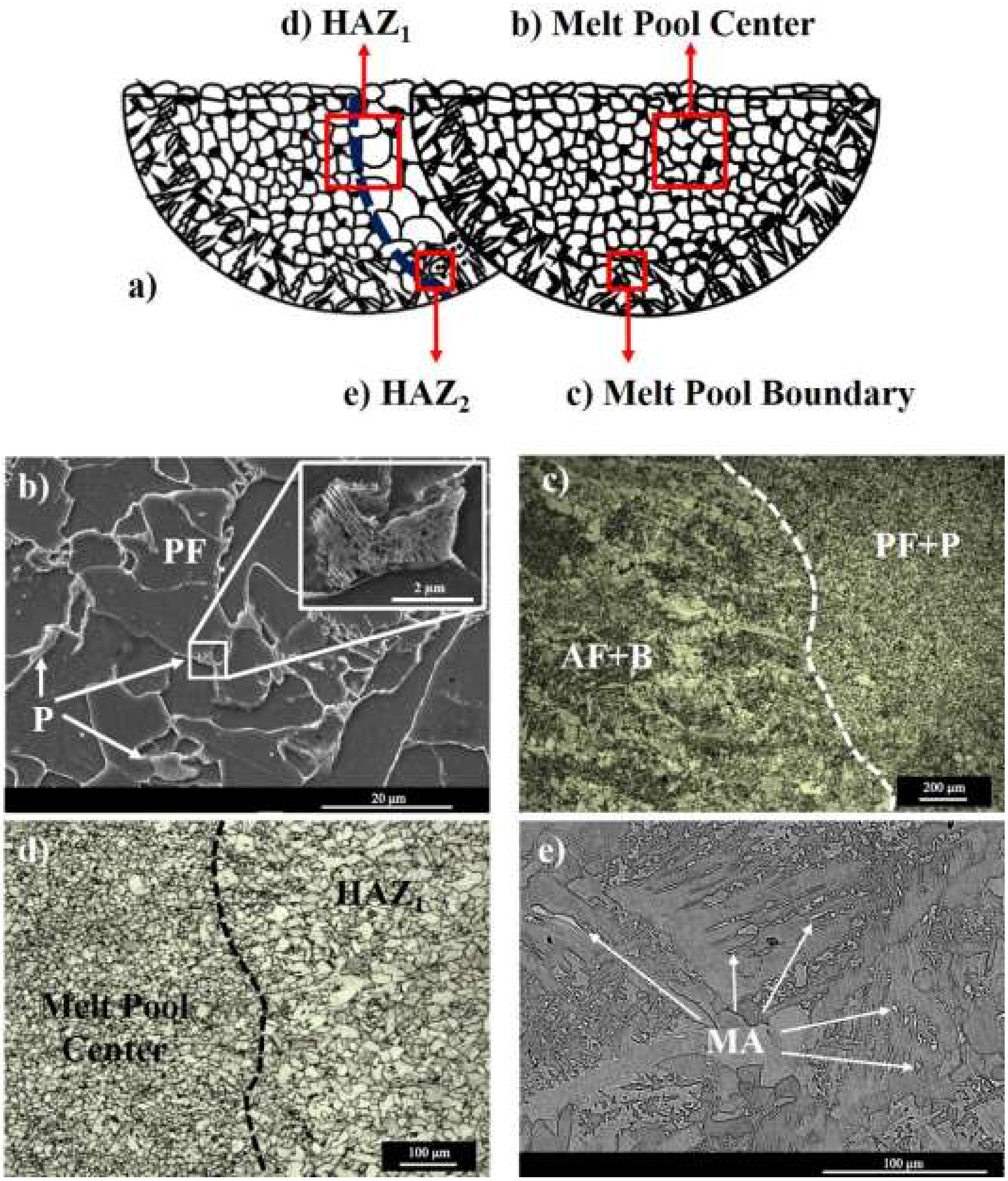

Figure I.2 a. Schematic illustration of two successive deposited beads, b. SEM image from the melt pool center, OM images from c. the fusion boundary, d. the HAZ_1, and e. SEM image from the HAZ_2.

Figure I.3 shows the engineering stress-strain curves of the as-printed part in the deposition and building directions. As clearly visible in Figure I.3, the yield and ultimate tensile strengths are approximately constant in both orientations (~ 400 MPa and ~ 500 MPa, respectively), suggesting that there is no noticeable anisotropy in the tensile strength of the WAAM fabricated part. However, the significantly higher elongation percentage of 35 ± 2% in the horizontal direction as opposed to that in the vertical direction (12 ± 3%) implies that the fabricated part is much more ductile along the deposition direction than the building direction. It should also be mentioned that no difference in mechanical properties along the building direction was observed due to the similarities of the microstructural features in all deposited layers.

To further investigate the fracture mechanism of the component in the building and deposition directions, the fractured surfaces of the samples after the tensile testing were characterized. The enclosed SEM micrographs in Figure I.3 represent the morphologies of the fractured surfaces. In the horizontal sample, the fractograph contains a large number of cuplike depressions and conical dimples without any sign of discontinuities such as lack of fusion or crack, confirming that the fracture mechanism is entirely governed by a ductile failure [232]. Contrarily, the fracture mechanism has transformed to a mixed-mode of ductile and brittle fracture in the vertical sample, since river-like cleavage facets, cracks and lack of fusions have also appeared in addition to the equiaxed dimples. The fractography analysis is consistent with the results of the uniaxial tensile testing and confirmed the anisotropic mechanical behavior of the as-printed component.

Regardless of the feedstock material, additively manufactured parts are commonly prone to such anisotropic mechanical properties, especially in ductility and toughness. Previous studies have reported this behavior in a variety of AM fabricated metals and alloys, including stainless steel [233], Ti-6Al-4V [234], tantalum [235], and steel [236]. The observed anisotropy in ductility of the WAAM fabricated low carbon low alloy steel (ER70S-6) herein can be attributed to the formation of solidification defects, such as interpass lack of fusions as a discontinuity, and two microstructural imperfections/defects, including (*i*) grain coarsening in the HAZ_1 and (*ii*) formation of localized brittle zones corresponding to the formation of brittle martensite-austenite phases in the HAZ_2.

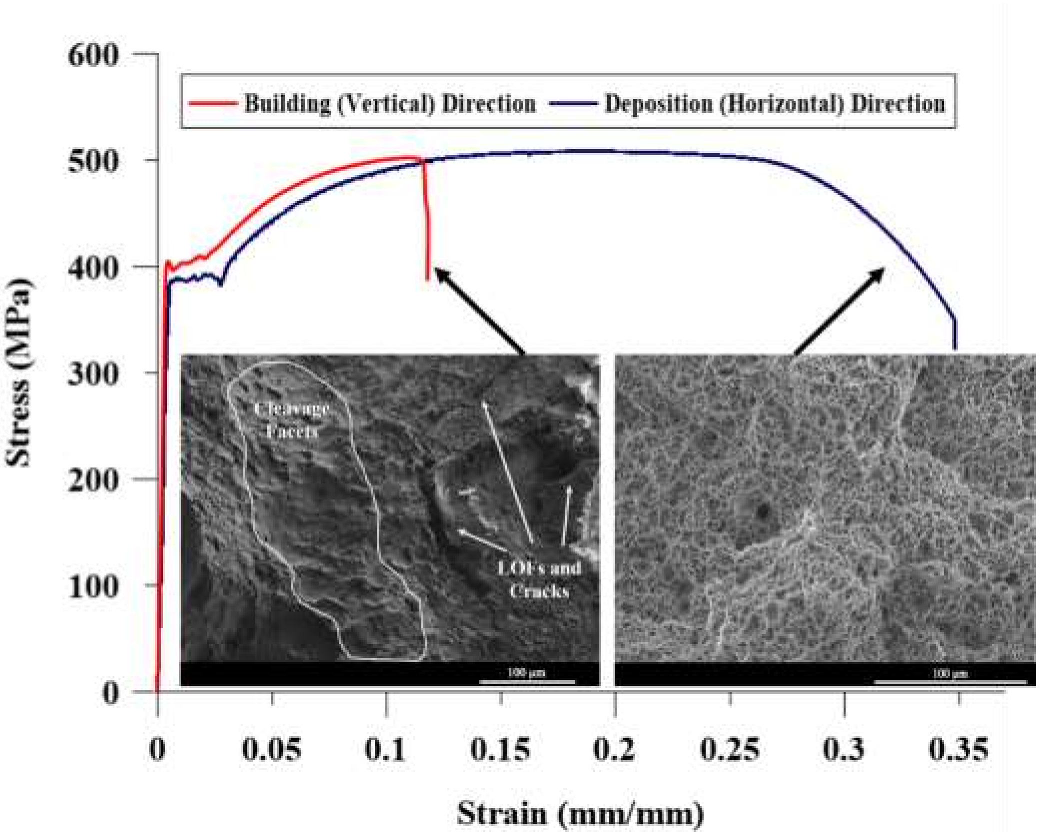

Figure I.3 The engineering stress-strain curves of the as-printed part in the deposition (horizontal) and building (vertical) directions.

Figure I.4 shows the horizontal and vertical tensile samples before and after applying uniaxial tensile loading. Equidistance solidification defects were visible on both samples prior to performing the tensile testing (depicted by the white arrows). The presence of similar defects with intervals equal to the width of each individual deposited beads indicates that these defects are lack of fusions formed along the interpass regions. Formation of internal defects, such as porosity, localized residual stress, solidification crack, and interpass lack of fusion, is always inevitable, regardless of the selected additive manufacturing process, attributed to unstable melt pool dynamics, multiple and complex thermal cycles, inferior programming strategy, non-optimized parameters setup, and environmental contaminations as a result of insufficient shielding gas [103][237]. For example, Sridharan *et al.* [238] studied the toughness scatter in a low alloy C-Mn steel component produced by wire arc additive manufacturing and reported that the high heat removal capacity from the interpass regions could lead to a higher portion of the lack of fusions within the adjacent beads.

Various non-destructive methods, such as radiographic testing (RT), liquid penetrant inspection (LPI) and ultrasonic testing (UT), have been utilized to detect the lack of fusions in additive manufactured ER70S-6 [212]. The presence of the interpass lack of fusions can potentially result in the lack of an efficient bonding between deposited layers and consequently delamination or separation of adjacent beads during tensile loading [103]. The stress concentration at the tips of a defect is the primary reason leading to the brittle fracture of a component [239]. That is why planar or linear defects with sharp tips are more dangerous than the volumetric defects with round corners [240].

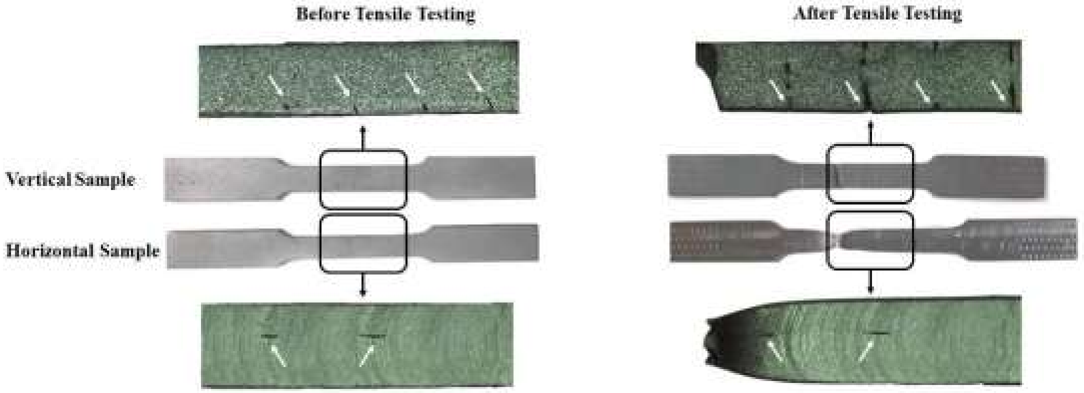

Figure I.4 The horizontal and vertical tensile samples before and after applying tensile loading showing crack propagation during the tensile testing of the vertical sample, but not the horizontal sample.

Another critical factor affecting the contribution of a discontinuity in degrading the mechanical properties is its orientation with respect to the loading direction [241]. As shown in Figure I.5, if the discontinuity's major axis is parallel to the loading direction, the minimum stress concentration will occur at the tip of the defect, while if the major axis of the lack of fusion is oriented perpendicular to the loading direction, in the neighborhood of the defect, the uniform stress field is altered and it rises sharply with its maximum value near the edge of the lack of fusion defect, causing the propagation and growth of the discontinuity [240]. The former case has happened in the horizontal sample containing longitudinal lack of fusions (Figure I.5a), and the latter scenario is associated with the vertical sample owning transverse lack of fusions (Figure I.5b). Figure I.4 also confirms that the lack of fusion defects have grown during tensile testing of the vertical sample, while there is no sign of defect propagation in the horizontal sample as a result of tensile loading. Consequently, the early stage crack propagation in the vertical sample resulted in the reduction of the test span, and accordingly the amount of strain prior to the fracture was decreased significantly.

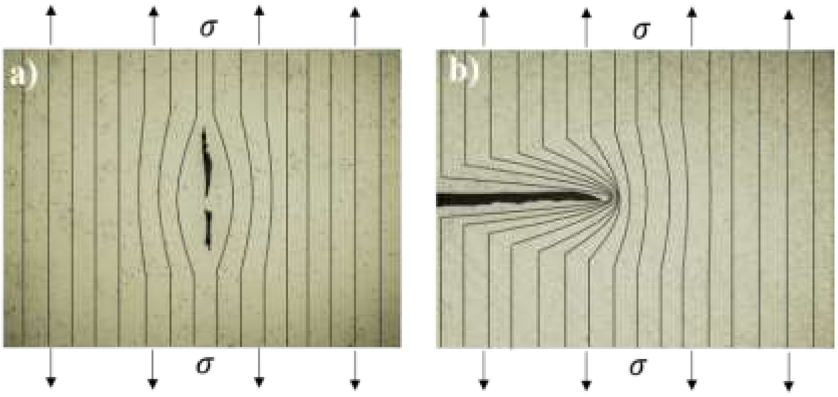

Figure I.5 The schematic illustration of the stress concentration adjacent to the lack of fusion defect in the optical micrographs of a. the longitudinal lack of fusion in the horizontal tensile sample and b. the transverse lack of fusion in the vertical tensile sample.

It should also be noted that the toughness of the material adjacent to the defect tip considerably controls the growth rate of the discontinuity. Therefore, it is crucial to particularly characterize the microstructure of both HAZ_1 and HAZ_2 at the vicinity of the interpass lack of fusions. According to Figure I.2d, the microstructure of the HAZ_1 comprised of coarser ferrite grains compared to the melt pool center. In order to obtain more accurate quantitative information about the degree of grain coarsening in the HAZ_1, an electron backscatter diffraction (EBSD) analysis was performed on an area covering the transition from the melt pool center to the HAZ_1 (shown in Figure I.6). The inverse pole figure (IPF) map in Figure I.6 shows the grain growth in the HAZ_1 with an average grain size of 15.76 ± 2.34 µm, while the melt pool center contains significantly smaller polygonal ferrite grains (4.94 ± 1.26 μm). It is well-established that the grain size is one of the major factors that control both hardness and ductility of a component [242]. Therefore, the grain coarsening in the HAZ_1 can be considered as a microstructural imperfection or defect, potentially causing a substantial softening in this region, leading to a lower localized hardness and strength [231]. Such microstructural imperfections can deteriorate the mechanical properties of the part, contributing to the anisotropy in mechanical properties, especially the ductility in the case of WAAM-ER70S-6. Furthermore, the uniform distribution of grain orientations shown in the IPF map (Figure I.6) confirmed the formation of a non-textured solidified structure in the printed ER70S-6 part.

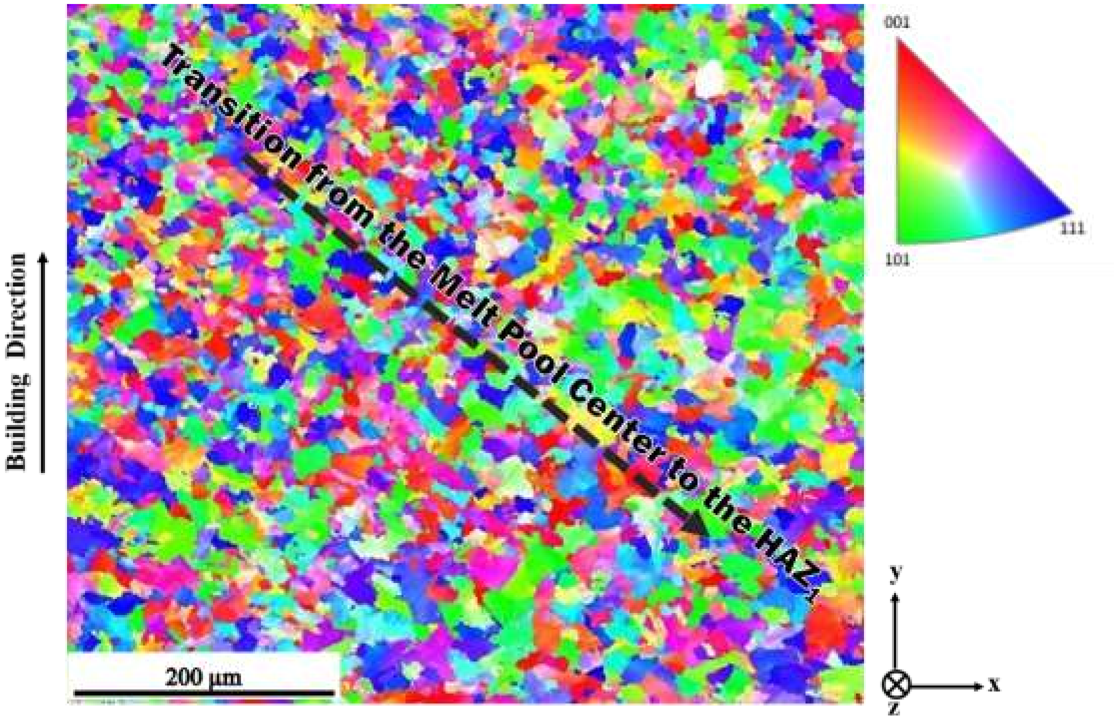

Figure I.6 EBSD inverse pole figure map of the WAAM-ER70S-6 showing the transition from the melt pool center to the HAZ_1.

Further analysis of the microstructure in the HAZ_2 (Figure I.2e) revealed the formation of a low volume fraction of martensite-austenite phase among the acicular ferrite (AF) and bainite (B) constituents. As previously reported in many studies [243][244][245][246], during fusion welding of steels, the heat affected zone is exposed to a temperature between lower (Ac_1) and upper (Ac_3) critical temperatures of the steel, where both ferrite and austenite phases co-exist. This region is called intercritical HAZ [245][246], which is precisely adjacent to the boundary of two consecutive deposited beads in the case of WAAM-ER70S-6. When the temperature of the intercritical HAZ is raised above Ac_1, the austenite phase regions nucleate and immediately become enriched from carbon since this phase with an FCC structure has the highest carbon solubility compared to the other constituents in steel. Moreover, temperature, as the dominant driving force for atom diffusion, is fairly high in the heat affected zone, facilitating the carbon enrichment of the nucleated austenite phases. It should also be noted that the nucleated austenite phases cannot become very large because the heat source is traveling fast, and the austenite grain growth will be ceased shortly. During the subsequent cooling cycle, the high heat sink effect of the previously solidified layers leads to rapid cooling of tiny austenite regions. Due to the high cooling rate associated with the process and the absence of enough austenite stabilizer alloying elements in the feedstock wire (ER70S-6), the tiny austenite constituents transform to brittle martensite-austenite phase and create some localized brittle zones.

The presence of localized brittle zones in the interlayer regions, where the interpass lack of fusions are more favored to form, will cause a dramatic drop in the toughness of the material in the neighborhood of the defect, provoking its growth. In addition to the brittle nature of martensite-austenite phase [247], the induced residual tensile stresses on the matrix as a result of the martensite formation, the incoherency between the martensite-austenite phase and the ferrite matrix [238], and its considerable microhardness difference from the matrix [244] can further contribute to the reduced toughness of the intercritical HAZ . Hence, the presence of localized brittle zones containing martensite-austenite phases in the HAZ_2 is considered as another microstructural imperfection, which can deteriorate the mechanical properties of the as-printed low carbon low alloy steel part. Since the density of the interpass regions is much higher in the vertical direction compared to the horizontal direction, the detrimental impact of the localized brittle zones mostly contributed to the reduction of ductility in the vertical samples.

Although the formation of lack of fusions can be minimized through optimizing process parameters and possibly scanning strategy, it is known that fabricating a flawless component utilizing welding based processes free from defects and discontinuities is practically impossible. Therefore, another approach to improve the ductility and also to minimize the anisotropic mechanical behavior of the 3D-printed component is to modify the inhomogeneous microstructure and improve the toughness of the material at the periphery of the existing defects to postpone their growth.

Among various heat treatment cycles, normalizing heat treatment is capable of homogenizing the microstructure by heating the sample up to a temperature above the upper critical line of the Fe-Fe_3C binary phase diagram; which is above Ac_3 for hypoeutectoid steels and above Ac_m for hypereutectoid steels followed by cooling in still or slightly agitated air [248]. Notably, the Ac_3 temperature of the feedstock material (ER70S-6) was predicted to be at 883.6 °C. To calculate the austenite formation temperature (Ac_3) for this alloy, the empirical equation (1), proposed by Andrews [249] for low alloy steels with less than 0.6 wt.% C, was used.

$$Ac_3(°C) = 910 - 230(C)^{0.5}Mn - 15.2Ni + 44.7Si + 104V + 31.5Mo + 13.1W \quad \text{(AI.1)}$$

Hence, the as-printed samples were normalized at 900 °C (above Ac_3) for 1 h, followed by still-air cooling. Figure I.7 depicts the microstructure of the normalized WAAM-ER70S-6 at different magnifications. The low magnification OM micrograph (Figure I.7a) confirms that the inherent microstructural inhomogeneities of the as-printed sample have been completely eliminated through the normalizing heat treatment since neither a microstructural transition from a fine to a coarse grain structure nor the formation of non-equilibrium acicular ferrite and bainite constituents were detected in the microstructure. Therefore, it is deduced that the microstructural imperfections/defects, *i.e.*, grain coarsening in the HAZ_1 and the martensite-austenite phase formation (localized brittle zones) in the HAZ_2, were entirely annihilated as a result of normalizing heat treatment.

The higher magnification SEM micrograph (Figure I.7b) indicates that the microstructure of the component after normalizing heat treatment consisted of polygonal ferrite grains as the primary phase containing a low volume fraction of lamellar pearlite formed at the grain boundaries. At the initial austenitizing step, once the sample is heated to above Ac_3 temperature, all the pre-existing phases, including ferrite, cementite, and martensite-austenite, start to transform to the austenite, and holding time of 1 h at austenite stability region provides sufficient time for a complete transformation of the entire microstructure to homogenous and uniform austenite grains in all regions. Afterward, the relatively slow cooling of the sample in still-air hinders the formation of non-equilibrium martensite, bainite, or acicular ferrite phases, leading to the formation of a ferritic and lamellar pearlitic structure.

Although the microstructure of the normalized sample was similar to the melt pool centers of the as-printed sample, the grain size distribution became more homogeneous after normalizing with a relatively uniform grain size of 10.44 ± 0.97 µm. Similarly, Natividad *et al*. [250] reported that normalizing heat treatment on Grade X70 pipeline steel with an analogous chemical composition to ER70S-6 resulted in the formation of a homogenous ferritic-pearlitic microstructure, depicting a more uniform grain size as compared to the as-received material.

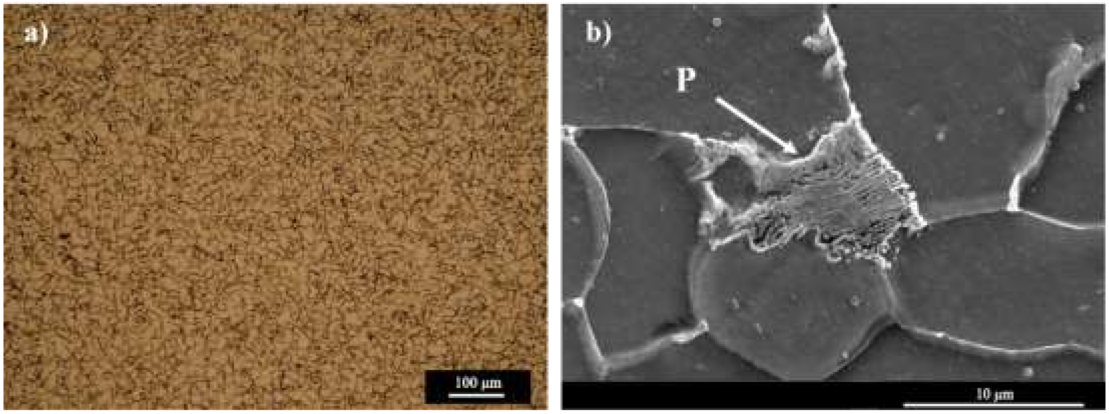

Figure I.7 a. Low magnification OM and b. high magnification SEM micrographs taken from the normalized sample.

Microhardness measurements revealed a large fluctuation of the hardness values in a range of 150 HV to 175 HV in the as-printed component with an average of 160 ± 7 HV compared with 154 ± 1 HV for the average microhardness of the normalized sample. The high variance of the microhardness in the as-printed sample can be associated with the microstructural variations from the melt pool center to its boundaries, and to the heat affected zones. Albeit the average microhardness of the normalized sample has been decreased to 154 ± 1 HV, the fluctuation in the microhardness values was significantly lower in the normalized sample due to the homogeneity of the microstructure. The slight drop in the microhardness of the normalized sample can be ascribed to (*i*) the slight grain growth, (*ii*) elimination of the AF and B phases from the fusion boundaries, and also dissolving the hard and brittle martensite-austenite phases in the HAZ_2, along with (*iii*) the release of the residual stresses from the as-printed sample, and (*iv*) reduction of lattice defects generated during the WAAM [251]. It is worth noting that the average microhardness value was the same along the building direction in both as-printed and heat treated samples.

Figure I.8 compares the results of tensile testing of the as-printed and heat-treated WAAM-ER70S-6 in both horizontal and vertical directions. The reduced microhardness of the normalized sample was found to be accompanied by a slightly lower tensile strength (~ 465 MPa) as compared to the as-printed sample with ~ 500 MPa tensile strength. On the other hand, as a contribution from the normalizing heat treatment, the significant difference between the ductility of the horizontal and vertical samples in the as-printed component (23% in elongation) was reduced to a relatively negligible amount of 5%. Accordingly, the microstructural modifications resulted from applying the post-printing normalizing heat treatment of WAAM-ER70S-6, transformed the microstructure of the material in the neighborhood of the existing cracks from either a coarse ferritic structure in HAZ_1 or localized brittle zones containing martensite-austenite constituents in HAZ_2 into a tougher and more homogenized structure of ferrite and pearlite, and potentially reduced the discontinuities' growth rate. Consequently, the anisotropy in the ductility of the as-printed component was successfully minimized through the normalizing heat treatment.

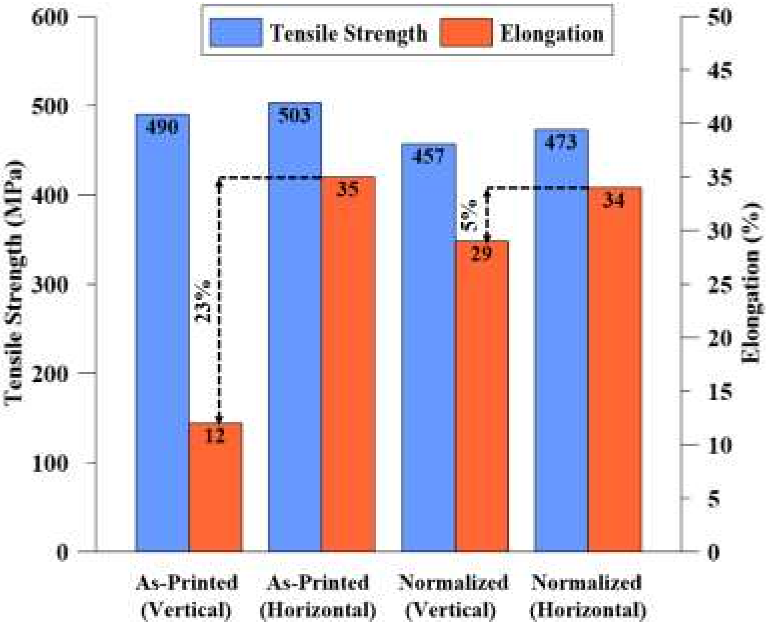

Figure I.8 The results of tensile testing of the as-printed and heat-treated WAAM-ER70S-6 in both horizontal and vertical directions.

AI.5 CONCLUSIONS

In this study, the effects of solidification defects, including interpass lack of fusions and microstructural imperfections, on the anisotropic mechanical properties of a wire arc additively manufactured low carbon low alloy steel (ER70S-6) wall have been investigated. The findings from the microstructure and mechanical properties analysis of the fabricated part led to the following conclusions:

1. The complex thermal cycle associated with the WAAM process contributed to the microstructural imperfections and inhomogeneity, such as grain coarsening in the HAZ, formation of non-equilibrium constituents in the vicinity of the melt pool boundaries along with the formation of localized brittle zones containing brittle martensite-austenite phases in the intercritical HAZ.
2. The tensile strength of the as-printed component was found to be isotropic along the building and deposition directions, whereas the ductility of fabricated samples

revealed a significant anisotropic property, showing three times higher ductility along the deposition direction (horizontal) than that along the building direction (vertical).

3. The fracture surface of the horizontal samples revealed the formation of a large number of dimples, confirming a ductile failure behavior, while the vertical samples showed a mixed-mode of ductile and brittle fracture due to the co-existence of river-like cleavage facets, lack of fusions, cracks, and a limited number of dimples on its fracture surface.
4. The observed anisotropic mechanical properties were ascribed to the presence of solidification defects, including interpass lack of fusions as a discontinuity and microstructural defects, such as brittle martensite-austenite phases, which leads to the formation of localized brittle zones, and grain coarsening in the heat affected zones. The detrimental effects of the solidification defects mostly contributed to the reduction of ductility in the vertical samples since the density of the interpass regions is much higher in the vertical direction compared to the horizontal direction.
5. Normalizing heat treatment was found to be effective in minimizing the anisotropic ductility of the WAAM-ER70S part through modifying the microstructure of the component by eliminating the formation of localized brittle zones and grain growth in the heat affected zones, consequently leading to a homogenized microstructure from the melt pool centers towards the melt pool boundaries and the heat affected zones.

Acknowledgments

The authors gratefully acknowledge the support of Natural Sciences and Engineering Research Council of Canada (NSERC) [grant number RGPIN-2017-04368] for sponsoring this work.

APPENDIX AII INTERFACIAL BONDING BETWEEN A WIRE ARC ADDITIVE MANUFACTURED 420 MARTENSITIC STAINLESS STEEL PART AND ITS WROUGHT BASE PLATE

Mahya Ghaffari[1], Alireza Vahedi Nemani[2], Ali Nasiri[3]

1- Graduate Student, Dalhousie University, Halifax, Nova Scotia, Canada
2- Post-Doctoral Fellow, Dalhousie University, Halifax, Nova Scotia, Canada
3- Assistant Professor, Dalhousie University, Halifax, Nova Scotia, Canada

Status: Published Journal Paper, Journal of Materials Chemistry and Physics (IF= 4.778), Volume 251, Page 123199.

Authors' Contribution

Mahya Ghaffari: Conceptualization, Fabrication Process, Investigation, Writing - original draft.

Alireza Vahedi Nemani: Methodology, Validation, Investigation, Writing - review & editing.

Ali Nasiri: Supervision, Writing - review & editing, Funding acquisition.

AII.1 ABSTRACT

This study investigates the interfacial microstructure and mechanical properties of the joint between a wire arc additive manufactured 420 stainless steel part and its AISI420 wrought base plate. The results revealed a defect-free metallurgical bonding possessing a desired microstructure with better mechanical performance as compared to the substrate.

AII.2 INTRODUCTION

Different from various subtractive production technologies, such as casting and machining, in additive manufacturing (AM) material is deposited in a layer-by-layer fashion until a near-net-shape component is fabricated [104][252]. One of the momentous applications of additive manufacturing is repairing and remanufacturing of the materials being subjected to in-service damages [253][254]. This application leads to expanding the service life of the part by restoring the component to its original shape instead of replacing it with a new part [255]. When additive manufacturing is being utilized as an effective repair procedure for a damaged functional component, the metallurgical bonding between the substrate and deposited layers would be of great importance.

AISI420 martensitic stainless steel (MSS) is widely used in plastic molds and dies [256]. It has been reported that the life cycle of dies and molds are usually shorter than their anticipated lifetime due to the occurrence of different in-service defects, including dents, digging, plastic deformation, crack, and edge deterioration [255][257]. Therefore, the costs associated with their replacement can be eliminated by repairing them to a workable condition [257]. Although additive manufacturing of martensitic stainless steels has been reported in different studies [49][144][256][258], investigation on the metallurgical bonding between the wrought MSS base plate (representing the defected part) and the AM deposited layers (the remanufactured portion) is still lacking in the literature, which is covered in the current study.

AII.3 EXPERIMENTAL PROCEDURE

In this experiment, ER420 MSS solid wire was employed to fabricate a single-pass thin-wall-shape component on the AISI420 stainless steel substrate via wire arc additive manufacturing (WAAM). The chemical compositions (wt. %) of both the feedstock wire and the base plate contain of 0.3-0.4% C, 12-14% Cr, less than 1% of other alloying elements, and Fe balanced. A GMAW torch with a surface tension transfer (STT) mode as the heat source was mounted on a six-axis robot in order to provide the degrees of freedom following the deposition pattern. The wall was deposited using the following parameters: arc voltage of 29 V, arc current of 135 A, traveling speed of 3.6 mm/s, wire feed speed of 67.7 mm/s, and pure argon as the shielding gas with the flow rate of 20 L/min. Microstructural details of the sample were characterized using optical microscopy (OM) and scanning electron microscope (SEM) equipped with an electron backscatter diffraction (EBSD) detector and also energy dispersive spectrometer (EDS). In addition, a Buehler Micromet hardness test machine with a load of 300 g and an Instron load frame equipped with an extensometer and a cross-head speed of 1 mm/min were utilized to measure the mechanical properties across the base plate-WAAM fabricated wall interface. The tensile test specimens with dimensions of 100 mm total length, 25 mm gauge length, 5 mm thickness, and 5 mm width were prepared according to ASTM E8m-04 [259]. It is notable that both hardness and tensile tests were repeated at least five times for reproducibility.

AII.4 RESULTS AND DISCUSSION

AII.4.1 Microstructural Characterizations

Figure II.1a depicts the locations of the tensile specimens and the metallographic sample prepared from the substrate-WAAM part interface (the enclosed area in Figure II.1a), and Figure II.1b shows a low-magnification OM image from the metallurgical bonding between the AISI420 steel base plate and the first layer of the WAAM 420 MSS wall. According to the Fe-13Cr pseudo-binary phase diagram of AISI420 alloy [260] (Figure II.1c), five distinct microstructural regions, including (*i*) base metal, (*ii*) far heat affected zone (HAZ), (*iii*) close HAZ, (*iv*) partially melted zone (PMZ), and (*v*) fusion zone, can be identified based on the peak temperatures experienced by each region during the fabrication process. The EBSD inverse pole figure (IPF) map of the base metal (Figure II.2a) illustrates that the material mainly composed of randomly oriented equiaxed (aspect ratio < 3) Iron-BCC (ferrite) grains with an average grain size of 6.87 ± 3.83 µm as the matrix containing a relatively large amount of tiny (~ 0.5 µm) carbide particles (Figure II.2c), which is the typical microstructure of annealed AISI420 stainless steel plate [261]. The obtained pole figures (PFs) from the EBSD data (Figure II.2b) also revealed a weak texture in the base metal, representing a random texture with a maximum intensity of 2.19 above the random background. As reported in previous studies [261][262], the formed carbides in this alloy are primarily $M_{23}C_6$ and M_7C_3 phases. Based on the EDS elemental maps (Figure II.2d-f), the carbides are enriched by Cr and C and depleted of Fe, confirming the presence of chromium carbides in the substrate.

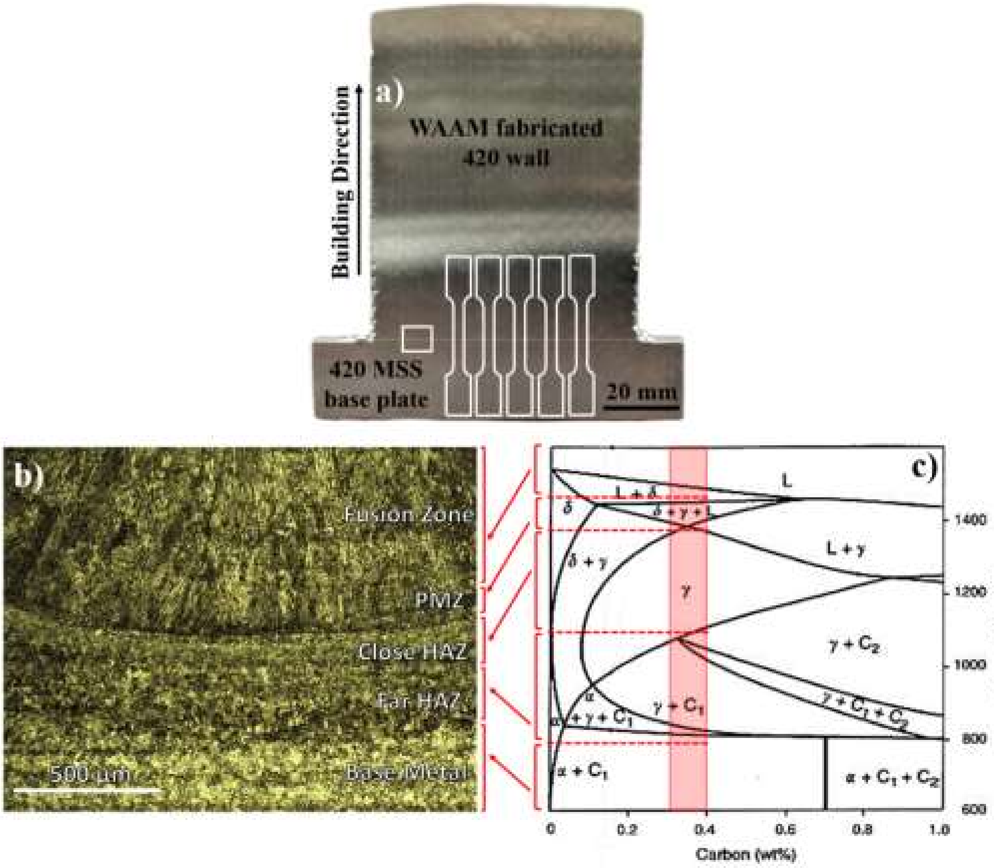

Figure II.1 (a) The WAAM fabricated 420 MSS wall, (b) low-magnification OM image from the 420 MSS base plate-WAAM fabricated portion interface, and (c) Fe-13Cr pseudo-binary phase diagram of AISI420 alloy (modified from [260]).

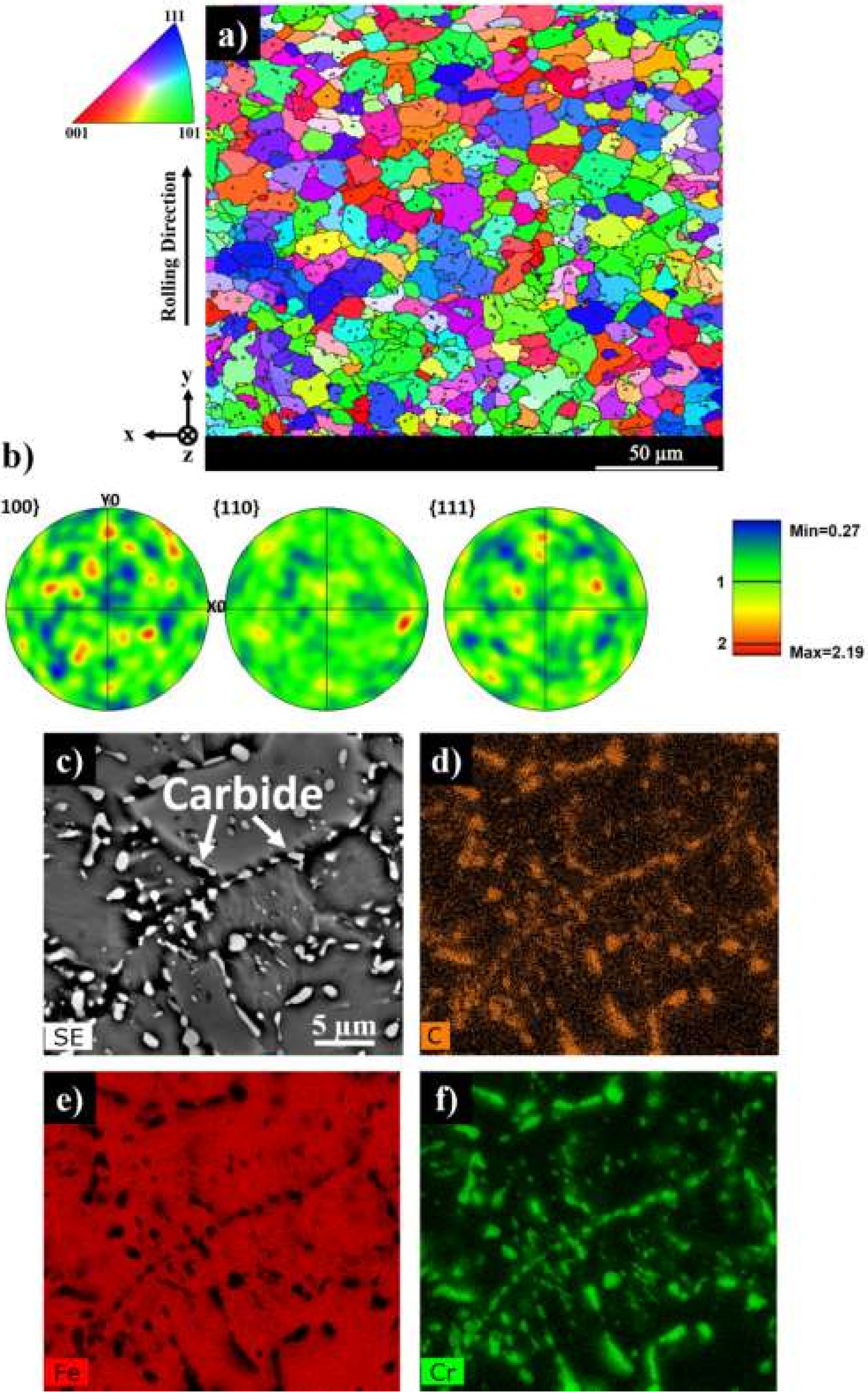

Figure II.2 (a) The EBSD-IPF map, (b) PFs, (c) SEM image, and (d-f) EDS elemental (C, Fe, Cr) maps of the 420 MSS base metal.

Figure II.3a shows the SEM image from the microstructural features formed in the entire HAZ, which can be divided into two main subzones, *i.e.* the region close to the fusion zone (close HAZ) and the region far from the fusion zone (far HAZ). According to the phase diagram (Figure II.1c), during the fabrication process, the close HAZ undergoes a temperature increase up to the austenite phase field (~ 1100-1350 °C) (Figure II.3b), followed by martensitic (M) transformation in the matrix during the cooling cycle. On the other hand, the far HAZ (Figure II.3c) still consists of a ferritic (F) matrix including carbide particles, resulted from the occurrence of zero to partial transformation of this region to austenite due to the lower temperature (~ 800-1000 °C) experienced by this region. The experienced high temperature associated with the deposition of the first layer has stimulated the precipitation of carbides in the HAZ, leading to a higher volume fraction of carbides in this region. Hao *et al.* [263] reported the formation of carbides by both the precipitation mechanism and the presence of undissolved particles in the HAZ during fast heating and cooling cycles. The pre-existing carbides remain undissolved in the HAZ since this zone stays at the elevated temperature just for a limited time, mitigating the full dissolution of the carbides into the austenite. In addition, according to the thermodynamic calculations developed by Hao *et al.* [263], M_7C_3 carbide initially precipitates at 1168 °C, and then $M_{23}C_6$ phase forms at 983 °C during the cooling cycle from the austenite. The M_7C_3 phase is considered as a meta-stable phase, which starts dissolving during the cooling cycle, providing the conditions for the precipitation of $M_{23}C_6$ as a stable phase at room temperature [264]. It should be noted that the presence of M_7C_3 as a meta-stable phase at room temperature is mostly due to the fast cooling rate in the HAZ, limiting the atomic diffusion and dissolution rate of M_7C_3 phase. It has been also reported [261][265] that the volume fraction of carbides increases in the HAZ not only by precipitation of new particles, but also by coarsening of $M_{23}C_6$ carbides at elevated temperatures. According to Figure II.3a, carbides were formed both along the grain boundaries (inter-granular) and inside the grains (intra-granular). Hao *et al.* [263] measured the carbon content of inter- and intra-granular carbides and showed that the inter-granular carbides are always $M_{23}C_6$; however, the intra-granular carbides can be either $M_{23}C_6$ or M_7C_3.

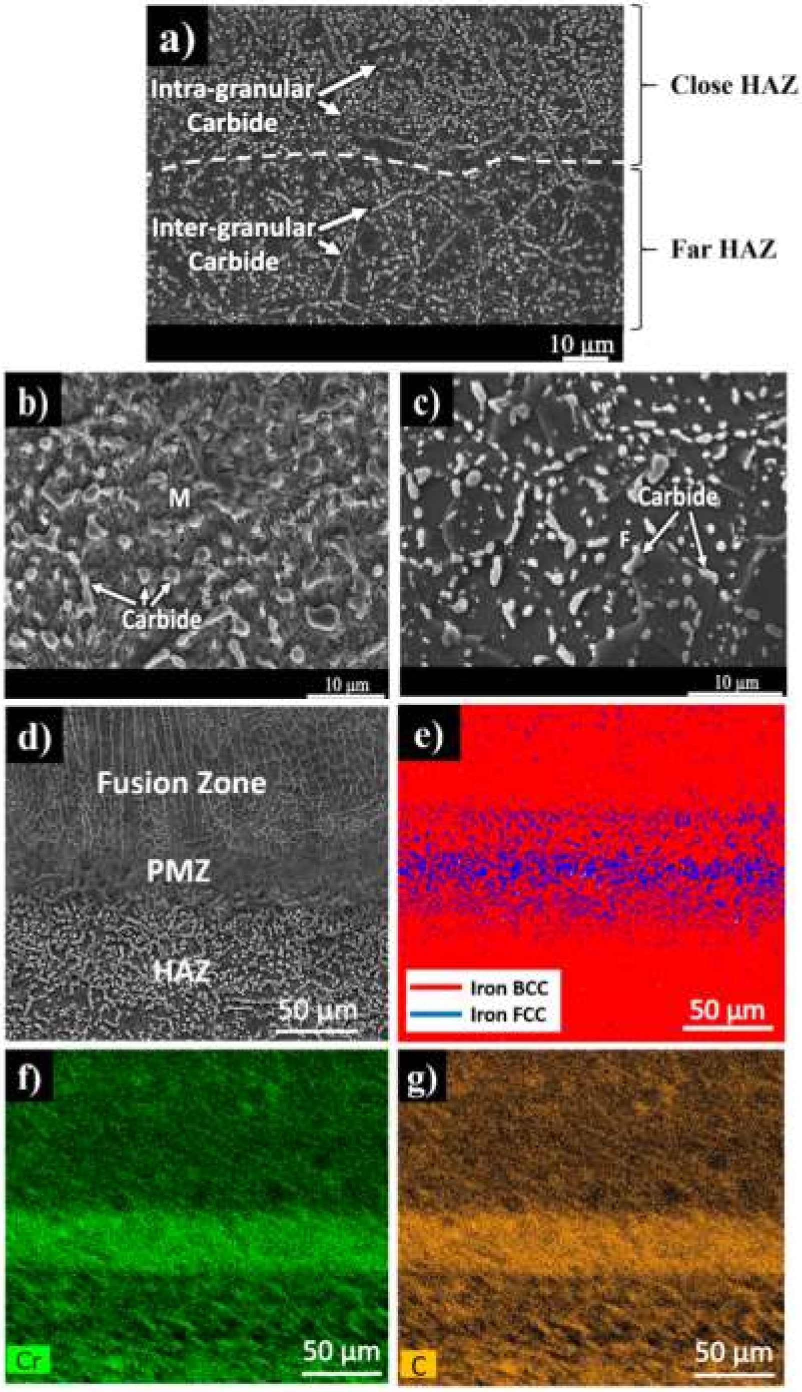

Figure II.3 SEM images from the microstructure of (a) the entire HAZ, (b) close HAZ, (c) far HAZ, and (d) transition from the HAZ to the fusion zone, (e) the EBSD phase map, and (f-g) the EDS elemental maps of Cr and C taken from the 420 MSS base plate-WAAM fabricated wall interface.

It is worth noting that the higher volume fraction of the formed inter-granular carbides versus the intra-granular ones is correlated to the accelerated diffusion rate of Cr and C along the grain boundaries as compared to their bulk diffusivity [266]. It is also interesting to mention that the formation of inter-granular carbides can potentially improve the toughness of the HAZ by preventing grain growth in this region through Zener pinning effect on the grain boundaries [267]. On the other hand, the dislocations plugging and stress concentration at the interface of the carbide and grain boundary can potentially increase the possibility of inter-granular crack initiation, and consequently deteriorate the mechanical properties of the HAZ [263]. The mechanical properties results, which clarify the effect of the precipitated carbides in the HAZ, will be discussed in the following section.

A closer look at the transition from the HAZ to the first layer of the wall (see Figure II.3d) reveals a narrow partially melted zone (PMZ), where the temperature has been increased to ~ 1350-1450 °C, reaching to the stability region of δ, γ, and L phases according to the phase diagram (Figure II.1c). One of the major microstructural features differentiating PMZ from the HAZ is the complete dissolution of the carbide particles in the PMZ due to the higher temperature experienced by this region. Moreover, the EBSD phase map (Figure II.3e) revealed the formation of a phase with FCC crystal structure having a high volume fraction in the PMZ, confirming the formation of retained austenite in this region. The EDS elemental maps (Figure II.3f and g) indicate that the dissolution of carbides in the PMZ contributed to the increased concentration of chromium and carbon in this region. According to the equation that predicts martensite start (M_s) temperature [260], an increase in the carbon and chromium concentrations decreases M_s temperature, promoting the stability of retained austenite at room temperature. It is known that the formation of retained austenite in a martensitic microstructure improves the mechanical properties of the material by increasing the toughness and ductility at the expense of a relatively slight reduction in the hardness and strength [268]. It is also worth noting that no solidification defects, such as cracks, lack of fusions, or porosities, were detected along the interface between the substrate and the first WAAM deposited layer.

Figure II.4a illustrates the SEM micrograph of the fusion zone showing a columnar dendritic structure expanded along the deposition direction parallel to the heat dissipation direction during the solidification. The solidification of the fusion zone starts with the formation of δ-ferrite phase, followed by an isothermal Peritectic reaction at ~ 1450 °C, resulting in the formation of austenite. However, the rapid cooling associated with the WAAM leads to a non-equilibrium phase transformation condition, and consequently, the austenite phase transforms to the martensite in the matrix. It should be mentioned that the formation of austenite from delta ferrite is a diffusion-controlled phase transformation and its completion is strongly time-dependant, which was not provided during the fast solidification of the fusion zone herein. Moreover, as shown by the EDS elemental map, segregation of Cr as a ferrite stabilizer alloying element has led to the stability of delta ferrite in the inter-dendritic regions (see Figure II.4b and c). Therefore, the final microstructure of the WAAM fabricated 420 MSS wall comprised of inter-dendritic δ-ferrite phase formed in a martensitic matrix.

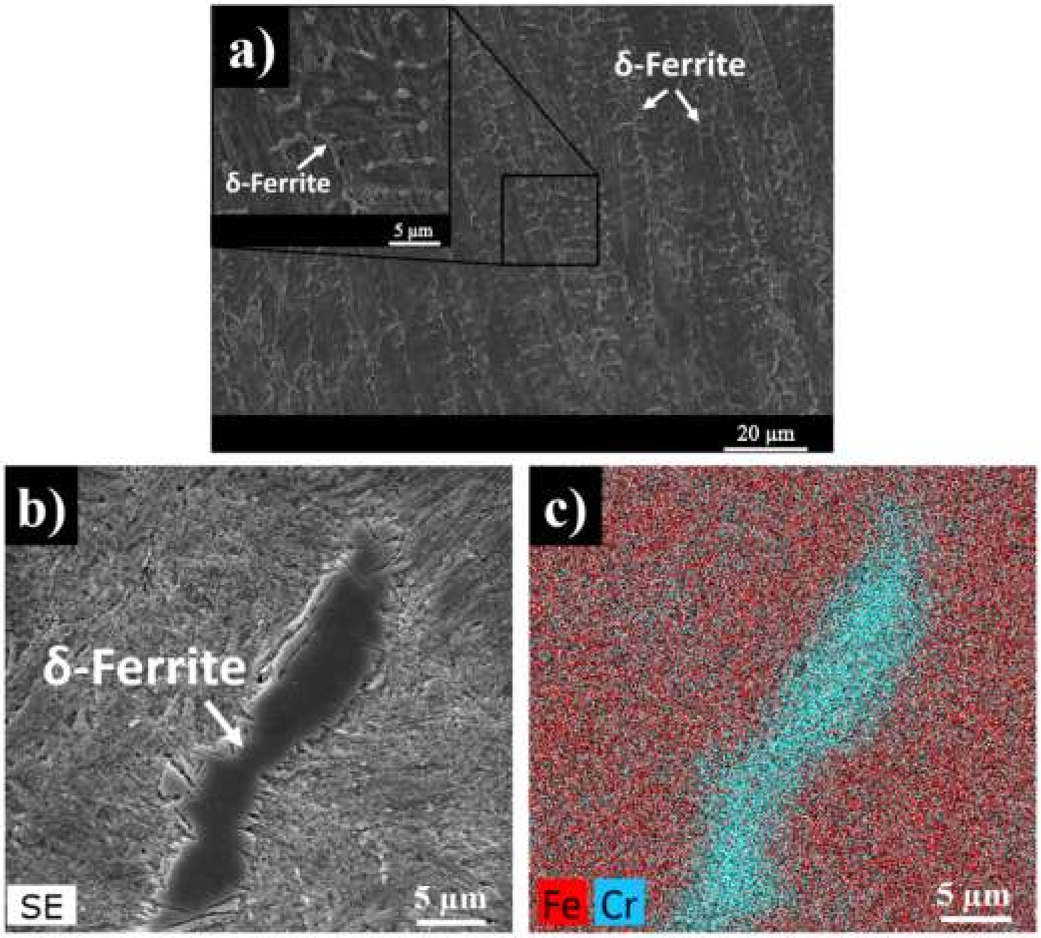

Figure II.4 (a) Low-magnification SEM image of the fusion zone, (b) high-magnification SEM image showing the δ-ferrite in the fusion zone, and (c) EDS elemental map of Fe and Cr.

AII.4.2 Mechanical Properties

Figure II.5a illustrates the microhardness profile from the base metal through the fusion zone (first layer) of the WAAM fabricated wall. The lowest microhardness (~ 190 ± 2 HV) corresponded to the base metal with a microstructure containing carbide particles embedded in a ferritic matrix. The relative increase in the volume fraction of carbide particles in the far HAZ resulted in a higher average microhardness (~ 240 ± 2 HV). The close HAZ showed a significantly higher microhardness (~ 350 ± 3 HV) as compared to the far HAZ, attributed to the formation of the martensitic matrix in this region. The microhardness value abruptly dropped to ~ 280 ± 2 HV in the PMZ due to the formation of localized retained austenite in this region. The fusion zone was characterized by the maximum microhardness value (~ 550 ± 3 HV) ascribed to its hard martensitic matrix.

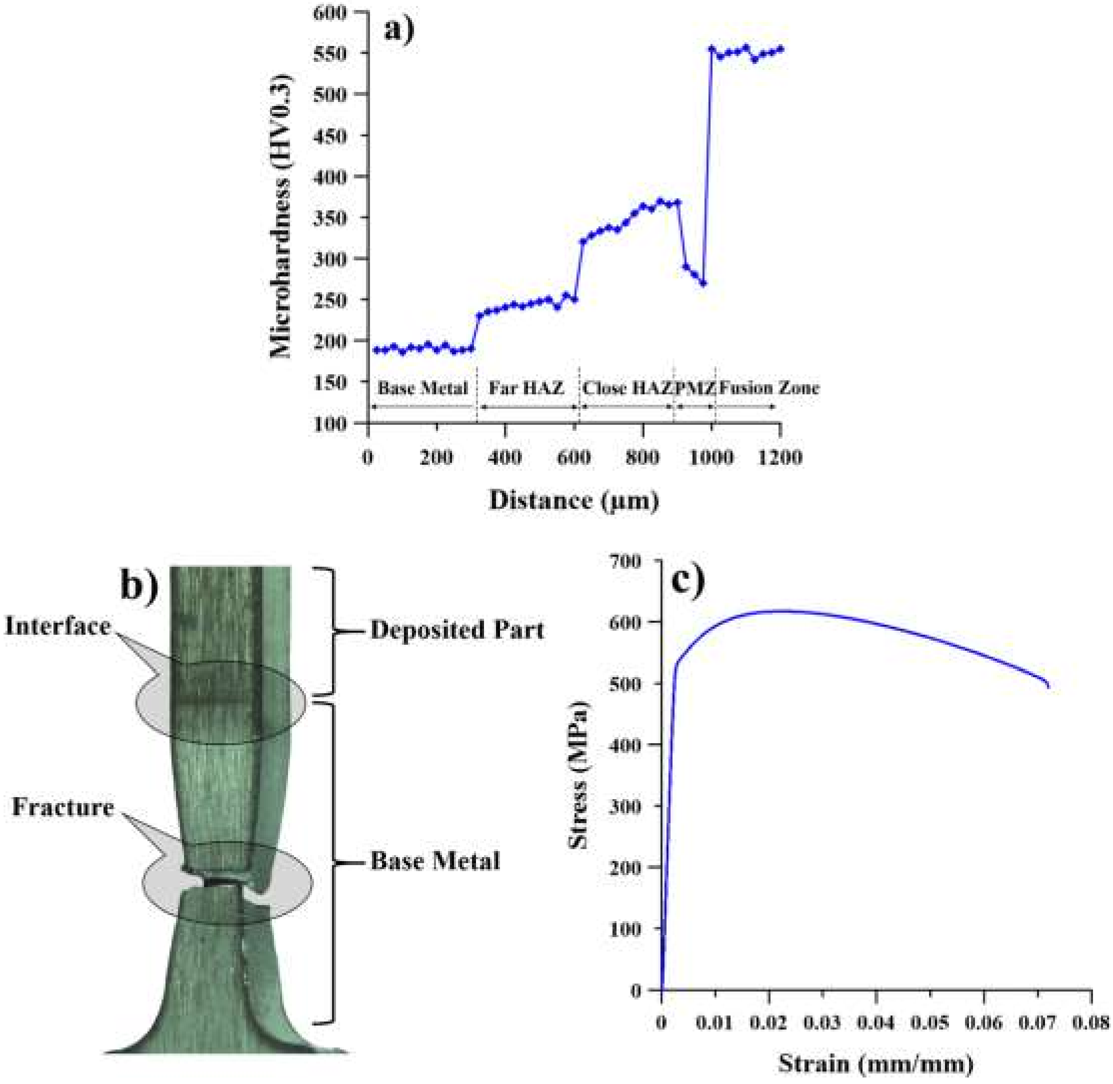

Figure II.5 (a) Microhardness profile across the 420 MSS base plate-WAAM fabricated part interface covering the base metal, HAZs, PMZ, and fusion zone, (b) the fracture location of the tensile sample, and (c) the stress-strain curve obtained from the uniaxial tensile testing.

To further study the impact of the observed microstructural variations on the mechanical properties across the base plate-WAAM fabricated part interface, the tensile test coupons, prepared perpendicular to the interface (shown in Figure II.1a), were polished and etched before the tensile test to illustrate the location of the fracture during uniaxial tensile loading. Figure II.5b shows that the fracture occurred in the base metal far from the HAZ, confirming 100% joint efficiency between the 420 MSS base plate and its WAAM fabricated counterpart. Therefore, the precipitation of extra carbides in the HAZ and the formation of retained austenite in the PMZ were not found effective in deterioration of the mechanical integrity of the formed interface. The measured tensile properties across the interface of the fabricated sample were found to be a yield strength of 520 ± 12 MPa, an ultimate tensile strength of 618 ± 10 MPa, a uniform elongation of 2.4 ± 0.05 %, and a total elongation of 7.2 ± 0.1 % (Figure II.5c).

AII.5 CONCLUSIONS

This study confirmed the formation of a defect-free metallurgical bonding between an AISI420 martensitic stainless steel substrate and its wire arc additive manufactured counterpart using ER420 MSS feedstock wire. The substrate contained carbide particles embedded in a ferritic matrix. The volume fraction of these carbides was found to increase in the HAZ adjacent to the first WAAM deposited layer, ascribed to the high temperature experienced during the fabrication process. A narrow partially melted zone was also revealed between the HAZ and the fusion zone containing a high volume fraction of retained austenite. The fusion zone experienced a columnar dendritic solidification with a microstructure comprised of inter-dendritic δ-ferrite phase in a martensitic matrix. The results of mechanical testing confirmed the formation of strong metallurgical bonding between the deposited part and the substrate with mechanical properties, *i.e*. microhardness and strength, superior to the base plate.

Acknowledgments

The authors would like to thank the support of the Natural Sciences and Engineering Research Council of Canada (NSERC) [grant number RGPIN-2017-04368] and the Memorial University of Newfoundland for sponsoring this work.

APPENDIX B COPYRIGHT PERMISSION

Elsevier Release (Chapter 2)

Microstructure and mechanical behavior of PH 13–8Mo martensitic stainless steel fabricated by wire arc additive manufacturing

Author: Mahya Ghaffari,Alireza Vahedi Nemani,Ali Nasiri

Publication: Additive Manufacturing

Publisher: Elsevier

Date: January 2022

© 2021 Elsevier B.V. All rights reserved.

Journal Author Rights

Please note that, as the author of this Elsevier article, you retain the right to include it in a thesis or dissertation, provided it is not published commercially. Permission is not required, but please ensure that you reference the journal as the original source. For more information on this and on your other retained rights, please visit: https://www.elsevier.com/about/our-business/policies/copyright#Author-rights

Elsevier Release (Chapter 3)

Microstructural evolution and mechanical performance after precipitation hardening of PH 13-8Mo martensitic stainless steel fabricated by wire arc additive manufacturing

Author: Mahya Ghaffari,Alireza Vahedi Nemani,Ali Nasiri

Publication: Materialia

Publisher: Elsevier

Date: August 2022

© 2022 Acta Materialia Inc. Published by Elsevier B.V. All rights reserved.

Journal Author Rights

Please note that, as the author of this Elsevier article, you retain the right to include it in a thesis or dissertation, provided it is not published commercially. Permission is not required, but please ensure that you reference the journal as the original source. For more information on this and on your other retained rights, please visit: https://www.elsevier.com/about/our-business/policies/copyright#Author-rights

Elsevier Release (Appendix AII)

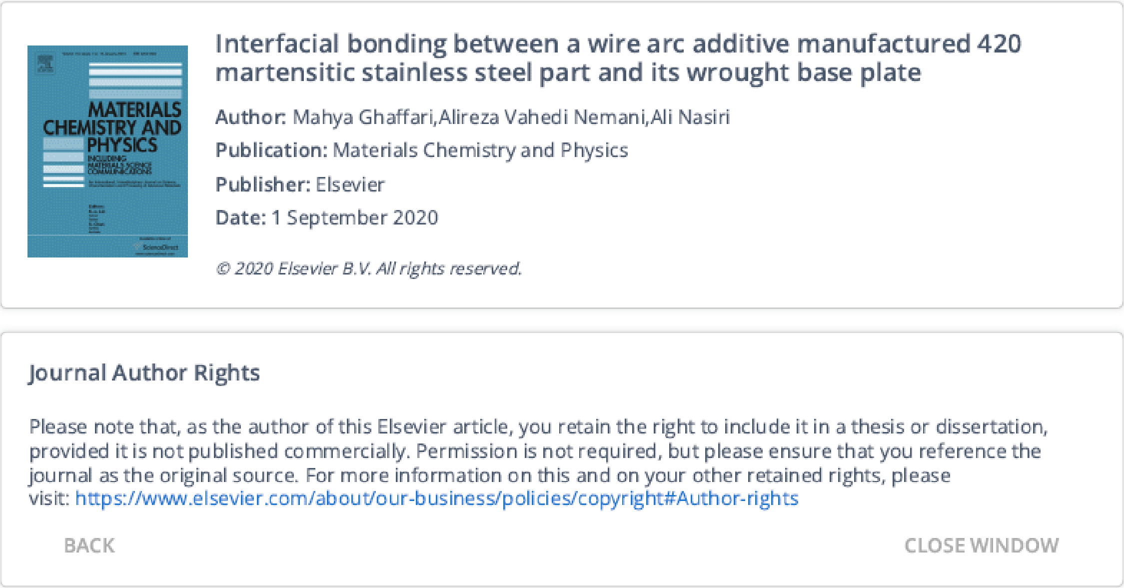

Interfacial bonding between a wire arc additive manufactured 420 martensitic stainless steel part and its wrought base plate

Author: Mahya Ghaffari,Alireza Vahedi Nemani,Ali Nasiri

Publication: Materials Chemistry and Physics

Publisher: Elsevier

Date: 1 September 2020

© 2020 Elsevier B.V. All rights reserved.

Journal Author Rights

Please note that, as the author of this Elsevier article, you retain the right to include it in a thesis or dissertation, provided it is not published commercially. Permission is not required, but please ensure that you reference the journal as the original source. For more information on this and on your other retained rights, please visit: https://www.elsevier.com/about/our-business/policies/copyright#Author-rights

Springer Nature Release (Appendix AI)

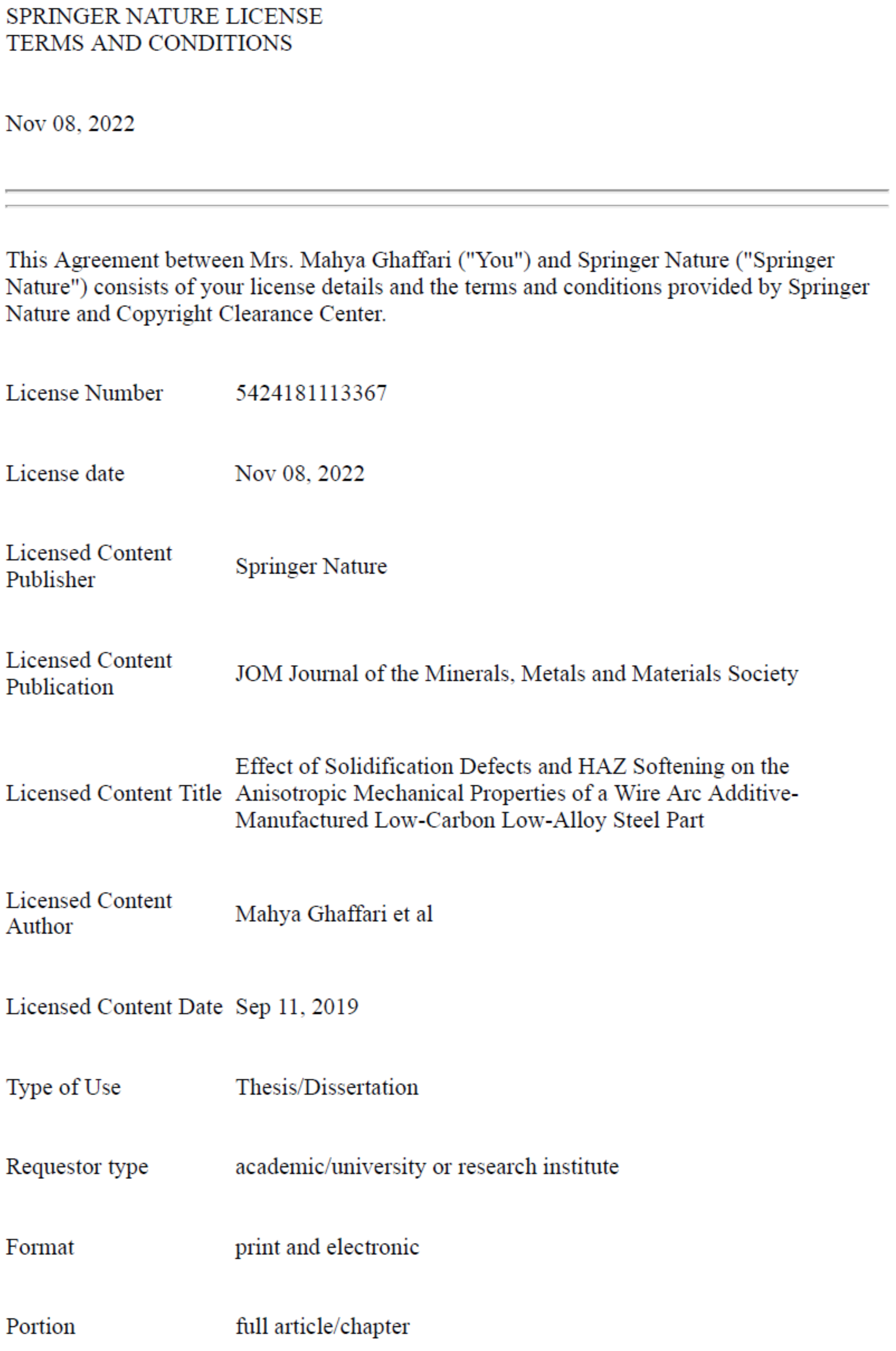

SPRINGER NATURE LICENSE
TERMS AND CONDITIONS

Nov 08, 2022

This Agreement between Mrs. Mahya Ghaffari ("You") and Springer Nature ("Springer Nature") consists of your license details and the terms and conditions provided by Springer Nature and Copyright Clearance Center.

License Number	5424181113367
License date	Nov 08, 2022
Licensed Content Publisher	Springer Nature
Licensed Content Publication	JOM Journal of the Minerals, Metals and Materials Society
Licensed Content Title	Effect of Solidification Defects and HAZ Softening on the Anisotropic Mechanical Properties of a Wire Arc Additive-Manufactured Low-Carbon Low-Alloy Steel Part
Licensed Content Author	Mahya Ghaffari et al
Licensed Content Date	Sep 11, 2019
Type of Use	Thesis/Dissertation
Requestor type	academic/university or research institute
Format	print and electronic
Portion	full article/chapter

Will you be translating?	no
Circulation/distribution	50000 or greater
Author of this Springer Nature content	yes
Title	EFFECTS OF POST-PRINTING HEAT TREATMENT AND ADDITION OF CERAMIC-BASED NANOPARTICLES ON THE MICROSTRUCTURE AND MECHANICAL PROPERTIES OF WIRE ARC ADDITIVE MANUFACTURED PH 13-8MO MARTENSITIC STAINLESS STEEL
Institution name	Dalhousie University
Expected presentation date	Dec 2022
Order reference number	Copyright permission for reusing in the author's thesis at Dalhousie University
Requestor Location	Dalhousie University C350-5269 Morris Street Department of Mechanical Engineering Halifax, NS B3H 4R2 Canada Attn: Dalhousie University
Total	0.00 CAD
Terms and Conditions	

Springer Nature Customer Service Centre GmbH
Terms and Conditions

This agreement sets out the terms and conditions of the licence (the **Licence**) between you and **Springer Nature Customer Service Centre GmbH** (the **Licensor**). By clicking 'accept' and completing the transaction for the material (**Licensed Material**), you also confirm your acceptance of these terms and conditions.

1. **Grant of License**

1. 1. The Licensor grants you a personal, non-exclusive, non-transferable, world-wide licence to reproduce the Licensed Material for the purpose specified in your order only. Licences are granted for the specific use requested in the order and for no other use, subject to the conditions below.

1. 2. The Licensor warrants that it has, to the best of its knowledge, the rights to license reuse of the Licensed Material. However, you should ensure that the material you are requesting is original to the Licensor and does not carry the copyright of another entity (as credited in the published version).

1. 3. If the credit line on any part of the material you have requested indicates that it was reprinted or adapted with permission from another source, then you should also seek permission from that source to reuse the material.

2. Scope of Licence

2. 1. You may only use the Licensed Content in the manner and to the extent permitted by these Ts&Cs and any applicable laws.

2. 2. A separate licence may be required for any additional use of the Licensed Material, e.g. where a licence has been purchased for print only use, separate permission must be obtained for electronic re-use. Similarly, a licence is only valid in the language selected and does not apply for editions in other languages unless additional translation rights have been granted separately in the licence. Any content owned by third parties are expressly excluded from the licence.

2. 3. Similarly, rights for additional components such as custom editions and derivatives require additional permission and may be subject to an additional fee. Please apply to Journalpermissions@springernature.com/bookpermissions@springernature.com for these rights.

2. 4. Where permission has been granted **free of charge** for material in print, permission may also be granted for any electronic version of that work, provided that the material is incidental to your work as a whole and that the electronic version is essentially equivalent to, or substitutes for, the print version.

2. 5. An alternative scope of licence may apply to signatories of the STM Permissions Guidelines, as amended from time to time.

3. Duration of Licence

3. 1. A licence for is valid from the date of purchase ('Licence Date') at the end of the relevant period in the below table:

Scope of Licence	**Duration of Licence**
Post on a website	12 months
Presentations	12 months
Books and journals	Lifetime of the edition in the language purchased

4. Acknowledgement

4. 1. The Licensor's permission must be acknowledged next to the Licenced Material in print. In electronic form, this acknowledgement must be visible at the same time as the figures/tables/illustrations or abstract, and must be hyperlinked to the journal/book's homepage. Our required acknowledgement format is in the Appendix below.

5. Restrictions on use

5. 1. Use of the Licensed Material may be permitted for incidental promotional use and minor editing privileges e.g. minor adaptations of single figures, changes of format, colour and/or style where the adaptation is credited as set out in Appendix 1 below. Any other changes including but not limited to, cropping, adapting, omitting material that affect the meaning, intention or moral rights of the author are strictly prohibited.

5. 2. You must not use any Licensed Material as part of any design or trademark.

5. 3. Licensed Material may be used in Open Access Publications (OAP) before publication by Springer Nature, but any Licensed Material must be removed from OAP sites prior to final publication.

6. Ownership of Rights

6. 1. Licensed Material remains the property of either Licensor or the relevant third party and any rights not explicitly granted herein are expressly reserved.

7. Warranty

IN NO EVENT SHALL LICENSOR BE LIABLE TO YOU OR ANY OTHER PARTY OR ANY OTHER PERSON OR FOR ANY SPECIAL, CONSEQUENTIAL, INCIDENTAL OR INDIRECT DAMAGES, HOWEVER CAUSED, ARISING OUT OF OR IN CONNECTION WITH THE DOWNLOADING, VIEWING OR USE OF THE MATERIALS REGARDLESS OF THE FORM OF ACTION, WHETHER FOR BREACH OF CONTRACT, BREACH OF WARRANTY, TORT, NEGLIGENCE, INFRINGEMENT OR OTHERWISE (INCLUDING, WITHOUT LIMITATION, DAMAGES BASED ON LOSS OF PROFITS, DATA, FILES, USE, BUSINESS OPPORTUNITY OR CLAIMS OF THIRD PARTIES), AND
WHETHER OR NOT THE PARTY HAS BEEN ADVISED OF THE POSSIBILITY OF SUCH DAMAGES. THIS LIMITATION SHALL APPLY NOTWITHSTANDING ANY FAILURE OF ESSENTIAL PURPOSE OF ANY LIMITED REMEDY PROVIDED HEREIN.

8. Limitations

8. 1. ***BOOKS ONLY:***Where **'reuse in a dissertation/thesis'** has been selected the following terms apply: Print rights of the final author's accepted manuscript (for clarity, NOT the published version) for up to 100 copies, electronic rights for use only on a personal website or institutional repository as defined by the Sherpa guideline (www.sherpa.ac.uk/romeo/).

8. 2. For content reuse requests that qualify for permission under the STM Permissions Guidelines, which may be updated from time to time, the STM Permissions Guidelines supersede the terms and conditions contained in this licence.

9. Termination and Cancellation

9. 1. Licences will expire after the period shown in Clause 3 (above).

9. 2. Licensee reserves the right to terminate the Licence in the event that payment is not received in full or if there has been a breach of this agreement by you.

Appendix 1 — Acknowledgements:

For Journal Content:
Reprinted by permission from [**the Licensor**]: [**Journal Publisher** (e.g. Nature/Springer/Palgrave)] [**JOURNAL NAME**] [**REFERENCE CITATION** (Article name, Author(s) Name), [**COPYRIGHT**] (year of publication)

For **Advance Online Publication papers:**
Reprinted by permission from [**the Licensor**]: [**Journal Publisher** (e.g. Nature/Springer/Palgrave)] [**JOURNAL NAME**] [**REFERENCE CITATION** (Article name, Author(s) Name), [**COPYRIGHT**] (year of publication), advance online publication, day month year (doi: 10.1038/sj.[JOURNAL ACRONYM].)

For Adaptations/Translations:
Adapted/Translated by permission from [**the Licensor**]: [**Journal Publisher** (e.g. Nature/Springer/Palgrave)] [**JOURNAL NAME**] [**REFERENCE CITATION** (Article name, Author(s) Name), [**COPYRIGHT**] (year of publication)

Note: For any republication from the British Journal of Cancer, the following credit line style applies:

Reprinted/adapted/translated by permission from [**the Licensor**]: on behalf of Cancer Research UK: : [**Journal Publisher** (e.g. Nature/Springer/Palgrave)] [**JOURNAL NAME**] [**REFERENCE CITATION** (Article name, Author(s) Name), [**COPYRIGHT**] (year of publication)

For **Advance Online Publication** papers:
Reprinted by permission from The [**the Licensor**]: on behalf of Cancer Research UK: [**Journal Publisher** (e.g. Nature/Springer/Palgrave)] [**JOURNAL NAME**] [**REFERENCE CITATION** (Article name, Author(s) Name), [**COPYRIGHT**] (year of publication), advance online publication, day month year (doi: 10.1038/sj. [JOURNAL ACRONYM])

For Book content:
Reprinted/adapted by permission from [**the Licensor**]: [**Book Publisher** (e.g.

Palgrave Macmillan, Springer etc) [**Book Title**] by [**Book author**(s)] [**COPYRIGHT**] (year of publication)

BIBLIOGRAPHY

[1] A. Sathyanath, A. Meena, Microstructural evolution and strain hardening behavior of heat-treated 17-4 PH stainless steel, Mater. Today Commun. 25 (2020) 101416. https://doi.org/https://doi.org/10.1016/j.mtcomm.2020.101416.

[2] J.A. Brooks, W.M. Garrison, Weld microstructure development and properties of precipitation-strengthened martensitic stainless steels, Weld. J. (Miami, Fla). 78 (1999) 280–291.

[3] J. Kazior, A. Szewczyk-Nykiel, T. Pieczonka, M. Hebda, M. Nykiel, Properties of precipitation hardening 17-4 PH stainless steel manufactured by powder metallurgy technology, Adv. Mater. Res. 811 (2013) 87–92. https://doi.org/10.4028/www.scientific.net/AMR.811.87.

[4] X. Li, J. Zhang, Q. Fu, E. Akiyama, X. Song, S. Shen, Q. Li, Hydrogen embrittlement of high strength steam turbine last stage blade steels: Comparison between PH17-4 steel and PH13-8Mo steel, Mater. Sci. Eng. A. 742 (2019) 353–363.

[5] Z. Guo, W. Sha, D. Vaumousse, Microstructural evolution in a PH13-8 stainless steel after ageing, Acta Mater. 51 (2003) 101–116. https://doi.org/10.1016/S1359-6454(02)00353-1.

[6] H. Asgari, M. Mohammadi, Microstructure and mechanical properties of stainless steel CX manufactured by Direct Metal Laser Sintering, Mater. Sci. Eng. A. 709 (2018) 82–89. https://doi.org/10.1016/j.msea.2017.10.045.

[7] P.W. Hochanadel, G.R. Edwards, C. V Robino, M.J. Cieslak, Heat treatment of investment cast PH 13-8 Mo stainless steel: Part I. Mechanical properties and microstructure, Metall. Mater. Trans. A. 25 (1994) 789–798.

[8] D.H. Ping, M. Ohnuma, Y. Hirakawa, Y. Kadoya, K. Hono, Microstructural evolution in 13Cr-8Ni-2.5Mo-2Al martensitic precipitation-hardened stainless steel, Mater. Sci. Eng. A. 394 (2005) 285–295. https://doi.org/10.1016/j.msea.2004.12.002.

[9] J.C. Lippold, D.J. Kotecki, Precipitation-hardening stainless steels, in: Weld. Metall. Weldability Stainl. Steels, New Jersey, 2005: pp. 264–286.

[10] R.J. Hamlin, J.N. DuPont, Microstructural Evolution and Mechanical Properties of Simulated Heat-Affected Zones in Cast Precipitation-Hardened Stainless Steels 17-4 and 13-8+Mo, Metall. Mater. Trans. A Phys. Metall. Mater. Sci. 48 (2017) 246–264. https://doi.org/10.1007/s11661-016-3851-6.

[11] W. Sha, H. Leitner, Z. Guo, W. Xu, 11 - Phase transformations in maraging steels, in: E. Pereloma, D. V Edmonds (Eds.), Phase Transform. Steels, Woodhead Publishing, 2012: pp. 332–362. https://doi.org/https://doi.org/10.1533/9780857096111.2.332.

[12] J.H. Shin, J. Jeong, J.W. Lee, Microstructural evolution and the variation of

tensile behavior after aging heat treatment of precipitation hardened martensitic steel, Mater. Charact. 99 (2015) 230–237. https://doi.org/10.1016/j.matchar.2014.11.024.

[13] W. Chen, B. Xiao, L. Xu, Y. Han, L. Zhao, H. Jing, Additive manufacturing of martensitic stainless steel matrix composites with simultaneously enhanced strength-ductility and corrosion resistance, Compos. Part B Eng. 234 (2022) 109745. https://doi.org/10.1016/j.compositesb.2022.109745.

[14] M. Akita, Y. Uematsu, T. Kakiuchi, M. Nakajima, R. Kawaguchi, Defect-dominated fatigue behavior in type 630 stainless steel fabricated by selective laser melting, Mater. Sci. Eng. A. 666 (2016) 19–26. https://doi.org/10.1016/j.msea.2016.04.042.

[15] A. Caballero, J. Ding, S. Ganguly, S. Williams, Wire + Arc Additive Manufacture of 17-4 PH stainless steel: Effect of different processing conditions on microstructure, hardness, and tensile strength, J. Mater. Process. Technol. 268 (2019) 54–62. https://doi.org/10.1016/j.jmatprotec.2019.01.007.

[16] M. Ghaffari, A. Vahedi Nemani, M. Rafieazad, A. Nasiri, Effect of Solidification Defects and HAZ Softening on the Anisotropic Mechanical Properties of a Wire Arc Additive-Manufactured Low-Carbon Low-Alloy Steel Part, JOM. (2019). https://doi.org/10.1007/s11837-019-03773-5.

[17] B. AlMangour, D. Grzesiak, J.-M. Yang, Rapid fabrication of bulk-form TiB2/316L stainless steel nanocomposites with novel reinforcement architecture and improved performance by selective laser melting, J. Alloys Compd. 680 (2016) 480–493. https://doi.org/https://doi.org/10.1016/j.jallcom.2016.04.156.

[18] M. Nematollahi, A. Jahadakbar, M.J. Mahtabi, M. Elahinia, 12 - Additive manufacturing (AM), in: M.B.T.-M. for B.D. (Second E. Niinomi (Ed.), Woodhead Publ. Ser. Biomater., Woodhead Publishing, 2019: pp. 331–353. https://doi.org/https://doi.org/10.1016/B978-0-08-102666-3.00012-2.

[19] B. AlMangour, D. Grzesiak, Jenn-MingYang, Selective laser melting of TiC reinforced 316L stainless steel matrix nanocomposites: Influence of starting TiC particle size and volume content, Mater. Des. 104 (2016) 141–151. https://doi.org/https://doi.org/10.1016/j.matdes.2016.05.018.

[20] T.D. Ngo, A. Kashani, G. Imbalzano, K.T.Q. Nguyen, D. Hui, Additive manufacturing (3D printing): A review of materials, methods, applications and challenges, Compos. Part B Eng. 143 (2018) 172–196. https://doi.org/10.1016/j.compositesb.2018.02.012.

[21] J.J. Lewandowski, M. Seifi, Metal Additive Manufacturing: A Review of Mechanical Properties, Annu. Rev. Mater. Res. 46 (2016) 151–186. https://doi.org/10.1146/annurev-matsci-070115-032024.

[22] W.E. Frazier, Metal Additive Manufacturing: A Review, J. Mater. Eng. Perform. 23 (2014) 1917–1928. https://doi.org/10.1007/s11665-014-0958-z.

[23] K. Moeinfar, F. Khodabakhshi, S.F. Kashani-bozorg, M. Mohammadi, A.P. Gerlich, A review on metallurgical aspects of laser additive manufacturing

(LAM): Stainless steels, nickel superalloys, and titanium alloys, J. Mater. Res. Technol. 16 (2022) 1029–1068. https://doi.org/https://doi.org/10.1016/j.jmrt.2021.12.039.

[24] A. Adeyemi, E.T. Akinlabi, R.M. Mahamood, Powder bed based laser additive manufacturing process of stainless steel: A review, Mater. Today Proc. 5 (2018) 18510–18517. https://doi.org/10.1016/j.matpr.2018.06.193.

[25] C.Y. Yap, C.K. Chua, Z.L. Dong, Z.H. Liu, D.Q. Zhang, L.E. Loh, S.L. Sing, Review of selective laser melting: Materials and applications, Appl. Phys. Rev. 2 (2015). https://doi.org/10.1063/1.4935926.

[26] B. AlMangour, D. Grzesiak, Jenn-MingYang, Selective laser melting of TiC reinforced 316L stainless steel matrix nanocomposites: Influence of starting TiC particle size and volume content, Mater. Des. 104 (2016) 141–151. https://doi.org/10.1016/j.matdes.2016.05.018.

[27] L.E. Murr, S.M. Gaytan, D.A. Ramirez, E. Martinez, J. Hernandez, K.N. Amato, P.W. Shindo, F.R. Medina, R.B. Wicker, Metal fabrication by additive manufacturing using laser and electron beam melting technologies, J. Mater. Sci. Technol. 28 (2012) 1–14.

[28] G. Sander, J. Tan, P. Balan, O. Gharbi, D.R. Feenstra, L. Singer, S. Thomas, R.G. Kelly, J.R. Scully, N. Birbilis, Corrosion of additively manufactured alloys: A review, Corrosion. 74 (2018) 1318–1350. https://doi.org/10.5006/2926.

[29] M. Galati, L. Iuliano, A literature review of powder-based electron beam melting focusing on numerical simulations, Addit. Manuf. 19 (2018) 1–20. https://doi.org/https://doi.org/10.1016/j.addma.2017.11.001.

[30] C.R. Cunningham, J.M. Flynn, A. Shokrani, V. Dhokia, S.T. Newman, Invited review article: Strategies and processes for high quality wire arc additive manufacturing, Addit. Manuf. 22 (2018) 672–686. https://doi.org/10.1016/j.addma.2018.06.020.

[31] W. Jin, C. Zhang, S. Jin, Y. Tian, D. Wellmann, W. Liu, Wire Arc Additive Manufacturing of Stainless Steels: A Review, Appl. Sci. . 10 (2020). https://doi.org/10.3390/app10051563.

[32] D. Ding, Z. Pan, D. Cuiuri, H. Li, A multi-bead overlapping model for robotic wire and arc additive manufacturing (WAAM), Robot. Comput. Integr. Manuf. 31 (2015) 101–110. https://doi.org/10.1016/j.rcim.2014.08.008.

[33] M.O. Couto, A.G. Rodrigues, F. Coutinho, R.R. Costa, A.C. Leite, F. Lizarralde, J.C.P. Filho, Mapping of Bead Geometry in Wire Arc Additive Manufacturing Systems Using Passive Vision, J. Control. Autom. Electr. Syst. 33 (2022) 1136–1147. https://doi.org/10.1007/s40313-021-00880-0.

[34] T.A. Rodrigues, V. Duarte, R.M. Miranda, T.G. Santos, J.P. Oliveira, Current status and perspectives on wire and arc additive manufacturing (WAAM), Materials (Basel). 12 (2019). https://doi.org/10.3390/ma12071121.

[35] J. Xiong, R. Li, Y. Lei, H. Chen, Heat propagation of circular thin-walled parts

fabricated in additive manufacturing using gas metal arc welding, J. Mater. Process. Technol. 251 (2018) 12–19. https://doi.org/10.1016/j.jmatprotec.2017.08.007.

[36] D. Yang, C. He, G. Zhang, Forming characteristics of thin-wall steel parts by double electrode GMAW based additive manufacturing, J. Mater. Process. Technol. 227 (2016) 153–160. https://doi.org/10.1016/j.jmatprotec.2015.08.021.

[37] J. Gu, J. Ding, S.W. Williams, H. Gu, J. Bai, Y. Zhai, P. Ma, The strengthening effect of inter-layer cold working and post-deposition heat treatment on the additively manufactured Al–6.3Cu alloy, Mater. Sci. Eng. A. 651 (2016) 18–26. https://doi.org/https://doi.org/10.1016/j.msea.2015.10.101.

[38] C. Brice, R. Shenoy, M. Kral, K. Buchannan, Precipitation behavior of aluminum alloy 2139 fabricated using additive manufacturing, Mater. Sci. Eng. A. 648 (2015) 9–14. https://doi.org/https://doi.org/10.1016/j.msea.2015.08.088.

[39] B. Baufeld, Mechanical Properties of INCONEL 718 Parts Manufactured by Shaped Metal Deposition (SMD), J. Mater. Eng. Perform. 21 (2012) 1416–1421. https://doi.org/10.1007/s11665-011-0009-y.

[40] F. Xu, Y. Lv, Y. Liu, F. Shu, P. He, B. Xu, Microstructural evolution and mechanical properties of Inconel 625 alloy during pulsed plasma arc deposition process, J. Mater. Sci. Technol. 29 (2013) 480–488.

[41] F. Martina, J. Mehnen, S.W. Williams, P. Colegrove, F. Wang, Investigation of the benefits of plasma deposition for the additive layer manufacture of Ti–6Al–4V, J. Mater. Process. Technol. 212 (2012) 1377–1386. https://doi.org/https://doi.org/10.1016/j.jmatprotec.2012.02.002.

[42] B. Wu, Z. Pan, S. Li, D. Cuiuri, D. Ding, H. Li, The anisotropic corrosion behaviour of wire arc additive manufactured Ti-6Al-4V alloy in 3.5% NaCl solution, Corros. Sci. 137 (2018) 176–183.

[43] X. Xu, S. Ganguly, J. Ding, S. Guo, S. Williams, F. Martina, Microstructural evolution and mechanical properties of maraging steel produced by wire+ arc additive manufacture process, Mater. Charact. 143 (2018) 152–162.

[44] C. Gao, X. Chen, C. Su, R.A. Singh, S. Jayalakshmi, Microstructure and mechanical properties of 9Cr martensitic heat-resistant steel fabricated by wire and arc additive manufacture technology, Mater. Express. 9 (2019) 179–184. https://doi.org/10.1166/MEX.2019.1485.

[45] T. Wang, Y. Zhang, Z. Wu, C. Shi, Microstructure and properties of die steel fabricated by WAAM using H13 wire, Vaccum. 149 (2018) 185–189. https://doi.org/10.1016/j.vacuum.2017.12.034.

[46] X. Chen, J. Li, X. Cheng, B. He, H. Wang, Z. Huang, Microstructure and mechanical properties of the austenitic stainless steel 316L fabricated by gas metal arc additive manufacturing, Mater. Sci. Eng. A. 703 (2017) 567–577. https://doi.org/10.1016/j.msea.2017.05.024.

[47] L. Wang, J. Xue, Q. Wang, Correlation between arc mode, microstructure, and

mechanical properties during wire arc additive manufacturing of 316L stainless steel, Mater. Sci. Eng. A. 751 (2019) 183–190. https://doi.org/10.1016/j.msea.2019.02.078.

[48] X. Zhang, K. Wang, Q. Zhou, J. Ding, S. Ganguly, Materials Science & Engineering A Microstructure and mechanical properties of TOP-TIG-wire and arc additive manufactured super duplex stainless steel (ER2594), Mater. Sci. Eng. A. 762 (2019) 138097. https://doi.org/10.1016/j.msea.2019.138097.

[49] J. Ge, J. Lin, Y. Chen, Y. Lei, H. Fu, Characterization of wire arc additive manufacturing 2Cr13 part: Process stability, microstructural evolution, and tensile properties, J. Alloys Compd. 748 (2018) 911–921.

[50] J. Lunde, M. Kazemipour, S. Salahi, A. Nasiri, Microstructure and Mechanical Properties of AISI 420 Stainless Steel Produced by Wire Arc Additive Manufacturing, in: TMS 2020 149th Annu. Meet. Exhib. Suppl. Proc., Springer, 2020: pp. 413–424.

[51] A.V. Nemani, M. Ghaffari, A. Nasiri, Comparison of microstructural characteristics and mechanical properties of shipbuilding steel plates fabricated by conventional rolling versus wire arc additive manufacturing, Addit. Manuf. 32 (2020) 101086.

[52] F. Martina, J. Ding, S. Williams, A. Caballero, G. Pardal, L. Quintino, Tandem metal inert gas process for high productivity wire arc additive manufacturing in stainless steel, Addit. Manuf. 25 (2019) 545–550. https://doi.org/10.1016/j.addma.2018.11.022.

[53] D. Ding, Z. Pan, D. Cuiuri, H. Li, Wire-feed additive manufacturing of metal components: technologies, developments and future interests, Int. J. Adv. Manuf. Technol. 81 (2015) 465–481. https://doi.org/10.1007/s00170-015-7077-3.

[54] C. Xia, Z. Pan, J. Polden, H. Li, Y. Xu, S. Chen, Y. Zhang, A review on wire arc additive manufacturing: Monitoring, control and a framework of automated system, J. Manuf. Syst. 57 (2020) 31–45. https://doi.org/https://doi.org/10.1016/j.jmsy.2020.08.008.

[55] X. Chen, J. Li, X. Cheng, B. He, H. Wang, Z. Huang, Microstructure and mechanical properties of the austenitic stainless steel 316L fabricated by gas metal arc additive manufacturing, Mater. Sci. Eng. A. 703 (2017) 567–577. https://doi.org/https://doi.org/10.1016/j.msea.2017.05.024.

[56] J. Xiong, Y. Li, R. Li, Z. Yin, Influences of process parameters on surface roughness of multi-layer single-pass thin-walled parts in GMAW-based additive manufacturing, J. Mater. Process. Technol. 252 (2018) 128–136. https://doi.org/10.1016/j.jmatprotec.2017.09.020.

[57] N. Sridharan, M.W. Noakes, A. Nycz, L.J. Love, R.R. Dehoff, S.S. Babu, On the toughness scatter in low alloy C-Mn steel samples fabricated using wire arc additive manufacturing, Mater. Sci. Eng. A. 713 (2018) 18–27. https://doi.org/https://doi.org/10.1016/j.msea.2017.11.101.

[58] Y. Sun, R.J. Hebert, M. Aindow, Effect of heat treatments on microstructural

evolution of additively manufactured and wrought 17-4PH stainless steel, Mater. Des. 156 (2018) 429–440. https://doi.org/10.1016/j.matdes.2018.07.015.

[59] J. Ge, J. Lin, Y. Lei, H. Fu, Location-related thermal history, microstructure, and mechanical properties of arc additively manufactured 2Cr13 steel using cold metal transfer welding, Mater. Sci. Eng. A. 715 (2018) 144–153.

[60] Z. Lyu, Y.S. Sato, S. Tokita, Y. Zhao, J. Jia, A. Wu, Microstructural evolution in a thin wall of 2Cr13 martensitic stainless steel during wire arc additive manufacturing, Mater. Charact. 182 (2021) 111520. https://doi.org/https://doi.org/10.1016/j.matchar.2021.111520.

[61] S. Salahi, A.V. Nemani, M. Ghaffari, J. Lunde, A. Nasiri, On microstructure, crystallographic orientation, and corrosion properties of wire arc additive manufactured 420 martensitic stainless steel: Effect of the inter-layer temperature, Addit. Manuf. 46 (2021) 102157. https://doi.org/https://doi.org/10.1016/j.addma.2021.102157.

[62] S. Roy, B. Silwal, A. Nycz, M. Noakes, E. Cakmak, P. Nandwana, Y. Yamamoto, Investigating the effect of different shielding gas mixtures on microstructure and mechanical properties of 410 stainless steel fabricated via large scale additive manufacturing, Addit. Manuf. 38 (2021) 101821. https://doi.org/https://doi.org/10.1016/j.addma.2020.101821.

[63] P. Wang, S.P. Lu, N.M. Xiao, D.Z. Li, Y.Y. Li, Effect of delta ferrite on impact properties of low carbon 13Cr–4Ni martensitic stainless steel, Mater. Sci. Eng. A. 527 (2010) 3210–3216.

[64] Y.C. Lin, S.C. Chen, Effect of residual stress on thermal fatigue in a type 420 martensitic stainless steel weldment, J. Mater. Process. Technol. 138 (2003) 22–27. https://doi.org/https://doi.org/10.1016/S0924-0136(03)00043-8.

[65] M. Ghaffari, A. Vahedi Nemani, M. Rafieazad, A. Nasiri, Effect of Solidification Defects and HAZ Softening on the Anisotropic Mechanical Properties of a Wire Arc Additive-Manufactured Low-Carbon Low-Alloy Steel Part, JOM. 71(11) (2019) 4215–4224. https://doi.org/10.1007/s11837-019-03773-5.

[66] D. Zhang, A. Prasad, M.J. Bermingham, C.J. Todaro, M.J. Benoit, M.N. Patel, D. Qiu, D.H. StJohn, M. Qian, M.A. Easton, Grain Refinement of Alloys in Fusion-Based Additive Manufacturing Processes, Metall. Mater. Trans. A Phys. Metall. Mater. Sci. 51 (2020) 4341–4359. https://doi.org/10.1007/s11661-020-05880-4.

[67] T.A. Rodrigues, V.R. Duarte, D. Tomás, J.A. Avila, J.D. Escobar, E. Rossinyol, N. Schell, T.G. Santos, J.P. Oliveira, In-situ strengthening of a high strength low alloy steel during Wire and Arc Additive Manufacturing (WAAM), Addit. Manuf. 34 (2020). https://doi.org/10.1016/j.addma.2020.101200.

[68] M. Ghaffari, A. Vahedi Nemani, A. Nasiri, Microstructure and mechanical behavior of PH 13–8Mo martensitic stainless steel fabricated by wire arc additive manufacturing, Addit. Manuf. 49 (2022) 102374. https://doi.org/https://doi.org/10.1016/j.addma.2021.102374.

[69] M. Liberini, A. Astarita, G. Campatelli, A. Scippa, F. Montevecchi, G. Venturini,

M. Durante, L. Boccarusso, F.M.C. Minutolo, A. Squillace, Selection of Optimal Process Parameters for Wire Arc Additive Manufacturing, Procedia CIRP. 62 (2017) 470–474. https://doi.org/10.1016/j.procir.2016.06.124.

[70] R. Sun, L. Li, Y. Zhu, W. Guo, P. Peng, B. Cong, J. Sun, Z. Che, B. Li, C. Guo, L. Liu, Microstructure, residual stress and tensile properties control of wire-arc additive manufactured 2319 aluminum alloy with laser shock peening, J. Alloys Compd. 747 (2018) 255–265. https://doi.org/https://doi.org/10.1016/j.jallcom.2018.02.353.

[71] J. Donoghue, A.A. Antonysamy, F. Martina, P.A. Colegrove, S.W. Williams, P.B. Prangnell, The effectiveness of combining rolling deformation with Wire-Arc Additive Manufacture on β-grain refinement and texture modification in Ti-6Al-4V, Mater. Charact. 114 (2016) 103–114. https://doi.org/10.1016/j.matchar.2016.02.001.

[72] N. Kumar, H. Bhavsar, P.V.S. Mahesh, A.K. Srivastava, B.J. Bora, A. Saxena, A.R. Dixit, Wire Arc Additive Manufacturing – A revolutionary method in additive manufacturing, Mater. Chem. Phys. 285 (2022) 126144. https://doi.org/https://doi.org/10.1016/j.matchemphys.2022.126144.

[73] M.J. Bermingham, S.D. McDonald, M.S. Dargusch, Effect of trace lanthanum hexaboride and boron additions on microstructure, tensile properties and anisotropy of Ti-6Al-4V produced by additive manufacturing, Mater. Sci. Eng. A. 719 (2018) 1–11. https://doi.org/https://doi.org/10.1016/j.msea.2018.02.012.

[74] Y. Snir, S. Haroush, A. Danon, A. Landau, Y. Gelbstein, D. Eliezer, Metallurgical and hydrogen effects on the small punch tested mechanical properties of PH-13-8Mo stainless steel, Materials (Basel). 11 (2018) 7–16. https://doi.org/10.3390/ma11101966.

[75] G.F. Vander Voort, G.M. Lucas, E.P. Manilova, Metallography and Microstructures of Stainless Steels and Maraging Steels, in: Metallogr. Microstruct. Vol 9, ASM International: Materials Park, Ohio, 2004: pp. 670–700. https://doi.org/10.1361/asmhba0003771.

[76] R.J. Hamlin, Microstructural Evolution and Mechanical Properties of Simulated Microstructural Evolution and Mechanical Properties of Simulated Heat Affected Zones in Cast Precipitation Hardened Stainless Heat Affected Zones in Cast Precipitation Hardened Stainless Ste, (2015). https://preserve.lehigh.edu/etd/2625.

[77] X. Li, J. Zhang, J. Chen, S. Shen, G. Yang, T. Wang, X. Song, Effect of aging treatment on hydrogen embrittlement of PH 13-8 Mo martensite stainless steel, Mater. Sci. Eng. A. 651 (2016) 474–485. https://doi.org/10.1016/j.msea.2015.09.116.

[78] M.J. Cieslak, C.R. Hills, P.F. Hlava, S.A. David, An investigation of the high-temperature and solidification microstructures of PH 13-8 Mo stainless steel, Metall. Trans. A. 21 (1990) 2465–2475. https://doi.org/10.1007/BF02646991.

[79] Y. Snir, S. Haroush, A. Dannon, A. Landau, D. Eliezer, Y. Gelbstein, Aging condition and trapped hydrogen effects on the mechanical behavior of a

precipitation hardened martensitic stainless steel, J. Alloys Compd. 805 (2019) 509–516. https://doi.org/https://doi.org/10.1016/j.jallcom.2019.07.112.

[80] L.W. Tsay, H.H. Chen, M.F. Chiang, C. Chen, The influence of aging treatments on sulfide stress corrosion cracking of PH 13-8 Mo steel welds, Corros. Sci. 49 (2007) 2461–2473. https://doi.org/10.1016/j.corsci.2006.12.006.

[81] Y. Sun, R.J. Hebert, M. Aindow, Effect of heat treatments on microstructural evolution of additively manufactured and wrought 17-4PH stainless steel, Mater. Des. 156 (2018) 429–440. https://doi.org/https://doi.org/10.1016/j.matdes.2018.07.015.

[82] S. Cheruvathur, E.A. Lass, C.E. Campbell, Additive Manufacturing of 17-4 PH Stainless Steel: Post-processing Heat Treatment to Achieve Uniform Reproducible Microstructure, JOM. 68 (2016) 930–942. https://doi.org/10.1007/s11837-015-1754-4.

[83] A. Hadadzadeh, A. Shahriari, B.S. Amirkhiz, J. Li, M. Mohammadi, Additive manufacturing of an Fe–Cr–Ni–Al maraging stainless steel: Microstructure evolution, heat treatment, and strengthening mechanisms, Mater. Sci. Eng. A. 787 (2020) 139470. https://doi.org/10.1016/j.msea.2020.139470.

[84] Material data sheet - FlexLine EOS Stainless Steel 316L, 49 (2016) 1–4.

[85] C. Chang, X. Yan, R. Bolot, J. Gardan, S. Gao, M. Liu, H. Liao, M. Chemkhi, S. Deng, Influence of post-heat treatments on the mechanical properties of CX stainless steel fabricated by selective laser melting, J. Mater. Sci. 55 (2020) 8303–8316. https://doi.org/10.1007/s10853-020-04566-x.

[86] A. Shahriari, M. Ghaffari, L. Khaksar, A. Nasiri, A. Hadadzadeh, B.S. Amirkhiz, M. Mohammadi, Corrosion resistance of 13wt.% Cr martensitic stainless steels: Additively manufactured CX versus wrought Ni-containing AISI 420, Corros. Sci. 184 (2021) 109362.

[87] B. Song, S. Dong, C. Coddet, Rapid in situ fabrication of Fe/SiC bulk nanocomposites by selective laser melting directly from a mixed powder of microsized Fe and SiC, Scr. Mater. 75 (2014) 90–93. https://doi.org/https://doi.org/10.1016/j.scriptamat.2013.11.031.

[88] J. Hu, H. Zhu, J. Zhang, M. Ouyang, C. Qiu, J. Duan, Effects of TiC addition on microstructure, microhardness and wear resistance of 18Ni300 maraging steel by direct laser deposition, J. Mater. Process. Technol. 296 (2021) 117213. https://doi.org/10.1016/j.jmatprotec.2021.117213.

[89] H. Chen, D. Gu, H. Zhang, L. Xi, T. Lu, L. Deng, U. Kühn, K. Kosiba, Novel WC-reinforced iron-based composites with excellent mechanical properties synthesized by laser additive manufacturing: Underlying role of reinforcement weight fraction, J. Mater. Process. Technol. 289 (2021) 116959. https://doi.org/https://doi.org/10.1016/j.jmatprotec.2020.116959.

[90] H. Chen, D. Gu, L. Deng, T. Lu, U. Kühn, K. Kosiba, Laser additive manufactured high-performance Fe-based composites with unique strengthening structure, J. Mater. Sci. Technol. 89 (2021) 242–252.

https://doi.org/https://doi.org/10.1016/j.jmst.2020.04.011.

[91] S. Wen, H. Hu, Y. Zhou, Z. Chen, Q. Wei, Y. Shi, Enhanced hardness and wear property of S136 mould steel with nano-TiB 2 composites fabricated by selective laser melting method, Appl. Surf. Sci. 457 (2018) 11–20. https://doi.org/10.1016/j.apsusc.2018.06.220.

[92] X. Zhao, Q.S. Wei, N. Gao, E.L. Zheng, Y.S. Shi, S.F. Yang, Rapid fabrication of TiN/AISI 420 stainless steel composite by selective laser melting additive manufacturing, J. Mater. Process. Technol. 270 (2019) 8–19. https://doi.org/https://doi.org/10.1016/j.jmatprotec.2019.01.028.

[93] B. AlMangour, D. Grzesiak, J.-M. Yang, In-situ formation of novel TiC-particle-reinforced 316L stainless steel bulk-form composites by selective laser melting, J. Alloys Compd. 706 (2017) 409–418. https://doi.org/https://doi.org/10.1016/j.jallcom.2017.01.149.

[94] M. Sharifitabar, J. Vahdati Khaki, M. Haddad Sabzevar, Microstructure and wear resistance of in-situ TiC-Al2O3 particles reinforced Fe-based coatings produced by gas tungsten arc cladding, Surf. Coatings Technol. 285 (2016) 47–56. https://doi.org/10.1016/j.surfcoat.2015.11.019.

[95] B. AlMangour, D. Grzesiak, J.-M. Yang, Nanocrystalline TiC-reinforced H13 steel matrix nanocomposites fabricated by selective laser melting, Mater. Des. 96 (2016) 150–161. https://doi.org/https://doi.org/10.1016/j.matdes.2016.02.022.

[96] C.L. Wu, S. Zhang, C.H. Zhang, J.B. Zhang, Y. Liu, Formation mechanism and phase evolution of in situ synthesizing TiC-reinforced 316L stainless steel matrix composites by laser melting deposition, Mater. Lett. 217 (2018) 304–307. https://doi.org/10.1016/j.matlet.2018.01.097.

[97] B. AlMangour, M.S. Baek, D. Grzesiak, K.A. Lee, Strengthening of stainless steel by titanium carbide addition and grain refinement during selective laser melting, Mater. Sci. Eng. A. 712 (2018) 812–818. https://doi.org/10.1016/j.msea.2017.11.126.

[98] B. AlMangour, Y.-K. Kim, D. Grzesiak, K.-A. Lee, Novel TiB2-reinforced 316L stainless steel nanocomposites with excellent room- and high-temperature yield strength developed by additive manufacturing, Compos. Part B Eng. 156 (2019) 51–63. https://doi.org/https://doi.org/10.1016/j.compositesb.2018.07.050.

[99] B. AlMangour, D. Grzesiak, J.M. Yang, Selective laser melting of TiB2/H13 steel nanocomposites: Influence of hot isostatic pressing post-treatment, J. Mater. Process. Technol. 244 (2017) 344–353. https://doi.org/10.1016/j.jmatprotec.2017.01.019.

[100] W. Chen, L. Xu, Y. Zhang, Y. Han, L. Zhao, H. Jing, Additive manufacturing of high-performance 15-5PH stainless steel matrix composites, Virtual Phys. Prototyp. 17 (2022) 366–381. https://doi.org/10.1080/17452759.2021.2019793.

[101] J. Samei, H. Asgari, C. Pelligra, M. Sanjari, S. Salavati, A. Shahriari, M. Amirmaleki, M. Jahanbakht, A. Hadadzadeh, B.S. Amirkhiz, M. Mohammadi, A hybrid additively manufactured martensitic-maraging stainless steel with superior

strength and corrosion resistance for plastic injection molding dies, Addit. Manuf. 45 (2021). https://doi.org/10.1016/j.addma.2021.102068.

[102] J. Xiong, G. Zhang, W. Zhang, Forming appearance analysis in multi-layer single-pass GMAW-based additive manufacturing, (2015) 1767–1776. https://doi.org/10.1007/s00170-015-7112-4.

[103] B. Wu, Z. Pan, D. Ding, D. Cuiuri, H. Li, J. Xu, J. Norrish, A review of the wire arc additive manufacturing of metals: Properties, defects and quality improvement, J. Manuf. Process. 35 (2018) 127–139.

[104] M. Rafieazad, M. Ghaffari, A.V. Nemani, A. Nasiri, Microstructural evolution and mechanical properties of a low-carbon low-alloy steel produced by wire arc additive manufacturing, Int. J. Adv. Manuf. Technol. (2019) 1–14.

[105] M. Ghaffari, A. Vahedi Nemani, A. Nasiri, Interfacial bonding between a wire arc additive manufactured 420 martensitic stainless steel part and its wrought base plate, Mater. Chem. Phys. 251 (2020) 123199.

[106] A. Vahedi Nemani, M. Ghaffari, A. Nasiri, On the Post-Printing Heat Treatment of a Wire Arc Additively Manufactured ER70S Part, Materials (Basel). 13 (2020) 2795.

[107] A. Vahedi Nemani, M. Ghaffari, A. Nasiri, Comparison of microstructural characteristics and mechanical properties of shipbuilding steel plates fabricated by conventional rolling versus wire arc additive manufacturing, Addit. Manuf. 32 (2020) 101086. https://doi.org/10.1016/j.addma.2020.101086.

[108] B. Baufeld, O. Van der Biest, R. Gault, Additive manufacturing of Ti-6Al-4V components by shaped metal deposition: Microstructure and mechanical properties, Mater. Des. 31 (2010) S106–S111. https://doi.org/10.1016/j.matdes.2009.11.032.

[109] S.W. Williams, F. Martina, A.C. Addison, J. Ding, G. Pardal, P. Colegrove, Wire + Arc Additive Manufacturing, Mater. Sci. Technol. 32 (2016) 641–647. https://doi.org/10.1179/1743284715Y.0000000073.

[110] C. V Haden, G. Zeng, F.M. Carter, C. Ruhl, B.A. Krick, D.G. Harlow, Wire and arc additive manufactured steel: Tensile and wear properties, Addit. Manuf. 16 (2017) 115–123. https://doi.org/https://doi.org/10.1016/j.addma.2017.05.010.

[111] D.T. Sarathchandra, M.J. Davidson, G. Visvanathan, Parameters effect on SS304 beads deposited by wire arc additive manufacturing, Mater. Manuf. Process. 35 (2020) 852–858. https://doi.org/10.1080/10426914.2020.1743852.

[112] O. Yilmaz, A.A. Ugla, Microstructure characterization of SS308LSi components manufactured by GTAW-based additive manufacturing: shaped metal deposition using pulsed current arc, Int. J. Adv. Manuf. Technol. 89 (2017) 13–25. https://doi.org/10.1007/s00170-016-9053-y.

[113] V. A Hosseini, M. Högström, K. Hurtig, M.A. Valiente Bermejo, L.E. Stridh, L. Karlsson, Wire-arc additive manufacturing of a duplex stainless steel: thermal cycle analysis and microstructure characterization, Weld. World. 63 (2019) 975–

987. https://doi.org/10.1007/s40194-019-00735-y.

[114] F. Hejripour, F. Binesh, M. Hebel, D.K. Aidun, Thermal modeling and characterization of wire arc additive manufactured duplex stainless steel, J. Mater. Process. Technol. 272 (2019) 58–71. https://doi.org/10.1016/j.jmatprotec.2019.05.003.

[115] L. Zai, C. Zhang, Y. Wang, W. Guo, D. Wellmann, X. Tong, Y. Tian, Laser powder bed fusion of precipitation-hardened martensitic stainless steels: A review, Metals (Basel). 10 (2020) 1–25. https://doi.org/10.3390/met10020255.

[116] R. Singh, Applied welding engineering: processes, codes, and standards, second ed., Butterworth-Heinemann, Amsterdam, 2016.

[117] X. Li, J. Zhang, Q. Fu, E. Akiyama, X. Song, S. Shen, Q. Li, Hydrogen embrittlement of high strength steam turbine last stage blade steels: Comparison between PH17-4 steel and PH13-8Mo steel, Mater. Sci. Eng. A. 742 (2019) 353–363. https://doi.org/10.1016/j.msea.2018.10.086.

[118] Z. Hu, H. Zhu, H. Zhang, X. Zeng, Experimental investigation on selective laser melting of 17-4PH stainless steel, Opt. Laser Technol. 87 (2017) 17–25. https://doi.org/10.1016/j.optlastec.2016.07.012.

[119] M. Averyanova, E. Cicala, P. Bertrand, D. Grevey, Experimental design approach to optimize selective laser melting of martensitic 17-4 PH powder: Part i - Single laser tracks and first layer, Rapid Prototyp. J. 18 (2012) 28–37. https://doi.org/10.1108/13552541211193476.

[120] H.R. Lashgari, C. Kong, E. Adabifiroozjaei, S. Li, Microstructure, post thermal treatment response, and tribological properties of 3D printed 17-4 PH stainless steel, Wear. 456–457 (2020). https://doi.org/10.1016/j.wear.2020.203367.

[121] L.E. Murr, E. Martinez, J. Hernandez, S. Collins, K.N. Amato, S.M. Gaytan, P.W. Shindo, Microstructures and properties of 17-4 PH stainless steel fabricated by selective laser melting, J. Mater. Res. Technol. 1 (2012) 167–177. https://doi.org/10.1016/S2238-7854(12)70029-7.

[122] D. Wang, C.T. Chi, W.Q. Wang, Y.L. Li, M.S. Wang, X.G. Chen, Z.H. Chen, X.P. Cheng, Y.J. Xie, The effects of fabrication atmosphere condition on the microstructural and mechanical properties of laser direct manufactured stainless steel 17-4 PH, J. Mater. Sci. Technol. 35 (2019) 1315–1322. https://doi.org/10.1016/j.jmst.2019.03.009.

[123] S. Cheruvathur, E.A. Lass, C.E. Campbell, Additive Manufacturing of 17-4 PH Stainless Steel: Post-processing Heat Treatment to Achieve Uniform Reproducible Microstructure, Jom. 68 (2016) 930–942. https://doi.org/10.1007/s11837-015-1754-4.

[124] A. Yadollahi, N. Shamsaei, S.M. Thompson, A. Elwany, L. Bian, Effects of building orientation and heat treatment on fatigue behavior of selective laser melted 17-4 PH stainless steel, Int. J. Fatigue. 94 (2017) 218–235. https://doi.org/10.1016/j.ijfatigue.2016.03.014.

[125] P.D. Nezhadfar, R. Shrestha, N. Phan, N. Shamsaei, Fatigue behavior of additively manufactured 17-4 PH stainless steel: Synergistic effects of surface roughness and heat treatment, Int. J. Fatigue. 124 (2019) 188–204. https://doi.org/10.1016/j.ijfatigue.2019.02.039.

[126] T. LeBrun, T. Nakamoto, K. Horikawa, H. Kobayashi, Effect of retained austenite on subsequent thermal processing and resultant mechanical properties of selective laser melted 17–4 PH stainless steel, Mater. Des. 81 (2015) 44–53.

[127] S. Sarkar, C.S. Kumar, A.K. Nath, Effects of heat treatment and build orientations on the fatigue life of selective laser melted 15-5 PH stainless steel, Mater. Sci. Eng. A. 755 (2019) 235–245. https://doi.org/10.1016/j.msea.2019.04.003.

[128] B. AlMangour, J.M. Yang, Improving the surface quality and mechanical properties by shot-peening of 17-4 stainless steel fabricated by additive manufacturing, Mater. Des. 110 (2016) 914–924. https://doi.org/10.1016/j.matdes.2016.08.037.

[129] B. AlMangour, J.M. Yang, Integration of Heat Treatment with Shot Peening of 17-4 Stainless Steel Fabricated by Direct Metal Laser Sintering, Jom. 69 (2017) 2309–2313. https://doi.org/10.1007/s11837-017-2538-9.

[130] I. Tolosa, F. Garciandía, F. Zubiri, F. Zapirain, A. Esnaola, Study of mechanical properties of AISI 316 stainless steel processed by "selective laser melting", following different manufacturing strategies, Int. J. Adv. Manuf. Technol. 51 (2010) 639–647.

[131] A. Shahriari, L. Khaksar, A. Nasiri, A. Hadadzadeh, B.S. Amirkhiz, M. Mohammadi, Microstructure and corrosion behavior of a novel additively manufactured maraging stainless steel, Electrochim. Acta. 339 (2020) 135925. https://doi.org/10.1016/j.electacta.2020.135925.

[132] U.S. Welding Corporation, Technical Data Sheets & Safety Data Sheets – Iron Base Alloys, (n.d.). https://www.usweldingcorp.net/technical-data/tds-sds-iron-base-alloys/ (accessed September 1, 2020).

[133] A. Vahedi Nemani, M. Ghaffari, S. Salahi, A. Nasiri, Effects of post-printing heat treatment on the microstructure and mechanical properties of a wire arc additive manufactured 420 martensitic stainless steel part, Mater. Sci. Eng. A. 813 (2021) 141167. https://doi.org/10.1016/j.msea.2021.141167.

[134] A. American Society for Testing and Materials, E8M Standard Test Methods for Tension Testing of Metallic Materials, ASTM International, West Conshohocken, PA, 2008. https://doi.org/10.1520/E0008_E0008M-13A.

[135] A. Lauro, M. Mandina, Welding and weldability of the 'super-austenitic' and 'super-martensitic' stainless steels, Weld. Int. 17 (2003) 710–720. https://doi.org/10.1533/wint.2003.3149.

[136] W. Wu, J. Xue, L. Wang, Z. Zhang, Y. Hu, C. Dong, Forming process, microstructure, and mechanical properties of thin-walled 316L stainless steel using speed-cold-welding additive manufacturing, Metals (Basel). 9 (2019). https://doi.org/10.3390/met9010109.

[137] S. Kou, Welding metallurgy, second ed., Wiley-Interscience, New Jersey, 2003.

[138] A. Eghlimi, M. Shamanian, M. Eskandarian, A. Zabolian, M. Nezakat, J.A. Szpunar, Evaluation of microstructure and texture across the welded interface of super duplex stainless steel and high strength low alloy steel, Surf. Coatings Technol. 264 (2015) 150–162. https://doi.org/10.1016/j.surfcoat.2014.12.060.

[139] A. Ziewiec, A. Zielińska-Lipiec, E. Tasak, Microstructure of welded joints of X5CrNiCuNb 16-4 (17-4 PH) martensitic stainless steel after heat treatment, Arch. Metall. Mater. 59 (2014) 965–970. https://doi.org/10.2478/amm-2014-0162.

[140] Y.W. Chao, T.S. Lui, L.H. Chen, Influence of Creq/Nieq ratio on solidification structures and tensile properties of strip cast austenitic stainless steels, Int. J. Cast Met. Res. 9 (1996) 175–181. https://doi.org/10.1080/13640461.1996.11819658.

[141] J.W. Fu, Y.S. Yang, Orientational dependence of lathy ferrite in Fe-Cr-Ni alloy during directional solidification, Mater. Lett. 81 (2012) 177–180. https://doi.org/10.1016/j.matlet.2012.04.149.

[142] K.P. Rao, Effect of weld cooling rate on delta-ferrite content of austenitic weld metals, J. Mater. Sci. Lett. 9 (1990) 675–677. https://doi.org/10.1007/BF00721800.

[143] X. Zhang, Q. Zhou, K. Wang, Y. Peng, J. Ding, J. Kong, S. Williams, Study on microstructure and tensile properties of high nitrogen Cr-Mn steel processed by CMT wire and arc additive manufacturing, Mater. Des. 166 (2019). https://doi.org/10.1016/j.matdes.2019.107611.

[144] P. Krakhmalev, I. Yadroitsava, G. Fredriksson, I. Yadroitsev, In situ heat treatment in selective laser melted martensitic AISI 420 stainless steels, Mater. Des. 87 (2015) 380–385.

[145] M.J. Cieslak, Hot-Cracking Mechanism in Co//2 Laser Beam Welds of Dissimilar Metals Involving Ph Martensitic Stainless Steels., Weld. J. (Miami, Fla). 66 (1987) 57–60.

[146] O.D. Sherby, J. Wadsworth, D.R. Lesuer, C.K. Syn, Revisiting the structure of martensite in iron-carbon steels, Mater. Trans. 49 (2008) 2016–2027. https://doi.org/10.2320/matertrans.MRA2007338.

[147] J.Y. Park, Y.S. Park, The effects of heat-treatment parameters on corrosion resistance and phase transformations of 14Cr-3Mo martensitic stainless steel, Mater. Sci. Eng. A. 448–451 (2007) 1131–1134. https://doi.org/10.1016/j.msea.2006.03.134.

[148] E. De Moor, S. Lacroix, A.J. Clarke, J. Penning, J.G. Speer, Effect of Retained Austenite Stabilized via Quench and Partitioning on the Strain Hardening of Martensitic Steels, Metall. Mater. Trans. A. 39 (2008) 2586. https://doi.org/10.1007/s11661-008-9609-z.

[149] A. Vahedi Nemani, M. Ghaffari, S. Salahi, J. Lunde, A. Nasiri, Effect of interpass temperature on the formation of retained austenite in a wire arc additive manufactured ER420 martensitic stainless steel, Mater. Chem. Phys. 266 (2021)

124555. https://doi.org/10.1016/j.matchemphys.2021.124555.

[150] S. Mereddy, M.J. Bermingham, D. Kent, A. Dehghan-Manshadi, D.H. StJohn, M.S. Dargusch, Trace Carbon Addition to Refine Microstructure and Enhance Properties of Additive-Manufactured Ti-6Al-4V, JOM. 70 (2018) 1670–1676. https://doi.org/10.1007/s11837-018-2994-x.

[151] M. Ghaffari, A.V. Nemani, A. Nasiri, Microstructure and mechanical behaviour of PH 13-8Mo martensitic stainless steel fabricated by wire arc additive manufacturing, Addit. Manuf. (2021) 102374. https://doi.org/10.1016/j.addma.2021.102374.

[152] R. Schnitzer, R. Radis, M. Nöhrer, M. Schober, R. Hochfellner, S. Zinner, E. Povoden-Karadeniz, E. Kozeschnik, H. Leitner, Reverted austenite in PH 13-8 Mo maraging steels, Mater. Chem. Phys. 122 (2010) 138–145.

[153] V. Seetharaman, M. Sundararaman, R. Krishnan, Precipitation hardening in a PH 13-8 Mo stainless steel, Mater. Sci. Eng. 47 (1981) 1–11. https://doi.org/10.1016/0025-5416(81)90034-3.

[154] H. Leitner, M. Schober, R. Schnitzer, Splitting phenomenon in the precipitation evolution in an Fe-Ni-Al-Ti-Cr stainless steel, Acta Mater. 58 (2010) 1261–1269. https://doi.org/10.1016/j.actamat.2009.10.030.

[155] R. Schnitzer, G.A. Zickler, E. Lach, H. Clemens, S. Zinner, T. Lippmann, H. Leitner, Influence of reverted austenite on static and dynamic mechanical properties of a PH 13-8 Mo maraging steel, Mater. Sci. Eng. A. 527 (2010) 2065–2070. https://doi.org/10.1016/j.msea.2009.11.046.

[156] M. Sanjari, A. Hadadzadeh, H. Pirgazi, A. Shahriari, B.S. Amirkhiz, L.A.I. Kestens, M. Mohammadi, Selective laser melted stainless steel CX: Role of built orientation on microstructure and micro-mechanical properties, Mater. Sci. Eng. A. 786 (2020) 139365. https://doi.org/10.1016/j.msea.2020.139365.

[157] H. Asgari, M. Mohammadi, Microstructure and mechanical properties of stainless steel CX manufactured by Direct Metal Laser Sintering, Mater. Sci. Eng. A. 709 (2018) 82–89. https://doi.org/10.1016/j.msea.2017.10.045.

[158] R. Mohammed, G.M. Reddy, K.S. Rao, Effect of filler wire composition on microstructure and pitting corrosion of nickel free high nitrogen stainless steel GTA welds, Trans. Indian Inst. Met. 69 (2016) 1919–1927. https://doi.org/10.1007/s12666-016-0851-6.

[159] A. Vahedi Nemani, M. Ghaffari, S. Salahi, J. Lunde, A. Nasiri, Effect of interpass temperature on the formation of retained austenite in a wire arc additive manufactured ER420 martensitic stainless steel, Mater. Chem. Phys. 266 (2021) 124555. https://doi.org/10.1016/j.matchemphys.2021.124555.

[160] Y. Liu, Q. Zhao, J. Zhao, Y. Huang, X. Cheng, L. Lu, Effect of Pre-passivation on the Corrosion Behavior of PH13-8Mo Stainless Steel in Industrial—Marine Atmospheric Environment, Front. Mater. 6 (2019) 1–13. https://doi.org/10.3389/fmats.2019.00296.

[161] H.R. Habibi Bajguirani, The effect of ageing upon the microstructure and mechanical properties of type 15-5 PH stainless steel, Mater. Sci. Eng. A. 338 (2002) 142–159. https://doi.org/10.1016/S0921-5093(02)00062-X.

[162] B.P.J. Sandvik, C.M. Wayman, Crystallography and substructure of lath martensite formed in carbon steels, Metallography. 16 (1983) 199–227.

[163] A.S.M. Handbook, Volume 4: Heat Treating, ASM Int. (1991) 1735–1740.

[164] C. V. Robino, M.J. Cieslak, P.W. Hochanadel, G.R. Edwards, Heat treatment of investment cast PH 13-8 Mo stainless steel: Part II. Isothermal aging kinetics, Metall. Mater. Trans. A. 25 (1994) 697–704. https://doi.org/10.1007/BF02665446.

[165] H. Leitner, R. Schnitzer, M. Schober, S. Zinner, Precipitate modification in PH13-8 Mo type maraging steel, Acta Mater. 59 (2011) 5012–5022. https://doi.org/10.1016/j.actamat.2011.04.053.

[166] F.R. Beckitt, B.R. Clark, The shape and mechanism of formation of M23C6 carbide in austenite, Acta Metall. 15 (1967) 113–129.

[167] Y.Y. Song, X.Y. Li, L.J. Rong, D.H. Ping, F.X. Yin, Y.Y. Li, Formation of the reversed austenite during intercritical tempering in a Fe-13%Cr-4%Ni-Mo martensitic stainless steel, Mater. Lett. 64 (2010) 1411–1414. https://doi.org/10.1016/j.matlet.2010.03.021.

[168] X. Li, J. Zhang, Y. Wang, S. Shen, X. Song, Effect of hydrogen on tensile properties and fracture behavior of PH 13-8 Mo steel, Mater. Des. 108 (2016) 608–617. https://doi.org/10.1016/j.matdes.2016.06.110.

[169] A. Hadadzadeh, E. Asadi, S. Imam Shakil, B. Shalchi Amirkhiz, M. Mohammadi, M. Haghshenas, Indentation-derived mechanical properties of Ti-6Al-4V: Laser-powder bed fusion versus electron beam melting, Mater. Lett. 301 (2021) 130273. https://doi.org/10.1016/j.matlet.2021.130273.

[170] M. Muhammad, J.W. Pegues, N. Shamsaei, M. Haghshenas, Effect of heat treatments on microstructure/small-scale properties of additive manufactured Ti-6Al-4V, Int. J. Adv. Manuf. Technol. 103 (2019) 4161–4172. https://doi.org/10.1007/s00170-019-03789-w.

[171] S.I. Shakil, A.S. Zoeram, H. Pirgazi, B. Shalchi-Amirkhiz, B. Poorganji, M. Mohammadi, M. Haghshenas, Microstructural-micromechanical correlation in an Al–Cu–Mg–Ag–TiB2 (A205) alloy: additively manufactured and cast, Mater. Sci. Eng. A. 832 (2022). https://doi.org/10.1016/j.msea.2021.142453.

[172] J. Fornell, N. Van Steenberge, A. Varea, E. Rossinyol, E. Pellicer, S. Suriñach, M.D. Baró, J. Sort, Enhanced mechanical properties and in vitro corrosion behavior of amorphous and devitrified Ti 40Zr 10Cu 38Pd 12 metallic glass, J. Mech. Behav. Biomed. Mater. 4 (2011) 1709–1717. https://doi.org/10.1016/j.jmbbm.2011.05.028.

[173] S. Ehtemam-Haghighi, G. Cao, L.C. Zhang, Nanoindentation study of mechanical properties of Ti based alloys with Fe and Ta additions, J. Alloys Compd. 692 (2017) 892–897. https://doi.org/10.1016/j.jallcom.2016.09.123.

[174] W. Wu, J. Xue, L. Wang, Z. Zhang, Y. Hu, C. Dong, Forming process, microstructure, and mechanical properties of thin-walled 316L stainless steel using speed-cold-welding additive manufacturing, Metals (Basel). 9 (2019) 109.

[175] ASTM-A564/A564M-13e1, Standard Specification for Hot-Rolled and Cold-Finished Age-Hardening Stainless Steel Bars and Shapes, ASTM Int. (2019).

[176] N. Hasani, M.H. Ghoncheh, R.M. Kindermann, H. Pirgazi, M. Sanjari, S. Tamimi, S. Shakerin, L.A.I. Kestens, M.J. Roy, M. Mohammadi, Dislocations mobility in superalloy-steel hybrid components produced using wire arc additive manufacturing, Mater. Des. 220 (2022) 110899. https://doi.org/https://doi.org/10.1016/j.matdes.2022.110899.

[177] M. Ghaffari, A. Vahedi Nemani, A. Nasiri, Microstructural evolution and mechanical performance after precipitation hardening of PH 13-8Mo martensitic stainless steel fabricated by wire arc additive manufacturing, Materialia. 24 (2022) 101507. https://doi.org/https://doi.org/10.1016/j.mtla.2022.101507.

[178] Y. Liu, M. Tang, Q. Hu, Y. Zhang, L. Zhang, Densification behavior, microstructural evolution, and mechanical properties of TiC/AISI420 stainless steel composites fabricated by selective laser melting, Mater. Des. 187 (2020) 1–13. https://doi.org/10.1016/j.matdes.2019.108381.

[179] R. Koc, C. Meng, G.A. Swift, Sintering properties of submicron TiC powders from carbon coated titania precursor, J. Mater. Sci. 35 (2000) 3131–3141. https://doi.org/10.1023/A:1004876121000.

[180] R.G. Munro, Material properties of titanium diboride, J. Res. Natl. Inst. Stand. Technol. 105 (2000) 709.

[181] B. AlMangour, D. Grzesiak, J.-M. Yang, Scanning strategies for texture and anisotropy tailoring during selective laser melting of TiC/316L stainless steel nanocomposites, J. Alloys Compd. 728 (2017) 424–435. https://doi.org/https://doi.org/10.1016/j.jallcom.2017.08.022.

[182] E. Bahramizadeh, S. Nourouzi, H. Jamshidi Aval, In-situ fabrication of TiC-Al2O3 and TiB2-TiC-Al2O3 composite coatings on 304 stainless steel surface using GTAW process, Kov. Mater. 57 (2019) 177–188. https://doi.org/10.4149/km_2019_3_177.

[183] J. Huang, Z. Li, S. Yu, X. Yu, D. Fan, Real-time observation and numerical simulation of the molten pool flow and mass transfer behavior during wire arc additive manufacturing, Weld. World. 66 (2022) 481–494. https://doi.org/10.1007/s40194-021-01214-z.

[184] D. Dong, C. Chang, H. Wang, X. Yan, W. Ma, M. Liu, S. Deng, J. Gardan, R. Bolot, H. Liao, Selective laser melting (SLM) of CX stainless steel: Theoretical calculation, process optimization and strengthening mechanism, J. Mater. Sci. Technol. 73 (2021) 151–164. https://doi.org/https://doi.org/10.1016/j.jmst.2020.09.031.

[185] W. Zhai, W. Zhou, S.M.L. Nai, In-situ formation of TiC nanoparticles in selective laser melting of 316L with addition of micronsized TiC particles, Mater. Sci. Eng.

A. 829 (2022) 142179. https://doi.org/10.1016/j.msea.2021.142179.

[186] J. Wang, Y. Ding, H. Cheng, Y. Wang, In situ production of Fe-TiC surface composite, Adv. Mater. Res. 335–336 (2011) 80–85. https://doi.org/10.4028/www.scientific.net/AMR.335-336.80.

[187] X. Li, P. Wu, S. Zhao, C. Chen, R. Yin, N. Chen, First-principle Study of the Solution Type of Boron in γ-iron, Energy Procedia. 16 (2012) 661–666. https://doi.org/10.1016/j.egypro.2012.01.107.

[188] N. Filonenko, Solubility of boron and carbon in ferrite of the fe-bc system alloys, East Eur. J. Phys. (2019) 52–57.

[189] E. Sigolo, J. Soyama, G. Zepon, C.S. Kiminami, W.J. Botta, C. Bolfarini, Wear resistant coatings of boron-modified stainless steels deposited by Plasma Transferred Arc, Surf. Coatings Technol. 302 (2016) 255–264. https://doi.org/10.1016/j.surfcoat.2016.06.023.

[190] G. Zepon, R.P. Nogueira, C.S. Kiminami, W.J. Botta, C. Bolfarini, Electrochemical Corrosion Behavior of Spray-Formed Boron-Modified Supermartensitic Stainless Steel, Metall. Mater. Trans. A Phys. Metall. Mater. Sci. 48 (2017) 2077–2089. https://doi.org/10.1007/s11661-017-3980-6.

[191] E.R. dos Santos, W.A. da Silva, G.Y. Koga, C. Bolfarini, G. Zepon, Corrosion Resistant Boron-Modified Ferritic and Austenitic Stainless Steels Designed by CALPHAD, Metall. Mater. Trans. A Phys. Metall. Mater. Sci. 52 (2021) 2708–2719. https://doi.org/10.1007/s11661-021-06226-4.

[192] J. Platl, H. Leitner, C. Turk, R. Schnitzer, Determination of Martensite Start Temperature of High-Speed Steels Based on Thermodynamic Calculations, Steel Res. Int. 91 (2020) 2000063.

[193] D.W. Kim, S. Kim, J. Yang, S. Lee, S.S. Sohn, Enhancement of ballistic performance enabled by boron-doping in subzero-treated (ferrite+austenite+martensite) triplex lightweight steel, Mater. Charact. 190 (2022) 112021. https://doi.org/10.1016/j.matchar.2022.112021.

[194] H. Zhu, M. Ouyang, J. Hu, J. Zhang, C. Qiu, Design and development of TiC-reinforced 410 martensitic stainless steel coatings fabricated by laser cladding, Ceram. Int. 47 (2021) 12505–12513. https://doi.org/10.1016/j.ceramint.2021.01.108.

[195] W. Zhai, W. Zhou, S.M.L. Nai, Grain refinement and strengthening of 316L stainless steel through addition of TiC nanoparticles and selective laser melting, Mater. Sci. Eng. A. 832 (2022) 142460. https://doi.org/10.1016/j.msea.2021.142460.

[196] M.J. Bermingham, S.D. McDonald, M.S. Dargusch, D.H. StJohn, The mechanism of grain refinement of titanium by silicon, Scr. Mater. 58 (2008) 1050–1053. https://doi.org/10.1016/j.scriptamat.2008.01.041.

[197] M.J. Bermingham, S.D. McDonald, D.H. StJohn, M.S. Dargusch, Beryllium as a grain refiner in titanium alloys, J. Alloys Compd. 481 (2009) 20–23.

https://doi.org/10.1016/j.jallcom.2009.03.016.

[198] M.J. Bermingham, S.D. McDonald, M.S. Dargusch, D.H. St.John, Grain-refinement mechanisms in titanium alloys, J. Mater. Res. 23 (2008) 97–104. https://doi.org/10.1557/jmr.2008.0002.

[199] S. Tamirisakandala, R.B. Bhat, J.S. Tiley, D.B. Miracle, Grain refinement of cast titanium alloys via trace boron addition, Scr. Mater. 53 (2005) 1421–1426. https://doi.org/10.1016/j.scriptamat.2005.08.020.

[200] S. Mereddy, M.J. Bermingham, D. Kent, A. Dehghan-Manshadi, D.H. StJohn, M.S. Dargusch, Trace Carbon Addition to Refine Microstructure and Enhance Properties of Additive-Manufactured Ti-6Al-4V, Jom. 70 (2018) 1670–1676. https://doi.org/10.1007/s11837-018-2994-x.

[201] H.S. Furtado, A.T. Bernardes, R.F.F. MacHado, C.A. Silva, The effect of adding boron in solidification microstructure of dilute iron-carbon alloy as assessed by Phase-Field modeling, Mater. Res. 14 (2011) 195–205. https://doi.org/10.1590/S1516-14392011005000029.

[202] X. Li, J. Zhang, Q. Fu, E. Akiyama, X. Song, S. Shen, Q. Li, Hydrogen embrittlement of high strength steam turbine last stage blade steels: Comparison between PH17-4 steel and PH13-8Mo steel, Mater. Sci. Eng. A. 742 (2019) 353–363. https://doi.org/https://doi.org/10.1016/j.msea.2018.10.086.

[203] T.M. Williams, A.M. Stoneham, D.R. Harries, The segregation of boron to grain boundaries in solution-treated Type 316 austenitic stainless steel, Met. Sci. 10 (1976) 14–19. https://doi.org/10.1179/030634576790431471.

[204] I. Fedorova, F. Liu, F.B. Grumsen, Y. Cao, O. V. Mishin, J. Hald, Fine (Cr,Fe)2B borides on grain boundaries in a 10Cr–0.01B martensitic steel, Scr. Mater. 156 (2018) 124–128. https://doi.org/10.1016/j.scriptamat.2018.07.021.

[205] D.I. Adebiyi, A.P.I. Popoola, S.L. Pityana, Microstructural evolution at the overlap zones of 12Cr martensitic stainless steel laser alloyed with TiC, Opt. Laser Technol. 61 (2014) 15–23. https://doi.org/10.1016/j.optlastec.2014.01.014.

[206] H. Springer, R. Aparicio Fernandez, M.J. Duarte, A. Kostka, D. Raabe, Microstructure refinement for high modulus in-situ metal matrix composite steels via controlled solidification of the system Fe-TiB2, Acta Mater. 96 (2015) 47–56. https://doi.org/10.1016/j.actamat.2015.06.017.

[207] A.A.M. da Silva, J.F. dos Santos, T.R. Strohaecker, Microstructural and mechanical characterisation of a Ti6Al4V/TiC/10p composite processed by the BE-CHIP method, Compos. Sci. Technol. 65 (2005) 1749–1755. https://doi.org/10.1016/j.compscitech.2005.03.005.

[208] J. Xiong, Z. Yin, W. Zhang, Closed-loop control of variable layer width for thin-walled parts in wire and arc additive manufacturing, J. Mater. Process. Technol. 233 (2016) 100–106. https://doi.org/10.1016/j.jmatprotec.2016.02.021.

[209] D. Ding, Z. Pan, D. Cuiuri, H. Li, A practical path planning methodology for wire and arc additive manufacturing of thin-walled structures, Robot. Comput. Integr.

Manuf. 34 (2015) 8–19. https://doi.org/10.1016/j.rcim.2015.01.003.

[210] D. Yang, C. He, G. Zhang, Forming characteristics of thin-wall steel parts by double electrode GMAW based additive manufacturing, J. Mater. Process. Technol. 227 (2016) 153–160. https://doi.org/10.1016/j.jmatprotec.2015.08.021.

[211] F. Montevecchi, G. Venturini, N. Grossi, A. Scippa, G. Campatelli, Finite Element mesh coarsening for effective distortion prediction in Wire Arc Additive Manufacturing, Addit. Manuf. 18 (2017) 145–155. https://doi.org/10.1016/j.addma.2017.10.010.

[212] A. Lopez, R. Bacelar, I. Pires, T.G. Santos, J.P. Sousa, L. Quintino, Non-destructive testing application of radiography and ultrasound for wire and arc additive manufacturing, Addit. Manuf. 21 (2018) 298–306. https://doi.org/10.1016/j.addma.2018.03.020.

[213] S. Das, D.L. Bourell, S.S. Babu, Metallic materials for 3D printing, MRS Bull. 41 (2016) 729–741.

[214] N. Takayama, G. Miyamoto, T. Furuhara, Chemistry and three-dimensional morphology of martensite-austenite constituent in the bainite structure of low-carbon low-alloy steels, Acta Mater. 145 (2018) 154–164.

[215] R.B. Dinwiddie, R.R. Dehoff, P.D. Lloyd, L.E. Lowe, J.B. Ulrich, Thermographic in-situ process monitoring of the electron-beam melting technology used in additive manufacturing, in: Thermosense Therm. Infrared Appl. XXXV, International Society for Optics and Photonics, 2013: p. 87050K.

[216] A. Chaudhary, Modeling of laser-additive manufacturing processes, ASM Handb. 22 (2009) 240–252.

[217] N. Sridharan, M.W. Noakes, A. Nycz, L.J. Love, R.R. Dehoff, S.S. Babu, On the toughness scatter in low alloy C-Mn steel samples fabricated using wire arc additive manufacturing, Mater. Sci. Eng. A. 713 (2018) 18–27. https://doi.org/10.1016/j.msea.2017.11.101.

[218] P. Zhang, J. Liu, A.C. To, Role of anisotropic properties on topology optimization of additive manufactured load bearing structures, Scr. Mater. 135 (2017) 148–152. https://doi.org/10.1016/j.scriptamat.2016.10.021.

[219] E. Herderick, Additive manufacturing of metals: A review, Mater. Sci. Technol. (2011) 1413.

[220] X. Xu, S. Ganguly, J. Ding, S. Guo, S. Williams, F. Martina, Microstructural evolution and mechanical properties of maraging steel produced by wire+arc additive manufacture process, Mater. Charact. (2017). https://doi.org/10.1016/j.matchar.2017.12.002.

[221] B.D. Deruntz, Assessing the Benefits of Surface Tension Transfer Welding to Industry, J. Ind. Technol. 19 (2003) 2–8.

[222] A.O. Benscoter, B.L. Bramfitt, Metallography and microstructures of low-carbon and coated steels, Metallogr. Microstruct. 9 (2004) 588–607.

[223] ASTM Int., Standard Test Methods for Tension Testing of Metallic Materials 1,

Astm. i (2015) 1–27. https://doi.org/10.1520/E0008.

[224] C. V Haden, G. Zeng, F.M. Carter III, C. Ruhl, B.A. Krick, D.G. Harlow, Wire and arc additive manufactured steel: Tensile and wear properties, Addit. Manuf. 16 (2017) 115–123.

[225] A. Shirizly, O. Dolev, From Wire to Seamless Flow-Formed Tube: Leveraging the Combination of Wire Arc Additive Manufacturing and Metal Forming, JOM. 71 (2019) 709–717.

[226] B. Shassere, A. Nycz, M.W. Noakes, C. Masuo, N. Sridharan, Correlation of Microstructure and Mechanical Properties of Metal Big Area Additive Manufacturing, Appl. Sci. 9 (2019) 787.

[227] M. Liberini, A. Astarita, G. Campatelli, A. Scippa, F. Montevecchi, G. Venturini, M. Durante, L. Boccarusso, F.M.C. Minutolo, A. Squillace, Selection of Optimal Process Parameters for Wire Arc Additive Manufacturing, Procedia CIRP. 62 (2017) 470–474. https://doi.org/10.1016/j.procir.2016.06.124.

[228] H.K. Lee, K.S. Kim, C.M. Kim, Fracture resistance of a steel weld joint under fatigue loading, Eng. Fract. Mech. 66 (2000) 403–419.

[229] A.S. Haselhuhn, B. Wijnen, G.C. Anzalone, P.G. Sanders, J.M. Pearce, In situ formation of substrate release mechanisms for gas metal arc weld metal 3-D printing, J. Mater. Process. Technol. 226 (2015) 50–59. https://doi.org/10.1016/j.jmatprotec.2015.06.038.

[230] C. Zhang, X. Song, P. Lu, X. Hu, Effect of microstructure on mechanical properties in weld-repaired high strength low alloy steel, Mater. Des. 36 (2012) 233–242. https://doi.org/10.1016/j.matdes.2011.11.016.

[231] T. Mohandas, G.M. Reddy, B.S. Kumar, Heat-affected zone softening in high-strength low-alloy steels, J. Mater. Process. Technol. 88 (1999) 284–294.

[232] X. Shi, S. Ma, C. Liu, Q. Wu, J. Lu, Y. Liu, W. Shi, Selective laser melting-wire arc additive manufacturing hybrid fabrication of Ti-6Al-4V alloy: Microstructure and mechanical properties, Mater. Sci. Eng. A. 684 (2017) 196–204. https://doi.org/10.1016/j.msea.2016.12.065.

[233] Z. Wang, T.A. Palmer, A.M. Beese, Effect of processing parameters on microstructure and tensile properties of austenitic stainless steel 304L made by directed energy deposition additive manufacturing, Acta Mater. 110 (2016) 226–235. https://doi.org/10.1016/j.actamat.2016.03.019.

[234] B.E. Carroll, T.A. Palmer, A.M. Beese, Anisotropic tensile behavior of Ti-6Al-4V components fabricated with directed energy deposition additive manufacturing, Acta Mater. 87 (2015) 309–320. https://doi.org/10.1016/j.actamat.2014.12.054.

[235] L. Thijs, M.L.M. Sistiaga, R. Wauthle, Q. Xie, J.-P. Kruth, J. Van Humbeeck, Strong morphological and crystallographic texture and resulting yield strength anisotropy in selective laser melted tantalum, Acta Mater. 61 (2013) 4657–4668.

[236] S. Suryakumar, K.P. Karunakaran, U. Chandrasekhar, M.A. Somashekara, A study of the mechanical properties of objects built through weld-deposition, Proc.

Inst. Mech. Eng. Part B J. Eng. Manuf. 227 (2013) 1138–1147. https://doi.org/10.1177/0954405413482122.

[237] B.A. Szost, S. Terzi, F. Martina, D. Boisselier, A. Prytuliak, T. Pirling, M. Hofmann, D.J. Jarvis, A comparative study of additive manufacturing techniques: Residual stress and microstructural analysis of CLAD and WAAM printed Ti-6Al-4V components, Mater. Des. 89 (2016) 559–567. https://doi.org/10.1016/j.matdes.2015.09.115.

[238] N. Sridharan, M.W. Noakes, A. Nycz, L.J. Love, R.R. Dehoff, S.S. Babu, On the toughness scatter in low alloy C-Mn steel samples fabricated using wire arc additive manufacturing, Mater. Sci. Eng. A. 713 (2018) 18–27. https://doi.org/https://doi.org/10.1016/j.msea.2017.11.101.

[239] Q. Zhang, J. Chen, Z. Zhao, H. Tan, X. Lin, W. Huang, Microstructure and anisotropic tensile behavior of laser additive manufactured TC21 titanium alloy, Mater. Sci. Eng. A. 673 (2016) 204–212. https://doi.org/10.1016/j.msea.2016.07.040.

[240] M.A. Meyers, K.K. Chawla, Mechanical Behavior of Materials, Cambridge University Press, 2009.

[241] Z. Wang, A.M. Beese, Effect of chemistry on martensitic phase transformation kinetics and resulting properties of additively manufactured stainless steel, Acta Mater. 131 (2017) 410–422. https://doi.org/10.1016/j.actamat.2017.04.022.

[242] L.I. Hua-bing, Z. Jiang, Z. Zhang, Y. Yang, H. Li, Z. Jiang, Z. Zhang, Y. Yan, Effect of grain size on mechanical properties of nickel-free high nitrogen austenitic stainless steel, J. Iron Steel Res. Int. 16 (2009) 58–61. https://doi.org/10.1016/S1006-706X(09)60011-X.

[243] X. Luo, X. Chen, T. Wang, S. Pan, Z. Wang, Effect of morphologies of martensite–austenite constituents on impact toughness in intercritically reheated coarse-grained heat-affected zone of HSLA steel, Mater. Sci. Eng. A. 710 (2018) 192–199. https://doi.org/10.1016/j.msea.2017.10.079.

[244] N. Huda, A.R.H. Midawi, J. Gianetto, R. Lazor, A.P. Gerlich, Influence of martensite-austenite (MA) on impact toughness of X80 line pipe steels, Mater. Sci. Eng. A. 662 (2016) 481–491. https://doi.org/https://doi.org/10.1016/j.msea.2016.03.095.

[245] B.C. Kim, S. Lee, N.J. Kim, D.Y. Lee, Microstructure and local brittle zone phenomena in high-strength low-alloy steel welds, Metall. Trans. A. 22 (1991) 139–149. https://doi.org/10.1007/BF03350956.

[246] O.M. Akselsen, Ø. Grong, J.K. Solberg, Structure–property relationships in intercritical heat affected zone of low-carbon microalloyed steels, Mater. Sci. Technol. 3 (1987) 649–655. https://doi.org/10.1179/mst.1987.3.8.649.

[247] A. Lambert, A. Lambert, J. Drillet, A.F. Gourgues, T. Sturel, A. Pineau, Microstructure of martensite–austenite constituents in heat affected zones of high strength low alloy steel welds in relation to toughness properties, Sci. Technol. Weld. Join. 5 (2000) 168–173. https://doi.org/10.1179/136217100101538164.

[248] Volume 4 ASM Handbook, Heat treating, ASM Int. 1012 (1991).

[249] K.W. Andrews, Empirical formulae for the calculation of some transformation temperatures, J. Iron Steel Inst. (1965) 721–727.

[250] C. Natividad, R. García, V.H. López, L.A. Falcón, M. Salazar, Mechanical and Metallurgical Properties of Grade X70 Steel Linepipe Produced by Non-conventional Heat Treatment, in: Charact. Met. Alloy., Springer, 2017: pp. 3–11.

[251] S. Bordbar, M. Alizadeh, S.H. Hashemi, Effects of microstructure alteration on corrosion behavior of welded joint in API X70 pipeline steel, Mater. Des. 45 (2013) 597–604.

[252] M. Ghaffari, A. Vahedi Nemani, M. Rafieazad, A. Nasiri, Effect of Solidification Defects and HAZ Softening on the Anisotropic Mechanical Properties of a Wire Arc Additive-Manufactured Low-Carbon Low-Alloy Steel Part, JOM. 71(11) (2019) 4215–4224. https://doi.org/10.1007/s11837-019-03773-5.

[253] N.A. Kistler, D.J. Corbin, A.R. Nassar, E.W. Reutzel, A.M. Beese, Effect of processing conditions on the microstructure, porosity, and mechanical properties of Ti-6Al-4V repair fabricated by directed energy deposition, J. Mater. Process. Technol. 264 (2019) 172–181.

[254] Q. Liu, Y. Wang, H. Zheng, K. Tang, H. Li, S. Gong, TC17 titanium alloy laser melting deposition repair process and properties, Opt. Laser Technol. 82 (2016) 1–9.

[255] A. Saboori, A. Aversa, G. Marchese, S. Biamino, M. Lombardi, P. Fino, Application of directed energy deposition-based additive manufacturing in repair, Appl. Sci. 9 (2019) 3316.

[256] X. Zhao, Q. Wei, B. Song, Y. Liu, X. Luo, S. Wen, Y. Shi, Fabrication and characterization of AISI 420 stainless steel using selective laser melting, Mater. Manuf. Process. 30 (2015) 1283–1289.

[257] A. Persson, S. Hogmark, J. Bergström, Thermal fatigue cracking of surface engineered hot work tool steels, Surf. Coatings Technol. 191 (2005) 216–227.

[258] J. Ge, J. Lin, H. Fu, Y. Lei, R. Xiao, A spatial periodicity of microstructural evolution and anti-indentation properties of wire-arc additive manufacturing 2Cr13 thin-wall part, Mater. Des. 160 (2018) 218–228.

[259] ASTM E8M-04, Standard Test Methods for Tension Testing of Metallic Materials [Metric], ASTM International, West Conshohocken, PA, 2008. https://doi.org/10.1520/E0008M-04.

[260] J.C. Lippold, D.J. Kotecki, Welding metallurgy and weldability of stainless steels, ISBN 0-471-47379-0. Wiley-VCH. (2005) 376.

[261] S.H. Baghjari, S.A.A.A. Mousavi, Effects of pulsed Nd: YAG laser welding parameters and subsequent post-weld heat treatment on microstructure and hardness of AISI 420 stainless steel, Mater. Des. 43 (2013) 1–9.

[262] C. Köse, R. Kaçar, The effect of preheat & post weld heat treatment on the laser weldability of AISI 420 martensitic stainless steel, Mater. Des. 64 (2014) 221–

226.

[263] K. Hao, C. Zhang, X. Zeng, M. Gao, Effect of heat input on weld microstructure and toughness of laser-arc hybrid welding of martensitic stainless steel, J. Mater. Process. Technol. 245 (2017) 7–14.

[264] M. Kang, G. Park, J.-G. Jung, B.-H. Kim, Y.-K. Lee, The effects of annealing temperature and cooling rate on carbide precipitation behavior in H13 hot-work tool steel, J. Alloys Compd. 627 (2015) 359–366.

[265] S.R. Allahkaram, S. Borjali, H. Khosravi, Investigation of weldability and property changes of high pressure heat-resistant cast stainless steel tubes used in pyrolysis furnaces after a five-year service, Mater. Des. 33 (2012) 476–484.

[266] D.A. Porter, K.E. Easterling, M. Sherif, Phase Transformations in Metals and Alloys, (Revised Reprint), CRC press, 2009.

[267] B. AlMangour, M.-S. Baek, D. Grzesiak, K.-A. Lee, Strengthening of stainless steel by titanium carbide addition and grain refinement during selective laser melting, Mater. Sci. Eng. A. 712 (2018) 812–818.

[268] H. Nakagawa, T. Miyazaki, Effect of retained austenite on the microstructure and mechanical properties of martensitic precipitation hardening stainless steel, J. Mater. Sci. 34 (1999) 3901–3908.